

**Best
Available
Copy**

AD-761 203

WAVE PROPAGATION IN ANISOTROPIC ROCKS

Werner Goldsmith, et al

California University

Prepared for:

Advanced Research Projects Agency
Bureau of Mines

1 June 1973

DISTRIBUTED BY:

NTIS

National Technical Information Service
U. S. DEPARTMENT OF COMMERCE
5285 Port Royal Road, Springfield Va. 22151

AD 761203

WAVE PROPAGATION IN ANISOTROPIC ROCKS

Final Technical Report

Contract No. H0220021

Sponsored by Advanced Research Projects
Agency, ARPA Order No. 1579, Amend. 3

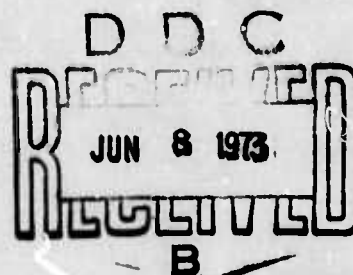
Program Code 62701D

Principal Investigator: Dr. W. Goldsmith
Faculty Investigator: Dr. J. L. Sackman

University of California
Berkeley, California 94720

June 1, 1973

Reproduced by
NATIONAL TECHNICAL
INFORMATION SERVICE
U S Department of Commerce
Springfield VA 22151



DISTRIBUTION STATEMENT A
Approved for public release
Distribution Unlimited

Unclassified

Security Classification

DOCUMENT CONTROL DATA - R & D

(Security classification of title, body of abstract and indexing annotation must be entered when the overall report is classified)

1. ORIGINATING ACTIVITY (Corporate author)		2a. REPORT SECURITY CLASSIFICATION	
University of California, Berkeley		Unclassified	
		2b. GROUP	
3. REPORT TITLE			
WAVE PROPAGATION IN ANISOTROPIC ROCKS			
4. DESCRIPTIVE NOTES (Type of report and inclusive dates)			
Final Technical Report, February 23, 1972 to June 1, 1973			
5. AUTHOR(S) (First name, middle initial, last name)			
Werner Goldsmith and Jerome L. Sackman			
6. REPORT DATE		7a. TOTAL NO. OF PAGES	7b. NO. OF REFS
June 1, 1973		247 260	81
8a. CONTRACT OR GRANT NO.		9a. ORIGINATOR'S REPORT NUMBER(S)	
H0220021		4	
8b. PROJECT NO.		9b. OTHER REPORT NO(S) (Any other numbers that may be assigned this report)	
ARPA Order No. 1579, Amend. 3			
8c. Program Code No. 62701D			
10. DISTRIBUTION STATEMENT			
Distribution of this document is unlimited			
11. SUPPLEMENTARY NOTES		12. SPONSORING MILITARY ACTIVITY	
		Advanced Research Projects Agency	
13. ABSTRACT			
<p>This report summarizes the results of a two-year analytical and experimental effort concerned with the investigation of body waves and surface waves in isotropic and anisotropic half-spaces. These were modeled by large blocks of limestone and Yule marble, respectively, that were subjected to pulses produced by the impact of steel spheres on loading bars attached normally to the surface of these blocks. The measured input served as the boundary condition for an analysis of the system that yielded the field parameters both by means of an integral transform solution and a finite element procedure. The results were compared with stress histories measured by specially-designed and calibrated crystal transducers. The dynamic constants needed for the anisotropic analysis were obtained from wave velocity measurements in various directions on the Yule marble block and an optimization procedure subjected to certain physical constraints. Static and dynamic tests in tension and compression for various orientations of Yule marble samples, as well as cyclic loading, creep and some fracture tests have also been executed on samples of Yule marble.</p>			

DD FORM 1473
1 NOV 66

Unclassified

Security Classification

14. KEY WORDS	LINK A		LINK B		LINK C	
	ROLE	WT	ROLE	WT	ROLE	WT
Rock mechanics Properties of rock Fracture of rock Wave propagation Anisotropic half-spaces Impact Transient signals in rocks Transducers Finite element analysis Integral transform techniques						

WAVE PROPAGATION IN ANISOTROPIC ROCKS

Final Technical Report

Contract No. H0220021

Sponsored by Advanced Research Projects
Agency, ARPA Order No. 1579, Amend. 3

Program Code 62701D

Principal Investigator: Dr. W. Goldsmith
Faculty Investigator: Dr. J. L. Sackman

University of California
Berkeley, California 94720

June 1, 1973

FINAL TECHNICAL REPORT

ARPA Order Number: 1579, Amendment 3
Program Code Number: 62701D
Contractor: The Regents of the University of California
Effective Date of Contract: February 23, 1972
Contract Expiration Date: June 30, 1973
Amount of Contract: \$62,436.00
Contract Number: H0220021
Principal Investigator: Professor W. Goldsmith, (415)642-3739
Project Engineer: Professor J. L. Sackman (415)642-2950
Title: "Wave Propagation in Anisotropic Rocks"
Report Period: February 23, 1972 to June 1, 1973

Sponsored by

Advanced Research Projects Agency

ARPA Order No. 1579 Amend. 3

Program Code 62701D

This research was supported by the Advanced Research Projects Agency of the Department of Defense and was monitored by the Bureau of Mines under Contract No. H0220021.

The views and conclusions contained in this document are those of the authors and should not be interpreted as necessarily representing the official policies, either expressed or implied, of the Advanced Research Projects Agency or the U. S. Government.

ABSTRACT

This is the final report of a two-year activity involving a theoretical and experimental investigation of non-destructive wave propagation resulting from the impact of steel spheres on a Yule marble block, including a determination of its static and dynamic mechanical properties. The basic system was modeled as a transversely isotropic half-space with the axis of elastic symmetry lying in the free surface loaded by means of a specified normal force of variable shape and duration. This simulates the experimental conditions where a large block of Yule marble is loaded by metallic bars in intimate contact that are subjected to longitudinal impact of steel spheres with the input monitored by a sandwiched crystal arrangement. Calibrated crystal transducer packages that were developed as part of the program have been embedded at various points of two Yule marble blocks and have provided records of the transient stresses and wave velocities at both interior and surface positions.

A solution of the mathematical model has been accomplished using integral transform methods that make use of an inversion procedure in the complex plane involving a Cagniard-de Hoop path. An important part of the manipulation involves the evaluation of the roots of this path from a sextic algebraic equation that breaks down into a quartic and a quadratic factor. Formulations for the displacements, strains and stresses within the entire domain resulting from the application of a point load on the surface of the half-space representing a Heaviside function of time have been obtained, characterizing a basic solution of the problem. The determination of these parameters for an actual impact situation is accomplished by convolving the measured input for each case with the basic solution. A computer program has been developed that has yielded numerical results for the predicted stress histories at selected stations corresponding to certain experimentally-determined inputs.

A finite element program corresponding to the integral transform analysis has also been developed. The initial application of this program was the prediction of the field variables in a block of limestone, representing an essentially isotropic material, and a comparison of these with corresponding experimental data obtained by means of internal transducer packages under loading conditions similar to those described above; excellent correlation was obtained. The program was extended to the transversely isotropic case; satisfactory correspondence was found to prevail between the predictions both of the integral transform and the finite element solution with recorded test information. However, better correlation with the data existed with the finite element technique close in, and with the integral transform solution at more distant stations. The elastic constants employed in these evaluations were deduced from wave speed data in different directions involving the actual specimen and an optimization procedure subject to constraints based on presumed positive values of these parameters.

The macroscopic properties of the marble were obtained both by petrographic and mechanical methods. The axis of transverse isotropy was ascertained by means of crystallography; the material exhibited an average crystal size of 0.5 mm. The five constants describing the presumed purely elastic behavior were obtained for quasi-static uniaxial compression; creep tests on specimens oriented both parallel and perpendicular to the symmetry axis indicated little viscoelastic behavior at low stress levels, but dominance of this effect near fracture. Compressive quasi-static stress-strain curves to fracture were obtained at rates from 10^{-6} to 10^{-2} per second for the two directions of interest, and numerous tensile quasi-static curves were also secured. Hopkinson-bar experiments on rods cut from three different directions yielded the values of the dynamic constants for both tensile and compressive low stress levels, amounting to about twice the corresponding quasi-static values. Compressive and tensile fracture stresses parallel and perpendicular to the axis of symmetry were obtained from split

Hopkinson-bar specimens possessing a special contour at rates of 10 per second. The totality of the tests conducted indicated that the material behaves in a very complicated manner even at low stress levels and that the use of appropriate material constants is crucially dependent on both stress level and loading history.

TABLE OF CONTENTS

	<u>Page</u>
Abstract	i
Introduction	1
Tecinical Accomplishments	4
References	18
Table	19
List of Figures	20
Appendix A	
Section 1. Introduction	A-1
Section 2. Statement and Solution of the Problem	A-4
2.1 Statement of the Problem	A-4
2.2 Formal Solution	A-7
2.3 Transformation of the Formal Solution	A-12
2.4 The Cagniard-de Hoop Transformation and Inversion of the Laplace-Transformed Displacements	A-14
2.5 Displacements due to a Normal Impact Force on the Free Surface	A-17
2.6 The Rayleigh Wave	A-19
Section 3. Numerical Procedures	A-21
3.1 Introduction	A-21
3.2 Computer Program	A-22
3.3 Results	A-22
Section 4. Discussion and Conclusions	A-23
4.1 Introduction	A-23
4.2 Comparison of Analytical Results for Body Waves in an Isotropic Medium	A-23
4.3 Comparison of the Analytical Results with the Finite Element Method and Experimental Data	A-25
4.4 Surface Waves	A-28
4.5 Conclusions	A-29
References	A-31
Table	A-34
List of Figures	A-35

Appendix B

Users Manual and Fortran Listing for the Finite Element Method
Applied to Wave Propagation Analysis in Isotropic and Anisotropic
Media

Appendix C Experimental Examination of Wave Processes in Natural Rock

Section I. Scope and Objectives	C-1
I.1 Scope of the Experimental Investigation	C-1
I.2 Objectives of the Experimental Work	C-2
Section II. Design, Development and Calibration of the Piezoelectric Transducers	C-4
II.1 Design and Development of the Transducer	C-4
II.2 Choice of the Piezoelectric Crystal Element	C-9
II.3 Construction and Assembly of the Transducers	C-11
II.4 Development of a Split Hopkinson Bar Arrangement for Calibration	C-11
II.5 External Calibration of the Transducers	C-13
II.6 In Situ Calibration	C-15
II.7 Correlation of the External Calibration with In Situ Calibration in Rock Bars	C-16
Section III. Body Wave Propagation in an Isotropic Rock Model	C-19
III.1 Introduction	C-19
III.2 Installation of the Transducers	C-20
III.3 Generation and Measurement of Input Pulse	C-21
III.4 Measurement of Body Wave Propagation	C-22
Section IV. Body Wave Propagation in an Anisotropic Rock Model	C-24
IV.1 Direction of the Axis of Elastic Symmetry	C-24
IV.2 Determination of Transducer Locations	C-24
IV.3 Transducers Employed	C-27
IV.4 Preparation of the Yule Marble Block	C-27
IV.5 Body Wave Propagation Measurements	C-28
Section V. Surface Wave Propagation in the Anisotropic Rock	C-30
V.1 Anisotropic Model for Surface Waves	C-30
V.2 Objectives	C-31
V.3 Transducer Modification	C-31
V.4 Location and Installation of Transducers	C-32
V.5 Surface Wave Propagation Measurements	C-33

	<u>Page</u>
Section VI. Summary of the Experimental Investigation	C-34
VI.1 Stress Factors from External Calibration Constants	C-34
VI.2 Body Wave Measurements in the Isotropic Model	C-34
VI.3 Body Wave Measurements in the Yule Marble Block	C-34
VI.4 Surface Wave Measurements in the Yule Marble Block	C-34
Section VII. Determination of Dynamic Elastic Properties From Arrival Times	C-35
VII.1 Dynamic Elastic Constants of Yule Marble	C-35
VII.2 Elastic Stiffness Matrix and Velocity Equation	C-35
VII.3 Velocities from Experimental Measurements	C-38
VII.4 Determination of c_{11} and c_{33} from p-Wave Tests	C-38
VII.5 Requirements Imposed by the Positive Definite Form of the Strain Energy	C-39
VII.6 Formulation for Determining the Elastic Constants	C-40
VII.7 Minimization Technique	C-40
VII.8 Remarks	C-42
Section VIII. Discussion	C-43
VIII.1 General Outline	C-43
VIII.2 Body Wave Measurements in the Isotropic Model	C-43
VIII.3 Body Wave Measurements in the Anisotropic Model	C-47
VIII.4 Surface Wave Propagation Measurements in the Anisotropic Model	C-52
VIII.5 Determination of Dynamic Elastic Constants from Body Wave and Surface Wave Measurements	C-53
VIII.6 Stress Wave Measurements with Embedded Transducers	C-54
References	C-56
Tables	C-58
List of Figures	C-67
Appendix D Determination of Static and Dynamic Mechanical Properties of Yule Marble	
I. Introduction	D-1
II. Physical and Geometrical Characteristics	D-3
III. Quasi-Static Tests	D-5
IV. Creep Tests	D-11
V. Dynamic Tests	D-12
VI. Discussion and Conclusions	D-16

References

D-21

List of Figures

D-23

INTRODUCTION

This report represents the final annual technical report under contract H0220021 between the U.S. Bureau of Mines and the University of California on the subject entitled "Wave Propagation in Anisotropic Rocks", representing the culmination of a two-year effort. The current contract period, originally destined to expire February 22, 1973, has been extended to June 30, 1973 in order to permit the proper correlation of the various aspects of the program and suitable documentation of these phases. The body of the report will delineate the objectives, methodology and principal results of each of these subdivisions of the investigation and their overall connection; the details of the individual efforts are recorded in appendices which are self-contained.

The scope of the program was detailed in proposals identified as UCB-Eng 3154, dated August 19, 1970, and UCB-Eng 3286, dated April 26, 1971, and submitted on behalf of the University of California, Berkeley, by Werner Goldsmith as Principal Investigator; it is also spelled out in Article I of the subject contract. Briefly, the investigation can be divided into the following categories:

- (a) Theoretical Examination of the Propagation of Body Waves in a Transversely Isotropic Elastic Solid resulting from an Impact on the Free Surface by means of
 - (1) Integral Transform Techniques
 - (2) Finite Element Methods;
- (b) Experimental Examination of the Wave Processes corresponding to (a) and the Measurement of Stress Histories at various Selected Positions in the Interior or near and at the Surface resulting from Projectile Impact on a Loading Bar in intimate Contact with a large Block of Yule Marble simulating a Half-space;
- (c) Determination of Mechanical Properties of Yule Marble under Static and Dynamic Loading of variously-oriented Specimens.

Many of the results obtained have been reported previously in References (1) and (2).

The following personnel have had a major share of the responsibility of the execution of the various tasks: (i) Mr. S. L. Suh who pursued the integral transform solution and produced a computer program that yields the field variables at any position for any predetermined input, (ii) Messrs. M. Katona and G. Dasgupta who successively aided in the development of a finite element program for the subject problem that has been successfully applied for the evaluation of the desired parameters both for an isotropic and a transversely isotropic half-space loaded by a point force of arbitrary time variation, (iii) Mr. K. Krishnamoorthy who was responsible for the design, development, testing, calibration, installation and use of the transducers and their packaging that have yielded stress histories within and on the surface of limestone and Yule marble blocks under impact loading from steel spheres, and who also obtained the data and devised the technique for the specification of the dynamic elastic constants pertaining to the actual test sample, and (iv) Mr. S. Howe who conducted the crystallographic, petrographic and mechanical tests that delineated the geometric and static and dynamic material properties of the Yule marble. These students are utilizing the results of the investigation as the content of their masters theses and doctoral dissertations. Werner Goldsmith, Professor of Applied Mechanics, Department of Mechanical Engineering and Jerome L. Sackman, Professor of Engineering Science, Department of Civil Engineering, have jointly supervised the program from its inception to its conclusion and are responsible for its conduct. In addition, the project has received noticeable technical assistance from Mr. R. Kenner in the Fortran programming, from Mr. E. Lin in specimen preparation, from Mr. Tom Jones in instrumentation development, from Mr. G. Wilcox in general laboratory assistance, and from Mr. R. M. Hamilton of the Glassblowing Shop of the Department of Electrical Engineering in the fabrication of the transducers. The expert assistance of

Professor R. L. Taylor of the Department of Civil Engineering in the development of the finite element program is gratefully acknowledged.

The objectives of the program have been substantially fulfilled with the possible exception of certain aspects of fracture initiation and propagation. It was originally anticipated that this portion of the work would require a period in excess of the two years that represented the life of the contract. When advice was received that a continuation of the support was not to be expected, it was decided, with the consent of the Technical Monitor, not to initiate such an investigation since it would have to be abandoned before successful techniques could be adequately developed. On the other hand, a host of information not specifically contained in the contract has been obtained as a byproduct of the research. This includes information on surface waves obtained experimentally, and the definition (and, in a manner of speaking, the resolution) of difficulties associated with an analytical investigation of surface waves produced by impact on transversely isotropic half-spaces.

The results obtained represent not only a significant advancement of the field of wave propagation in elastic, anisotropic media, but should have considerable applicability to the interpretation of signals that might be employed by transmitters in rapid tunneling or excavation situations to send the character of the rock formations ahead of the boring device, and also should be of utility for parallel circumstances in the field of geophysical prospecting. The transducer package developed and its successful application for the measurement of internal transient stresses could find widespread employment in a multitude of fields involving basic research, design and development, testing and production of large-scale components with potential problems due to local stress concentrations or overloads. Finally, the techniques employed for the property determination of the rock employed here are individually not new, but the totality of the various tests has not been previously brought to bear on a single natural rock to ascertain its behavior pattern.

It had been the intention of the research team to suggest the continuation of the effort for the purpose of extending the results to a variety of natural rocks. With very little effort, the finite element program developed could be adapted to an orthotropic material such as Barre granite, which occurs widely in the field. With further modifications, it should be possible to include the effects of fault zones or other discontinuities in the program, and to incorporate the effects of reflections from bounding surfaces. This aspect of a continuing investigation might lead to the identification of specific discontinuities in rock strata, a subject believed to be of vast interest. It was further hoped to attack a new phase of importance in rock removal, namely a fundamental study of the comminution process. Some very preliminary experiments in this direction appeared to indicate potential for a successful pursuit of this objective. Such investigations will now have to be relegated to the future, and if initiated at all, will be sponsored and monitored by different agencies, although the group having primary interest in these domains is the U.S. Bureau of Mines.

TECHNICAL ACCOMPLISHMENTS

- (a) Theoretical Examination of the Propagation of Body Waves in a Transversely Isotropic Elastic Solid resulting from a Normal Impact on the Free Surface.

The governing equations for the physical problem involve the constitutive relations, the equations of motion and compatibility, and suitable initial and boundary conditions. For a generally anisotropic half-space subject to a normal, concentrated time-dependent load, the constitutive equations are given by

$$\sigma_{ij} = c_{ijkl} \epsilon_{kl} = \frac{1}{2} c_{ijkl} (u_{k,l} + u_{l,k}) \quad (1)$$

where u_i is the displacement vector, σ_{ij} and ϵ_{kl} are the stress and strain tensors, respectively, and c_{ijkl} is the fourth-order tensor defining the elastic constants that must satisfy symmetry relations

$$c_{ijkl} = c_{jikl} = c_{ijlk} = c_{klij} \quad (2)$$

As usual, a comma denotes differentiation with respect to the succeeding variable (s) and a summation convention applies to repeated indices for the spatial variables. For small displacements in a homogeneous medium, the equation of motion in the absence of body forces is

$$c_{ijkl} u_{k,lj} = \rho u_{i,tt} \quad (3)$$

in a Cartesian coordinate system with ρ as the mass density and t as time. For a free surface defined by the plane $x_2 = 0$, the boundary conditions prescribed is given by

$$c_{12kl} u_{k,l} \langle \alpha_1, 0, x_3, t \rangle = \delta_{12} f \langle t \rangle \delta \langle \alpha_1, x_3 \rangle \quad (4)$$

where δ_{ij} is the Kronecker delta, $f \langle t \rangle$ is the arbitrary preselected force history, and $\delta \langle \alpha_1, x_3 \rangle$ is the two-dimensional Dirac delta function. The radiation condition at infinity is also invoked, and initial quiescence is presumed. Unfortunately, a solution of the general problem, while well posed, is probably beyond the state of the art and of computational aids at the present time by purely analytical means, although its evaluation by purely numerical techniques appears quite feasible.

However, the stipulation of a transversely isotropic medium as a special case simplifies the problem sufficiently so as to permit a solution essentially in closed form by means of integral transform methods. It should be emphasized that this situation is considerably more complicated than the quasi-isotropic case treated by Kraut⁽³⁾ where the axis of elastic symmetry is perpendicular to the free surface; in the present case this axis lies in the surface of the half space. A theoretical and experimental investigation for such a situation had been undertaken previously for the particular purpose of examining surface wave motion⁽⁴⁾⁽⁵⁾. The experiments yielded surface wave group velocity, group slowness,

amplitude and attenuation curves for the Yule marble. The slowness curves were compared to corresponding analytical phase and group slowness predictions using both static and dynamic constants determined in that study, with reasonable correspondence. The present program addresses itself to the much more difficult problem of the analysis of body wave propagation.

The stress-displacement equations for the solid under consideration are given by

$$\begin{aligned}
 \sigma_{11} &= c_{11} u_{1,1} + c_{12} u_{2,2} + c_{13} u_{3,3} \\
 \sigma_{22} &= c_{12} u_{1,1} + c_{11} u_{2,2} + c_{13} u_{3,3} \\
 \sigma_{33} &= c_{13} (u_{1,1} + u_{2,2}) + c_{33} u_{3,3} \\
 \sigma_{23} &= c_{44} (u_{3,2} + u_{2,3}) \\
 \sigma_{13} &= c_{44} (u_{3,1} + u_{1,3}) \\
 \sigma_{12} &= \frac{1}{2} (c_{11} - c_{12}) (u_{1,2} + u_{2,1})
 \end{aligned} \tag{5}$$

employing standard contracted notation c_{mn} with $m, n = 1, \dots, 6$ instead of the four-index notation employed in Eq. (1). The equations of motion for this case reduce to

$$\begin{aligned}
 c_1 u_{1,11} + c_2 u_{1,22} + c_3 u_{1,33} + (c_1 - c_2) u_{2,21} + c_4 u_{3,31} &= u_{1,tt} \\
 (c_1 - c_2) u_{1,21} + c_2 u_{2,11} + c_1 u_{2,22} + c_3 u_{2,33} + c_4 u_{3,32} &= u_{2,tt} \\
 c_4 u_{1,31} + c_4 u_{2,32} + c_3 u_{3,11} + c_3 u_{3,22} + c_5 u_{3,33} &= u_{3,tt}
 \end{aligned} \tag{6}$$

where five new independent constants have been introduced using the abbreviations

$$c_1 \equiv c_{11}/\rho ; c_2 \equiv \frac{1}{2}(c_{11} - c_{12})/\rho ; c_3 \equiv c_{44}/\rho ; c_4 \equiv (c_{13} + c_{44})/\rho ; c_5 \equiv c_{33}/\rho \tag{7}$$

Equations (6) together with the initial and boundary conditions previously cited constitute the boundary value problem to be solved for the wave propagation problem in a transversely isotropic half-space due to arbitrary surface loading.

(i) Integral Transform Technique

The governing relations for the problem were subjected to a one-sided Laplace transform and a double Fourier transform as described in Refs. (1) and (5). This leads to a system of three second-order coupled ordinary differential equations. A solution assumed in the form of an exponential decaying with direction x_2 leads to a homogeneous system of algebraic equations in terms of the coefficients of the twice transformed displacement. The conditions for a non-trivial evaluation of this system yields a sextic algebraic equation that decomposes into the product of a biquadratic and a quadratic factor which define the slowness surfaces of the medium. These surfaces constitute the reciprocal vectors of the phase velocity for the material, consisting, in general, of three surfaces for a transversely isotropic material⁽⁵⁾⁽⁶⁾⁽⁷⁾. The method described is the solution of an eigenvalue problem which provides both the eigenvalues and the associated eigenvectors that are ipso facto the coefficients of the transformed displacement components.

Use of the transformed boundary conditions eliminates the unknown arbitrary constants and provides the displacement in the transform space; the Fourier inversion theorem permits the restatement of the displacement components solely in the Laplace transform space. Inversion of this expression into the real time domain is expedited by use of a spherical polar coordinate system $R, \tilde{\theta}, \phi$, with $\tilde{\theta}$ as the meridional and ϕ as the azimuthal angle for the x_1 - x_3 plane and the use of complex variables for employment of a method of solution due to Cagniard and de Hoop⁽⁸⁾⁽⁹⁾. This transformation yields a path in the complex plane whose intersection with the real axis defines the slowness surfaces of the medium and represents an absolutely necessary condition for the solution of the problem. A major portion of the numerical effort was concerned with this subsection of the analysis and its evaluation provided some important physical insight into the possible behavior patterns of the substance characterized by different polar angles. Upon employment of this procedure, the time-transformed solution could

be inverted into the real plane by inspection, and the displacement field for the entire half-space was readily programmed. A corresponding procedure was adopted for the delineation of the strain and stress variables, utilizing an initial analytical definition for these quantities from derivatives of the displacement components rather than utilizing a numerical differentiation from the evaluated displacement solutions. The numerical procedure was effected by calculating a solution for a "basic" input consisting of a Heaviside step function and then convolving a realistic input with this solution. Both a sine-squared input, considered to be a reasonable representation of sphere impact loading on a half-space, as well as actually measured pressure-time inputs were convolved with the basic solution to provide the history of the field variables for the actual physical situation that was to be analyzed.

An attempt was also made to evaluate the field variables on the free surface of the medium by taking the limiting conditions of the solution for the case when the angle of the ray along which these parameters were to be obtained approached 90 degrees relative to the normal to the free surface. Here, the Cagniard-de Hoop path collapses to the real axis which contains a Rayleigh pole. Since the path of integration must be deformed to exclude this singularity, the resulting detour around this pole no longer corresponds to real time and the contributions from the Rayleigh pole must be evaluated separately; this requirement introduced serious numerical difficulties as it yielded rapid and extreme oscillations into the solution of the basic problem so that the numerical results were significantly suspect. Since the solutions within the free surface were thus not amenable to treatment by the method indicated, results for such stations were deduced by considering rays at very small angles, of the order of 0.1 degrees from the free surface direction where the numerical solution exhibited regular behavior, although portraying its tendency towards singular behavior with a diminishing value of this angle.

Details of this portion of the investigation are presented in Appendix A. A comprehensive description of this work and its background will also be found in the doctoral dissertation by S. L. Suh presented to the Graduate Division of the University of California, Berkeley, in 1973.

(ii) Finite Element Technique

A finite element computer code, FEAP-71, developed at the University of California has been adapted and extended for application to the present problem. It is a research-oriented finite element assembly program with a selection library of twenty elements, extensive input-output utility routines and automatic error checking. The present formulation includes the construction of a three-dimensional element, associated time integration schemes suitable for use in a wave propagation problem, which are represented by an important subroutine entitled EXPLCT, a printer plot subroutine, DYNPLT, for the visualization of stress evolution, and options to utilize either analytically specified input functions or tabular information denoting the value of the impulsive load at each time step.

The dynamic formulation of the finite element method as derived from Lagrange's Central Principle was indicated in Ref. 1. The resultant set of coupled linear differential equations, given by

$$[M] \{\ddot{u}\} + [K] \{u\} = \{f\} \quad (8)$$

where $[M]$ is the diagonal mass matrix, $[K]$ is the global stiffness matrix, $\{u\}$ is the nodal displacement vector for the entire domain, $\{\ddot{u}\}$ is the nodal acceleration vector, and $\{f\}$ is the loading vector. The solution is executed by a step-by-step forward integration method known as Newmark's Beta method. The technique was initially applied to some test cases, but has since been employed for the evaluation of the stress field in an isotropic half-space, as modeled by a limestone block, where comparison with experimental information is available,

and has finally been applied to the evaluation of the corresponding transversely isotropic case as represented by sphere impact on the Yule marble block.

A report constituting a User's Manual for the use of the FEAP-72 program as applied to wave propagation problems, with several sample situations evaluated, was previously furnished⁽¹⁰⁾. An updated version of the program is included with this final report as Appendix B. This document differs from Ref. (10) primarily in some of the modifications providing for greater efficiency of execution, the inclusion of a provision for determination and use of a critical time step to avoid instabilities in the solution, and greater flexibility in the input-output arrangements of the program. The results from the program are presented along with corresponding information from the integral transform solution and from the experimental phase of the investigation.

(b) Experimental Examination of Wave Processes in Blocks of Natural Rock

The experimental determination of stress histories in the interior of rock blocks of sufficiently large dimensions to simulate half-spaces during the time of interest were conducted on a 15" x 15" x 11½" block of Bedford limestone and a 24" x 24" x 10" block of Yule marble. In addition, measurements very close to the free surface were performed on another Yule marble block of the same dimension; the axis of elastic symmetry was located in the free surface so that a normal load on the system paralleled an axis of a truly transversely isotropic half-space. The blocks were loaded by shooting 3/16" and ¼" diameter steel balls from an air gun at velocities of about 20 ft/sec against the plane end of a 1/8" diameter, or, occasionally, a ½" diameter aluminum loading bar, about 15" long, in intimate normal contact to the free surface of the specimens. The input pulse to the block was measured with a 1/8" or a ½" diameter X-cut quartz crystal sandwiched between the loading bar and the block.

The development of appropriate transducers designed to measure the stress histories in the block interiors, their construction, calibration, insertion and

fastening represented a major experimental effort as detailed in References (1) and (2). After many different devices had been tested, an optimal arrangement was produced consisting of a 1/8" diameter magnesium bar, with a length of about 10 in, at the front of which a 1/16" diameter x 0.020" thick PZT-4 crystal was sandwiched between another 1/16" long disk of magnesium of 1/8" diameter. The crystal was surrounded, but separated physically from an annular glass washer used as a spacer; the transducer leads were brought out through a slot in the magnesium bar. Voltage amplification was employed for stress measurement; the output was photographed on dual-beam oscilloscopes whose response was flat to 3 mega Hz. The transducer package exhibited a good acoustic impedance match relative to that of both the limestone and the Yule marble blocks, thus minimizing reflection problems as the result of internal mismatch. The rock blocks were cored to the desired depth in directions perpendicular to their surfaces using a 1/8" diameter drill; the installations of the transducers was accomplished by using a mixture of aluminum oxide and epoxy adhesive as the bonding agent.

All crystal transducers were individually calibrated prior to installation by the use of a split Hopkinson bar arrangement composed of magnesium with strain gages mounted on the bars furnishing a direct comparison with the crystal output. Each transducer was externally calibrated using a split Hopkinson bar. In addition, a comparison of in situ response in rock bars of the transducer with records from strain on the surface of these bars provided a relationship between the two piezoelectric constants obtained by these two types of measurements. This ratio is employed to compute a stress factor that converts measured voltage to the actual stress extant at the transducer station.

Appendix C which provides more detail on this phase of the investigation presents schematics of the locations of the transducer packages in the limestone and in the two marble blocks. The results of representative tests are shown in Figs. 1-4 together with the measured input; these data are also compared to the

analytical or numerical predictions shown, with the degree of agreement varying from excellent, in most instances, to unsatisfactory in a few cases. Excellent correspondence between the measured values and both the integral transform and finite element calculations was uniformly obtained for the isotropic limestone block which, analytically had to be regarded as a slightly anisotropic material. For Yule marble, results near the source were found to be very well predicted by the finite element method, whereas farther into the medium, the integral transform procedure yielded a much better shape for the first portion of the stress history, although deviating significantly from measured values after one cycle. The finite element technique yielded an oscillatory pattern for the normal stress in the direction perpendicular to the free surface at positions just below and close to the load, but not on the other rays in the half-space. This behavior may be due to an inherent characteristic of the procedure stemming from displacement boundary conditions along this ray and/or noise introduced into the input by the discretization. It is not a priori obvious whether other failures to produce an acceptable degree of correlation are the result of numerical or analytical difficulties, such as convergence problems, experimental vagaries, or a combination of these causes.

On the whole, considering the difficulties involved in all these processes, the predictions are very reasonable, agreeing qualitatively almost everywhere and quantitatively in the majority of instances with an acceptable degree of error. One of the problems involved in this comparison is the lack of precise knowledge of the elastic constants (which were obtained by the best available procedure described above) at the various stations, i.e. a possible degree of local inhomogeneity and/or anisotropy. It is also possible that the presumed elastic model must be modified to account for dissipative effects, particularly in view of the aberrant behavior of the material exhibited by a variety of static and dynamic tests as described in the sequel that does not conform to any published version of a "simple" substance.

The impact tests on the Yule marble blocks also furnished 46 measurements of wave arrival times at various stations that were employed to devise a procedure of determining the five dynamic elastic constants required to be specified by the theory. The procedure involved the use of the phase velocity equation and devising an objective function by a weighted least-square method and a minimizing procedure with certain embedded constraints determined by the positive definiteness of the elastic stiffness matrix that yielded values of ρc_1 to ρc_5 ranging from 11.2×10^6 psi to 2.52×10^6 psi. These values were intermediate between those used in previous dynamic analyses for Yule marble⁽⁴⁾⁽⁵⁾ and those obtained independently during the present investigation from a separate slab of the material.

(c) Determination of Static and Dynamic Mechanical Properties of Yule Marble

The macroscopic mechanical properties of Yule marble were obtained both under static and dynamic conditions in an attempt to completely characterize its constitutive behavior that is required both for an interpretation of test results and the application of analytical techniques. Yule marble was chosen as the basic substance for the present investigation because (a) numerous tests indicated that it was macroscopically homogeneous (with respect to typical wave length produced by impact) and transversely isotropic, (b) it was available in sufficiently large blocks without discontinuities to satisfy the requirements for a physical model in the present tests, (c) it had been previously examined on a number of occasions so that some correlative information, particularly in the geologic and petrographic domain, was available for comparison, and (d) it had been previously utilized for a study of surface wave phenomena under the direction of the Principal Investigator⁽⁴⁾.

All specimens were obtained from a separate marble slab obtained commercially. The specific gravity was ascertained to be 2.81, with average crystal sizes ranging from 0.2 mm to 0.7 mm. It was originally assumed that the axis of transverse

isotropy was coincident with the average normal of the bedding planes which are visually evident from grey bands of opaque mineral running through the slab. Although these planes are sometimes warped and are not completely parallel through the rock mass, their average normal was found to be relatively constant and was located in the largest plane of the slab. From thin sections taken from planes perpendicular to the bedding normal (and thus orthogonal to the assumed axis of transverse isotropy, or Z-direction) the orientation of each of 100 calcite crystals was obtained spectroscopically and the results supported both the hypothesis of transverse isotropy and its direction as properly being perpendicular to the bedding planes.

Static uniaxial compression specimens with a diameter of 1.05 in. and lengths of $1\frac{1}{2}$ in. and 2 in. for the X and the Y, Z directions, respectively, were tested in an Instron machine at rates ranging from 10^{-6} to 10^{-2} per second; strain was determined from 1/8" foil gages mounted in pairs on each specimen at the opposite end of a diameter and connected so as to eliminate flexural components. The results appeared to be independent of strain rate within this domain; however, the curves were uniformly concave upward near the origin, nearly straight in the middle third of the stress range, and concave downward in the upper third, the data in the Z-direction indicating a higher failure level than for specimens in the other two directions. These tests were also employed to obtain Young's modulus and Poisson's ratio in the directions along and perpendicular to the axis of elastic symmetry and the shear modulus in any plane perpendicular to the plane of isotropy; these were obtained on the 7th cycle of a 0-1200 psi-0 loading. The results from these as well as from the dynamic tests are presented in Table 1. It was necessary to avoid a so-called first-cycle effect which yielded appreciable hysteresis; subsequent loading along the same path yielded essentially reversible deformations.

Quasi-static tensile tests at rates ranging from 10^{-8} to 10^{-3} per second were run in the Instron tester for various sample directions and with various specimen configurations, including a modification of a special contour previously utilized in tests on bone specimens⁽¹¹⁾⁽¹²⁾. Difficulties were experienced when uniform specimens were cemented to aluminum holding pieces placed in the grips of the tester by failure occurring through such bonds; stress-strain curves obtained here may be in error due to the higher section where the gages are located and any apparent strain-rate sensitivity may be largely a property of the glue rather than that of the specimen proper. Z-direction special contour specimens were tested; as in other cases, the fracture stress was a function of the distance of the strain gage from the break, but the fracture strain in all cases was about 0.025 percent.

Y- and Z-direction specimens were subjected to both compressive and tensile creep tests in order to determine the approximate stress levels at which visco-elastic effects begin to dominate the material behavior. Compressive specimens were loaded to failure in approximately 700 psi increments at a rate of 700 psi/sec using an MTS testing machine in the constant load mode, whereas tensile specimens were loaded by weights as well as by an Instron machine, with loading rates for the latter operation limited to 30 psi/sec; these were not tested to failure. No significant creep was observed in any of the cases except in the vicinity of the failure point (6,900 and 10,000 psi for the compressive Y- and Z- specimens, respectively).

Hopkinson bars composed of three sections of rods initially 6" x 3/4", of the same orientation and glued together were supplied with aluminum endcaps to prevent local shattering under the impact of 1/2" diameter steel balls dropped from a height of 22.5 in. Longitudinal and transverse gages monitored the pulses so produced and measured wave speeds were employed to yield the dynamic elastic

constants equivalent to those determined from static tension and compression tests, shown also in Table 1, by means of a one-dimensional analysis. The latter type of hypothesis is validated by the ratio of bar radius to pulse length of 0.06 in the present case.

Split Hopkinson bar tests were performed on contoured Y- and Z-direction specimen $2\frac{1}{2}$ " long by $\frac{3}{4}$ " in diameter both in tension and compression. The samples were sandwiched between aluminum loading and recording bars all of which featured strain gage pairs connected to eliminate flexural components. A bending suppressor devised by Lewis⁽¹²⁾ was employed to minimize unwanted flexural transients. Pulses were produced by the impact of $\frac{1}{2}$ " diameter cylindrical steel projectiles with a 30° conical tip; bullets producing compressive failures had a shaft length of $2\frac{1}{2}$ in., while those inducing tensile fracture had a cylindrical section only 1 in. long. Pulses of 200 microsec duration with a nearly linear rise were produced, involving a relatively constant strain rate. The test analysis was performed based on the hypotheses of one-dimensional stress distribution, neglect of lateral inertia and shear, small elastic strains, an equivalent cylinder for the test specimen with diameter equal to that at the gage section, and the lack of effect of initial compressive wave passage on the tensile characteristics of the sample. The dynamic constants obtained from this series of tests are also presented in Table 1. Details of this phase of the work are given in Appendix D. There, Table 4 provides a comparison of the values of the elastic parameters c_1, \dots, c_5 defined by Eqs. (D-7) obtained here and in the previous investigation⁽⁴⁾⁽⁵⁾.

The presence of an initial non-linear range of the stress-strain curves followed by a secondary, nearly linear region may explain the anomaly reported in previous tests of lower values of "dynamic" constants than those of corresponding static parameters. This will be the case if the strain level for the former is considerably lower than for the latter. The rock examined does not conform to

a presently accepted three-dimensional (or even one-dimensional) constitutive relation. Initial elastic constants are valid only for small strains; tensile and compressive moduli differ both statically and dynamically, and the material exhibits a first-cycle effect. The rock is not completely brittle, but exhibits some small time-dependent plastic or viscous regions, and hysteresis accompanies unloading from any stress level beyond the initial domain. Thus the material must currently be characterized by a set of experimental data rather than by an analytical formulation.

References

- 1) Goldsmith, W. and Sackman, J. L., "Wave Propagation in Anisotropic Rocks", Annual Technical Report No. 1, Contract No. HO210022, ARPA Order No. 1579, Amend. 2, Program Code 1F10, University of California, Berkeley, 1972.
- 2) Goldsmith, W. and Sackman, J. L., "Wave Propagation in Anisotropic Rocks", Semiannual Technical Report No. 1, Contract No. HO210021, ARPA Order No. 1579, Amend. 3, Program Code 62701D, University of California, Berkeley, 1972.
- 3) Kraut, E. A., "Advances in the Theory of Anisotropic Elastic Wave Propagation", Rev. Geoph., v. 1, 1963, p. 401.
- 4) Ricketts, T. E., "Sphere Impact on an Anisotropic Half-Space", Ph.D. Dissertation, University of California, Berkeley, 1970.
- 5) Ricketts, T. E. and Goldsmith, W., "Wave Propagation in an Anisotropic Half-Space", Int. J. Rock Mech. Min. Sci., v.9, 1972, p. 493.
- 6) Buchwald, V. T., "Elastic Waves in Anisotropic Media", Proc. Roy. Soc. London, A, v. 253, 1959, p. 563.
- 7) Musgrave, M. J. P., "Elastic Waves in Anisotropic Media", Progress in Solid Mechanics, I. N. Sneddon and R. Hill, eds. v. 2. Amsterdam, North-Holland Publ. Co., 1961, p. 63.
- 8) DeHoop, A. T., "A Modification of Cagniard's Method for Solving Seismic Pulse Problems", Appl. Sci. Res., V., v. 8, 1960, p. 349.
- 9) Burridge, R., "Lamb's Problem for an Anisotropic Half-Space", Quar. J. Mech. Appl. Math., v. 24, pt. 1, 1971, p. 81.
- 10) Katona, M., "Wave Propagation with FEAP-72", Berkeley, University of California, 1972.
- 11) Heywood, R. B. Designing by Photoelasticity. London, Chapman and Hall, Ltd., 1952.
- 12) Lewis, J. L., "Dynamic Mechanical Properties of Compact Bone", Ph.D. Dissertation, University of California, Berkeley, 1972.

TABLE 1: COMPARISON OF STATIC AND DYNAMIC ELASTIC CONSTANTS

	STATIC $\dot{\epsilon} \sim 10^{-7}$ to 10^{-3} sec ⁻¹		DYNAMIC (HOPKINSON BAR) $\dot{\epsilon} \sim 1$ to 10 sec ⁻¹		DYNAMIC SPLIT HOPKINSON BAR $\dot{\epsilon} \sim 10$ - 50 sec ⁻¹	
	compression (average)	tension (average)	compression	tension	compression	tension
E ₁	4.7 x 10 ⁶ psi	8.8 x 10 ⁶ psi	11.6 x 10 ⁶ psi	10.8 x 10 ⁶ psi	10 x 10 ⁶ psi	11.3 x 10 ⁶ psi
E ₂	8.5 x 10 ⁶ psi	-	-	-	-	-
μ	.13	-	.29	.24	-	-
μ_2	.27	-	-	-	-	-
E' ₁	2.3 x 10 ⁶ psi	3.5 x 10 ⁶ psi	5.0 x 10 ⁶ psi	3.2 x 10 ⁶ psi	7.0 x 10 ⁶ psi	3.6 x 10 ⁶ psi
E' ₂	5.8 x 10 ⁶ psi	-	-	-	-	-
μ'	.05	-	.13	.09	-	-
μ'_2	.29	-	-	-	-	-
G' ₁	1.4 x 10 ⁶ psi	-	4.3 x 10 ⁶ psi	4.3 x 10 ⁶ psi	-	-
G' ₂	6.3 x 10 ⁶ psi	-	-	-	-	-

Superscript (') are || to axis of transverse isotropy (Z) for E, Young's modulus and μ , Poisson's ratio
 No superscript (') are constants in plane of isotropy
 G' is shear in any plane \perp to plane of isotropy
 Subscript 1 refers to initial nonlinear region, $\sim 1/3$ of total stress range to fracture
 Subscript 2 refers to middle linear region, $\sim 1/3 \sigma_m$ to $2/3 \sigma_m$

List of Figures

- Fig. 1 Comparison of Experimental Data for Body Waves, the Finite Element Results and the Integral Transform Analysis for the Stress σ_{zz} parallel to the Direction of Loading at a Point $1\frac{5}{8}$ " Deep with a Radial Distance of 2" from the Impact Position in a Limestone Block.
- Fig. 2 Comparison of Near-Field Experimental Data for Body Waves, the Finite Element Results and the Integral Transform Analysis for Stress σ_{yy} in a Direction Normal to the Load on the Free Surface and 55° Clockwise from the Axis of Elastic Symmetry. The Position of the Observation Station in Cylindrical Coordinates with the Impact Point as Origin is $r = 1$ ", $\theta = \pi/12$, and $z = 1\frac{1}{2}$ ".
- Fig. 3 Comparison of Far-Field Experimental Data for Body Waves, the Finite Element Results and the Integral Transform Analysis for the Stress σ_{zz} parallel to the Direction of Loading and Orthogonal to the Axis of Elastic Symmetry. The Position of the Observation Station in Cylindrical Coordinates with the Impact Point as Origin is $r = 2\frac{1}{4}$ ", $\theta = \frac{1}{2}\pi$, $z = 5$ ".
- Fig. 4 Comparison of the Experimental Data for Surface Waves with the Integral Transform Analysis for the Radial Surface Stress σ_{rr} at a Distance of 5" from the Impact Point in a Direction 30° Clockwise from the Axis of Elastic Symmetry in the Yule Marble Block.

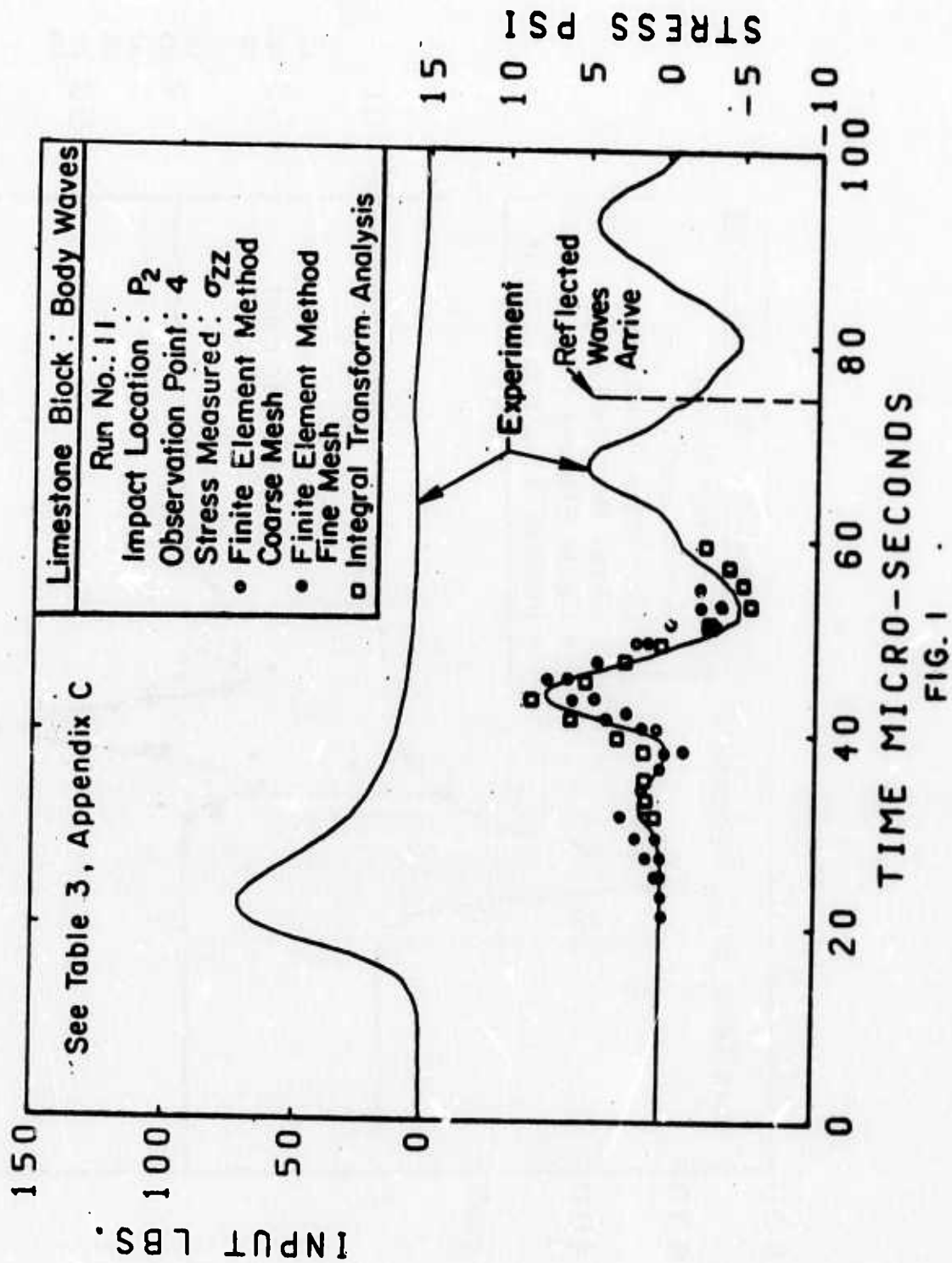


FIG. 1

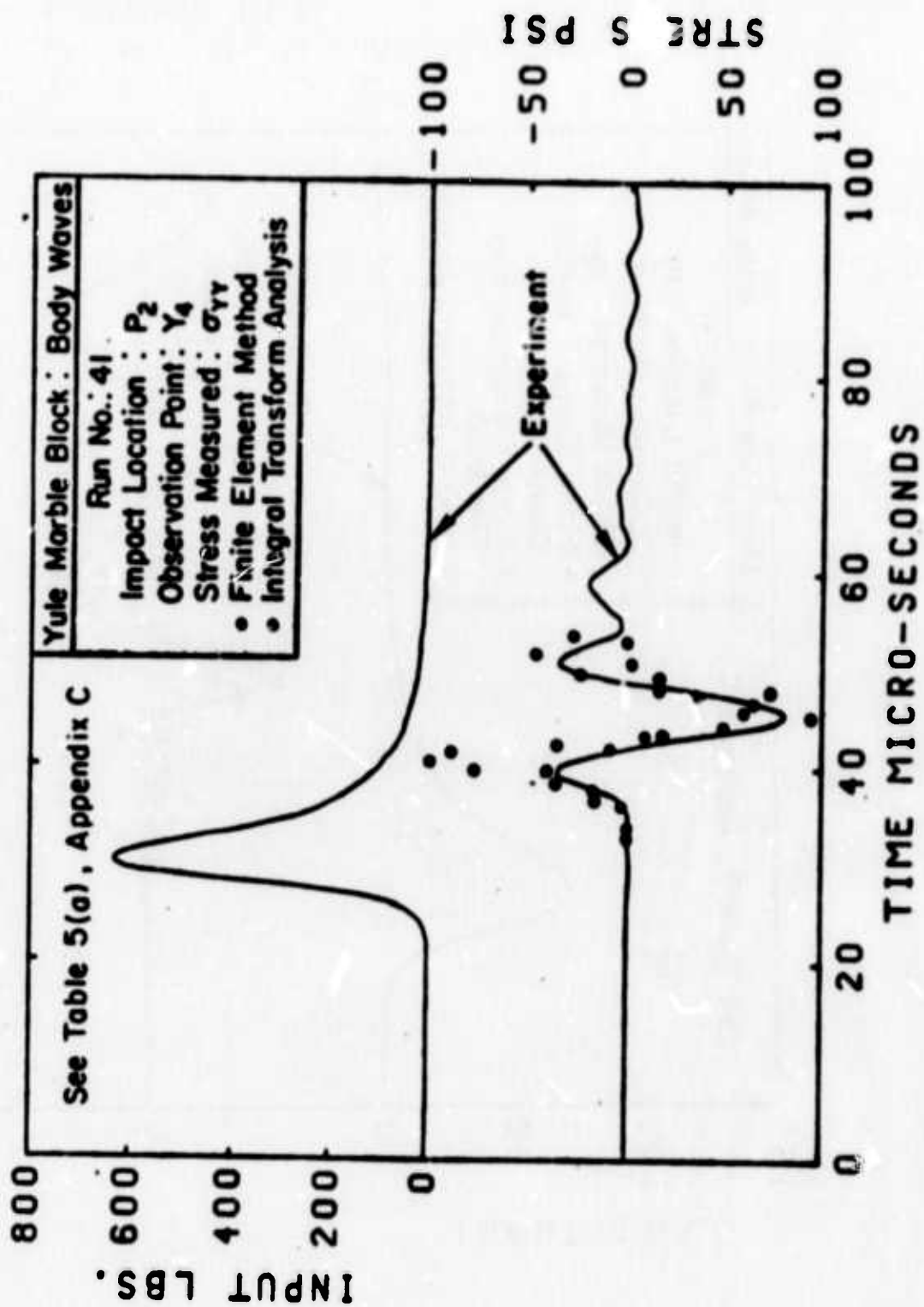


FIG. 2

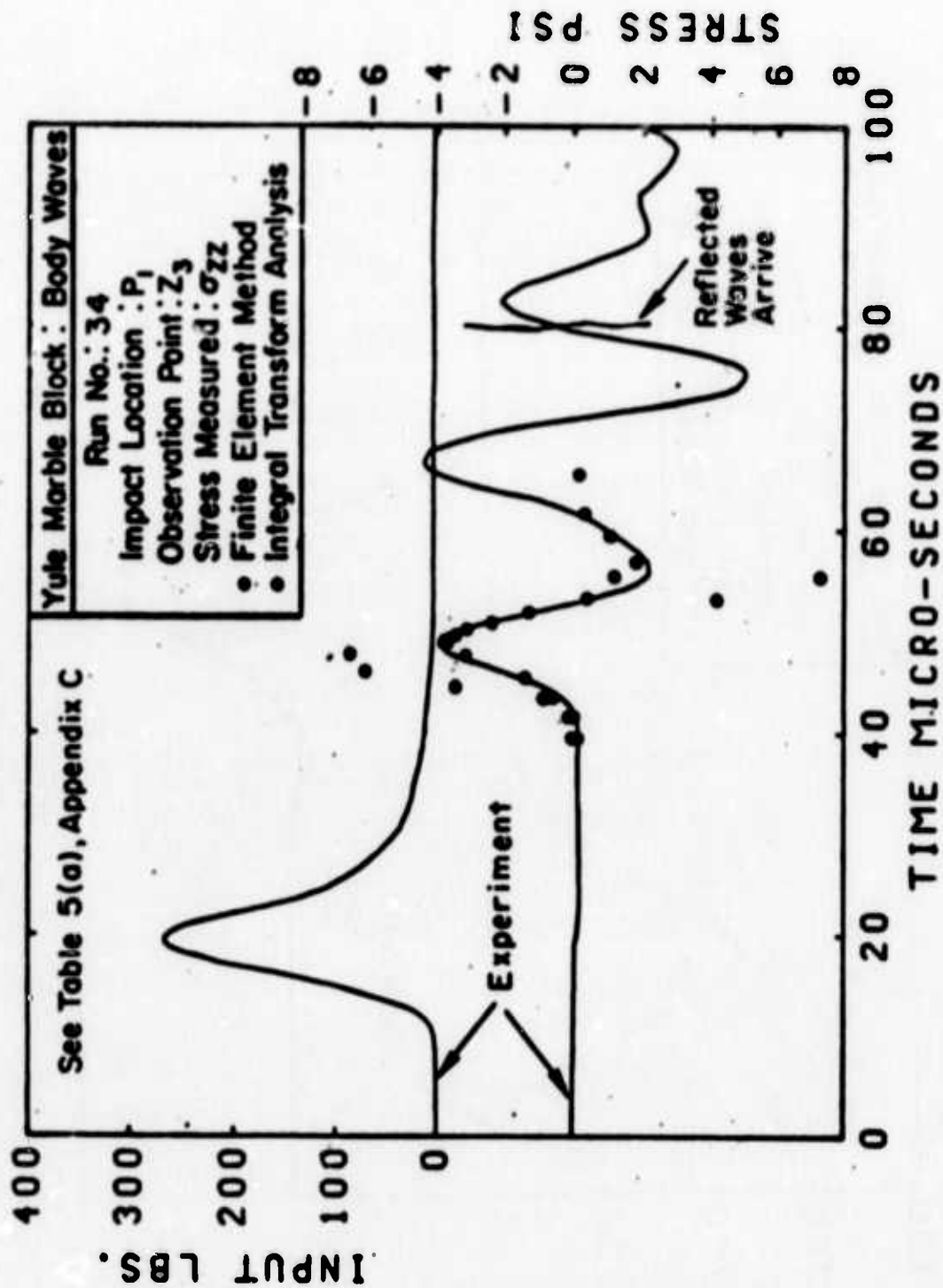


FIG. 3

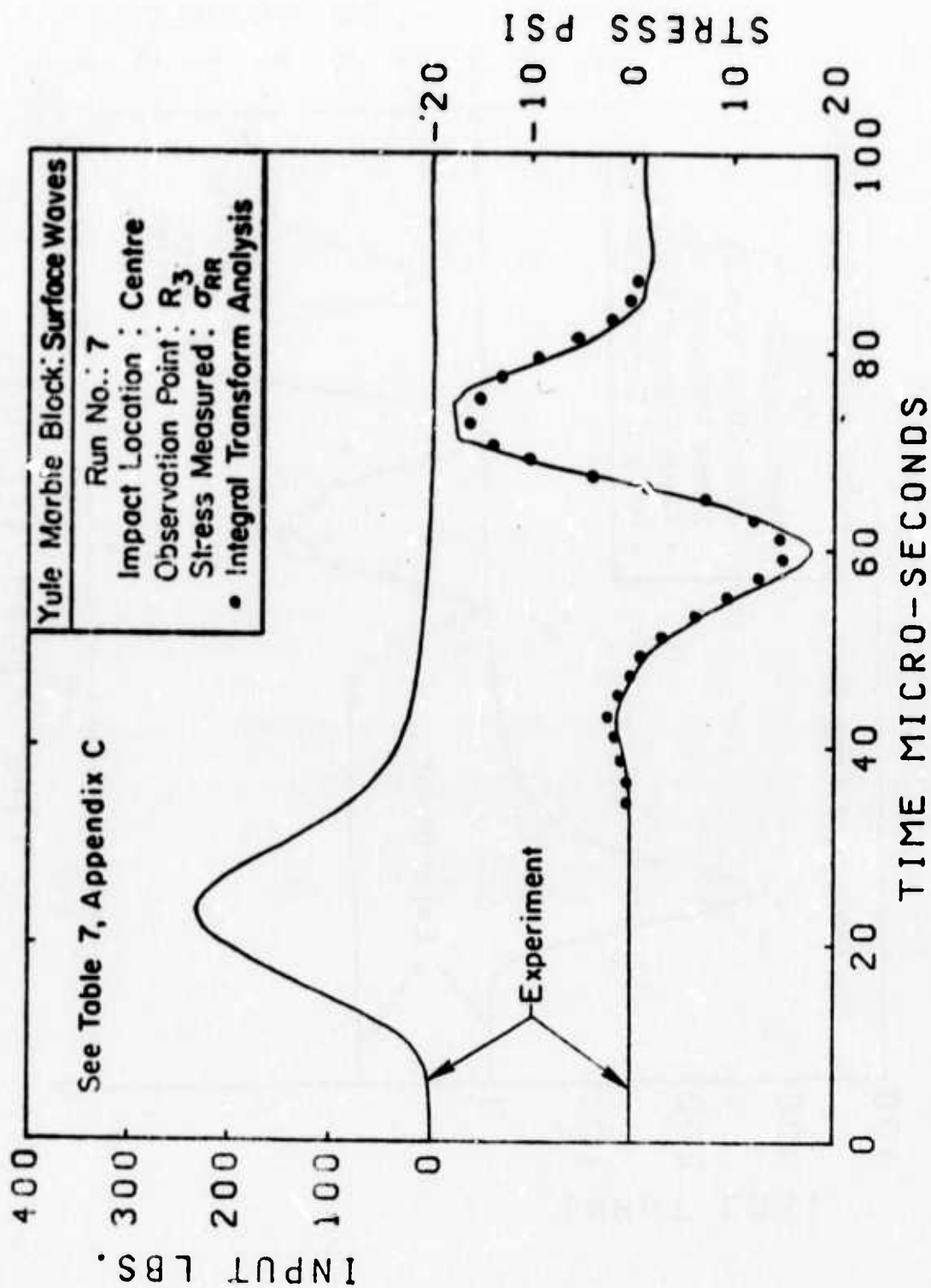


FIG. 4

APPENDIX A

Section I. Introduction

The subject treated in this investigation is concerned with wave propagation in a homogeneous, transversely isotropic, linearly elastic half-space produced by a normal concentrated time-dependent load applied to the free surface of the medium which contains the axis of elastic symmetry. This problem is known as Lamb's problem in an anisotropic half-space and it can be physically modelled by normal impact on a sufficiently large block of a transversely isotropic material such as Yule marble.

Lamb's problem for an isotropic elastic half-space has been investigated extensively^(1,2,3,4,5,6,7,8) and the wave processes in such a body are by now well understood. However, relatively few results have been obtained relating to wave propagation in anisotropic solids. An excellent summary of this topic has been presented by Musgrave⁽⁹⁾ who provided not only a classification of anisotropic media in terms of crystal symmetry but also discussed general features of the wave propagation in anisotropic substances in terms of three characteristic surfaces, that is, the velocity, slowness and wave surface. Lord Kelvin⁽¹⁰⁾ first introduced these surfaces in the course of formulating the laws of dynamics in elastic anisotropic media. The velocity surface is formed by all the radius vectors passing through a source, which is the origin of the space, each having a length proportional to the phase velocity permissible in its direction; the slowness surface is the inverse of the velocity surface with respect to a unit sphere, and the wave surface represents a surface of equal phase of waves at the time $t = 1$ that started at the origin at time $t = 0$, i.e., it is the shape of a wave front as it propagates outward from a point source, determined at the particular time $t = 1$. Musgrave also described wave processes in considerable detail for solids with specific symmetry such as hexagonal, cubic and trigonal as well as the lattice dynamics of crystals. Comprehensive references up to 1970 may be found in this volume.

Recently Burridge⁽¹¹⁾ executed a surface wave analysis for a generally anisotropic elastic half-space. He demonstrated that if a surface wave can exist in any particular direction, there will then exist a fan containing this direction along any one of whose rays such waves may propagate. This result was demonstrated by a reducio ad absurdum argument which shows that in the contrary case, a solution may be constructed to the equation of motion which is inconsistent with the principle of conservation of energy. This conclusion generalized a result by Buchwald⁽¹²⁾ and corrected a suggestion of Synge⁽¹³⁾ that, in general, undamped surface waves may only be propagated in discrete directions. In another article⁽¹⁴⁾, Burridge presented a solution for wave propagation in a generally anisotropic half-space due to a line source, employing a Fourier-Laplace transform and a Cagniard-de Hoop transformation^(15,16,17,18) that facilitates the inversion of the transformed function into the real time domain. It was shown that in spite of the possibility of certain branch points lying in a complex plane, the Cagniard-de Hoop transformation may be carried out irrespective of the orientation of the free surface or type of anisotropy. Numerical results of the surface waves for cubic copper were obtained in the form of theoretical seismograms. He also derived a solution to Lamb's problem in an anisotropic medium by integrating responses of line sources on the free surface over the unit circle.

Buchwald⁽¹⁹⁾ found the displacements due to surface waves radiating from a given harmonic source in terms of double Fourier integrals in transversely isotropic materials. He considered both the quasi-isotropic and anisotropic cases, which correspond to the axis of elastic symmetry of the medium being normal and parallel to the free surface, respectively; the slowness curve in the quasi-isotropic case was a circle and the wave curve a concentric circle. The anisotropic case exhibited more complicated behavior. He used a method developed by Lighthill⁽²⁰⁾ to estimate asymptotically the multidimensional Fourier integrals

and obtained all the geometrical properties of the waves, as well as asymptotic expressions for the wave amplitudes in terms of the distance from the source.

Kraut^(21,22) investigated a plane strain problem of pulse propagation resulting from a surface line load in a quasi-isotropic medium, a much simpler situation than for the truly transversely isotropic case. This appeared to be the first attempt of utilizing the Cagniard-de Hoop transformation in the solution of wave propagation problem in an anisotropic half-space. He discussed in full detail the physical significance of the Cagniard-de Hoop transformation in conjunction with the slowness and wave curves of the solid.

Cameron and Eason⁽²³⁾ discussed a problem involving a source which is suddenly applied at a point on the axis of elastic symmetry of an infinite transversely isotropic elastic solid. They obtained numerical values of the displacements for the quasi-isotropic case. Ryan⁽²⁴⁾ presented a solution to Lamb's problem for a transversely isotropic half-space. A Heaviside point load was directed along an axis of material symmetry which was taken as normal to the free surface so that the problem reduced to the quasi-isotropic case. Following Kraut⁽²¹⁾, a Cagniard-de Hoop transformation was employed which yielded a single finite integral for the displacement field, that was, however, evaluated numerically only for points on the surface. Ricketts⁽²⁵⁾ and Ricketts and Goldsmith⁽²⁶⁾ have attempted to solve the problem posed in this thesis, i.e., Lamb's problem for a transversely isotropic half-space with the axis of elastic symmetry located in the free surface. Although they did not obtain a solution for the displacement field in a form amenable for a numerical evaluation, the problem was formulated in a manner permitting its present utilization with only minor changes. Experimental data such as group velocity, group slowness and attenuation characteristics of the amplitude were also obtained for the surface waves produced by the normal impact of a spherical steel ball on the free plane of the half-space modelled by a large Yule marble block.

Section 2. Statement and Solution of the Problem

2.1 Statement of the Problem.

The problem will first be discussed for a general anisotropic medium and then be specialized for a transversely isotropic substance.

The anisotropic half-space is represented by a Cartesian coordinate system (x_1, x_2, x_3) as shown in Fig. 1 with the free surface defined by $x_2 = 0$ and the direction of x_2 positive toward the interior. Although the problem is formulated in a Cartesian system, cylindrical and spherical coordinate systems, indicated by (r, θ, x_2) and $(R, \tilde{\theta}, \phi)$, respectively, are also introduced in the development of the final solution. The anisotropic elastic half-space is assumed to be homogeneous and is governed by the generalized Hooke's law

$$\sigma_{ij}(\underline{x}, t) = c_{ijkl} \epsilon_{kl}(\underline{x}, t) \quad (i, j, k, l = 1, 2, 3) \quad (A2.1-1)$$

and the linearly elastic strain-displacement relation

$$\epsilon_{ij}(\underline{x}, t) = \frac{1}{2} (u_{i,j}(\underline{x}, t) + u_{j,i}(\underline{x}, t)) \quad (A2.1-2)$$

Here, \underline{x} is the position vector, t is time, and $u_i(\underline{x}, t)$, $\sigma_{ij}(\underline{x}, t)$ and $\epsilon_{ij}(\underline{x}, t)$ are the Cartesian components of the displacement vector, and the stress and strain tensor, respectively. Also, c_{ijkl} is the fourth-order tensor of the elastic constants that satisfy the symmetry relations

$$c_{ijkl} = c_{jikl} = c_{ijlk} = c_{klij} \quad (A2.1-3)$$

if a strain energy exists. Then among the 81 quantities in c_{ijkl} , only 21 are independent for the most general anisotropic elastic medium. Throughout the following discussion, the usual tensor notation and summation convention on spatial variables are employed. A comma indicates partial differentiation with respect

to the subsequent variable(s). In an elastic medium obeying relations (A2.1-1), (A2.1-2) and (A2.1-3), the displacement equation of motion in the absence of body forces is given by

$$c_{ijkl} u_{k,lj}(\underline{x},t) = \rho u_{i,tt}(\underline{x},t) \quad (A2.1-4)$$

where ρ is the mass density. A concentrated load with an arbitrary time history is considered to be applied on the free surface at $\underline{x} = 0$. The boundary condition then becomes

$$c_{i2kl} u_{k,l}(\underline{x}_1, 0, \underline{x}_3, t) = -F_i(t) \delta(\underline{x}_1, \underline{x}_3) \quad (A2.1-5)$$

on $x_2 = 0$, where $\delta(\underline{x}_1, \underline{x}_3)$ is the two-dimensional Dirac delta function and $F_i(t)$ are the components of the arbitrary force with $F_i(t) = 0$ for $t < 0$. The radiation condition at infinity is also invoked so that

$$\lim_{|\underline{x}| \rightarrow \infty} [u_i(\underline{x},t), u_{i,j}(\underline{x},t), \text{etc.}] = 0 \quad (A2.1-6)$$

Finally, the medium is assumed to be at rest initially; thus the initial condition is represented by

$$[u_i(\underline{x},0), u_{i,t}(\underline{x},0)] = 0 \quad \text{for } t \leq 0 \quad (A2.1-7)$$

As can be seen from the boundary condition (A2.1-5), the force applied on the boundary need not be confined to the case of a normal impact on the free surface $x_2 = 0$ since it can exhibit other components in the formulation and in the formal solution; however, numerical results have been obtained here only for the case of normal impact, i.e., when $F_1(t) \equiv F_3(t) \equiv 0$, and $F_2(t) \neq 0$.

The problem posed above may be solved formally in exact form in a single finite integral by using a Cagniard-de Hoop transformation⁽¹⁴⁾. However, in view of the complexity involved in the computer programming for the case of general

anisotropy, attention is here restricted to a transversely isotropic half-space with the axis of elastic symmetry, chosen as the x_3 -axis, located in the free surface. The symmetry of the medium permits a factorization of the characteristic equation of the system; this feature saves computing time in the numerical evaluation of field quantities from the formal solution obtained. Moreover, due to the choice of the direction of the applied force $F_2(t)$, which is normal to the free surface that contains the axis of elastic symmetry, the solution is obtained for a truly transversely isotropic medium rather than for the quasi-isotropic case. Out of 21 elastic constants necessary to describe the properties of a general anisotropic medium, only five independent non-zero values are required for the present case. Therefore, the stress-displacement relations, from Eqs. (A2.1-1) and (A2.1-2), are reduced to

$$\begin{aligned}
 \sigma_{11} &= c_{11}u_{1,1} + c_{12}u_{2,2} + c_{13}u_{3,3} \\
 \sigma_{22} &= c_{12}u_{1,1} + c_{11}u_{2,2} + c_{13}u_{3,3} \\
 \sigma_{33} &= c_{13}u_{1,1} + c_{13}u_{2,2} + c_{33}u_{3,3} \\
 \sigma_{23} &= c_{44}(u_{2,3} + u_{3,2}) \\
 \sigma_{13} &= c_{44}(u_{1,3} + u_{3,1}) \\
 \sigma_{12} &= \frac{1}{2}(c_{11} - c_{12})(u_{1,2} + u_{2,1})
 \end{aligned}
 \tag{A2.1-8}$$

where the standard contracted notation c_{MN} with $M, N = 1, 2, \dots, 6$ has been employed instead of a fourth-order tensor representation c_{ijkl} ⁽²⁷⁾. The displacement equations of motion (A2.1-4) reduce to

$$\begin{aligned}
 c_1 u_{1,11} + c_2 u_{1,22} + c_3 u_{1,33} + (c_1 - c_2) u_{2,21} + c_4 u_{3,31} &= u_{1,tt} \\
 (c_1 - c_2) u_{1,21} + c_2 u_{2,11} + c_1 u_{2,22} + c_3 u_{2,33} + c_4 u_{3,32} &= u_{2,tt}
 \end{aligned}$$

$$c_4 u_{1,31} + c_4 u_{2,32} + c_3 u_{3,11} + c_3 u_{3,22} + c_5 u_{3,33} = u_{3,tt} \quad (A2.1-9)$$

where five new independent velocity constants have been defined by

$$\begin{aligned} c_1 &= c_{11}/\rho, \quad c_2 = \frac{1}{2}(c_{11}-c_{12})/\rho, \quad c_3 = c_{44}/\rho \\ c_4 &= (c_{13} + c_{44})/\rho, \quad c_5 = c_{33}/\rho \end{aligned} \quad (A2.1-10)$$

For the transversely isotropic medium, the boundary conditions (A2.1-5) reduce to

$$\begin{aligned} c_2(u_{1,2} + u_{2,1}) &= -\frac{F_1(t)}{\rho} \delta(x_1, x_3) \\ (c_1 - 2c_2)u_{1,1} + c_1 u_{2,2} + (c_4 - c_3)u_{3,3} &= -\frac{F_2(t)}{\rho} \delta(x_1, x_3) \\ c_3(u_{3,2} + u_{2,3}) &= -\frac{F_3(t)}{\rho} \delta(x_1, x_3) \end{aligned} \quad (A2.1-11)$$

on $x_2 = 0$.

2.2 Formal Solution.

In view of the initial conditions (A2.1-7), the boundary conditions (A2.1-11), and the radiation condition (A2.1-6), an appropriate method of solution for the system of second order, linear partial differential equations (A2.1-9) governing the response of transversely isotropic media is represented by successive employment of the Laplace and double Fourier transforms

$$F^*(s) = \int_0^\infty F(t) e^{-st} dt, \quad F(t) = \frac{1}{2\pi i} \int_{Br} F^*(s) e^{st} ds \quad (A2.2-1)$$

$$\begin{aligned} \tilde{F}(\alpha_1, \alpha_3) &= \iint_{-\infty}^{\infty} F(x_1, x_3) e^{-is(\alpha_1 x_1 + \alpha_3 x_3)} dx_1 dx_3 \\ F(x_1, x_3) &= \frac{s^2}{(2\pi)^2} \iint_{-\infty}^{\infty} \tilde{F}(\alpha_1, \alpha_3) e^{is(\alpha_1 x_1 + \alpha_3 x_3)} d\alpha_1 d\alpha_3 \end{aligned} \quad (A2.2-2)$$

where s is the Laplace transform parameter, Br is the Bromwich contour in the right-half of the s -plane and $i = \sqrt{-1}$. α_1 and α_3 are real Fourier transform parameters, and a scaling factor s is introduced in the set (A2.2-2) for convenience in later computations. F^* and \tilde{F} represent Laplace and Fourier transformed quantities of the function F , respectively. The necessary transform and inversion theorems are discussed in detail in Ref. (28).

Applying these transforms to (A2.1-9) in conjunction with initial conditions (A2.1-7) and the radiation conditions (A2.1-6), the system of ordinary differential equations in x_2

$$\begin{aligned} [c_2 D^2 - s^2(c_1 \alpha_1^2 + c_3 \alpha_3^2 + 1)] \tilde{u}_1 - (c_1 - c_2) i s \alpha_1 D \tilde{u}_2 - c_4 s^2 \alpha_1 \alpha_3 \tilde{u}_3 &= 0 \\ -(c_1 - c_2) i s \alpha_1 D \tilde{u}_1 + [c_1 D^2 - s^2(c_2 \alpha_1^2 + c_3 \alpha_3^2 + 1)] \tilde{u}_2 - c_4 i s \alpha_3 D \tilde{u}_3 &= 0 \\ -c_4 s^2 \alpha_1 \alpha_3 \tilde{u}_1 - c_4 i s \alpha_3 D \tilde{u}_2 + [c_3 D^2 - s^2(c_3 \alpha_1^2 + c_5 \alpha_3^2 + 1)] \tilde{u}_3 &= 0 \end{aligned} \quad (A2.2-3)$$

is obtained where $D \equiv \frac{d}{dx_2}$.

The similarly transformed boundary conditions of (A2.1-11) are obtained as

$$\begin{aligned} c_2 [D \tilde{u}_1 - i s \alpha_1 \tilde{u}_2] &= - \frac{F_1^*(s)}{\rho} \\ (c_1 - 2c_2) i s \alpha_1 \tilde{u}_1 - c_1 D \tilde{u}_2 + (c_4 - c_3) i s \alpha_3 \tilde{u}_3 &= \frac{F_2^*(s)}{\rho} \\ c_3 (D \tilde{u}_3 - i s \alpha_3 \tilde{u}_2) &= - \frac{F_3^*(s)}{\rho} \end{aligned} \quad (A2.2-4)$$

which are again a system of ordinary differential equations in x_2 .

A solution of Eqs. (A2.2-3) for \tilde{u}_k is sought in the form

$$\tilde{u}_k^* = U_k e^{-s \lambda x_2} \quad (A2.2-5)$$

Substitution of (A2.2-5) into (A2.2-3) leads to a characteristic equation in λ^2 in the partially factored form⁽²⁵⁾

$$\Omega(\lambda, \alpha_1, \alpha_3) = [c_2 \lambda' - M][(c_1 \lambda' - M)(c_3 \lambda' - N) + c_4 \alpha_3^2 \lambda'] = 0 \quad (\text{A2.2-6})$$

where

$$\begin{aligned} \lambda' &= (\lambda^2 - \alpha_1^2), \\ M &= (c_3 \alpha_3^2 + 1), \\ N &= (c_5 \alpha_3^2 + 1). \end{aligned} \quad (\text{A2.2-7})$$

Eq. (A2.2-6) represents the slowness surface of the medium. The linear factor in λ' defines a separable sheet of this surface associated with a true transverse mode of displacement, while the quadratic factor in λ' is associated with coupled quasi-longitudinal and quasi-transverse modes of displacements.

The bounded solution of (A2.2-3) satisfying radiation condition (A2.1-6) for large x_2 is found to be

$$\tilde{u}_k^* = \sum_{j=1}^3 U_{kj} e^{-s \lambda_j x_2}, \quad \text{Re}(\lambda_j) > 0 \quad (\text{A2.2-8})$$

where Re denotes the real part of the quantities indicated, and the λ_j are defined by

$$\begin{aligned} \lambda_1' &= M/c_2, \\ \lambda_{2,3}' &= \left[\frac{c_1 N + c_3 M - c_4^2 \alpha_3^2 \pm \{(c_1 N + c_3 M - c_4^2 \alpha_3^2)^2 - 4c_1 c_3 M N\}^{\frac{1}{2}}}{2c_1 c_3} \right] \end{aligned} \quad (\text{A2.2-9})$$

Only three of the nine U_{kj} are independent and they can be determined from the three boundary conditions (A2.2-4) on $x_2 = 0$. In terms of these three independent U_{kj} , say, $U_{1j} \equiv R_j$, the solution (A2.2-8) may be expanded as

$$\begin{aligned}
\tilde{u}_1^* &= R_1 e^{-s\lambda_1 x_2} + R_2 e^{-s\lambda_2 x_2} + R_3 e^{-s\lambda_3 x_2} \\
\tilde{u}_2^* &= i \frac{\alpha_1}{\lambda_1} R_1 e^{-s\lambda_1 x_2} - i \frac{\lambda_2}{\alpha_1} R_2 e^{-s\lambda_2 x_2} - i \frac{\lambda_3}{\alpha_1} R_3 e^{-s\lambda_3 x_2} \\
\tilde{u}_3^* &= \frac{c_1 \lambda_2' - M}{c_4 \alpha_1 \alpha_3} R_2 e^{-s\lambda_2 x_2} + \frac{c_1 \lambda_3' - M}{c_4 \alpha_1 \alpha_3} R_3 e^{-s\lambda_3 x_2}
\end{aligned} \tag{A2.2-10}$$

Upon substitution of Eqs. (A2.2-10) in the boundary conditions, Eqs. (A2.2-4), the following system of algebraic equations for the three unknowns R_i is obtained

$$\begin{aligned}
\frac{\lambda_1^2 + \alpha_1^2}{\lambda_1} R_1 + 2\lambda_2 R_2 + 2\lambda_3 R_3 &= \frac{F_1^*(s)}{s c_2 \rho} \\
B_1 R_1 + B_2 R_2 + B_3 R_3 &= \frac{i \alpha_1 F_2^*(s)}{s \rho} \\
\alpha_1^2 \alpha_3^2 R_1 + \lambda_1 \lambda_2 (\alpha_3^2 + b_2) R_2 + \lambda_1 \lambda_3 (\alpha_3^2 + b_3) R_3 &= \frac{\lambda_1 \alpha_1 \alpha_3}{s c_3} \frac{F_3^*(s)}{\rho}
\end{aligned} \tag{A2.2-11}$$

where $B_1 = 2c_2 \alpha_1^2$

$$B_j = c_1 \lambda_j' + 2c_2 \alpha_1^2 - (c_4 - c_3) b_j; \quad j = 2, 3$$

$$b_j = (c_1 \lambda_j' - M)/c_4; \quad j = 2, 3$$

and the λ' and M are defined by Eq. (A2.2-7). Solving the system (A2.2-11) and rearranging the result, R_i may be put in the matrix form

$$R_i = D_{ij} F_j \tag{A2.2-12}$$

where

$$D_{11} = \frac{1}{c_2} \{B_2 \lambda_1 \lambda_3 (\alpha_3^2 + b_3) - B_3 \lambda_1 \lambda_2 (\alpha_3^2 + b_2)\}$$

$$D_{12} = i \alpha_1 \{2 \lambda_1 \lambda_2 \lambda_3 (\alpha_3^2 + b_2) - 2 \lambda_1 \lambda_2 \lambda_3 (\alpha_3^2 + b_3)\}$$

$$D_{13} = \frac{\lambda_1 \alpha_1 \alpha_3}{c_3} \{2 \lambda_2 B_3 - 2 \lambda_3 B_2\}$$

$$D_{21} = \frac{1}{c_2} \{B_3 \alpha_1^2 \alpha_3^2 - B_1 \lambda_1 \lambda_3 (\alpha_3^2 + b_3)\}$$

$$D_{22} = i \alpha_1 \{(\lambda_1^2 + \alpha_1^2) \lambda_3 (\alpha_3^2 + b_3) - 2 \lambda_3 \alpha_1^2 \alpha_3^2\}$$

$$\begin{aligned}
D_{23} &= \frac{\lambda_1 \alpha_1 \alpha_3}{c_3} \{ 2\lambda_3 B_1 - B_3 \frac{\lambda_1^2 + \alpha_1^2}{\lambda_1} \} \\
D_{31} &= \frac{1}{c_2} \{ B_1 \lambda_1 \lambda_2 (\alpha_3^2 + b_2) - B_2 \alpha_1^2 \alpha_3 \} \\
D_{32} &= i\alpha_1 \{ 2\lambda_2 \alpha_1^2 \alpha_3^2 - \lambda_2 (\alpha_3^2 + b_2) (\lambda_1^2 + \alpha_1^2) \} \\
D_{33} &= \frac{\lambda_1 \alpha_1 \alpha_3}{c_3} \{ \frac{\lambda_1^2 + \alpha_1^2}{\lambda_1} B_2 - 2B_1 \lambda_2 \}
\end{aligned} \tag{A2.2-13}$$

$$F_{T1} = \frac{1}{\rho} \frac{F_1^*(s)}{D_0}, \quad F_{T2} = \frac{1}{\rho} \frac{F_2^*(s)}{D_0}, \quad F_{T3} = \frac{1}{\rho} \frac{F_3^*(s)}{D_0} \tag{A2.2-14}$$

with the determinant of the coefficients of R_i in Eqs. (A2.2-11) given by

$$D_0 = \begin{vmatrix} \frac{\lambda_1^2 + \alpha_1^2}{\lambda_1} & 2\lambda_2 & 2\lambda_3 \\ B_1 & B_2 & B_3 \\ \alpha_1^2 \alpha_3^2 & \lambda_1 \lambda_2 (\alpha_3^2 + b_2) & \lambda_1 \lambda_3 (\alpha_3^2 + b_3) \end{vmatrix} \tag{A2.2-15}$$

Upon substituting Eq. (A2.2-12) into the system (A2.2-10), the displacement field in transformed space can be expressed in a matrix form as

$$\begin{bmatrix} \tilde{u}_1^*(\alpha_1, \alpha_3, s; x_2) \\ \tilde{u}_2^*(\alpha_1, \alpha_3, s; x_2) \\ \tilde{u}_3^*(\alpha_1, \alpha_3, s; x_2) \end{bmatrix} = \frac{1}{s} \begin{bmatrix} R_1 & R_2 & R_3 \\ -i \frac{\alpha_1}{\lambda_1} R_1 & -i \frac{\lambda_2}{\alpha_1} R_2 & -i \frac{\lambda_3}{\alpha_1} R_3 \\ 0 & \frac{c_1 \lambda_2'^{-M}}{c_4 \alpha_1 \alpha_3} R_2 & \frac{c_1 \lambda_3'^{-M}}{c_4 \alpha_1 \alpha_3} R_3 \end{bmatrix} \begin{bmatrix} e^{-s\lambda_1 x_2} \\ e^{-s\lambda_2 x_2} \\ e^{-s\lambda_3 x_2} \end{bmatrix} \tag{A2.2-16}$$

The writing of the \tilde{u}_i^* in this fashion reflects the fact that they can be represented in terms of the sums of contributions from different components of the input force $F_i(t)$. As an example, the first column D_{i1} of D_{ij} will comprise the contributions to \tilde{u}_i^* arising from the x_1 -component $F_1^*(s)$ of the force $F_i(t)$.

Similarly D_{12} and D_{13} will comprise the contributions to \tilde{u}_1^* from $F_2^*(s)$ and $F_3^*(s)$, respectively.

After obtaining the Laplace-Fourier transformed solution \tilde{u}_1^* the application of the Fourier inversion formula given by expression (A2.2-2) yields the Laplace-transformed displacement as

$$u_1^*(\underline{x}, s) = \frac{s}{4\pi^2} \iint_{-\infty}^{\infty} v_{1j}^*(\alpha_1, \alpha_3) Q_j(\alpha_1, \alpha_3, s; \underline{x}) d\alpha_1 d\alpha_3 \quad (\text{A2.2-17})$$

where v_{1j}^* is the square matrix of the right-hand term in Eq. (A2.2-16) and

$$\begin{aligned} Q_1 &= e^{s[1(\alpha_1 x_1 + \alpha_3 x_3) - \lambda_1 x_2]}, \\ Q_2 &= e^{s[1(\alpha_1 x_1 + \alpha_3 x_3) - \lambda_2 x_2]}, \\ Q_3 &= e^{s[1(\alpha_1 x_1 + \alpha_3 x_3) - \lambda_3 x_2]}. \end{aligned} \quad (\text{A2.2-18})$$

The integrals in (A2.2-17) converge because $\text{Re}(\lambda_j) > 0$. It is still necessary to invert the Laplace-transformed solution into the real time domain. It is sufficient for the following calculations to assume that the Laplace transform parameter is real and positive. Then, Lerch's theorem⁽²⁹⁾ guarantees the existence and uniqueness of $u_1(\underline{x}, t)$.

2.3 Transformation of the Formal Solution.

Eq. (A2.2-17) together with Eqs. (A2.2-13) and (A2.2-15) comprise the Laplace-transformed displacement under arbitrary impact load; however, its form is not convenient for inversion. By a sequence of transformations and contour integrations, the integrals appearing in Eqs. (A2.2-17) will be converted into a form that allows the inversion of the Laplace-transformed solution by inspection. In this way, the exact inversion of each u_j^* will be accomplished as the sum of a single finite integral and algebraic expressions that are suitable

for numerical evaluation. For these purposes, two transformations are executed on the variables (x_1, x_3) and (α_1, α_3) .

First, a plane polar coordinate system on the free surface of the half-space is introduced, given by

$$\begin{aligned} x_1 &= r \cos \tilde{\theta} , \quad x_3 = r \sin \tilde{\theta} \\ (0 \leq r < \infty , \quad 0 \leq \tilde{\theta} < 2\pi) . \end{aligned} \quad (\text{A2.3-1})$$

Also, let

$$\begin{aligned} \alpha_1 &= w \cos \theta , \quad \alpha_3 = w \sin \theta \\ (-\infty < w < \infty , \quad -\frac{\pi}{2} < \theta \leq \frac{\pi}{2}) \end{aligned} \quad (\text{A2.3-2})$$

and let $w = -ip$ so that $d\alpha_1 d\alpha_3 = -p dp d\theta$, considering now p as a complex variable. Then, from the above transformations,

$$is(\alpha_1 x_1 + \alpha_3 x_3) = spr \cos(\tilde{\theta} - \theta) \quad (\text{A2.3-3})$$

so that Q_j in Eq. (2.2-18) becomes

$$Q_j(r, \tilde{\theta}, x_2; p, \theta, s) = e^{s[pr \cos(\tilde{\theta} - \theta) - \lambda_j x_2]} \quad (\text{A2.3-4})$$

Using the above result, the Laplace-transformed displacement (A2.2-17) may now be written as

$$u_1^*(x, s) = -\frac{s}{4\pi^2} \int_{-\frac{\pi}{2}}^{\frac{\pi}{2}} d\theta \int_{B_r} v_{1j}^*(p, \theta) Q_j(r, \tilde{\theta}, x_2; p, \theta, s) dp \quad (\text{A2.3-5})$$

where $v_{1j}^*(p, \theta)$ is defined by substitution of Eq. (2.3-2) in $v_{1j}^*(\alpha_1, \alpha_3)$.

2.4 The Cagniard-de Hoop Transformation and Inversion of the Laplace-Transformed Displacements.

As indicated earlier, inversion of the Laplace-transform will be accomplished by inspection of the solution after first performing another transformation that will be discussed here. This procedure essentially involves the rewriting of Eq. (A2.3-5) in a form that yields the Laplace transform of V_{ij} by

$$\int_0^{\infty} e^{-st} V_{ij}(\underline{x}, t; p, \theta, s) dt = u_i^*(\underline{x}, s) . \quad (A2.4-1)$$

As can be seen from Eq. (A2.2-1), which defines the Laplace transform pair, this is formally accomplished by three pairs of conformal transformations

$$\begin{aligned} \operatorname{Re}[pr \cos(\tilde{\theta} - \theta) + \lambda_j x_2] &= t , \\ \operatorname{Im}[pr \cos(\tilde{\theta} - \theta) + \lambda_j x_2] &= 0 , \quad (j = 1, 2, 3) \end{aligned} \quad (A2.4-2)$$

where t is positive and real. The above equations define the Cagniard-de Hoop transformation which is utilized in a contour integration to obtain the inversion of the Laplace transformed solution.

Substitution of the expression for λ_1 from Eq. (A2.2-9) into Eq. (A2.4-2) yields the Cagniard-de Hoop path for λ_1 in explicit form as

$$p_1^2 \left\{ \cos^2 \varphi \cos^2(\tilde{\theta} - \theta) + \left(\cos^2 \theta + \frac{c_3}{c_2} \sin^2 \theta \right) \sin^2 \varphi \right\} - p_1 \left\{ 2\tau \cos \varphi \cos(\tilde{\theta} - \theta) \right\} \left\{ \tau^2 - \frac{\sin^2 \varphi}{c_2} \right\} = 0 \quad (A2.4-3)$$

Similarly, the Cagniard-de Hoop paths for $\lambda_{2,3}$ are obtained from the expression

$$p_{2,3}^4 + A(\tau, \tilde{\theta}, \varphi, \theta) p_{2,3}^3 + B(\tau, \tilde{\theta}, \varphi, \theta) p_{2,3}^2 + C(\tau, \tilde{\theta}, \varphi, \theta) p_{2,3} + E(\tau, \tilde{\theta}, \varphi, \theta) = 0 \quad (A2.4-4)$$

Here, a transformation for the space variables was introduced, given by

$$\begin{aligned} R &= (r^2 + x_2^2)^{\frac{1}{2}} , \quad \varphi = \tan^{-1} \frac{x_2}{r} , \\ (0 \leq R < \infty , \quad -\frac{\pi}{2} \leq \varphi < \frac{\pi}{2}) \end{aligned}$$

and

$$\tau = \frac{t}{R} ,$$

where

$$\begin{aligned} A &= -\frac{2}{Z} [2\tau \cos^3 \varphi \cos^3(\tilde{\theta}-\theta) + \tau P \cos \varphi \cos(\tilde{\theta}-\theta) \sin^2 \varphi] , \\ B &= \frac{1}{Z} [6\tau^2 \cos^2 \varphi \cos^2(\tilde{\theta}-\theta) + \tau^2 P \sin^2 \varphi - \sin^2 \varphi \cos^2 \varphi \cos^2(\tilde{\theta}-\theta) e_1 - \sin^4 \varphi J] , \\ C &= -\frac{2}{Z} [2\tau^3 \cos \varphi \cos(\tilde{\theta}-\theta) - \tau \cos \varphi \sin^2 \varphi \cos(\tilde{\theta}-\theta) e_1] , \\ E &= \frac{1}{Z} [\tau^4 - \tau^2 \sin^2 \varphi e_1 + \sin^4 \varphi h_1] , \\ Z &= \cos^4 \theta + (2-m_1) \sin^2 \theta \cos^2 \theta + \frac{c_5}{c_1} \sin^4 \theta , \\ J &= e_1 \cos^2 \theta + f_1 \sin^2 \theta , \\ P &= 2 - m_1 \sin^2 \theta , \\ m_1 &= h_1 (2c_1 c_3 - c_1 c_5 - c_3^2 + c_4^2) , \\ e_1 &= h_1 (c_1 + c_3) , \\ f_1 &= h_1 (c_3 + c_5) , \\ g_1 &= h_1 (c_1 - c_5) , \\ h_1 &= 1/(c_1 c_3) . \end{aligned} \tag{A2.4-5}$$

Eq. (A2.4-3) is quadratic in p with real coefficients which can be easily solved and will yield either two real or a pair of complex conjugate roots. Eq. (A2.4-4) is quartic in p with real coefficients and will yield 4 real, or 2 real and one pair of complex conjugate or 2 pairs of complex conjugate roots. These will be found numerically as discussed in the sequel.

Following Kraut⁽²²⁾ for the construction of the Riemann surfaces of p to establish the analyticity of $\lambda_j = \lambda_j(p)$ and introducing the Cagniard-de Hoop transformation discussed above, the Laplace transformed displacement, Eq. (A2.3-5), can be written as

$$u_i^*(\underline{x}, s) = - \frac{1}{2\pi^2} \int_{-\pi/2}^{\pi/2} d\theta \int_{t_j}^{\infty} s \sum_{j=1}^3 v_{ij}^*(p_j, \theta) p_j \frac{dp_j}{dt} e^{-st} dt \quad (j=1,2,3) \quad (A2.4-6)$$

where t_j are the arrival times of the body wave fronts given by the double points of the paths. This relation is written in the desired form for an inversion of the Laplace transform and inspection yields immediately the solution in the time domain as

$$u_i(\underline{x}, t) = - \frac{1}{2\pi^2 R} \int_{-\pi/2}^{\pi/2} d\theta \int_{t_j}^t \operatorname{Re} \left[\sum_{j=1}^3 v_{ij}(t, t', p, \theta) p_j \frac{dp_j}{d\tau} \right] dt' H(t-t_j) \quad (A2.4-7)$$

Here p_j is that function of τ and \underline{x} defined in Eqs. (A2.4-3) and (A2.4-4), and

$$\begin{aligned} V_{11} &= D_{11}(p, \theta; t') \dot{F}_1(t-t') + D_{12} \dot{F}_2(t-t') + D_{13} \dot{F}_3(t-t') , \\ V_{12} &= D_{21} \dot{F}_1(t-t') + D_{22} \dot{F}_2(t-t') + D_{23} \dot{F}_3(t-t') , \\ V_{13} &= D_{31} \dot{F}_1(t-t') + D_{32} \dot{F}_2(t-t') + D_{33} \dot{F}_3(t-t') , \\ V_{21} &= - \frac{i\alpha_1}{\lambda} V_{11} , \quad V_{22} = - i \frac{\lambda_2}{\alpha_1} V_{12} , \\ V_{23} &= - \frac{\lambda_3}{i\alpha_1} V_{13} , \quad V_{31} = 0 , \\ V_{32} &= - \frac{c_1 \lambda_2'^{-M}}{c_4 \alpha_1 \alpha_3} V_{12} , \quad V_{33} = \frac{c_1 \lambda_3'^{-M}}{c_4 \alpha_1 \alpha_3} V_{13} \end{aligned} \quad (A2.4-8)$$

where the superposed dot represents differentiation with respect to time.

A fundamental solution is defined as the displacement field of the solid due to a Heaviside point load $H(t)$. Eq. (A2.4-7) can be then used to obtain the fundamental solution as follows

$$u_i^H(\underline{x}, t) = - \frac{1}{2\pi^2 R} \int_{-\pi/2}^{\pi/2} d\theta \left\{ \operatorname{Re} \left[\sum_{j=1}^3 v_{ij}^H p_j \frac{dp_j}{d\tau} \right] \right\} H(t-t_j) \quad (A2.4-9)$$

where

$$V_{11}^H = D_{11}(p, \theta) + D_{12}(p, \theta) + D_{13}(p, \theta) ,$$

$$V_{12}^H = D_{21}(p, \theta) + D_{22}(p, \theta) + D_{23}(p, \theta) ,$$

$$V_{13}^H = D_{31}(p, \theta) + D_{32}(p, \theta) + D_{33}(p, \theta) ,$$

and similar expressions for V_{2j}^H and V_{3j}^H are obtained from Eqs. (A2.4-8) upon replacing V_{ij} by V_{ij}^H for $i = 2, 3$ and $j = 1, 2, 3$. When $F_1(t)$ is replaced by the Dirac delta function $\delta(t)$, then Green's function for the system is obtained as

$$u_i^\delta(\underline{x}, t) = - \frac{1}{2\pi R} \int_{-\pi/2}^{\pi/2} d\theta \left\{ \frac{\partial}{\partial t} \operatorname{Re} \left[\sum_{j=1}^3 V_{ij}^H p_j \frac{dp_j}{d\tau} \right] \right\} H(t-t_j) \quad (\text{A2.4-10})$$

It is to be noticed that since Green's function, Eq. (A2.4-10), involves a time differentiation which generally yields poor results in numerical procedures, Eq. (A2.4-9) constitutes a better representation for the numerical evaluation of field quantities.

2.5 Displacement due to a Normal Impact Force on the Free Surface.

Since considerable effort and expense are involved in a numerical evaluation of the field quantities such as displacements and stresses, only responses due to a normal force will be considered. Thus taking $F_2(t) = F_3(t) \equiv 0$ in the above formulations, a solution is obtained for the case of normal impact. This problem, which is Lamb's problem for a transversely isotropic medium, is considerably simpler than that for an arbitrarily directed input force. Furthermore, such a numerical evaluation was compared with corresponding results for an isotropic medium and also with data that was obtained from laboratory experiments on a suitable model. If $F_2(t)$ is chosen as $F(t)$ and $F_1(t) = F_3(t) \equiv 0$ in Eq. (A2.1-11), the boundary conditions become

$$u_{1,2} + u_{2,1} = 0$$

$$(c_1 - 2c_2)u_{1,1} + c_1 u_{2,2} + (c_4 - c_3)u_{3,3} = - \frac{F(t)}{\rho} \delta(x_1, x_3)$$

$$u_{3,2} + u_{2,3} = 0$$

(A2.5-1)

on $x_2 = 0$.

Thus, all terms in Eq. (A2.4-7) which are multiplied by either $F_1(t)$ or $F_3(t)$ must vanish. The displacement for the normal impact force is obtained as

$$u_{iN}(\underline{x}, t) = - \frac{1}{2\pi \rho R} \int_{-\pi/2}^{\pi/2} d\theta \left[\int_{t_j}^t \dot{F}(t-t') \operatorname{Re} \left[\sum_{j=1}^3 W_{ij}(\underline{x}, t, t'; p, \theta) p_j \frac{dp_j}{d\tau} \right] dt' \right] H(t-t_j) \quad (A2.5-2)$$

where

$$\begin{aligned} W_{1j} &= \frac{i\alpha_1}{D_{ON}} A_j \quad ; j = 1, 2, 3 \\ W_{21} &= \frac{\alpha_1}{\lambda_1 D_{ON}} A_1 \quad ; W_{2j} = \frac{\lambda_j}{D_{ON}} A_j \quad ; j = 2, 3 \\ W_{31} &= 0 \quad , W_{3j} = \frac{ib_j}{\alpha_3 D_{ON}} A_j \quad , j = 2, 3 , \end{aligned}$$

where

$$\begin{aligned} A_1 &= - 2\lambda_1 \lambda_2 \lambda_3 (b_3 - b_2) , \\ A_2 &= \lambda_3 [\lambda_1'(\alpha_3^2 + b_3) + 2\alpha_1^2 b_3] , \\ A_3 &= - \lambda_2 [\lambda_1'(\alpha_3^2 + b_2) + 2\alpha_1^2 b_2] , \\ b_j &= (c_1 \lambda_j' - M)/c_4 \quad , j = 2, 3 \\ B_1 &= 2c_2 \alpha_1^2 , \\ B_j &= c_1 \lambda_j' + 2c_2 \alpha_1^2 - (c_4 - c_3) b_j \quad , j = 2, 3 \end{aligned} \quad (A2.5-3)$$

and

$$D_{ON} = A_1 B_1 + A_2 B_2 + A_3 B_3 .$$

λ_j' , λ_j and M are defined in Eqs. (A2.2-7) and (A2.2-9). The subscript N is used to represent the fact that quantities discussed here are derived for a normal impact force. p_j are again given by Eqs. (A2.4-3) and (A2.4-4) since these are related only to the characteristic equation of the medium considered. The fundamental solution similar to Eq. (A2.4-9) for this case can be written as

$$u_{iN}^H(\underline{x}, t) = - \frac{1}{2\pi^2 \rho R} \int_{-\pi/2}^{\pi/2} d\theta \operatorname{Re} \left[\sum_{j=1}^3 W_{ij}(\underline{x}, t; p, \theta) p_j \frac{dp_j}{d\tau} \right] H(t-t_j) \quad (\text{A2.5-4})$$

for $F(t) = H(t)$ and the Green's function corresponding to Eq. (A2.4-10) is

$$u_{iN}^\delta(\underline{x}, t) = - \frac{1}{2\pi^2 \rho R} \int_{-\pi/2}^{\pi/2} d\theta \frac{\partial}{\partial t} \left\{ \operatorname{Re} \left[\sum_{j=1}^3 W_{ij}(\underline{x}, t; p, \theta) p_j \frac{dp_j}{d\tau} \right] \right\} H(t-t_j) \quad (\text{A2.5-5})$$

for $F(t) = \delta(t)$.

The integrand of Eq. (A2.5-4) is similar to that of the line source problem obtained by Kraut⁽²¹⁾. It can be considered as the sum of responses generated by a continuous spectrum of line sources spread angularly on the free surface through the impact point⁽¹⁴⁾.

2.6 The Rayleigh Wave.

As the normal distance from the plane boundary into the medium goes to zero, Eq. (A2.4-2) becomes

$$pr \cos(\tilde{\theta} - \theta) = t \quad (\text{A2.6-1})$$

so that the Cagniard-de Hoop path runs along the real axis of the right-hand half of the complex p -plane. The presence of a simple pole P_R on the real axis, known as the Rayleigh pole^(11,12,19), requires an indentation of the path of integration to avoid this singularity. Thus, when $x_2 \rightarrow 0$, the points on a small

semi-circular indentation about the pole no longer correspond to real time. Therefore, the contribution to the time-transformed displacement field arising from the semi-circular indentation must be evaluated separately, then inverted into the time domain and added to the displacement field arising from integration along the Cagniard-de Hoop path. As an example, when $F(t) = H(t)$ the contribution from the Rayleigh pole is given by

$$u_{1N\text{pole}}^{*H}(x_1, 0, x_3, s) = \frac{-1}{2\pi p} \int_{-\pi/2}^{\pi/2} d\theta \{ (\pi i) \cdot \text{Res} \left[\sum_{j=1}^3 W_{1j}(r, \tilde{\theta}; p, \theta) e^{-spr \cos(\tilde{\theta} - \theta)} \right]_{p=p_R} \} \quad (\text{A2.6-2})$$

in the transformed space where Res denotes residue of the indicated quantities at the given location of p . Inversion to real time yields

$$\begin{aligned} u_{1N\text{pole}}^H(x_1, 0, x_3, t) &= -\frac{1}{2\pi pr} \int_{-\pi/2}^{\pi/2} d\theta \{ \text{Res} \left[\sum_{j=1}^3 W_{1j}(r, \tilde{\theta}; p, \theta) \right] \cdot \delta[\tau - p \cos(\tilde{\theta} - \theta)] \}_{p=p_R} \\ &= -\frac{1}{2\pi pr} \left\{ \text{Res} \left[\sum_{j=1}^3 W_{1j}(r, \tilde{\theta}; p_R, \theta) \right] \frac{H(\tau - \tau_R)}{|p_R \sin(\tilde{\theta} - \theta_0)|} \right\} \end{aligned} \quad (\text{A2.6-3})$$

where $\tau_R = p_R \cos(\tilde{\theta} - \theta_0)$ and $\theta_0 = \tilde{\theta} - \cos^{-1}(\frac{\tau_R}{p_R})$. The factor $p_R \sin(\tilde{\theta} - \theta_0)$ is introduced in Eq. (A2.6-3) since the Dirac delta function involved is an implicit function of θ ⁽³⁰⁾. The displacement field at a station on the free surface due to a unit normal impact force $H(t)$ is thus

$$u_{1N\text{surface}}^H(x_1, 0, x_3, t) = u_{1N}^H(x_1, 0, x_3, t) + \frac{1}{2\pi pr} \text{Im} \left\{ \text{Res} \left[\sum_{j=1}^3 W_{1j}(r, \tilde{\theta}; p_R, \theta_0) \frac{H(\tau - \tau_R)}{|p_R \sin(\tilde{\theta} - \theta_0)|} \right] \right\} \quad (\text{A2.6-4})$$

where the first term on the right-hand side represents contributions due to body wave disturbances while the second term arises from the Rayleigh pole.

Section 3. Numerical Procedures

3.1 Introduction.

Displacement fields such as given by Eq. (A2.4-7) obtained in the previous chapter are generally expressed in terms of complicated algebraic functions of \underline{x} , p and t and are intractable analytically. Therefore, the fundamental solution, Eq. (A2.5-4) the displacement field of the medium under a Heaviside normal impact, has been programmed for evaluation by a digital computer. The Green's function (A2.5-5) may also be used for such an evaluation that will exhibit the basic character of the response of the medium; however, it involves the time differentiation indicated in Eq. (A2.5-5) which must be carried out numerically; as a consequence, this procedure often leads to unsatisfactory results.

In most practical problems, physical input forces are not realized in a Dirac delta function form and the desired solution is a combination of several functions of which the Green's function is only one. For an example, if $F(t)$ is the actual input force of the problem and $\frac{\partial}{\partial t} [u_{1N}^H(\underline{x}, t)]$ is the Green's function from Eqs. (A2.5-4) and (A2.5-5), the displacement field due to $F(t)$ is then

$$u_1(\underline{x}, t) = F(t) \otimes \frac{\partial}{\partial t} [u_{1N}^H(\underline{x}, t)] = u_{1N}^H(\underline{x}, t) \otimes \dot{F}(t) \quad (A3.1-1)$$

where the symbol \otimes denotes a convolution product in time. Eq. (A3.1-1) is identical to Eq. (A2.5-2). Thus, the fundamental solution, Eq. (A2.5-4), can be used for evaluation to avoid the numerical differentiation involved in the Green's function, Eq. (A2.5-5). Numerical differentiation of the input function is needed in this case; however, this operation is simpler and generally yields more accurate results than that indicated above.

3.2 Computer Program.

The computer program developed calculates i) the fundamental displacement field given by Eq. (A2.5-4), ii) the components of the fundamental strain and stress, iii) the actual displacements, strains and stresses obtained by the convolution integral, Eq. (A3.1-1) for a given input $f(t)$.

In order to compute the fundamental displacement, 14 subroutines are used of which two are very important. One of these is a routine which finds roots of the quartic algebraic equation (A2.4-4). This routine uses Bairstow's scheme⁽³⁴⁾ which is general enough to solve any even degree algebraic equation so that this routine may be used to find roots of the sextic equation arising in the form of the characteristic equation of a generally anisotropic medium. The method provides a corresponding number of quadratic factors of the given even degree polynomial by an iteration scheme. Fast and accurate convergence requires a quite good initial approximation and this is obtained easily from a few trial and error techniques. Another routine of importance computes the complex quantities W_{ij} in Eq. (A2.5-4). These two routines take most of the computer time necessary to solve the problem.

3.3 Results.

Several sets of numerical results which are considered to be representative of the solution obtained are shown in the following.

- (i) Three components of the fundamental displacements at various locations are shown in Figs. 2, 3 and 4.
- (ii) These displacements convolved with
 - (a) an input force given by $F(t) = \sin^2\left(\frac{\pi t}{\tau}\right)$, where τ is the duration of the input pulse are shown in Figs. 5, 6, 7 and 8, and
 - (b) the stresses produced by the input force observed from experiments are shown in Figs. 1, 2, 3, 4 of the main report and Appendix C.
- (iii) slowness and wave curves are shown in Figs. 9, 10, 11, 12 and 13.

Section 4. Discussion and Conclusions

4.1 Introduction.

It appears that the solution presented here is the first available for Lamb's problem in three dimensions involving a truly transversely isotropic medium. A three-dimensional formulation is introduced in the course of the solution and the problem is solved using a modified Cagniard method. This procedure may be used to solve the same type of problem formally for any anisotropic, elastic medium even though it may take a substantial amount of computer time for evaluation. Burrige⁽¹⁴⁾ suggested essentially the same form of the solution to Lamb's problem as presented here in three dimensions for a generally anisotropic medium; however, he used a two-dimensional result to construct the solution for the three-dimensional space and he presented only numerical results for two-dimensional solutions on the free surface for a cubic crystal. Ricketts⁽²⁵⁾ presented a formal solution for the same problem investigated here but he was not able to obtain any numerical results since the solution he suggested includes an integral operation whose limit is, in general, not finite.

Since the solution obtained here is in the form of quadratures, it must be evaluated numerically. However, the evaluation of Eq. (A2.4-7) for cases other than a normal impact is beyond the scope of the present study. Numerical results for the responses of the solid due to a pure shear load might be of interest to geophysicists in relation to earthquake phenomena; these could be obtained with a certain modification of the program developed here.

4.2 Comparison of Analytical Results for Body Waves in an Isotropic Medium.

One type of investigation to check the validity of the numerical results was carried out by comparing the present fundamental solution to corresponding values obtained by Pekeris and Lipson⁽⁴⁾ and Shibuya and Nakahara⁽³¹⁾ for the isotropic

half-space. To carry out such an analysis, it should be recalled that the solution and the computer program developed in this investigation apply to a transversely isotropic solid which exhibits three distinct sheets of the slowness surface except for a finite number of singular points, which are the branch points in the complex p -plane. Thus, it was not possible to use the program to obtain responses for a truly isotropic solid in which two sheets of the slowness surface corresponding to shear waves coalesce, resulting in a singular surface. Instead, a set of elastic constants for a slightly transversely isotropic solid derived from a set of elastic constants for an isotropic solid was employed in the computational routine. A case where $\mu = \frac{1}{4}$ was selected so that $\lambda = G$ with λ and G as the Lamé constants and μ as Poisson's ratio. Velocity constants c_1 and c_3 defined in Eq. (A2.1-9) were obtained from the relations

$$\begin{aligned} c_1 &= \left(\frac{\lambda + 2G}{\rho} \right) \\ c_3 &= G/\rho \end{aligned} \quad (A4.1-1)$$

while c_2 , c_4 and c_5 were chosen by means of small perturbations involving c_1 and c_3 to realize slight anisotropy. In the computations, a 2 percent transverse anisotropy was employed using the values

$$\begin{aligned} c_5 &= c_1(1 - .02) , \\ c_2 &= c_3(1 - .02) , \\ c_4 &= (c_1 - c_3)(1 - .02) . \end{aligned} \quad (A4.1-2)$$

The slowness curves resulting from the above constants using $\lambda = G = 2.0 \times 10^6$ psi and $\rho = 2.0 \times 10^{-4}$ are shown in Fig. 12, which indicate the presence of anisotropy so that the present computer program can be used. As shown in Fig. 14, the results from the present investigation fall between those of References (4) and (31). Since Pekeris and Lipson obtained an exact solution in terms of elementary functions,

it appears that the present investigation does yield a better approximation than that of Shibuya and Nakahara who obtained their solution by a direct numerical inversion of the Laplace-transformed problem. It should be noted that the response in the interior of an isotropic half-space obtained from the solution of Pekeris and Lipson were determined here from those responses on the surface due to a buried point source (given in Ref. (4)) by use of a dynamical reciprocal theorem⁽²⁷⁾.

The only analytical results pertaining to the fundamental stress, even for an isotropic solid, are to be found in Shibuya and Nakahara's paper. Using the elastic constants cited above for the nearly isotropic solid, normal components of the fundamental stress, $\sigma_{22}^H(\underline{x}, t)$, were computed and plotted together with the data of Ref. (31) in Fig. 15. Although the agreement is reasonable, the results from the present investigation appear to provide a more realistic solution for the earlier part of the pulse. This is so because $u_2^H(\underline{x}, t)$ displays a virtual discontinuity at $\tau = 1$ in Fig. 15 and $\sigma_{22}^H(\underline{x}, t)$ is proportional to $\frac{\partial u_2^H}{\partial x_2}$ so that the fundamental stress must be nearly like a Dirac delta function.

4.3 Comparison of the Analytical Results with the Finite Element Method and Experimental Data.

The convolution integral indicated in Eq. (A2.5-2) has been evaluated to obtain the actual stresses resulting from a realistic input force $F(t)$. The values obtained have been compared both with the results obtained from the finite element technique and with experimental data.

The experiments utilized a limestone block to model an isotropic half-space and a Yule marble block for a transversely isotropic semi-infinite solid. Details of the experimental investigation are presented in Ref. (32), which also includes the procedure of determining the dynamic elastic constants of Yule marble utilized in the computation. The constants were obtained from the body and surface wave

measurements on the two blocks used in the experimental work. The static constants determined by Ricketts⁽²⁵⁾ were based on data from a small specimen cut from one of the corners of one of the Yule marble blocks. The elastic constants for limestone were also taken from the data Ricketts obtained. These three sets of constants are listed in Table 1.

Experimental and/or analytical difficulties that could account for the disagreement between predicted and measured values (when extant) include

- (i) Discrepancies in the properties of the actual blocks and those assumed in the mathematical model. The rock samples employed exhibited local differences in properties and inhomogeneities and evidenced deviations from elastic behavior. The Yule marble manifested some small changes in the direction of the axis of elastic symmetry within the block.
- (ii) Errors in experimental measurements involved in determining the elastic constants and the axis of elastic symmetry.
- (iii) Experimental errors involved in the stress measurements which are discussed in Ref. (32).
- (iv) Numerical errors in the computation of the field quantities due to round-off or truncations built into various library routines used.
- (v) The distributional character of the solution which requires integration over 2π radians introducing a numerical approximation that involves an error of order $(\Delta h)^3$ for approximate quadrature based on Simpson's rule, Δh being the integration step.
- (vi) Approximations involved in numerical differentiation of the input data that brings in an error of order of (Δh) for a forward difference scheme.
- (vii) The difference in the finite area of application of the actual load and the point load assumed as the input in the analysis; the latter introduces a significant contribution to the responses from the higher components of the frequency spectrum of the Dirac-delta function input.

Some representative comparisons among the three types of results are shown in Appendix C. The agreement generally appears to be quite good. However, the analytical solution obtained nearer to the impact point, about 1.8" away, yielded higher stresses than obtained by either experimental or numerical means; this is mainly accounted for by discrepancy indicated in (vii) above. Generally, the agreements in the first part of the pulse are very good at locations farther away, about 5", from the point source where contributions from the higher frequency components become negligible. The analysis generally yields a lower amplitude than experimental data; this discrepancy may originate from experimental error that is described in detail in Ref. (32). Phase shifts between analytic and experimental solutions are also observed which may be explained by the difficulty in determining the exact rise time from the experiment and certain numerical errors resulting from the iterative scheme that is introduced to solve the discriminantal equation of the quartic equation (2.4-4). The solution of this equation is the arrival times of the body waves. Analytical results near the free surface with an angle ϕ less than 1° yield small spurious oscillations before the arrival of the surface wave; this is due to the round-off error resulting from such an operation as handling extremely large and small numbers simultaneously in the computer as Gakenheimer and Repnau⁽³³⁾ pointed out for the isotropic case. Numerical differentiation of the measured input force appears to introduce certain errors in the computation of the actual stresses from the stress convolution integral. This is expected since the order of magnitude of the time derivative of the input force is $10^6 \sim 10^8$ lbs/sec, and a slight error in the measurement of the oscillogram can produce a significant change in the calculated stress history. The influence of modified inputs in the amplitude and phase, as discussed in the following paragraph, can be seen from Fig. 16.

The computations based on a hypothetical input force given by

$$F(t) = \begin{cases} I_0 \sin^2 \frac{\pi t}{t^*} & ; \theta < t < t^* \\ 0 & ; t > t^* \end{cases} \quad (\text{where } I_0 \text{ is the peak of the measured force and } \theta \text{ is the time of impact})$$

t^* is twice the actual rise time) is shown in Fig. 17, and is in good correspondence with those results where the actual input is used in the calculations of the stress. However, the analytical expression for the input yields a slightly broader stress pulse than that computed from the measured values. The best agreement with the experiment was obtained when a symmetric pulse was used in the computation where the entire rise portion of the pulse was identical to that measured but where the rest of the pulse was artificially changed to consist of a mirror image of the rise. However, if the input pulse is already close to a symmetric shape, the improvement is, in general, not great relative to those calculations where the actual force history is used.

As shown in Fig. 2 of the main report, numerical results using the finite element technique were found to be in better correspondence with the data for receiver points nearer to the source. This would be expected since the load is inevitably spread over a finite area in the finite element method and thus the point source effect is substantially eliminated. Such a loading is required by the actual physical situation arising in the experiments. However, at distant stations a complete time history could not be obtained by the finite element method for a sufficient length of time to provide a meaningful comparison; this is mainly due to the limitations of the computer capacity and the time required for computation.

4.4 Surface Waves.

A computer program was written which evaluates surface results given by Eq. (2.6-4); however, an unstable oscillatory result was obtained due to round-off errors. Thus, the evaluation of the field quantities on the surface at $x_2 = 0$ was not pursued any further in this investigation.

Since the displacement must be continuous in the half-space, the field quantities computed on a ray at a shallow angle from the surface should yield a reasonable approximation for those right on the surface. The displacement fields and the comparison of the calculated components of stresses near the surface with the experimental results are shown in Fig. 4 of the main report and Appendix C, where good agreement is indicated.

4.5 Conclusions.

A solution to the wave propagation problem in a transversely isotropic half-space under arbitrary concentrated normal loading on the free surface has been presented within the scope of the linear theory of elasticity. A mixed Laplace and two-dimensional Fourier transform and a modified Cagniard-de Hoop technique were employed to solve the problem; it should be pointed out that this particular method can be used to solve similar three-dimensional problems in a solid possessing any type of anisotropy. The solution obtained in this manner may be considered as the sum of responses due to line sources spread uniformly over 0 to 2π radians on the free surface all of which are passing through the loading point. Therefore, the solutions to a line source input of any orientations located in the surface can be obtained easily from the present formulation of the three-dimensional solution.

A computer program which evaluates responses of displacement, stress and strain due both to a Heaviside and to an actual force input was developed for normal loading. The numerical results for a fundamental displacement and stress obtained from a set of elastic constants for a nearly isotropic solid exhibited good correspondence with the known analytical results for a corresponding isotropic solid. For both an isotropic and a transversely isotropic medium, the solution from the program provided good agreement with experimental data for the first part of the pulse for stations distant from the impact point, although the

remaining part of the pulse predicted lower amplitudes than the data. Predictions at stations nearer to the source were generally not as satisfactory due to the contributions from higher frequency components arising from the singularity of the point load used in the analytical model that does not actually correspond to the experiment. The responses on the surface of the half-space may be obtained approximately by computing them along a ray near the surface with a shallow angle, even though an exact evaluation was not realized in this investigation. The responses along a ray in the direction of the load may not be computed from the present program due to a singularity arising from the transverse isotropy of the medium; however, this is not a serious limitation since the responses along this ray may again be computed approximately as described in the above. Also, the program can be used to approximately evaluate the responses of an isotropic medium with reasonable accuracy by introducing nearly isotropic elastic constants. The mathematical model employed generally predicted the responses of the Yule marble block tested under a normal point load reasonably well in spite of discrepancies in modeling of the type discussed in section 4.3.

A computer program for the solution due to a tangential load on the surface may be developed utilizing the formulations presented here without much difficulty.

Bibliography

1. Lamb, H., "On the Propagation of Tremors over the Surface of Elastic Solids", Phil. Trans. Roy. Soc. London, A, v. 203, 1904, p. 1.
2. Pekeris, C. L., "The Seismic Buried Pulse", Proc. Nat. Acad. Sci., USA, v. 41, 1955, p. 629.
3. Pekeris, C. L., "The Seismic Surface Pulse", Proc. Nat. Acad. Sci., USA, v. 41, 1955, p. 469.
4. Pekeris, C. L. and Lipson, H., "Motion of the Surface of a Uniform Elastic Half-Space Produced by a Buried Pulse", J. Acous. Soc. Amer., v. 29, n. 11, 1957, p. 1233.
5. Chao, C. C., "Dynamical Response of an Elastic Half-Space to Tangential Surface Loadings", J. Appl. Mech., Trans. ASME, September 1960, p. 559.
6. Gabenheimer, D. C. and Miklowitz, J., "Transient Excitation of an Elastic Half-Space by a Point Load Travelling on the Surface", J. Appl. Mech., Trans. ASME, September 1969, p. 505.
7. Johnson, L. R., "A Collection of Solutions to Lamb's Problem", unpublished paper, U. C. Berkeley, Calif., 1973.
8. Ewing, W. M., Jardetzky, W. S. and Press, F., Elastic Waves in Layered Media, McGraw-Hill, New York, 1957.
9. Musgrave, M. J. P., Crystal Acoustics, Holden Day, San Francisco, Calif., 1970.
10. Kelvin, Lord, Baltimore Lectures, Cambridge Univ. Press, 1904.
11. Burridge, R., "The Directions in which Rayleigh Waves May Be Propagated on Crystals", Quart. J. Mech. Appl. Math., v. 23, pt. 2, 1970, p. 217.
12. Buchwald, V. T., "Rayleigh Waves in Anisotropic Media", Quart. J. Mech. Appl. Math., v. 14, pt. 4, 1961, p. 461.
13. Synge, J. L., "Elastic Waves in Anisotropic Media", J. Math. Physics, 35, 1957, p. 323.
14. Burridge, R., "Lamb's Problem for an Anisotropic Half-Space", Quart. J. Mech. Appl. Math., v. 24, pt. 1, 1972, p. 81.
15. Cagniard, L., Reflection and Refraction of Progressive Seismic Waves, translated and revised by E. A. Flinn and C. H. Dix, McGraw-Hill, New York, 1962.
16. Cagniard, L., Réflexion et réfraction des ondes séismiques progressives, Gauthier-Villars, Paris, 1939.

17. DeHoop, A. T., "A Modification of Cagniard's Method for Solving Seismic Pulse Problems", *Appl. Sci. Res., Sec. B*, v. 8, 1960, p. 349.
18. DeHoop, A. T., "Theoretical Determination of the Surface Motion of a Uniform Elastic Half-Space produced by a Dilatational, Impulsive, Point Source", *La Propagation des Ebranlements dans les Milieux Heterogenes, Colloques Internationaux du Centre National de la Recherche Scientifique, Marseille, 1961*, p. 21.
19. Buchwald, V. T., "Rayleigh Waves in Transversely Isotropic Media", *Quart. J. Mech. Appl. Math.*, v. 14, 1961, p. 293.
20. Lighthill, M. J., "Studies on Magneto-Hydrodynamic Waves and other Anisotropic Wave Motions", *Phil. Trans. Roy. Soc. London, A*, v. 252, 1960, p. 397.
21. Kraut, E. A., "Advances in the Theory of Anisotropic Elastic Wave Propagation" *Rev. Geophysics*, v. 1, 1963, p. 401.
22. Kraut, E. A., Propagation of a Pulse from a Surface Line Source on a Transversely Isotropic Elastic Half-Space, Ph.D. Thesis, Univ. of Calif., Los Angeles, 1962.
23. Cameron, N. and Eason, G., "Wave Propagation in an Infinite Transversely Isotropic Elastic Solid", *Quart. J. Mech. Appl. Math.*, v. 20, n. 1, 1967, p. 23.
24. Ryan, R. L., "Pulse Propagation in a Transversely Isotropic Half-Space", *J. Sound Vib.*, 14, 1971, p. 511.
25. Ricketts, T. E., Sphere Impact on an Anisotropic Half-Space, Ph.D. Thesis, Univ. of Calif., Berkeley, 1970.
26. Ricketts, T. E. and Goldsmith, W., "Wave Propagation in an Anisotropic Half-Space", *Int. J. Rock Mech. Min. Sci.*, v. 9, 1972, p. 493.
27. Sokolnikoff, I. S., Mathematical Theory of Elasticity, 2nd ed., McGraw-Hill, New York, 1956.
28. Sneddon, I. N., Fourier Transforms, McGraw-Hill, New York, 1951.
29. Carslaw, H. S. and Jaeger, J. C., Operational Methods in Applied Mathematics, Oxford Univ. Press, 1941.
30. Stakgold, I., Boundary Value Problems of Mathematical Physics, Vol. II, Macmillan Co., New York, 1968.
31. Shibuya, T. and Nakahara, I., "The Semi-Infinite Body Subjected to a Concentrated Impact Load on the Surface", *Bull. JSME*,
32. Krishnamoorthy, K., Internal Dynamic Stress Measurement in Model Half-Spaces of Rock, Ph.D. Thesis, Univ. of Calif., Berkeley, 1973.

33. Gakenheimer, D. and Repnau, T., "A Numerical Procedure for Evaluating Ground Motions Generated by Surface Blasts", WN-7208-PR, Rand Corp. Rept., 1971.
34. Buckingham, R. A., Numerical Methods, Pitman, New York, 1957.

Table 1. Velocity Constants

	c_1	c_2	c_3	c_4	c_5	ρ
Yule Marble [25]	3.8×10^{10}	1.28×10^{10}	$.745 \times 10^{10}$	1.89×10^{10}	3.30×10^{10}	2.73
Yule Marble [32]	4.525×10^{10}	1.50×10^{10}	1.34×10^{10}	2.36×10^{10}	2.36×10^{10}	2.66
Lime Stone [25]	3.14×10^{10}		$.93 \times 10^{10}$			2.24

Velocity Constants : $c_1, \text{in}^2/\text{sec}^2$

Specific Gravity : $\rho, \text{gr/cm}^3$

List of Figures

<u>Figure</u>	<u>Title</u>	<u>Page</u>
1	Coordinate Systems employed in the Analysis	A-37
2	Cartesian Displacements due to a Heaviside Input for $\tilde{\theta} = 85^\circ$ and $\varphi = 45^\circ$	A-38
3	Cartesian Displacements due to a Heaviside Input for $\tilde{\theta} = 0$ and $\varphi = 45^\circ$	A-39
4	Cartesian Displacements due to a Heaviside Input for $\tilde{\theta} = 90$ and $\varphi = 45^\circ$	A-40
5	Cartesian Displacements due to the Input Force $F(t) = \sin^2\left(\frac{\pi t}{t^*}\right)$ at $R = 1''$, $\tilde{\theta} = 80^\circ$, $\varphi = 45^\circ$ with Time Step $\Delta\tau = 1 \mu\text{sec/in}$ $t^* = 50 \mu\text{sec}$	A-41
6	Cartesian Displacements due to the $F(t)$ above at $R = 2''$, $\tilde{\theta} = 80^\circ$, $\varphi = 45^\circ$, with $\Delta\tau = 2.08 \mu\text{sec/in}$	A-42
7	Cartesian Displacements due to the $F(t)$ above at $R = 5''$, $\tilde{\theta} = 80^\circ$, $\varphi = 45^\circ$, with $\Delta\tau = .833 \mu\text{sec/in}$	A-43
8	Cartesian Displacements due to the $F(t)$ above at $R = 10''$, $\tilde{\theta} = 80^\circ$, $\varphi = 45^\circ$, with $\Delta\tau = .41 \mu\text{sec/in}$	A-44
9	Slowness Curves on x_1x_3 -plane Obtained by Employing Elastic Constants by Ricketts [25] for Yule Marble	A-45
10	Slowness Curves on x_1x_3 -plane Obtained by Employing Elastic Constants by Krishnamoorthy [32] for Yule Marble	A-46
11	Slowness Curves on x_1x_3 -plane Obtained by Employing 2% Variation of Elastic Constants by Ricketts [25] for Limestone	A-47
12	Wave Curves on x_1x_3 -plane for Elastic Constants by [25]	A-48
13	Wave Curves on x_1x_3 -plane for Elastic Constants by [32]	A-49
14	Comparison of Normal Fundamental Displacements $u_2^H\left(\frac{t}{R}, \tilde{\theta}, \varphi\right) = u_2^H\left(\frac{t}{R}, 45^\circ, 45^\circ\right)$ in an Isotropic Half-Space with $\lambda = G(\mu = \frac{1}{4})$	A-50
15	Comparison of Fundamental Stress $\sigma_{22}^H\left(\frac{t}{R}, \tilde{\theta}, \varphi\right) = \sigma_{22}^H\left(\frac{t}{R}, 45^\circ, 45^\circ\right)$ in an Isotropic Half-Space with $\lambda = G(\mu = \frac{1}{4})$	A-51

<u>Figure</u>	<u>Title</u>	<u>Page</u>
16	Effects of Modified Input; the Real Input and the Stress are the same as Fig. 17 for the Limestone Block	A-52
17	Comparison of σ_{xx} -Stress at $(r, \tilde{\theta}, z) = (1\frac{3}{4}'' , \frac{\pi}{2}, 5'')$ in the Yule Marble Block 1	A-53

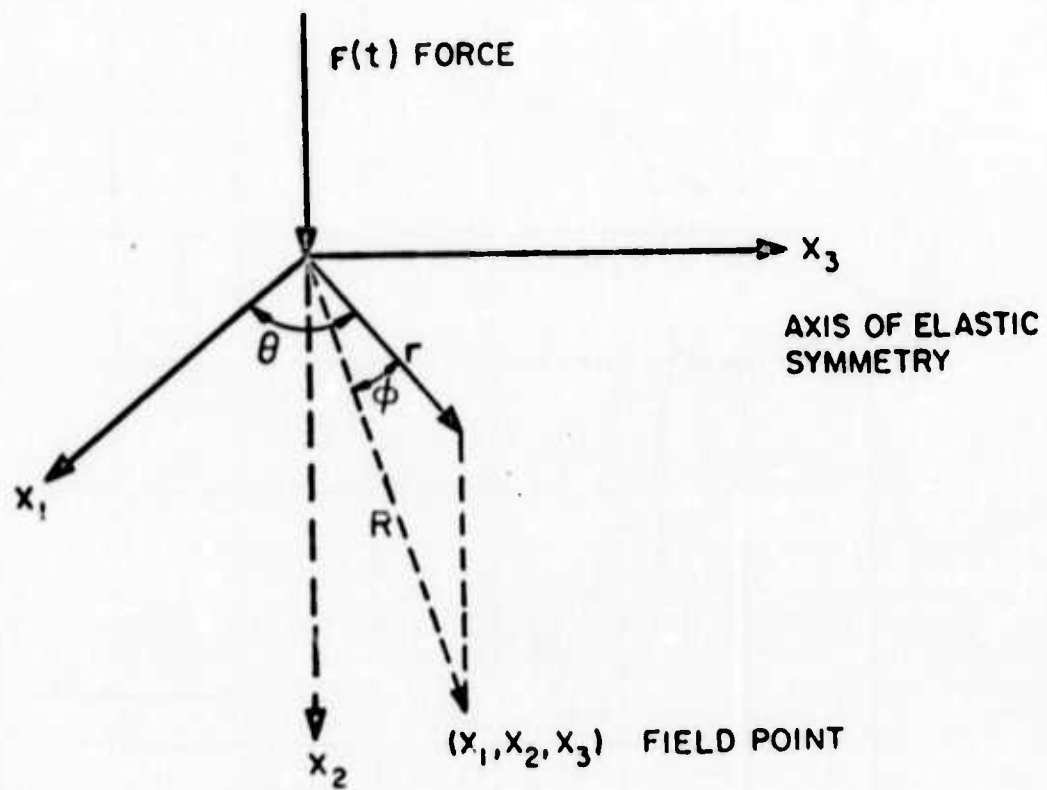


FIG. 1

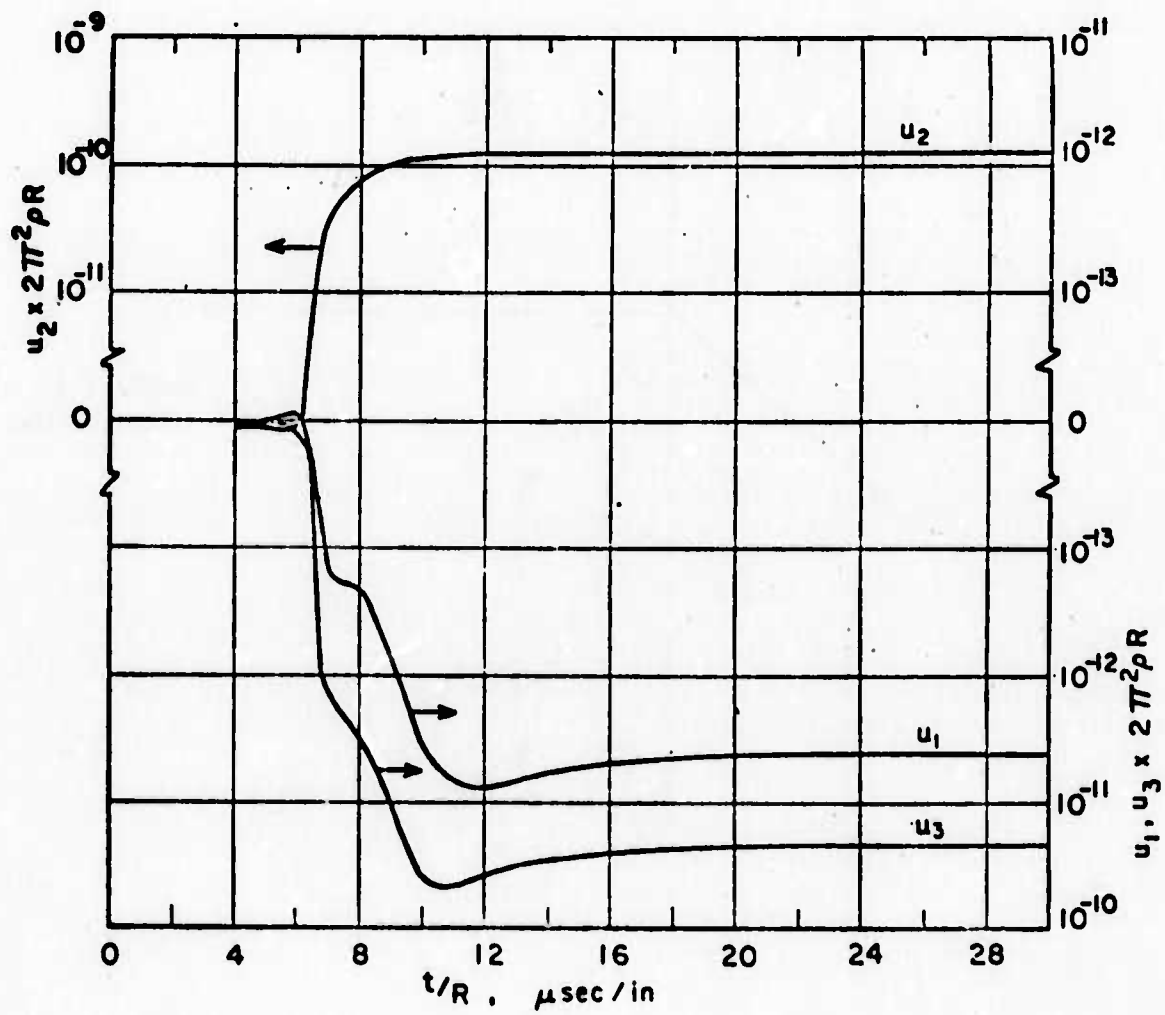


FIG. 2

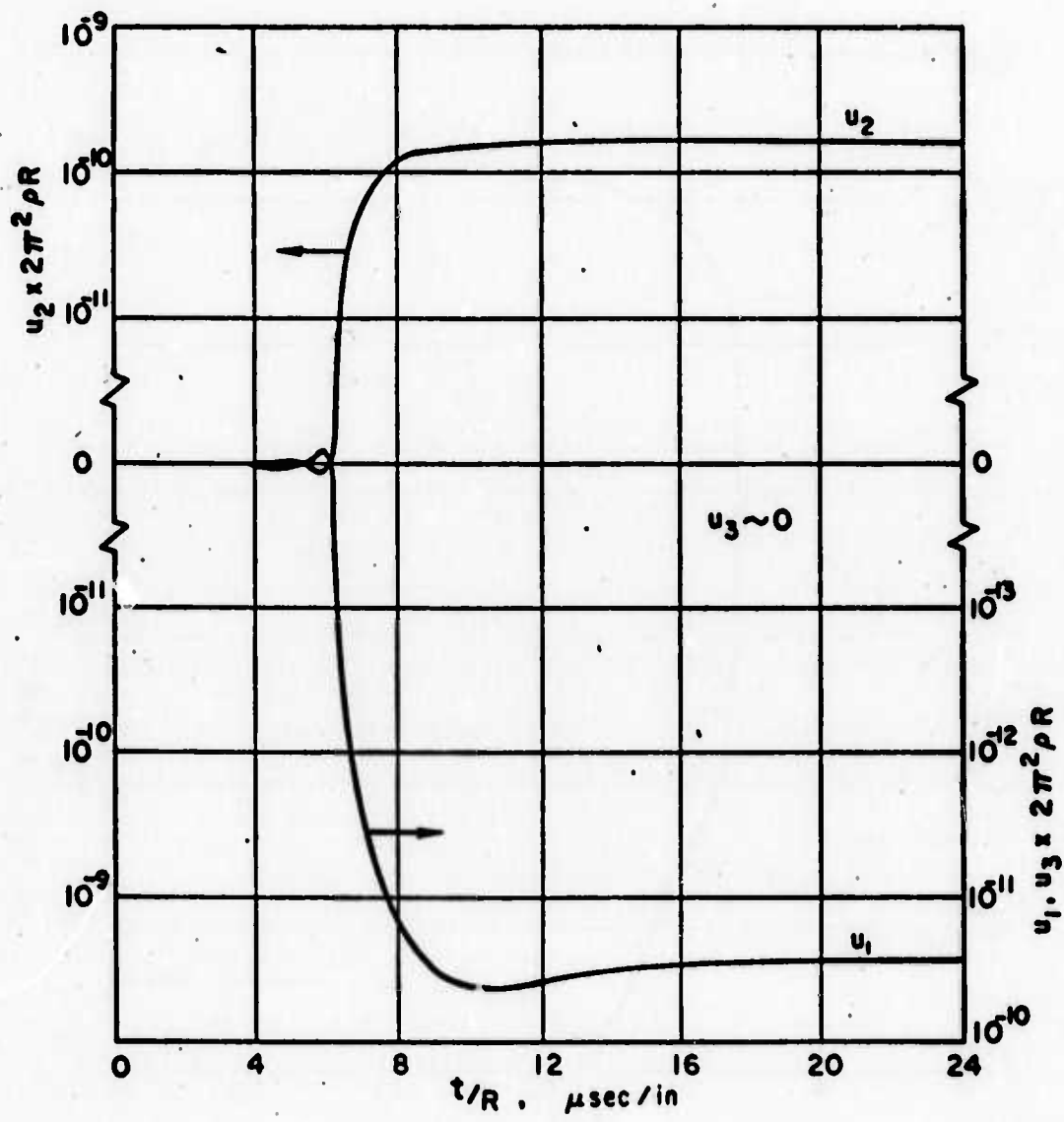


FIG. 3

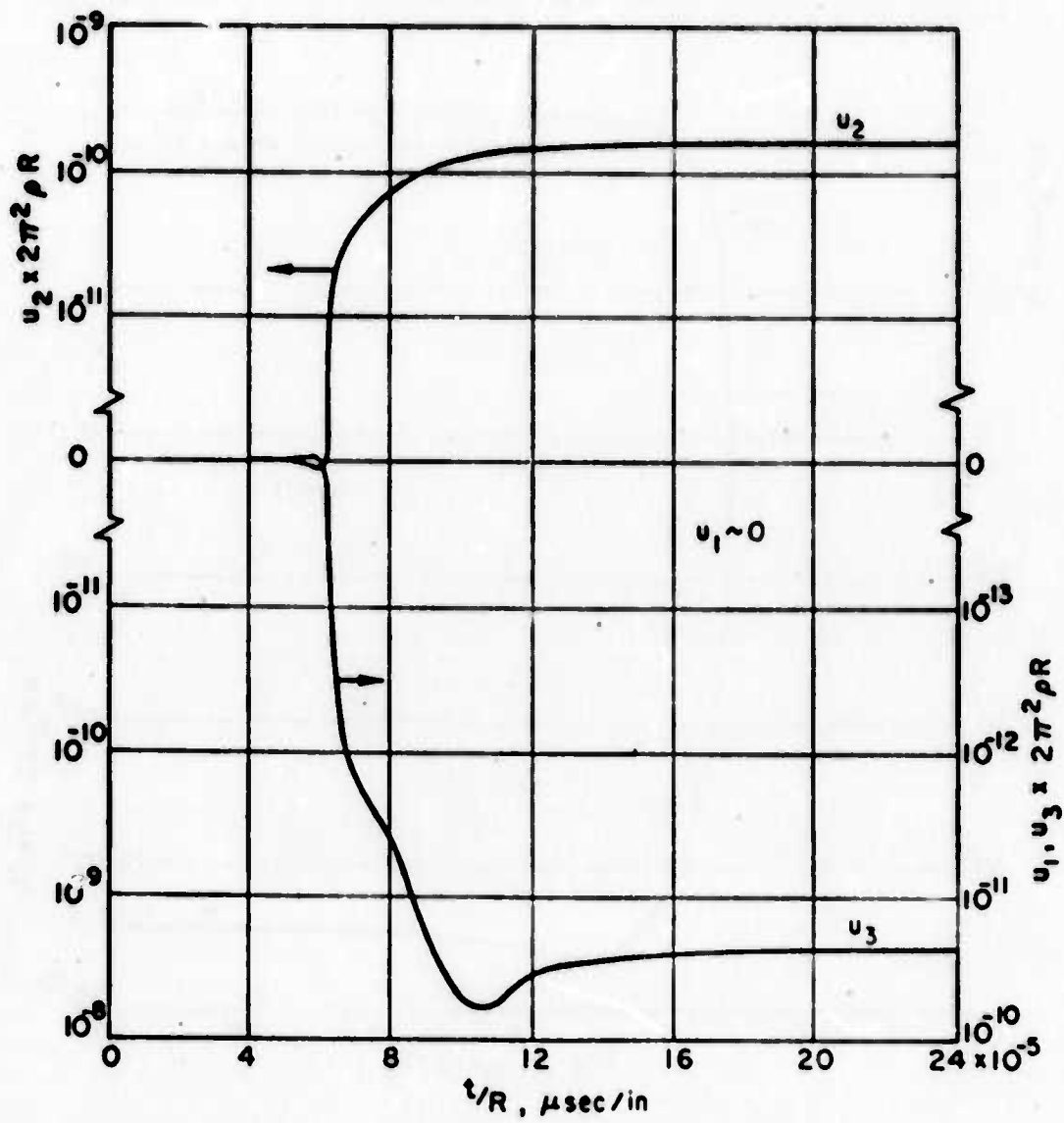
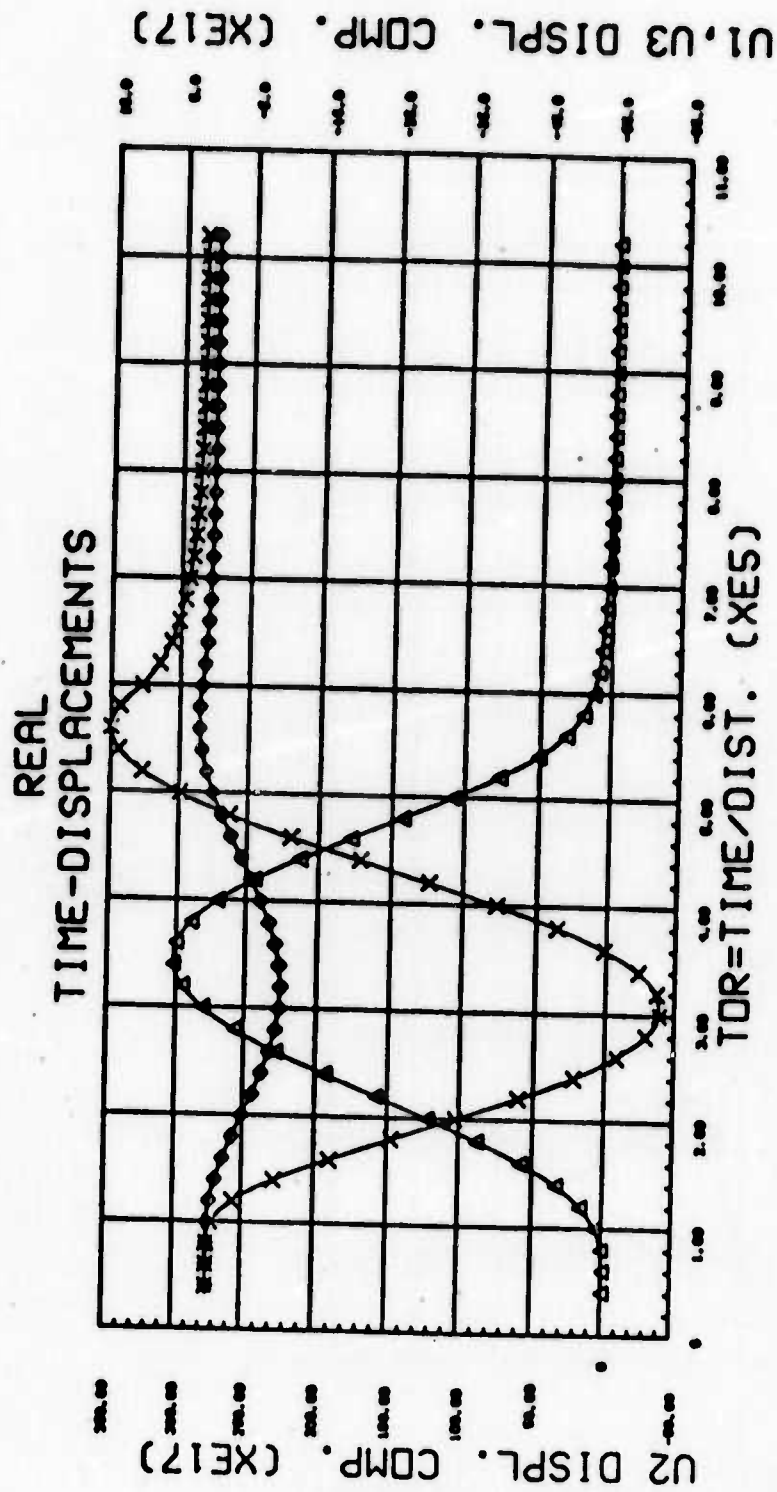
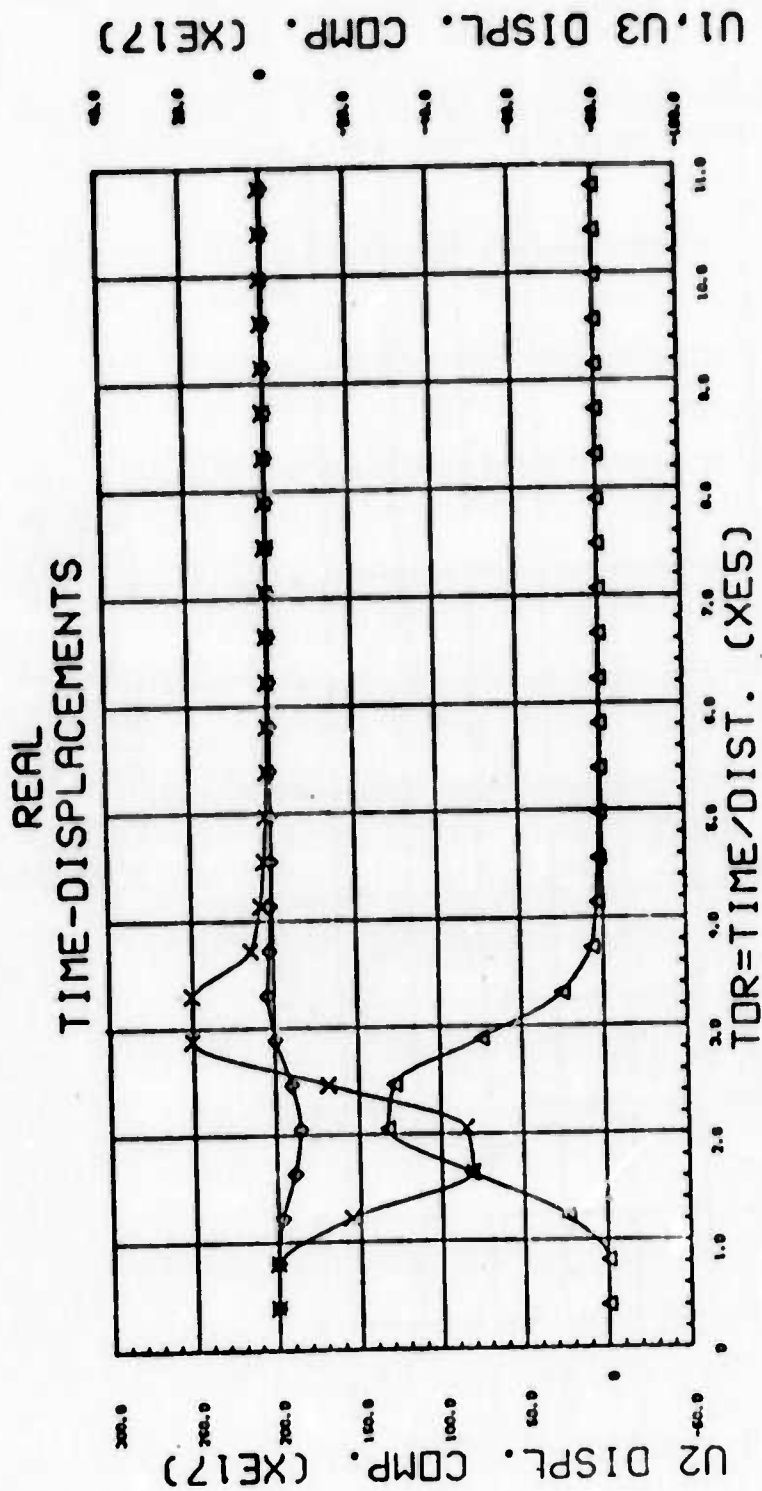


FIG. 4



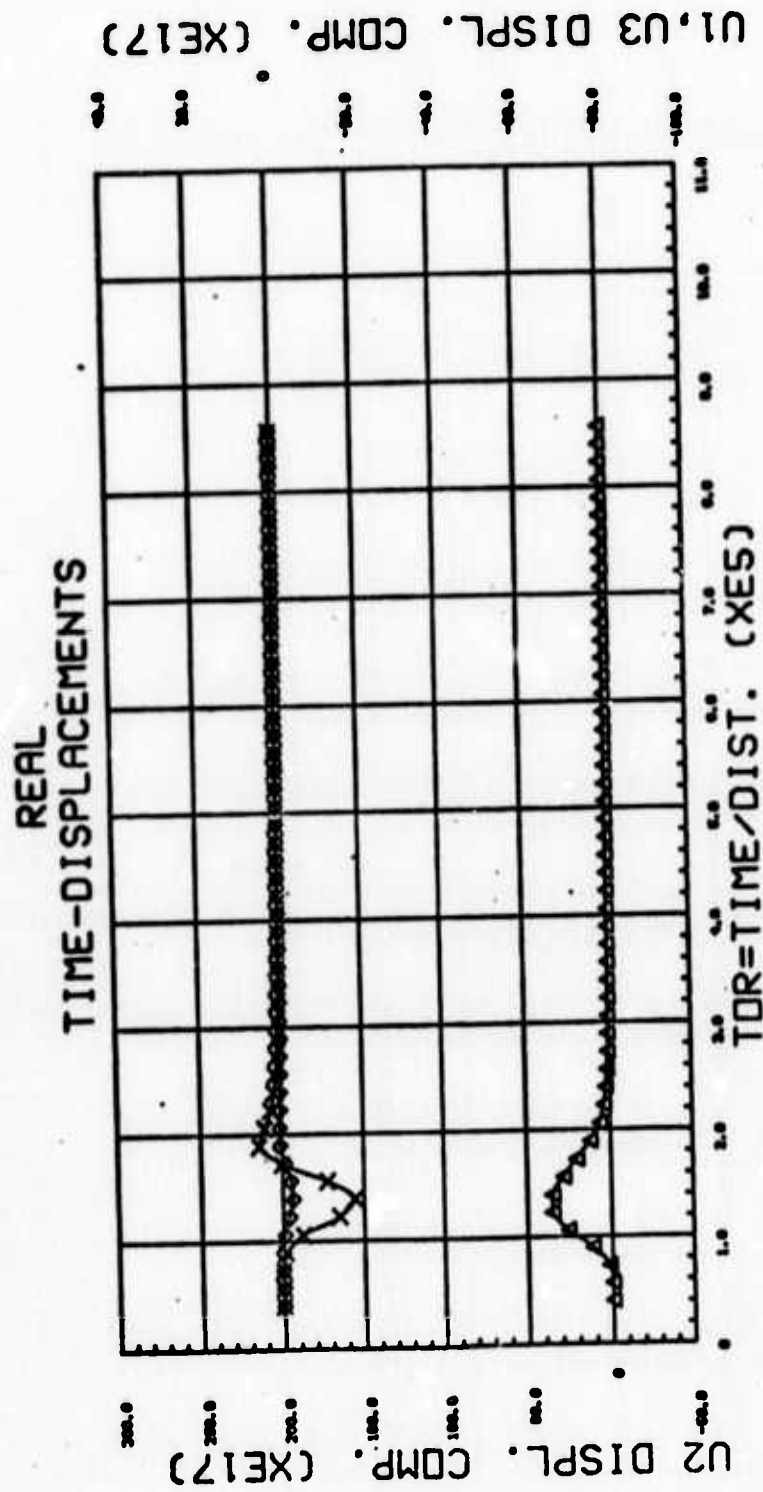
XU3 DISPL. COMP.
 XU2 DISPL. COMP.
 XU1 DISPL. COMP.

Fig. 5



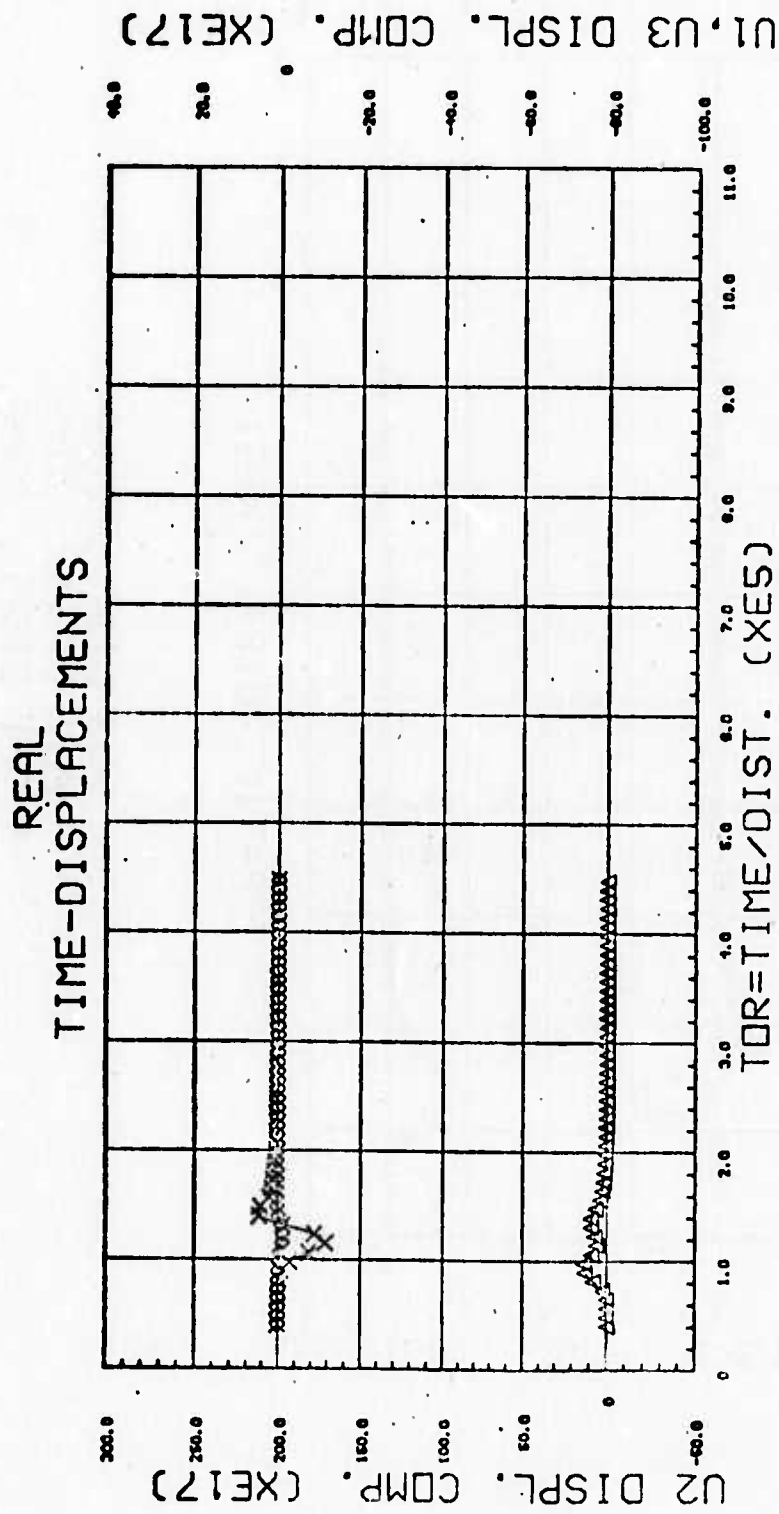
XU3 DISPL. COMP.
 XU2 DISPL. COMP.
 XU1 DISPL. COMP.

Fig. 6



XU3 DISPL. COMP.
 XU2 DISPL. COMP.
 XU1 DISPL. COMP.

Fig. 7



XU3 DISPL. COMP.
 XU2 DISPL. COMP.
 XU1 DISPL. COMP.

Fig. 8

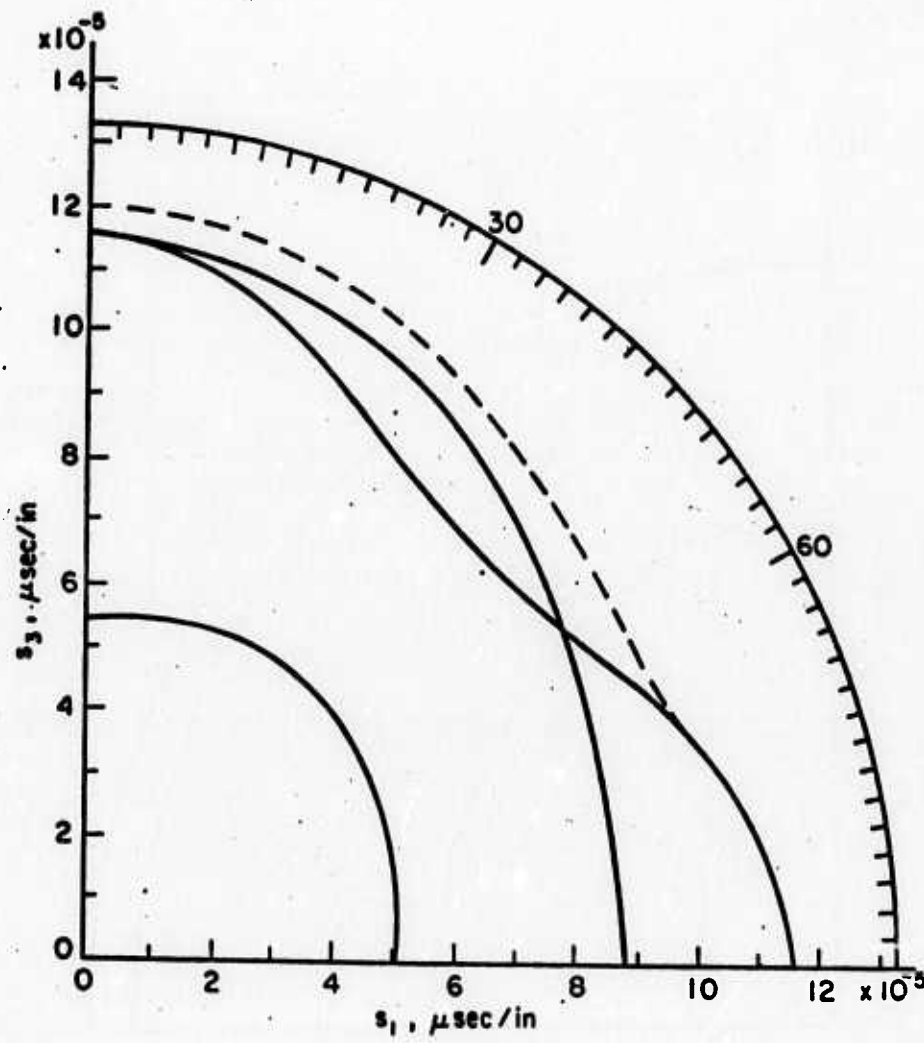


FIG. 9

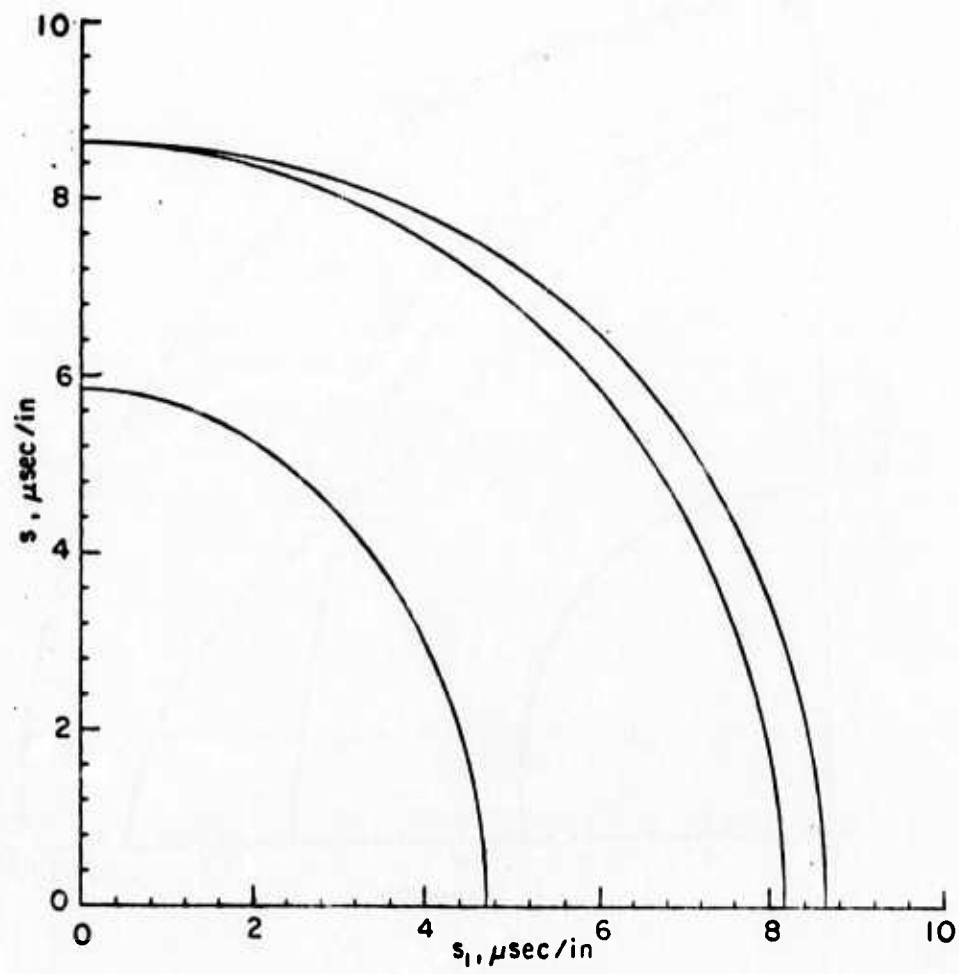


FIG. 10

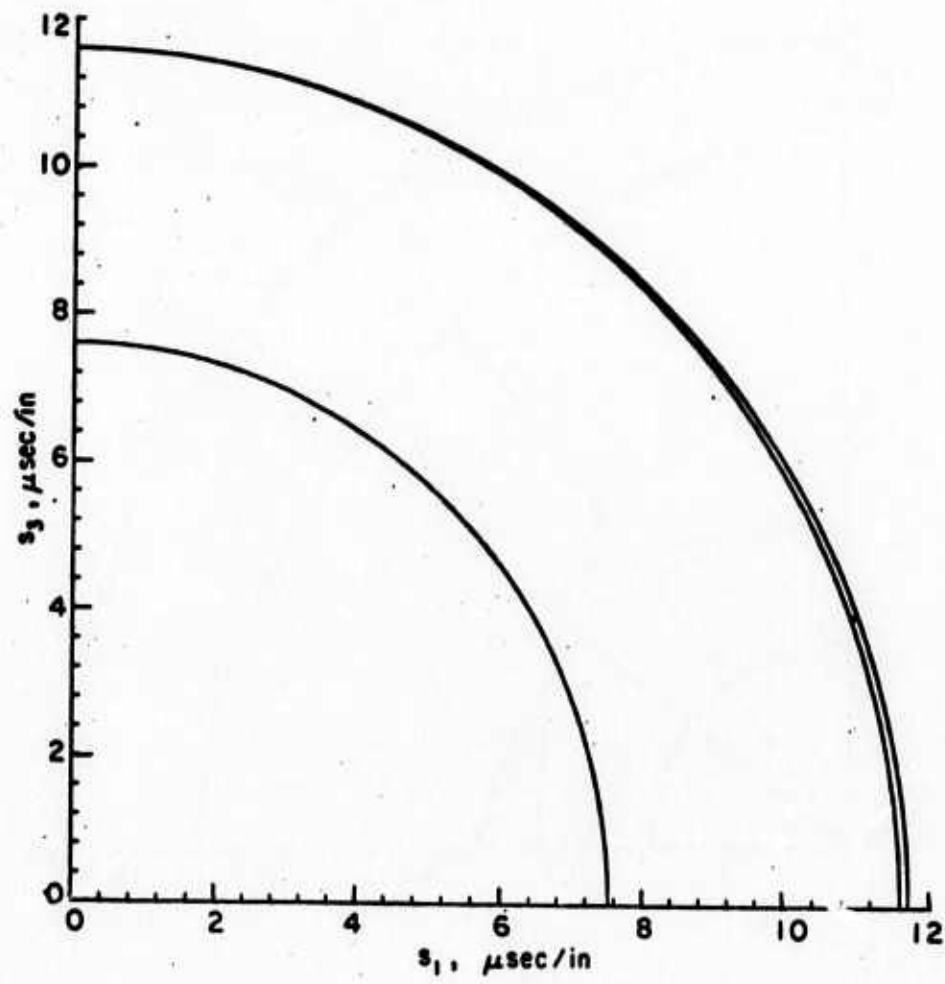


FIG. 11.

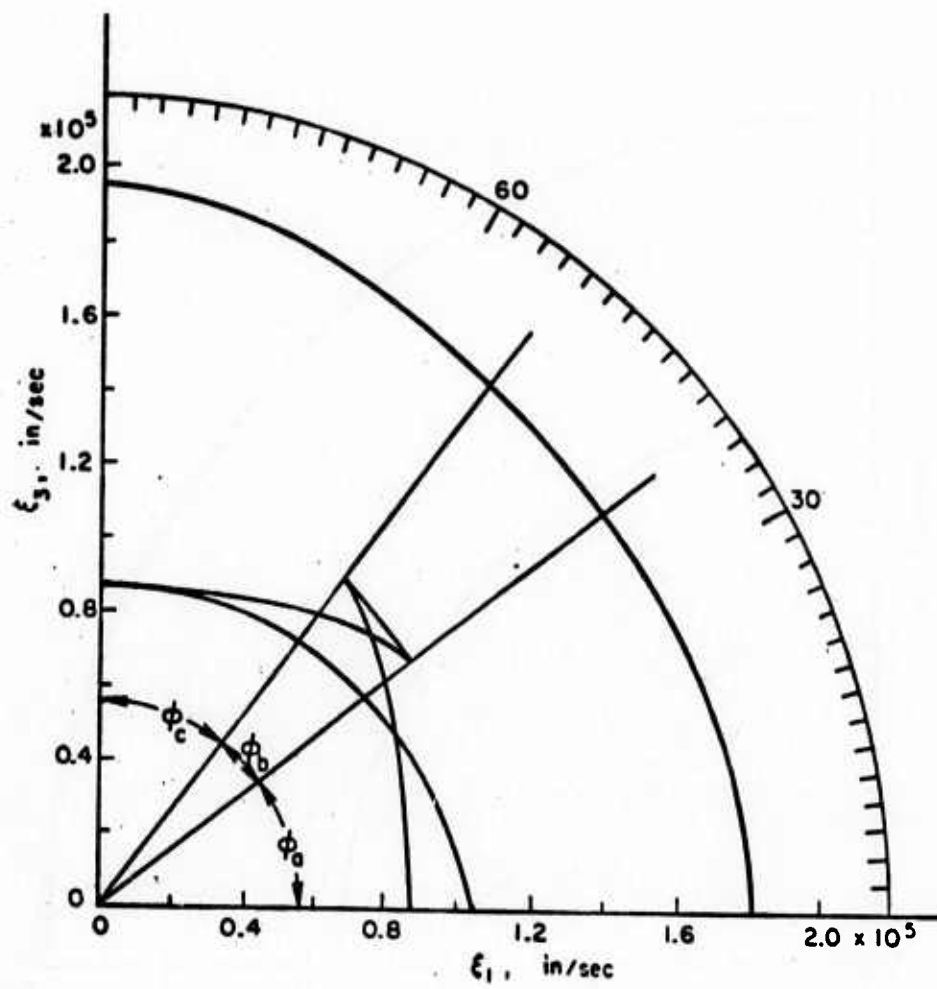


FIG.12

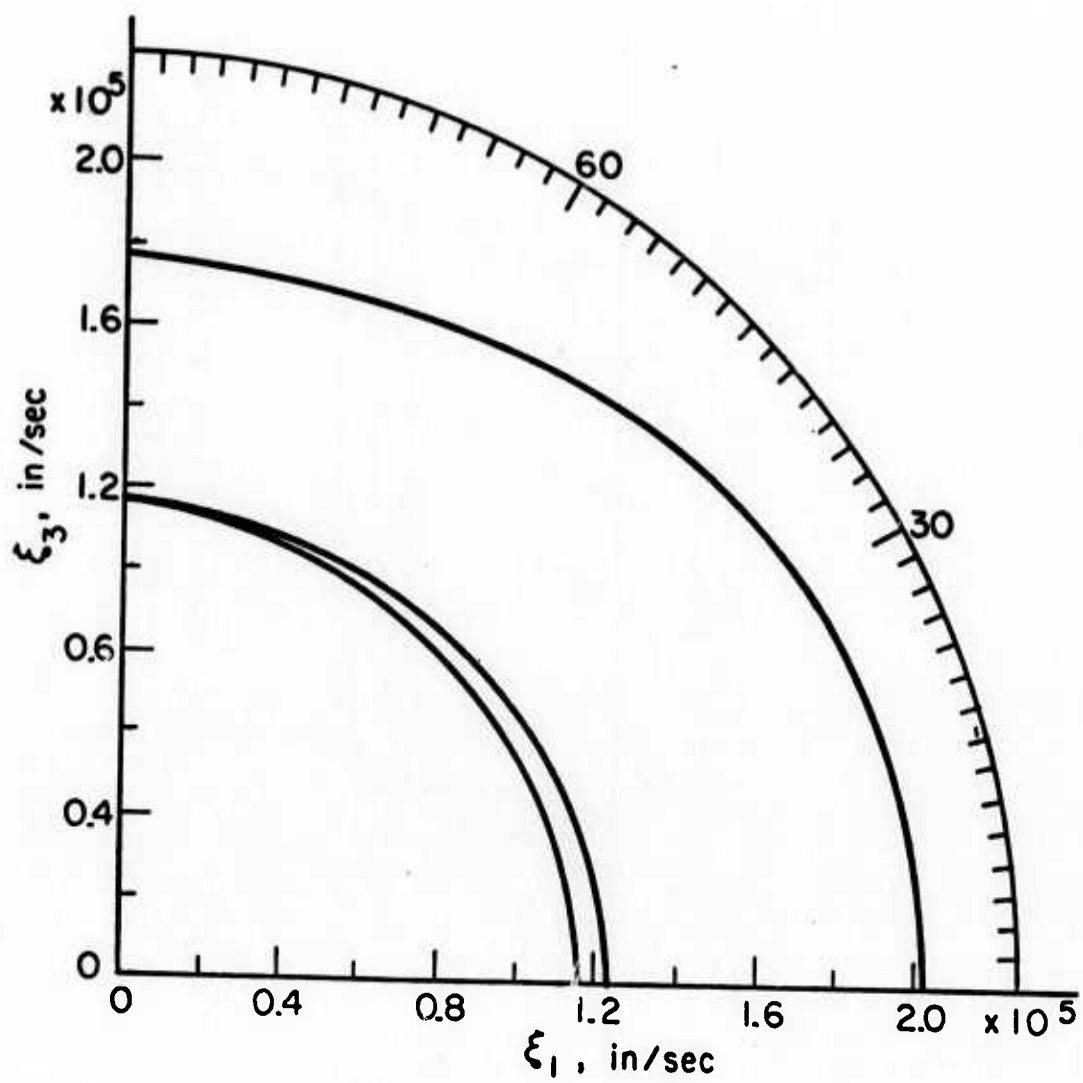


FIG. 13.

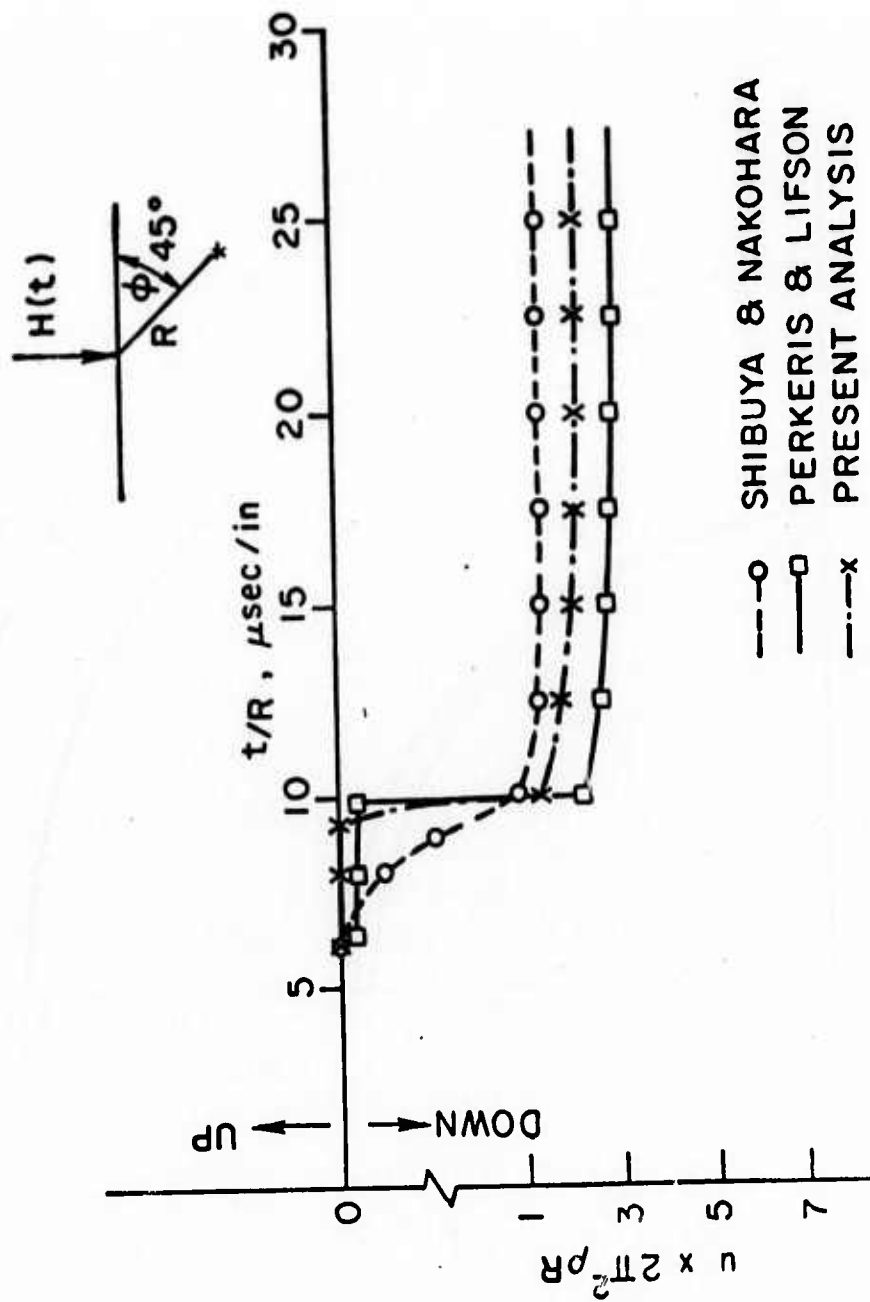


FIG. 14.

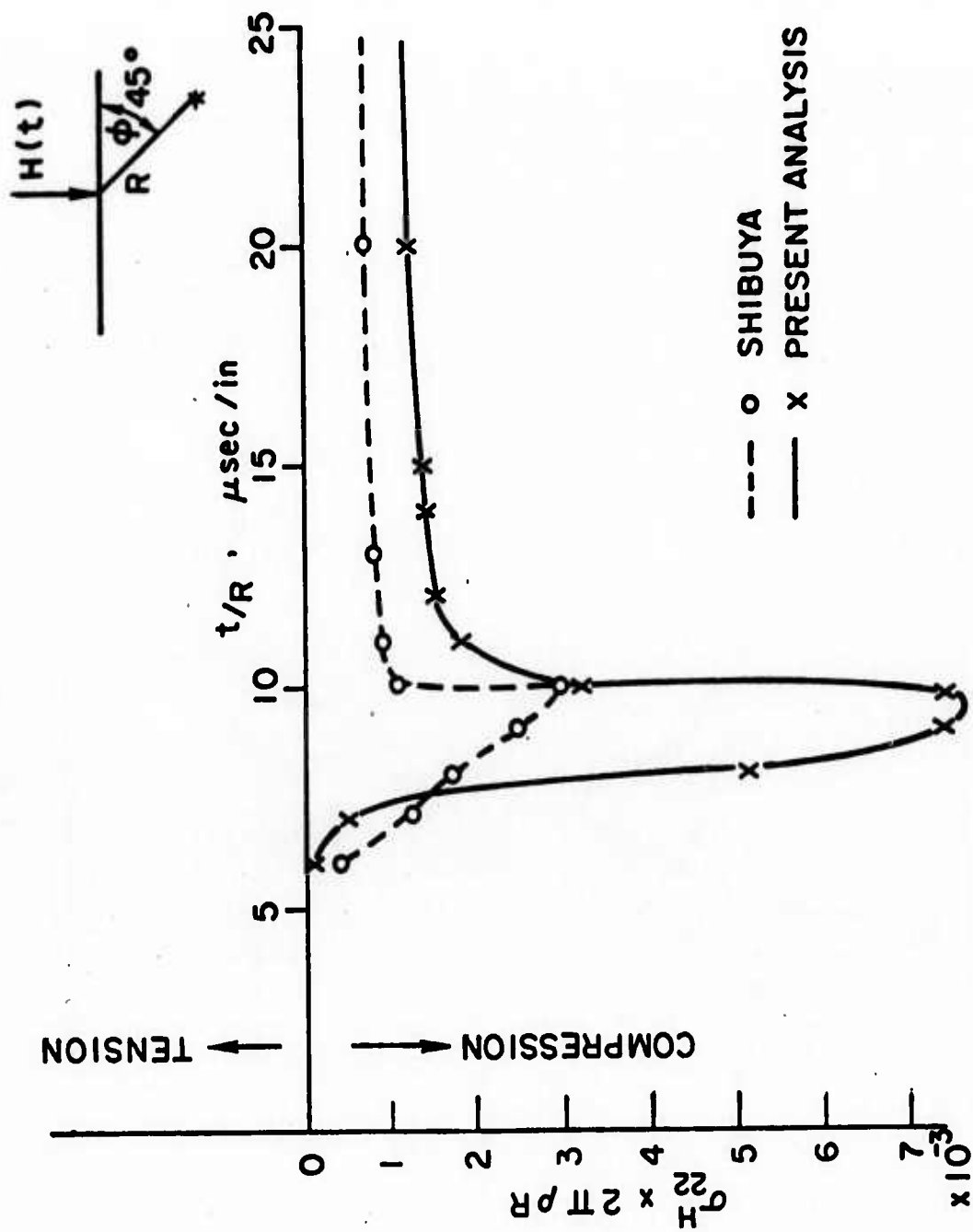


FIG. 15

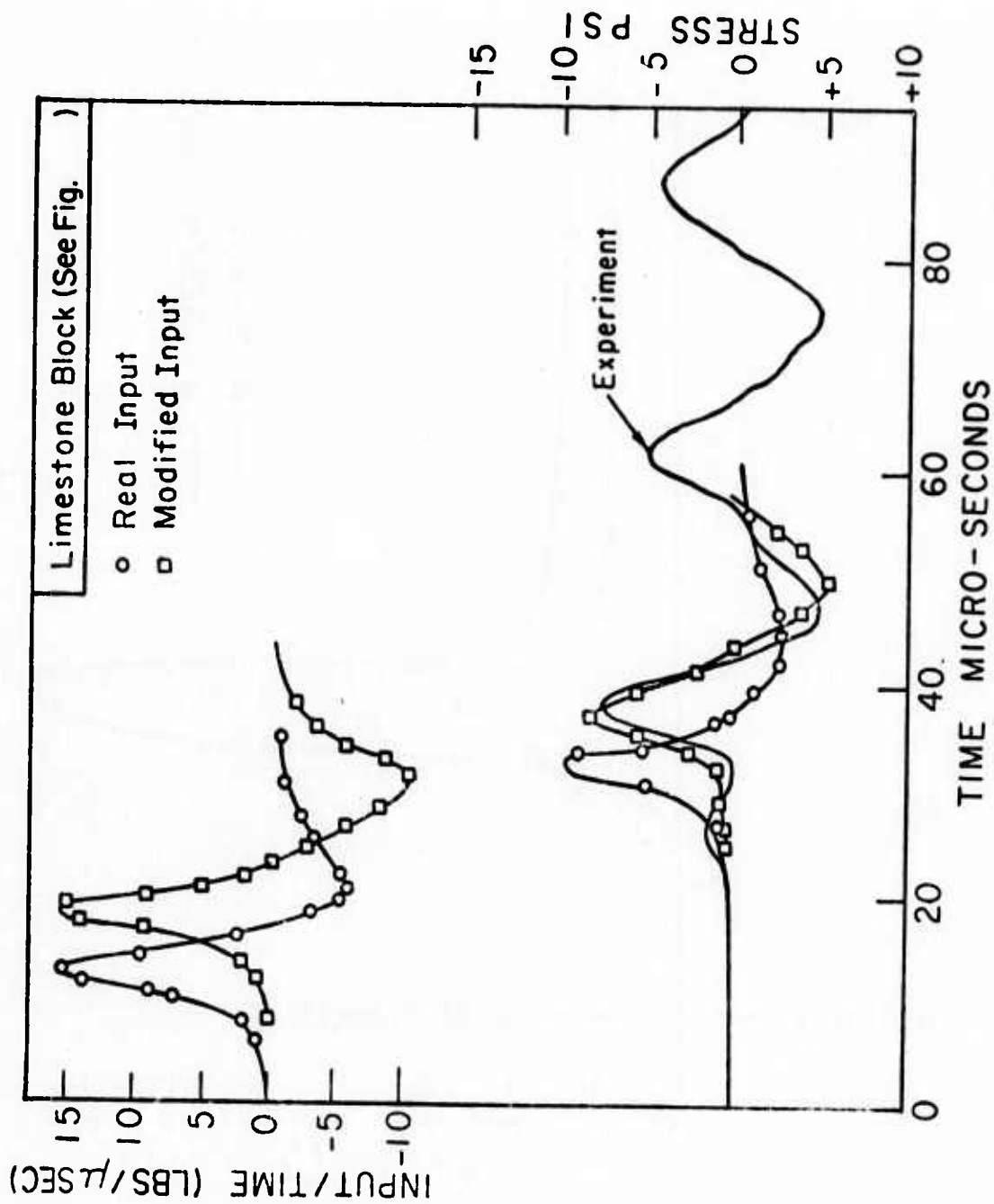


FIG. 16

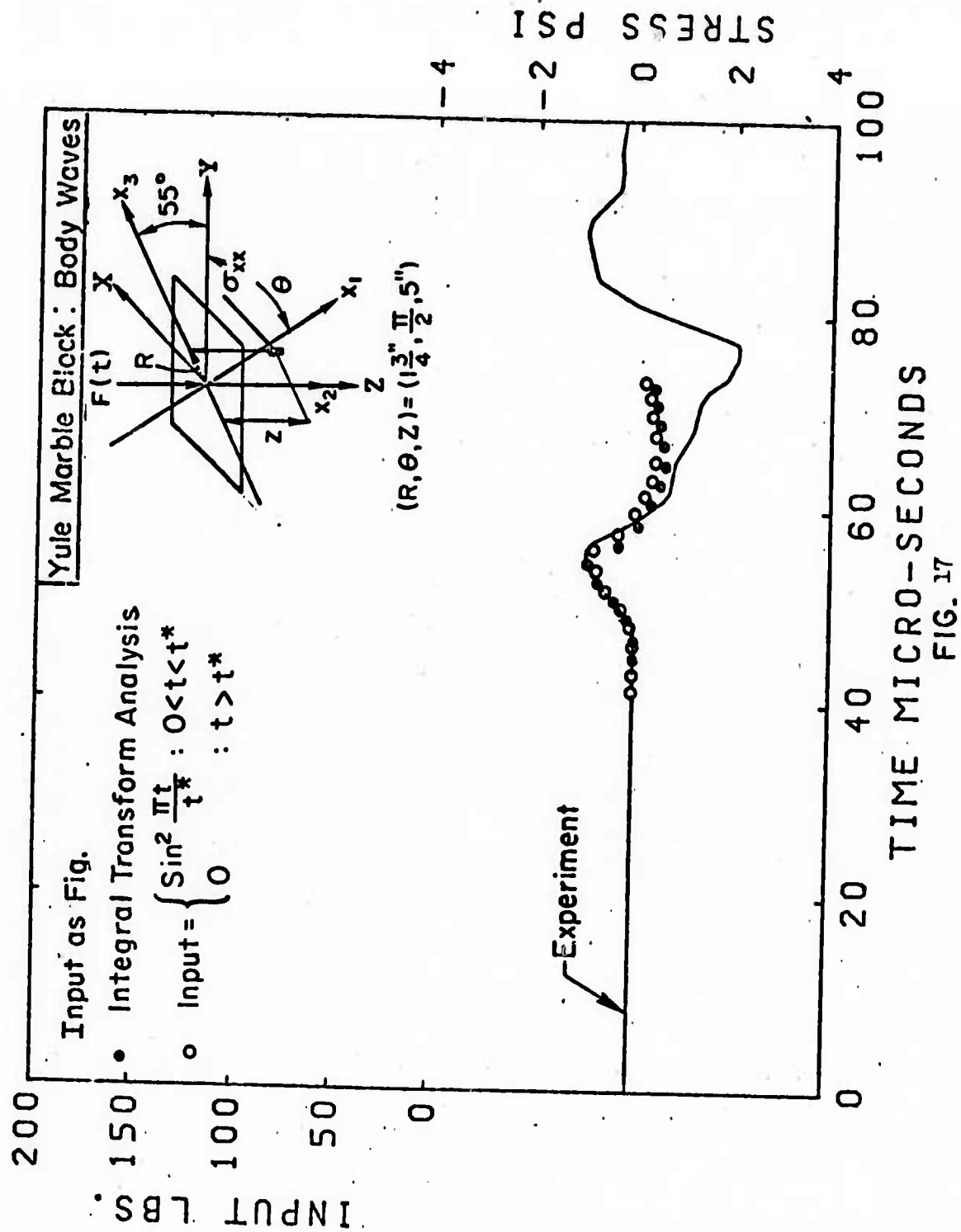


FIG. 17

Appendix B

Users Manual and Fortran Listing for the Finite
Element Method Applied to Wave Propagation
Analysis in Isotropic and Anisotropic Media

This document replaces and supplements the Users
Manual submitted previously (Reference 10 of Main Report).

SUBROUTINE MANUAL

*** USER INSTRUCTIONS AND INPUT FORMATS FOR FEAP-73 *****

FINITE ELEMENT ANALYSIS PROGRAM

FEAP73 IS A GENERAL FINITE ELEMENT ANALYSIS PROGRAM WHICH FURNISHES TO THE USER MESH INPUT/OUTPUT, ELEMENT ASSEMBLY AND SOLUTION OF EQUATIONS LINEAR, IMPLICIT AND EXPLICIT TIME DEPENDENT, NONLINEAR, PRESCRIBED GENERALIZED NODAL FORCES, PRESCRIBED NODAL AND ELEMENT DATA, AND OUTPUT OF THE GENERALIZED DISPLACEMENTS AND FORCES. ELEMENT MATRICES FOR TWO AND THREE DIMENSIONAL LINEAR ELASTICITY, SHELLS, PLATES, AND FIELD REPLACEMENT EQUATION PROBLEMS ARE AVAILABLE. ALTERNATIVELY USERS MAY SUPPLY THEIR OWN ELEMENT LIBRARY BY PROVIDING A SUBROUTINE CALLED ELMTNN, WHERE NN IS A TWO DIGIT NUMBER IDENTIFYING THE ELEMENT SUBROUTINE. EACH ELEMENT SUBROUTINE HAS AT LEAST FOUR BASIC FUNCTIONS WHICH ARE DELINEATED BY A SWITCHING PARAMETER, ISW, IN THE SUBROUTINE.

ELMTNN(MA,NOIM,NDF,NEL,NEL1,NSIF,NSIZV,NVEC,MCT,OM,0,XYZ,IX,F,FORCE,ESTIF,U,VECT,ISW)

N IS ELEMENT NUMBER.
MA IS THE MATERIAL NUMBER.
NOIM IS SPATIAL DIMENSION, 1, 2, OR 3.
NDF IS NUMBER OF DEGREES OF FREEDOM PER NODE.
NEL IS THE NUMBER OF EXTERNAL NODES PER ELEMENT.
NEL1 IS DIMENSION OF ELEMENT PROPERTY ARRAY.
NSIF IS THE SIZE OF THE ELEMENT STIFFNESS.
NSIZV IS THE SIZE OF UTILITY VECTORS.
NVEC IS THE NUMBER OF UTILITY VECTORS.
MCT IS A PRINTER LINE COUNTER.
OM IS A PARAMETER FOR MATERIAL IDENTIFICATION.
DIL(1) IS MATERIAL PROPERTY MATRIX 163 CELLS.
XYZ(INOIM,1) ARE NODAL COORDINATES.
I(NEL1,1) ARE ELEMENT PROPERTIES, NODES, ETC.
F(INOIM,1) ARE NODAL GENERALIZED FORCES.
FIPCEINSTE,21 IS ELEMENT FORCE VECTOR TO BE COMPUTED. COLUMN 2 IS LUMPED MASS.
ESTIF(NSIF,NSTF) IS ELEMENT MATRIX TO BE COMPUTED.
VECT(NSIZV,1) ARE PRESCRIBED NODAL OR ELEMENT QUANTITIES, TEMPERATURES ETC.
U(INDF,1) IS SOLUTION VECTOR.
ISW IS SWITCHING PARAMETER.

ISW = ** MATERIAL CHARACTERIZATION**

ISW=2, ** CHECK ELEMENT FOR POSITIVE AREA *
ISW=3, ** ELEMENT STIFFNESS COMPUTATION**
ISW=4, ** ELEMENT STRESSES AND PRINTOUT**
ISW=5, ** ELEMENT LOAD COMPUTATION
ISW=6, ** NONLINEAR GENERALIZED FORCES
OTHER ISW MAY BE USED FOR SPECIAL PURPOSES.

USERS CAN GENERATE SURFACE LOADINGS BY PROVIDING SLOMNN SUBROUTINES. WHERE NN IS A TWO DIGIT NUMBER BETWEEN 01 AND 09. THE SUBROUTINE IS ACCESSED BY THE CALL TO

SLOMNN(INOIM,NDF,NDF,NPRES,IPRES,PR,XYZ,FSI)

WHERE IN ADDITION TO QUANTITIES DEFINED ABOVE FOR ELMTNN,
NDF IS THE DIMENSION OF LOADED SURFACE
NPRES IS NUMBER OF LOADED NODES (MAX 8)
IPRES(1) ARE NODE NUMBERS OF LOADED NODES.
IPRES(2) ARE LOAD VALUES AT CORRESPONDING IPRES NODES.
FSI(8) ARE THE COMPUTED GENERALIZED NODAL FORCES FOR EACH DEGREE OF FREEDOM AT EACH IPRES NODE.

SEE SECTION 7.1 FOR DATA INPUT DETAILS.

INTEGRATION TABLE IS ACCESSED BY THE CALL

CALL INTEGL(LIM,NCL,NOIM,LINT,STUM)

STUM(4,M) INTEGRATION POINTS AND WEIGHTS.
NOTE M MUST BE SET EXPLICITLY AND BE LARGER THAN OR EQUAL TO LINT.
LINT - RETURNS WITH NUMBER INTEGRATION POINTS.
NCL = 0 RETURNS GAUSS POINTS AND WEIGHTS IN STUM.
LIM = 1 TO 5 IS NUMBER OF GAUSS POINTS/DIMENSION.
NCL = 1 RETURNS A SPECIAL 3-D GAUSS FORMULA.
SET LIM = 1 FOR 6 PT. CUBIC ACCURACY.
SET LIM = 2 FOR 14 PT. QUINTIC ACCURACY.
NCL = 2 RETURNS TRIANGULAR INTEGRATION FORMULA.
SET LIM = 1 FOR 1 PT. LINEAR ACCURACY.
SET LIM = 2 FOR 3 PT. QUADRATIC ACCURACY.
SET LIM = 3 FOR 7 PT. QUARTIC ACCURACY.

1.1 DATA TYPE IDENTIFICATION CARDS (15,IX,12A6).

EACH DATA SEGMENT IS PRECEDED BY A CARD WHICH IDENTIFIES THE TYPE OF DATA AND LIMITS ON THE AMOUNT OF DATA WHICH IMMEDIATELY FOLLOWS THE CARD. EXCEPT AS NOTED THE DATA SEGMENTS MAY APPEAR IN ANY ORDER. THE IDENTITY CARDS MAY ALSO AID THE USER IN INTERPRETING THE INPUT DATA CARDS. AS SUPPLIED THERE ARE TWENTY-FIVE DIFFERENT DATA IDENTIFICATION CARDS. THESE ARE

COL 7 TO 12	IDENTITY(RESTRICTIONS)
FEAP73	START OF EACH PROBLEM (MUST PRECEDE ALL OTHER DATA).
TITLE	CHANGE OUTPUT PAGE HEADINGS
REMARK	COMMENTS ON OUTPUT
MATERI	MATERIAL CHARACTERIZATION.
NODAL	NODAL CARDS
POLAR	POLAR CONVERSION. IPRECEDE BY NODAL, GENERA, OR BLOCK.
ELEMEN	ELEMENT CONNECTION CARDS.
GENERA	GENERATE NODES IN A LINEAR PATH BY ANY INCREMENT
BLOCK	GENERATE ALL MESH DATA (BOTH NODAL AND ELEMENT) FOR A 2, OR 3-DIMENSIONAL REGION WHOSE BOUNDARY MAY BE DEFINED BY 41810R 4120ICOLLOCATED POINTS
BOUND	BOUNDARY CODE DESCRIPTION (PRECEDE BY NODAL OR GENERA OR BLOCK)
VECTOP	PRESCRIBED NODAL OR ELEMENT DATA (PRECEDE BY NODAL OR POLAR AND ELEMEN)
FORCE	NODAL GENERALIZED FORCES (PRECEDE BY NODAL OR GENERA OR BLOCK).
LOADS	SURFACE LOADINGS (SAME AS FORCE).
ELoads	ELEMENT LOADINGS (SAME AS FORCE).
MESH	CHECK CONSISTENCY OF MESH ONLY (SAME AS SOLVE)
PLOT	PLOT MESH (SAME AS SOLVE)
INITIA	INITIAL CONDITION PRESCRIPTION FOR DYNAMIC ANALYSIS (PRECEDE BY NODAL, GENERA OR BLOCK)
SOLVE	COMPLETE FORMULATION AND SOLUTION FROM ELEMENTS (PRECEDE BY MATERI, NODAL OR GENERA, AND ELEMEN OR PRECEDE BY MATERI AND BLOCK)
RESOLV	USE PREVIOUS PROBLEM DESCRIPTION WITH NEW LOAD ONLY (PRECEDE BY SOLVE AND NEW LOADING CARDS).
EXPLIC	DYNAMIC SOLUTION BY EXPLICIT INTEGRATION. (SAME AS SOLVE)
IMPLIC	IMPLICIT INTEGRATION OF DYNAMIC PROBLEMS (PRECEDE BY SAME DATA AS FOR SOLVE)
VISCOE	QUASI-STATIC LINEAR VISCOELASTIC INTEGRATION (PRECEDE BY SAME DATA AS FOR SOLVE)
FOURIE	FOURIER COMPOSITION (SAME AS SOLVE)
ADDDP	ACCUMULATE FOURIER SOLUTION (AFTER FOURIE)
STOP	NORMAL EXIT (MUST FOLLOW ALL DATA)

NOTE EACH IDENTIFIER IS PUNCHED STARTING IN COL 7 (LEFT JUSTIFIED).

EXCESS CARDS MAY EXIST BETWEEN EACH SECTION OF DATA, HOWEVER, THE DATA TO BE USED MUST IMMEDIATELY FOLLOW THE TYPE CARD AND MUST BE IN PROPER ORDER. NO PARTICULAR ORDER OF THE TYPE CARDS IS NECESSARY EXCEPT THAT THE FEAP73 CARD MUST ALWAYS BE THE FIRST CARD IN EACH SET OF DATA, AND RESTRICTIONS MUST BE OBSERVED.

2.1 PROBLEM INITIATION AND CONTROL CARDS

CARD 1. 16X,12A61

COL 7 TO 12 MUST CONTAIN WORD FEAP73
COL 13 TO 78 OUTPUT PAGE HEADER

CARD 2. 115,1X,3A61

COL 1 TO 5 NOIM - SPATIAL DIMENSION OF PROBLEM (1 TO 3)
COL 7 TO 12 NAMES TO BE PRINTED AS OUTPUT HEADERS 10
COL 13 TO 19 COORDINATES - IF BLANK SET TO 1,2,3 AS NEEDED.
COL 19 TO 24

CARD 3. 115,1X,6A61

COL 1 TO 5 NDF - NUMBER OF UNKNOWN PER NODE (1 TO 6)
COL 7 TO 12 NAMES TO BE PRINTED AS OUTPUT HEADERS OF THE
COL 13 TO 18 GENERALIZED DISPLACEMENTS AND FORCES - IF
***** BLANK SET TO 1,2,3,4,5,6 AS NECESSARY
COL 37 TO 42

CARD 4. 1615,5F10.01

COL 1 TO 5 NEN - MAXIMUM NUMBER OF NODES CONNECTED TO ANY
ELEMENT (1 TO 20).
COL 6 TO 10 NEXTRA - INCREASES ELEMENT MATRIX SIZE FROM
NDF*NEN TO NDF*NEN + NEXTRA
COL 11 TO 15 IREC - COMPUTE GENERALIZED FORCE CHECK IF
NONZERO (FOR TIME INVARIANT ANALYSIS ONLY)
COL 16 TO 20 MRAN - MAXIMUM EXPECTED BANDWIDTH, DEFAULT IS
SET TO 100. USED AS AN ERROR CHECK TO PREVENT
RUNNING WITH AN OVERSIZED ERROR.
COL 21 TO 25 IBUF - BUFFER SIZE FOR STORAGE OF HISTORY
EFFECTS IN TIME DEPENDENT ANALYSIS, DEFAULT IS
IBUF = 1520720.

COL 26 TO 30 NCL - USER INTEGER CONSTANT
COL 31 TO 40 CNCL - USER DEFINED CONSTANT
COL 41 TO 50 CON2 - USER DEFINED CONSTANT

COL 51 TO 60 CON3111 - USER DEFINED CONSTANT
COL 61 TO 70 CON3121 - USER DEFINED CONSTANT
COL 71 TO 80 CON3131 - USER DEFINED CONSTANT

2.1) PREMARKER USE COMMENTS ON OUTPUT. (16X,12A6)

SUBSEQUENT CARDS

COL 1 TO 12 MUST CONTAIN REMARK
COL 13 TO 18 STATEMENTS TO BE OUTPUT, USE AS MANY REMARK
CARDS AS DESIRED. INSERT BEFORE ANY TYPE CARD.

2.2) TITLE CHANGE ON OUTPUT (16X,12A6)

COL 1 TO 12 MUST CONTAIN TITLE
COL 13 TO 18 NEW TITLE DESCRIPTOR

2.3) EXECUTION TERMINATION (16X,12A6)

COL 7 TO 10 MUST CONTAIN STOP, INSERT AFTER LAST PROBLEM.

3.1) MATERIAL CHARACTERIZATION (115,1X,12A6)

COL 1 TO 5 NUMMAT - NUMBER OF DIFFERENT MATERIAL CHARACTERIZATIONS TO FOLLOW.
COL 7 TO 12 MUST CONTAIN WORD MATERIAL

THE FOLLOWING CARDS ARE SUPPLIED FOR EACH MATERIAL TO BE CHARACTERIZED (MUST BE EXACTLY NUMMAT SETS OF CARDS)

CARD 1.1) ELEMENT SELECTOR CARD (115,1X,12A6)

COL 1 TO 5 MATERIAL NUMBER 11 TO NUMMAT
COL 7 TO 11 ELMNN - WHERE NN IS NUMBER OF ELEMENT CLASS (01 TO 30) TO WHICH THE CHARACTERIZATION BELONGS.
COL 12 TO 17 ALPHANUMERIC INFORMATION TO BE OUTPUT.

CARD 2.1, ETC. ** USER DEFINED FOR EACH ELEMENT TYPE PROVIDED.

4.1) NODAL CARDS (115,1X,12A6)

COL 1 TO 5 NUMNP - NUMBER OF NODAL POINTS
COL 7 TO 12 MUST CONTAIN NODAL

SUBSEQUENT CARDS LAST NODAL CARD MUST NOT BE GENERATED.
(115,115,3F10.0)

COL 1 TO 5 NODE NUMBER
COL 16 TO 20 1 IF 1 DISPLACEMENT IS SPECIFIED

COL 16 1 IF 2 DISPLACEMENT IS SPECIFIED
COL 17 1 IF 3 DISPLACEMENT IS SPECIFIED
COL 18 1 IF 4 DISPLACEMENT IS SPECIFIED
COL 19 1 IF 5 DISPLACEMENT IS SPECIFIED
COL 20 1 IF 6 DISPLACEMENT IS SPECIFIED
COL 21 TO 30 1 COORDINATE VALUE
COL 31 TO 40 2 COORDINATE VALUE * AS REQUIRED
COL 41 TO 50 3 COORDINATE VALUE

NODAL CARDS MUST BE IN ORDER. MISSING NODES ARE INTERPOLATED LINEARLY FROM INPUT NODES. IF SUCCEEDING CARDS HAVE IDENTICAL BOUNDARY CODES, THIS BOUNDARY CODE WILL BE ASSIGNED TO THE INTERVENING NODES. IN ALL OTHER CASES THE BOUNDARY CODE IS SET TO ZERO *TERMINATE ON NODE NUMNP OR A BLANK CARD

4.11 NON SEQUENTIAL NODAL GENERATOR OPTION. (115,1X,12A6)

COL 1 TO 5 NUMBER OF NODAL POINTS
COL 7 TO 12 MUST CONTAIN GENERA

SUBSEQUENT CARDS (115,110,3F10.0)

COL 1 TO 5 NODE-NUMBER
COL 6 TO 10 NODE-NUMBER-INCREMENT WHICH WILL BE SUCCESSIVELY ADDED TO NODE-NUMBER UNTIL SUM IS GREATER THAN NODE-NUMBER ON FOLLOWING CARD (ALGEBRAIC).
COL 15 TO 20 BOUNDARY CODE, SAME AS INPUT FOR NODAL. IF SUCCEEDING CARDS HAVE IDENTICAL BOUNDARY CODES, THIS BOUNDARY CODE WILL BE ASSIGNED TO THE INTERVENING NODES. IN ALL OTHER CASES THE BOUNDARY CODE IS SET TO ZERO.
COL 21 TO 30 1 COORDINATE VALUE *
COL 31 TO 40 2 COORDINATE VALUE * AS REQUIRED *
COL 41 TO 50 3 COORDINATE VALUE *

*TERMINATE WITH BLANK CARD *

4.21 BOUNDARY CODE PATCH-UP OPTION. (16X,12A6)

COL 6 TO 12 MUST CONTAIN BOUNDARY

SUBSEQUENT CARDS. (1615)

COL 1 TO 5 N, NODE NUMBER TO HAVE REDEFINED BOUNDARY CODE.
COL 6 TO 10 NX, GENERATOR INCREMENT TO BE ADDED ALGEBRAICALLY TO N, UNTIL SUM EXCEEDS (MAX OR MIN) THE N OF THE FOLLOWING CARD.
COL 11 TO 15 INC(1), (1=1,2,...,NOF) CODE FOR SPECIFYING FORCE
COL 16 TO 20 OR DISPLACEMENT BOUNDARY CONDITIONS.
COL ...

INC(1) .EQ. 0, FORCE SPECIFIED.
INC(1) .GT. 0, DISPLACEMENT SPECIFIED, NO INTERVENING GENERATION.
INC(1) .LT. 0, DISPLACEMENT SPECIFIED, GENERATE BETWEEN MISSING NODES IN ALGEBRAIC INCREMENTS OF NX.

* TERMINATE WITH A BLANK CARD. *

4.31 POLAR OR CYLINDRICAL COORDINATE CONVERSION TO CARTESIAN COORDINATES (16X,12A6)

COL 7 TO 12 MUST CONTAIN POLAR (LEFT JUSTIFIED)

CARD 1. (115,5X,2F10.0)

COL 11 TO 15 N1, INCREMENT ADDED (ALGEBRAICALLY), N1 TO N2
COL 1 TO 5 N1, FIRST NODE TO BE CONVERTED
COL 6 TO 10 N2, LAST NODE TO BE CONVERTED
COL 21 TO 30 X0, ORIGIN OF POLAR X-COORDINATE
COL 31 TO 40 Y0, ORIGIN OF POLAR Y-COORDINATE

5.1) ELEMENT CARDS (115,1X,12A6)

COL 1 TO 5 NUMEL - NUMBER OF ELEMENTS
COL 7 TO 12 MUST CONTAIN ELEMENT

SUBSEQUENT CARDS (115,2013/2014)

CARD 1.

COL 1 TO 5 ELEMENT NUMBER
COL 6 TO 10 MATERIAL NUMBER
COL 11 TO 15 NUMBER OF SUBSEQUENT ELEMENTS USING SAME STIFFNESS MATRIX * SAVES RECOMPUTATION OF SIMILAR MATRICES. ELEMENT MUST ALSO HAVE SAME ELEMENT FORCE VECTOR * IF THESE ARE IN THE STIFFNESS SUBROUTINE *
COL 16 TO 20 PRINT ELEMENT MATRIX IF NONZERO.
COL 21 TO 23 (XDI1) ELEMENT INCREMENT ARRAY ON NODE 1.
COL 24 TO 26 (XDI2) * IF NOT INPUT IS SET AUTOMATICALLY UP TO
COL 78 TO 80 (XDI201) FOR SERENDIPITY ELEMENTS * SEE REPORT

CARD 2.

COL 1 TO 4 NODE 1
COL 5 TO 8 NODE 2
COL 9 TO 12 NODE 3 (XINEL1,1) ARRAY
CONTINUE IN 14 FORMAT TO A MAXIMUM

COL 77 TO 80 NODE 20

NODES MUST BE NUMBERED AROUND ELEMENT BY RIGHT HAND SCREW RULE. ELEMENT CARDS MUST BE IN ORDER. MISSING ELEMENTS ARE GENERATED BY INCREMENTING NODES.

LAST ELEMENT CARD MUST NOT BE GENERATED.
* TERMINATE ON ELEMENT NUMEL OR A BLANK CARD *

5.11 BLOCK GENERATOR, GENERATES ALL MESH DATA. (16X,12A6)

COL 1 TO 5 NUMBER OF NODAL POINTS TO BE GENERATED.
COL 7 TO 12 MUST CONTAIN BLOCK

SUBSEQUENT CARDS (11015/615/110X,3F10.01)

CARD 1.

COL 1 TO 5 NN, NUMBER OF POINTS REQUIRED TO DEFINE BOUNDARY OF REGION. FOR 2-DIM., NN=4 OR 8. FOR 3-DIM., NN=8 OR 20.
COL 6 TO 10 NUMBER OF ELEMENTS IN R-DIRECTION.
COL 11 TO 15 NUMBER OF ELEMENTS IN S-DIRECTION.
COL 16 TO 20 NUMBER OF ELEMENTS IN T-DIRECTION.
COL 21 TO 25 INITIAL NODE NUMBER, DEFAULT = 1.
COL 26 TO 30 INITIAL ELEMENT NUMBER, DEFAULT = 1.
COL 31 TO 35 MATERIAL NUMBER OVER REGION, DEFAULT = 1.
COL 36 TO 40 BOUNDARY CODE SKIP. A NON-ZERO ENTRY WILL OMIT SETTING ALL INTERIOR BOUNDARY CODES TO ZERO.
COL 41 TO 45 IREFUSE - REUSE ELEMENT STIFFNESS OPTION - USES EACH ELEMENT STIFFNESS IREFUSE TIMES BEFORE GENERATING A NEW ELEMENT STIFFNESS MATRIX.
COL 46 TO 50 ELEMENT STIFFNESS-PRINT. A NON-ZERO ENTRY WILL CAUSE PRINT-OUT OF FIRST ELEMENT.
COL 51 TO 55 IMSH - IF NONZERO SUPPRESSES PRINT OF NODES.
COL 56 TO 60 IELM - IF NONZERO SUPPRESSES PRINT OF ELEMENTS.

CARD 2. BOUNDARY CODE AS DEFINED IN NODAL CARD.1

COL 1 TO 10 BOUNDARY CODE OVER FACE -R.
COL 11 TO 20 BOUNDARY CODE OVER FACE +R.
COL 21 TO 30 BOUNDARY CODE OVER FACE -S.
COL 31 TO 40 BOUNDARY CODE OVER FACE +S.
COL 41 TO 50 BOUNDARY CODE OVER FACE -T.
COL 51 TO 60 BOUNDARY CODE OVER FACE +T.

CARD 3. (REPEAT NN TIMES,1)

COL 11 TO 20 1-COORDINATE OF BOUNDARY-DEFINING-POINT.
COL 21 TO 30 2-COORDINATE OF BOUNDARY-DEFINING-POINT.
COL 31 TO 40 3-COORDINATE OF BOUNDARY-DEFINING-POINT.

NOTE: BLOCK GENERATES ONLY 4 PT. QUADRILATERALS OR 8 PT. BRICKS.
INPUT OF CARDS 3.1 FOLLOW ORDER RULES FOR ELEMENT INPUT (SEE 5.1)
R-S-T ARE LOCAL COORDINATES, I.E. 1-1 .LE. R,S,T .LE. 1.)
WHERE R IS DIRECTED FROM NODE 1 TO 2, S IS IN PLANE OF FIRST
THREE NODES, AND T IS NORMAL TO R-S PLANE.

6.1 VECTOR CARDS, I.E. USER DEFINED INPUT I15,1X,A61

COL 1 TO 5 NVEC, NUMBER OF DIFFERENT VECTORS IT MAXI
COL 7 TO 12 MUST CONTAIN VECTOR

SUBSEQUENT CARDS

CARD 1. 12151

COL 1 TO 5 NSIZV, VECTOR LENGTH, COMMON TO ALL NVEC VECTORS
COL 6 TO 10 IPICK, CODED PARAMETER,
IPICK = 0, VECTORS ASSOCIATED WITH NODES
IPICK = 1, VECTORS ASSOCIATED WITH DEG.FREEDOM
IPICK = 2, VECTORS ASSOCIATED WITH ELEMENTS

CARD 2. 16X, 2A61 REPEAT NVEC TIMES

COL 7 TO 16 DESCRIPTIVE TITLE FOR VECTOR

CARD 3. 1215,TF10,01

COL 1 TO 5 POSITION NUMBR OF VECTOR ELEMENT, 1 TO NSIZV
COL 11 TO 20 VECTOR ELEMENT VALUE OF VECTOR 1
COL 6 TO 10 GENERATOR INCREMENT
COL 21 TO 30 VECTOR ELEMENT VALUE OF VECTOR 2
COL AS REQUIRED FOR NVEC VECTORS

LINEAR INTERPOLATION IS PERFORMED ON ALL VECTORS BETWEEN
NON-CONSECUTIVE POSITION NUMBERS SPECIFIED IN COL 1 TO 5 IF
INCREMENT IS NONZERO.
IF DESCRIPTIVE TITLES OF ALL VECTORS ARE BLANK CARDS, PRINTING
OF THE VECTOR VALUES IS SUPPRESSED.

* TERMINATE ON BLANK CARD *

6.11 INITIAL CONDITIONS FOR TIME DEPENDENT ANALYSIS.

COL 1 TO 5 NICO, NUMBER OF INITIAL CONDITION VECTORS
COL 7 TO 12 MUST CONTAIN INITIA

SUBSEQUENT CARDS

COL 51 TO 55 INC(IN), INCREMENT VALUE ADDED TO (PRESIN) TO
COL 56 TO 59 IDENTIFY NODE NUMBERS OF A GENERATED SEQUENCE.
COL 60 TO 61 IDENTIFY FROM 2 TO 8 AS REQUIRED

CARD 2. (BF10,01

COL 1 TO 80 LOAD AT NODES GIVEN ON PREVIOUS CARD *
MUST CORRESPOND IN SEQUENCE TO THE NODE NUMBERS

7.21 ELEMENT LOAD CARDS I15,1X,A61

COL 1 TO 5 NLO, NUMBER OF ELEMENT LOAD CARDS.
COL 7 TO 11 MUST CONTAIN ELDAOS

SUBSEQUENT CARDS I15,1X,A5,14,15,6F10,01

COL 1 TO 5 IEL, INITIAL ELEMENT OF A GENERATED SEQUENCE.
COL 7 TO 11 ELMINN, ALPHA-NUMERIC NAME OF ELEMENT
SUBROUTINE WHERE ELEMENT LOADS ARE COMPUTED.
USED AS CHECK TO INSURE IEL, ET,2 ARE PROPER
ELEMENTS.
COL 12 TO 15 INC, INCREMENT NUMBR IN A GENERATED SEQUENCE.
(DEFAULT = 1).
COL 16 TO 20 JEL, TERMINAL ELEMENT NUMBER IN A GENERATED
SEQUENCE, IF JEL = 0, ONLY IEL IS COUNTED.
COL 21 TO 80 USER DEFINED VALUES FOR DETERMINING BODY LOADS
IN THE ISW=5 PORTION OF ELMINN).

NOTE: USER MUST PROVIDE COMPUTATION OF LOADS IN ELMTNN.
PR IS TRANSFERRED TO SUBROUTINE ELMTNN IN THE U VECTOR,
WHEN ISW = 5, ONLY.

7.31 PROPORTIONAL LOADS FOR TIME DEPENDENT ANALYSIS

TRANSFER TO THIS OPTION OCCURS ONLY FOR TIME ANALYSES.

ONE CARD FOR EACH PROPORTIONAL LOAD REQUIRED

COL 1 TO 5 PROPORTIONAL LOAD TYPE, 1,2 OR 3
COL 6 TO 10 K, TABLE CONSTANT
COL 11 TO 20 TMIN, SMALLEST TIME LOADING IS VALID
COL 21 TO 30 TMAX, LARGEST TIME LOADING IS VALID
COL 31 TO 40 A0
COL 41 TO 50 A1
COL 51 TO 60 A2
COL 61 TO 70 A3
COL 71 TO 80 A4

CARD 1. 16X,2A61 REPEAT NICO TIMES

COL 7 TO 16 DESCRIPTIVE TITLE FOR INITIAL CONDITIONS

CARD 2. 1215,TF10,01

COL 1 TO 5 POSITION NUMBER, AS IN VECTOR CARDS FOR IPICK=1
COL 6 TO 10 GENERATOR INCREMENT
COL 11 TO 20 INITIAL CONDITION 1
COL 21 TO 30 INITIAL CONDITION 2
COL AS REQUIRED FOR NICO INITIAL CONDITIONS

INTERPOLATION BETWEEN INPUT VALUES AS DESCRIBED IN VECTOR INPUT.
*** NOTE *** IF MISSING THE INITIAL CONDITIONS ARE SET ZERO

T.) FORCE CARDS I15,1X,A61

COL 1 TO 5 LAST NODE TO WHICH A FORCE IS TO BE SPECIFIED
COL 7 TO 12 MUST CONTAIN FORCE

SUBSEQUENT CARDS I15,5X,6F10,01

THE FOLLOWING VALUES ARE EACH INTERPRETTED AS FORCES IF THE
CORRESPONDING BOUNDARY CODE IS A 0 *ZERO* AND AS A DISPLACEMENT
IF THE CORRESPONDING BOUNDARY CODE IS 1 *ONE*.

COL 1 TO 5 NODE TO WHICH FORCE OR DISPLACEMENT IS APPLIED
COL 11 TO 20 VALUE OF 1 FORCE/DISPLACEMENT
COL 21 TO 30 VALUE OF 2 FORCE/DISPLACEMENT * AS *
COL 31 TO 40 VALUE OF 3 FORCE/DISPLACEMENT * REQUIRED *
COL 41 TO 50 VALUE OF 4 FORCE/DISPLACEMENT
COL 51 TO 60 VALUE OF 5 FORCE/DISPLACEMENT
COL 61 TO 70 VALUE OF 6 FORCE/DISPLACEMENT

T.1) SURFACE LOAD CARDS I15,1X,A61

COL 1 TO 5 NUMBER OF LOADED FACE CARDS
COL 7 TO 12 MUST CONTAIN LOADS

CARD 1. I15,1X,A5,14,815,8131

COL 1 TO 5 DIMENSION OF LOADING SURFACE, 11 OR 21.
COL 7 TO 11 SLODINN, ALPHA-NUMERIC NAME OF SURFACE LOADING
SURROUTINE INN IS BETWEEN 1 AND 51
COL 12 TO 15 NRT, NUMBER OF ADDITIONAL ELEMENT LOAD
SURFACES TO BE GENERATED FROM CURRENT MODEL.
COL 16 TO 20 (PRESIN), NODE NUMBERS DEFINING LOADING SURFACE
OF CURRENT ELEMENT.
COL 21 TO 25 IDENTIFY FROM 2 TO 8 AS REQUIRED

LOAD TYPE 1. T = TIME

PROP = A0 + A1*T + A2*T*T + A3*T*T*T + A4*T*T*T*T

LOAD TYPE 2.

PROP = A0*(SINTAT*T)**K + A2*(COSIA2*T)**K + A5

LOAD TYPE 3.

PROP = USER DEFINED FUNCTION FROM SUBROUTINE EXPRLODIPROP,T1

NOTE PROPORTIONAL LOADS CAN BE ACCUMULATED FROM DIFFERENT
TYPES AT THE SAME TIME.

8.1) INITIATION OF TIME INDEPENDENT SOLUTION I15,1X,A61

COL 1 TO 4 IOUT, OUTPUT CONTROL CODE.

IOUT .ED. 0, ALL STRESSES AND DISP. PRINTED
IFUT .NE. 0, SELECTED PRINTOUT, MORE DATA INPUT
SEE SECTION 9 FOR DATA PREPARATION.

COL 7 TO 12

MUST CONTAIN SOLVE *INDICATES ALL DATA INPUT*
COMPLETE FORMULATION AND SOLUTION OF EQUATIONS.
MUST CONTAIN RESOLV TO OBTAIN SUBSEQUENT
SOLUTIONS WHERE BOUNDARY CODES DO NOT CHANGE
AND ALL PRESCRIBED DISPLACEMENTS ARE ZERO.

8.11 INITIATION OF DYNAMIC SOLUTION BY EXPLICIT INTEGRATION.

COL 1 TO 4

IOUT, OUTPUT CONTROL FOR DISPLACEMENT AND
STRESS PRINTOUT. SEE SECT. 9 FOR DATA INPUT.
IF IOUT .NE. 0, THE SPATIAL CONTROL DATA
COMES AT THE END OF THE DYNAMIC SEGMENT.
MUST CONTAIN EXPLC

SUBSEQUENT CARDS I215,2F10,0,2151

COL 1 TO 5 NUMBER OF TIME STEPS
COL 6 TO 10 PRINT INTERVAL
COL 11 TO 20 TIME INCREMENT
COL 21 TO 30 NEWMARK DELTA-DAMPING TERM (GAMMA = .5)
COL 31 TO 35 NUMBER OF TIME EVOLUTION STRESS PLOTS.
COL 36 TO 40 NPROP, NUMBER OF PROPORTIONAL LOADS TO BE INPUT
COL 41 TO 45 NFORC, LAST NODE ON WHICH A FORCE IS CHANGED
DURING EACH TIME STEP.
COL 46 TO 50 KKK, STABILITY CHECK OVERRIDE * CAUTION USE
ONLY WHEN A BETTER ESTIMATE OF THE STABLE TIME

STEP IS AVAILABLE THAN CAN BE PERFORMED BY CODE
 KKK ZERO, USES INTERNAL STABILITY CHECK.
 KKK NONZERO, DISREGARDS STABILITY CHECK.

SUBSEQUENT CARDS (115) ONE FOR EACH STRESS PLOT.

COL 1 TO 5 ELEMENT NUMBER CONTAINING STRESS TO BE PLOTTED.
 COL 6 TO 10 LOCAL COORDINATE POINT CODE, 1 TO 7, AS
 PATTERNED AFTER, COL 11 TO COL 17, IN SOLVE.
 COL 11 TO 15 STRESS COMPONENT CODE, 1 TO 6 FOR SIGMA11,J1,
 I.E., SIGMA11,1)=1, SIGMA11,2)=2, SIGMA11,3)=3,
 SIGMA12,2)=4, SIGMA12,3)=5, SIGMA13,3)=6.

IFINPROP.NE.O1 READ PROPORTIONAL LOAD CARDS, SEE SECT. 7.3

IFINFORC.NE.O1 READ FORCE CARDS AT EACH TIME STEP. IF OUTPUT IS
 LIMITED BY IOUT NONZERO, THE FIRST FORCE CARD SET PRECEDES
 OUTPUT CARDS AND THE REMAINDER FOLLOW THE OUTPUT CARDS NO BLANK
 CARDS MAY BE USED BETWEEN SETS OF CARDS OTHER THAN THE USUAL
 BLANK TERMINATOR CARD FOR FORCE INPUT CARDS.

IFITOUT.NE.O1 DATA FOR SPATIAL PRINTOUT CONTROL, SEE SECT.9.

SPECIAL COMMENTS FOR DYNAMIC OPTION

- (1) ONLY COLUMNS 1 TO 60 ARE AVAILABLE FOR PAGE HEADING.
- (2) MAXIMUM ADVANTAGE OF ELEMENT REUSE OPTION SHOULD BE TAKEN.
- (3) INITIAL CONDITIONS FOR DISPLACEMENT AND VELOCITY VECTORS,
 AS WELL AS STORAGE FOR ACCELERATION VECTOR, MAY BE MADE
 THROUGH INPUT OF AN INITIAL CONDITION CARD SET, WITHOUT
 SPECIFIED INITIAL CONDITIONS THEY ARE AUTOMATICALLY SET ZERO.
- (4) SPATIAL LOADING IS INPUT THROUGH FORCE OR BOUNDARY
 PRESSURE CARDS. ALL LOADS VARY PROPORTIONALLY WITH TIME
- (5) EXTREME CAUTION ON ORDER OF DATA CARDS MUST BE OBSERVED. NO
 EXTRA CARDS ARE PERMITTED AND STRICT COUNTS ARE OBSERVED
 EXCEPT FOR THE NUMBER OF FORCE CARDS USED IN EACH TIME STEP.

8.21 INITIATION OF IMPLICIT TIME INTEGRATIONS (15,IX,A61)

COL 1 TO 5 NSEQ, NUMBER OF TIME SEQUENCES
 COL 7 TO 12 MUST CONTAIN VISCOE FOR LINEAR VISCOELASTIC
 QUASI-STATIC PROBLEMS ONE INITIAL CONDITION
 ONLY MUST BE USED
 COL 7 TO 12 MUST CONTAIN IMPLIC FOR DYNAMIC IMPLICIT
 INTEGRATIONS (THREE INITIAL CONDITIONS ARE
 REQUIRED, MORE CAN BE SPECIFIED WITHOUT ERROR)

SURSEQUENT CARDS, ONE SET FOR EACH TIME SEQUENCE

SUPPRESSED BY NON-ZERO ENTRIES AS FOLLOWS,
 E.G.

COL 11 SUPPRESS PRINT AT LOCAL POINT 1, (1 0, 0, 0)
 COL 12 SUPPRESS PRINT AT LOCAL POINT 2, (-1, 0, 0)
 COL 13 SUPPRESS PRINT AT LOCAL POINT 3, (1, 0, 0)
 COL 14 SUPPRESS PRINT AT LOCAL POINT 4, (0, -1, 0)
 COL 15 SUPPRESS PRINT AT LOCAL POINT 5, (0, 1, 0)
 COL 16 SUPPRESS PRINT AT LOCAL POINT 6, (0, 0, -1)
 COL 17 SUPPRESS PRINT AT LOCAL POINT 7, (0, 0, 1)

SURSEQUENT CARDS (215) SKIP IF NUMSTR = 0

COL 1 TO 5 ELEMENT NUMBER TO BE PRINTED.
 COL 6 TO 10 HIGHER ELEMENT NUMBER OF A GENERATED SEQUENCE,
 IF ZERO ONLY FIRST ELEMENT IS COUNTED.
 COL 11 TO 15 INCREMENT TO GENERATOR, DEFAULT = 1
 *** REPEAT UNTIL, NUMSTR CARDS HAVE BEEN READ

RETURN
 END

CARD 1. (F10.0,015,2F10.01

COL 1 TO 10 OT, TIME INCREMENT (NONZERO FOR IMPLICIT
 COL 11 TO 15 NTS, NUMBER OF TIME STEPS IN SEQUENCE
 COL 16 TO 20 INT, PRINT INTERVAL (DEFAULT 1)
 COL 21 TO 25 NNI, FIRST NODE PRINTED
 COL 26 TO 30 NNE, LAST NODE PRINTED
 COL 31 TO 35 NEI, FIRST ELEMENT STRESS TO BE PRINTED
 COL 36 TO 40 NEF, LAST ELEMENT STRESS TO BE PRINTED
 COL 41 TO 45 NPROP, NUMBER OF PROPORTIONAL LOADS IN SEQUENCE
 COL 46 TO 50 NFORC, LAST NODE FOR GENERALIZED FORCES TO BE
 INPUT FOR EACH TIME IN SEQUENCE (SEE SECT.7.
 FOR DATA PREPARATION FORMATS)
 COL 51 TO 60 BETA, NEWMARK INTEGRATION PARAMETER (IMPLICIT
 COL 61 TO 70 OEL = GAMMA - 0.5, NEWMARK INTEGRATION
 PARAMETER (IMPLICIT)

CARD 2. (215,7F10.01

ONE FOR EACH NPROP. SEE SECT.7.3 FOR DATA PREPARATION

SUBSEQUENT CARDS FOR EACH TIME STEP IN THE SEQUENCE

FORCE CARDS. SEE SECTION 7. FOR DATA PREPARATION FORMATS.

9.) OUTPUT CONTROL FOR LIMITED PRINTS

DISPLACEMENT OUTPUT CONTROL, IF IOUT .NE. 0.

CARD 1. (115)

COL 1 TO 5 NUMDIS - NUMBER OF DISPLACEMENT PRINT CARDS
 SUBSEQUENT CARDS (215) SKIP IF NUMDIS = 0
 COL 1 TO 5 NODAL NUMBER TO BE OUTPUT.
 COL 6 TO 10 HIGHER NODE NUMBER OF A GENERATED SEQUENCE,
 IF ZERO JUST FIRST NODE IS COUNTED.
 COL 11 TO 15 INCREMENT TO GENERATOR, DEFAULT = 1
 *** REPEAT UNTIL, NUMDIS CARDS HAVE BEEN READ

STRESS OUTPUT CONTROL, IF IOUT .NE. 0.

CARD 1. (115,5X,711)

COL 1 TO 5 NUMSTR - NUMBER OF STRESS OUTPUT CARDS
 COL 11 TO 17 NSIG17) - PRINT PATTERN WITHIN AN ELEMENT.
 LOCAL POINTS OF EACH ELEMENT CAN BE

PROGRAM FEAP731 INPUT=101,OUTPUT,PUNCH=101,PUNCHB=101,TAPE12=101
 X, TAPE4=PUNCH,TAPE5=INPUT,TAPE6=OUTPUT,TAPE7,TAPE9,TAPE10,
 X TAPE11,TAPE13,TAPE14,TAPEBB=PUNCHB)

C.... FINITE ELEMENT ASSEMBLY PROGRAM * STORAGE ALLOCATION

C COMMON OT(60001

C ***** ISZOT MUST COINCIDE WITH SIZE OF ARRAY OT

C ISZOT = 6000

C ***** REASONABLE MAXIMUM BAND WIDTH

C MBAND = 100
 CALL FELMT(OT,ISZOT,MBAND1
 STOP
 END

SUBROUTINE FELMTIOT,ISZOT,MBAND

MAIN ASSEMBLY PROGRAM AND STORAGE ALLOCATION FOR VARIABLES

```

REAL LABL
LOGICAL CHECK,FLAG,NPL
DIMENSION CONWD(24),FLAG(7),TITLE(12),TYME(7),DT(1SZOT),RE(21)
COMMON /TAPES/ ITP5,ITP6
COMMON /FORIER/ NF1501,XN,F1,F2,F3,F4
COMMON /GAUS/ LJM,SGAUSS(5,5),MGAUSS(5,5)
COMMON /LABELS/ LABL(6),XHEO(3),XH,FHEO(6),FH,UHEO(6),UH,RHEO(6),RH
X ,AWORD1,AWORD2,AWORD3,HEAO(12),START,CEASE,IPG,NSIR,WORD(30)
COMMON /SHAP/ XJAC,SHAPE(4,20),SG(3,3),SK(3,3),X13,201,LOI(120)
COMMON /TTLES/ XTTL(3),UTT(16)
COMMON /VALUES/ NC1,CON1,CON2,CON3(3)
COMMON /DYNAMO/ TIME,NSIG(7),NT,NSTEP,DS,NUMPL,NEDATA(20,3),NPR,NPL
DATA CONWD/6HMATERI,6HNODAL,6HPOLAR,6HELEME,6HSOLVE,6HRESOLV,
X 6HBOUND,6HFORCE,6HRLAOS,6HELQAS,6HVECTO,6HMESH,6HPLOT,
X 6HFDRUE,6HREMARK,6HINITIA,6HGENERA,6HTITLE,6HBLOCK,6HEXPIC,
X 6HADDP,6HVISCOE,6HIMPLIC,6HNEWTON/
DATA RE/4HNOT,4H /, BLANK/6H /
DATA NFLAG,NLIST/7,24/,M1,M2,M3,M4,M5,M6,MB/7*1/,ITA/9/

** INITIATE SEARCH FOR START OF PROBLEM
00 READ(ITP5,1000) CC,HEAD
CC=HEAD(1)
IF(CC.EQ.START) GO TO 240
IF(CC.EQ.6HFEAP73) GO TO 240
IF(CC.EQ.CEASE) RETURN
GO TO 100
CONTINUE
00 122 I=1,12
HEAD(1)=TITLE(1)
00 READ(ITP5,1000) CC,TITLE
NDIM = CC
00 150 I = 1,NDIM
CC = TITLE(1)
XHEO(1) = CC
IF(CC.EQ.BLANK) XHEO(1) = XTTL(1)
CONTINUE
READ(ITP5,1000) CC,TITLE
NDF = CC
00 152 I = 1,NDF
CC = TITLE(1)
IF(CC.EQ.BLANK) CC = UTT(1)
FHED(1) = CC
UHED(1) = CC
RHED(1) = CC
NUMEL = D
READ(ITP5,1001) NEN,NEXTRA,REC,MBAN,IBUF,NC1,CON1,CON2,CON3

```

```

131 WRITE(IP6,2003) (TITLE(1),2,12)
GO TO 125
00 134 I = 2,12
HEAD(1) = TITLE(1)
GO TO 125

... INPUT THE MATERIAL CHARACTERIZATIONS.
0 J = 1
IF(FLAG(1)) GO TO 215
FLAG(1) = .TRUE.
IF(1.LE.0) GO TO 700
NUMMAT = 1
M1 = MD
M2 = MD + NUMMAT
MD = MD + 64*NUMMAT
IF(MD.GT.1SZOT) GO TO 710
CALL MESH(1,NUMNP,NUMEL,NUMMAT,NOIM,NDF,NEN,NEL,
X OT,DT(M1),DT(M2),DT(M3),DT(M4),DT(M5),DT(M6))
IF(IPG.LE.0) GO TO 100
GO TO 125

... INPUT THE NODAL LOCATIONS AND BOUNDARY CONDITION CODES.
IF(FLAG(2)) GO TO 225
FLAG(2) = .TRUE.
IF(1.LE.0) GO TO 700
NUMNP = 1
M3 = MD
M4 = MD + NUMNP
M5 = M4 + NDIM*NUMNP
MD = MD + NDF*NUMNP
IF(MD.GT.1SZOT) GO TO 710
IF(1.LE.0) FLAG(3) = .TRUE.
CONTINUE
IF(CC.EQ.CONWD(19)) GO TO 227
J = 2
IF(CC.EQ.CONWD(17)) J = 4
GO TO 215
IF(1.LE.0) FLAG(2) GO TO 730
CALL CONVERT(NUMNP,NDIM,DT(M4))
GO TO 125
CONTINUE
CALL BRGEN(NUMNP,NUMEL,NDIM,NDF,NEN,NEL,DT(M3),DT(M4),DT(M5),
X DT(M6))
IF(IPG.LE.0) GO TO 705
IF(1.LE.0) FLAG(3) = .TRUE.
IF(MD.GT.1SZOT) GO TO 710

```

```

IF(MBAN.LE.0) MBAN = MBAND
1SIZ = 1SZOT
1OT = 1SZOT/2
NICO = 0
NVEC = 0
NPL = .TRUE.
NUMPL = 0
NT = 1
C.... INITIALISE TYME AND CLOCK
CALL TICTOC(TYME,0)
00 121 I=1,7
121 TYME(1) = 0.0
NEL1 = NEN + 2
REWINO 12
NTERM = 0
DO 10 I=1,NFLAG
FLAG(I) = .FALSE.
10 C
C.... STORAGE IS SET FOR A NSTF X NSTF ELEMENT MATRIX AND FORCE VECTOR
C.... MAXIMUM SIZE FOR NSTF IS 120, THIS IS CONTROLLED BY DIMENSION ON LD
C
NSTF = NOF*NEN + NEXTRA
M9 = 2*NSTF + 1
M0 = NSTF*INSTF + 1
IF(MD.GT.1OT) GO TO 710
IPG=1
IF(1BUF.LE.0) 1BUF = 1SZOT/20
IF(1REC.NE.0) 1REC = 1
WRITE(ITP6,2000) HEAD,IPG,NOIM,NDF,NEN,NSTF,REI(1),MBAN,1BUF,
X NC1,CON1,CON2,CON3
IPG = IPG + 1
IF(NOIM.GT.3.OR.NDF.GT.6.OR.NEN.GT.20) GO TO 720
C.... SEARCH THE LIST OF NAMES FOR A TRANSFER ADDRESS
C
125 READ(ITP5,1000) CC,TITLE
I = CC
CC=TITLE(1)
00 126 J = 1,NLIST
IF(CC.EQ.CONWD(J)) GO TO 127
126 CONTINUE
IF(CC.EQ.START) GO TO 120
IF(CC.EQ.6HFEAP73) GO TO 120
IF(CC.EQ.CEASE) RETURN
GO TO 125
C
C.... NAMESIMAT,NDO,POL,ELE,SOL,RES,BCS,FOR,BLO,ELD,VEC,MES,PLO,FQJ,REM,
127 GO TO(120,220,226,230,200,270,228,260,250,255,245,200,200,200,131,
X 345,220,133,220,200,200,200,200,200) J
C.... 1CO,GEN,TIT,BLO,EXP,AOD,VIS,IMP,NEW

```

```

GO TO 125
C
C.... BOUNDARY CODE OVERWRITE
C
228 IF(1.NOT.FLAG(2)) GO TO 730
CALL BCODES(NUMNP,OT(M3))
GO TO 125
C
C.... INPUT THE ELEMENT CONNECTION ARRAY.
C
230 J = 3
IF(FLAG(3)) GO TO 215
FLAG(3) = .TRUE.
IF(1.LE.0) GO TO 700
NUMEL = 1
M6 = MD
MD = MD + NEL1*NUMEL
GO TO 215
C
C.... INPUT THE VECTORS OF PRESCRIBED VALUE.
C
245 IF(1.LE.0) GO TO 730
IF(1.LE.0) GO TO 700
IF(FLAG(4)) GO TO 247
FLAG(4) = .TRUE.
READ(ITP5,1001) NSIZV,IPICK
NVEC = 1
MB = MD
MA = MB + NS(2V*1)
MO = MA
IF(MD+2*1.GT.1SZOT) GO TO 710
CALL VECIN (NUMNP,NUMEL,NDF,NSIZV,IPICK,NVEC,DT(M4),DT(M5))
IF(IPG.LE.0) GO TO 100
GO TO 125
250 CONTINUE
IF(1.LE.0) GO TO 125
C
C.... INPUT BOUNDARY LOADS
C
CALL BLOADS(1,NUMNP,NDIM,NDF,OT(M3),OT(M4),DT(M5))
IF(IPG.LE.0) GO TO 705
GO TO 125
C
C.... INPUT ELEMENT LOADS
C
255 IF(1.LE.0) GO TO 125
CALL ELOADS(1,NDIM,NDF,NEN,NEL1,NSTF,NSIZV,NVEC,DT(M1),DT(M2),
1 DT(M3),DT(M4),DT(M5),DT(M6),DT(M5),DT(M6),DT(M6),DT(M6))
IF(IPG.LE.0) GO TO 705
GO TO 125

```

... INPUT THE INITIAL CONDITIONS

```

4 IF (FLAG1) GO TO 347
  FLAG1 = .TRUE.
  NICO = 1
  NSICD = NDF * NUMNP
  MG = MO
  MO = MG + NICO * NSICD
  MG = MO
  IF (MO * 100. / GT. 1520) GO TO 710
7 CALL FICIN (NUMNP, NUMEL, NOF, NSICD, 1, NICO, DT(MG), DT(MG))
  IF (100. / LE. 0) GO TO 100
  GO TO 125

```

... START THE SOLUTION FOR FIRST LOADING CASE

```

10 IF (FLAG1) GO TO 401
  CHECK = .TRUE.
  CALL TICTOC (TIME, 1)
  DD 123 J = 1
  IF (NOT FLAG1) CHECK = .FALSE.
3 CONTINUE
  IF (NOT CHECK) GO TO 707
  NTM = 0
  IF (CC.NE.CONWD(22).AND.CC.NE.CONWD(23)) GO TO 515
... SET UP VISCOELASTIC/NONLINEAR SOLUTION CALL
  NTM = 1
  NSEQ = 1
  I = 0
  ISIZ = 1520 - 180F
  101 = ISIZ / 2
  IF (NICO.NE.0) GO TO 515
  WRITE (1TP6, 203B)
  NICO = 1
  IF (CC.EQ.CONWD(23)) NICO = 3
  NSICD = NDF * NUMNP
  MG = MO
  MO = MO + NICO * NSICD
  IF (MO * 100. / GT. 1520) GO TO 710
  DD 510 J = MG, MO
  DT(J) = 0.
  M7 = MO
  M7A = MO
  IF (100. / GE. 47) M7 = 101 + 1
  MU = M7
  101 = 101 + 1
  MO = M7 + NDF * NUMNP
  IF (MO * 100. / GT. 1520) GO TO 710
  M8 = MO - 1

```

```

  DT(M7A) = DT(M7)
  M7 = M7A
99 1A = M7 + J + 1
  MU = 1A + NDF * MAXBAN
  MK = MU + NUMNP * NDF
  MO = MK + NDF
  101 = NDF * MAXBAN + 1
  FLAG(5) = .TRUE.
  IF (NTM.EQ.1) GO TO 520
  CALL FORMST (NUMNP, NUMEL, NUMMAT, NOIM, NDF, NEN, NEL1, MB, DT, DT(M),
  X DT(M2), DT(M3), DT(M4), DT(M5), DT(M6), DT, DT(M9), DT(M7), DT(M8),
  X DT(MU), DT(LA), NSTF, 1BLK, NVEC, NSIZV, MAXBAN, 1REC, NOEG)
  CALL TICTOC (TIME, 3)
  IF (100. / LE. 0) GO TO 705
... FORM THE GLOBAL STIFFNESS AND SOLVE USING GAUSS ELIMINATION
  CALL SOLVEQ (NUMNP, NUMEL, NDF, 101, MO, MAXBAN, 1TA, NSTF, 1SZA, NEQB, 1BLK,
  X DT(LA), DT(M5), DT(MU), DT(M7), DT, DT(M9), DT(MK), NOEG)
  CALL TICTOC (TIME, 4)
  GO TO 420

```

... DYNAMIC SOLUTION BY EXPLICIT INTEGRATION

```

15 IF (NICO.NE.3) GO TO 418
  WRITE (1TP6, 203B)
  NICO = 3
  NSICD = NDF * NUMNP
  MG = MO
  MO = MO + NICO * NSICD
  IF (MO * 100. / GT. 1520) GO TO 710
  DD 417 J = MG, MO
  DT(J) = 0.0
  MG = MG + NSICD
  MO = MG + NSICD
  ME = MO
  ME = ME + NSTF
  MO = 2 * NSTF + ME
  IF (MO * 100. / GT. 1520) GO TO 710
  CALL EXPLCT (NUMNP, NUMEL, NUMMAT, NOIM, NDF, NEN, NEL1, NSTF, NVEC, NSIZV,
  X DT(M1), DT(M2), DT(M3), DT(M4), DT(M5), DT(M6), DT(M7), DT(M8),
  X DT(M9), DT(MG), DT(MC), DT(MD), DT(ME), DT(MF), TIME, 1OUT, NSICD)
  GO TO 125
270 1OUT = 1
  CALL TICTOC (TIME, 1)

```

... FORM THE NEW LOAD AND DO A RESOLUTION ONLY

```

  CALL RESVEQ (NUMNP, NOF, M1, 1, MAXBAN, 1SZA, NEQB, 1BLK, DT(LA), DT(M5),
  X DT(MU), DT(M5), DT(M7), DT(MK), NDF * NUMNP)

```

C... CHECK THE MESH FOR CONSISTENCY OF INPUT DATA

```

  CALL MESHCK (NUMNP, NUMEL, NUMMAT, NOIM, NDF, NEN, NEL1, 1OUT, 101, MB, MAXBAN,
  X DT, DT(M), DT(M2), DT(M3), DT(M4), DT(M5), DT(M6), DT(M7), 1SZA, NEQB, 1BLK, NOEG)
  MX = 101 - NEQB

```

C... PLOT THE MESH FOR TWO DIMENSIONAL TOPOLOGIES.

```

101 1OUT = 1
  IF (1.NE.0) WRITE (1TP6, 2039)
  IF (CC.EQ.CONWD(13))
1 CALL PLDTMSH (NUMNP, NUMEL, NOIM, NDF, NEN, NEL1, DT(M4), DT(M6), 1)
  CALL TICTOC (TIME, 2)
  IF (CC.EQ.CONWD(24)) NSEQ = 1
  IF (CC.EQ.CONWD(24)) GO TO 520
  IF (CC.EQ.CONWD(20)) GO TO 415
  IF (MAXBAN.GT.MBAN) GO TO 740
  IF (CC.EQ.CONWD(12)) DA, CC.EQ.CONWD(13) GO TO 125
  IF (100. / LE. 0) GO TO 705
  IF (CC.NE.CONWD(14)) GO TO 405

```

C... FOURIER COMPOSITION

```

  READ (1TP5, 1002) J, F1, F2, F3, F4
  WRITE (1TP6, 2002) HEAD, 1PG, J, F1, F2, F3, F4
  1PG = 1PG + 1
  NTERM = NTERM + 1
  NFINTERM = J
  XM = J

```

C... FORM THE STIFFNESS FOR THE ELEMENTS

```

405 IF (FLAG15) GO TO 410
  LA = 1
  J = 1 (MAXBAN) * NOEG + NOF * NUMNP + 1 + NTM1
  IF (152 - J, LT, M7A) GO TO 410

```

C... DMCORE SOLUTION IS POSSIBLE

```

  WRITE (1TP6, 2031)
  NEQB = NOEG
  1BLK = 0

```

C... CHECK TO SEE IF IDEST IS TO BE MOVED UP

```

  J = NUMNP * NDF - 1

```

C... SAVE FORCE VECTOR FOR NONLINEAR SOLUTION

```

  MK = MS + J
  REWIND 9
  WRITE (9) DT(1), M5, MK1
  IF (M7.EQ.M7A) GO TO 409
  DD 408 K = 1, J
408 DT(M7A + K) = DT(M7 + K)

```

```

  CALL TICTOC (TIME, 5)
  WRITE (2) DT(J), N = M7, MB)
C... COMPUTE AND OUTPUT THE NODAL DISPLACEMENTS AND ELEMENT STRESSES
  IF (1REC.GT.0.AND.1BLK.EQ.0) REWIND 7
  CALL DISTR (NUMNP, NUMEL, NUMMAT, NOIM, NDF, NEN, NEL1, NSTF, NVEC, NSIZV,
  X DT(M1), DT(M2), DT(M3), DT(M4), DT(M5), DT(M6), DT(M7), DT(M8),
  X 1OUT, 1REC, 1BLK)
  CALL TICTOC (TIME, 6)
  IF (1BLK.GT.0) REWIND 7
  IF (1BLK.GT.0) READ (7) DT(1), M5, MB)
  J = 0
  WRITE (1TP6, 2030) 7YME
  DD 271 N = 1, 7
  7YME(N) = 0.0
271

```

C... INPUT THE FORCE VECTORS ON MODES (RESET TO ZERO AUTOMATICALLY)

C... AFTER EACH PROBLEM SOLUTION OR RESOLUTION.

```

260 CONTINUE
  IF (NOT FLAG2) GO TO 730
  CALL RESET (NUMNP, NOF, DT(M5))
  GO TO 125

```

C... TIME INTEGRATION SUBROUTINE FOR DYNAMIC AND VISCOELASTIC SOLUTIONS

```

520 IF (FLAG17) GO TO 540
  FLAG(7) = .TRUE.
  J = MO + NSICD - 1
  IF (100. / GT. 1520) GO TO 710
  DD 530 J = MO, 1
530 DT(J) = 0.
  IF (1BLK.EQ.0) GO TO 540
  MU = MO + NSICD
  IF (MU * NSICD * GT. 1512) GO TO 710
540 IF (CC.EQ.CONWD(22).OR.CC.EQ.CONWD(23))
  X CALL TSOLVE (NUMNP, NUMEL, NUMMAT, NOIM, NDF, NEN, NEL1, NSTF, NVEC,
  NSIZV, NICO, NSICD, 1BLK, 1SZA, NEQB, MAXBAN, NOEG, 101, MB, 180F, DT,
  1 DT(M1), DT(M2), DT(M3), DT(M4), DT(M5), DT(M6), DT(M7), DT(M8),
  2 DT(M9), DT(MG), DT(ML), DT(LA), DT(MO), DT(MX), DT(1512 + 1), DT(MG), DT(MU),
  3 NSEQ, TIME)
  IF (CC.EQ.CONWD(24))
  XCALL NEWTON (NUMNP, NUMEL, NUMMAT, NOIM, NDF, NEN, NEL1, NSTF, NVEC, NSIZV,
  1 1BLK, 1SZA, NEQB, MAXBAN, NOEG, 101, MB, 180F, DT, DT(M1), DT(M2), DT(M3),
  2 DT(M4), DT(M5), DT(M6), DT(M7), DT(M8), DT(M9), DT(MG), DT(ML), DT(LA), DT(MO),
  3 DT(MX), DT(1512 + 1), DT(MU), NSEQ, TIME)
  J = 0
  GO TO 260
C... PROGRAM EXECUTION TIME ARRAY, REFERENCE SUBROUTINE CLOCK

```



```

705 WM1TP6,2030) TYME
GO TO 100
7 WRITE(1TP6,2033) (FLAG(J),J=1,3)
GO TO 100
703 WRITE(1TP6,2034) CC
GO TO 100
710 WRITE(1TP6,2035) MO,1512,CC
GO TO 100
720 WRITE(1TP6,2036) NDM,NDF,NEN
GO TO 100
730 WRITE(1TP6,2037) CC
GO TO 100
5 WRITE(1TP6,2038)
GO TO 100
0 WRITE(1TP6,2032) MAXBAN
GO TO 100

```

```

***
*** FORMATS
***

```

```

000 FORMAT (F5.0,1X,12A6)
01 FORMAT (I5,5F10.0)
02 FORMAT (15,5X,4F10.0)
03 FORMAT (1H1,12A6,30X,4HPAGE,14///
X/19X,32H FINITE ELEMENT ANALYSIS PROGRAM///13X, 2212H *) //
X 13X,2H *,18,34H DIMENSIONAL PROBLEM * * * * //
X 13X,2H *,18,34H DEGREES OF FREEDOM PER NODE * //
X 13X,2H *,18,34H NODES CONNECTED TO EACH ELEMENT * //
X 13X,2H *,18,34H ELEMENT STIFFNESS SIZE * * * * //13X,2212H *) //
X 13X,2H *,8X,34H A GENERALIZED FORCE CHECK HAS * //
X 13X,2H *,9X,44,14HREEN REQUESTED,14X,1H* //
X 13X,2H *,18,34H IS MAXIMUM PERMISSIBLE HALF BAND * //
X 13X,2H *,18,34H WORD BUFFER AREA RESERVED FOR H * //13X,2212H *) //
X 13X,2H *,8X,18H CONSTANT 1----- *,E12.4,4H //
X 13X,2H *,8X,18H CONSTANT 2----- *,E12.4,4H //
X 13X,2H *,8X,18H CONSTANT 3----- *,E12.4,4H //
X 13X,2H *,8X,18H CONSTANT 4----- *,E12.4,4H //
X 13X,2H *,8X,18H CONSTANT 5----- *,E12.4,4H //13X,2212H *) //
02 FORMAT (1H1,12A6,30X,4HPAGE,14///
X 5X,37HFOURIER COEFFICIENTS FOR HARMONIC NO. , 14//
X 10X, 25HRAIDIAL COEFFICIENT = E12.4//
X 10X, 25HTANGENTIAL COEFFICIENT = E12.4//
X 10X, 25HAXIAL COEFFICIENT = E12.4//
X 10X, 25HTHERMAL COEFFICIENT = E12.4// )
03 FORMAT (120X,11A6)
030 FORMAT (11H1,21X,12HELAPSED TIME///10X,25HINPUT PROPERTIES AND MESH
,F10.3/10X,25HCHECK AND PLOT INPUT DATA,F10.3/10X,14HFORM STIFFNESS
,F21.3/10X,21HSOLUTION OF EQUATIONS,F14.3/10X,23HSOLUTION OF EQUA
TIONS,F12.3/10X,14HOUTPUT ANSWERS,F21.3/10X,10HTOTAL TIME,F25.3 1
31 FORMAT (1// 5X,16HMIN-CORF SOLUTION 1

```

```

BLOCK DATA
PEAL LABL
LOGICAL NPR,NPL
COMMON/DYNAMO/TIME,NSIG(17),NT,NSTEP,OT,NUMPLY,NEQAT(20,3),NPR,NPL
COMMON/GAUS/ LIM,SGAUSS(5,5),WGAUSS(5,5)
COMMON/LABELS/ LABL(61),XHEO(13),XH,FHEO(6),FH,UHED(6),UH,RHED(6),RH
X ,AWORD1,AWORD2,AWORD3,HEAD(12),START,CEASE,1PG,NSTR,WORD(30)
COMMON/SHAP/ XJAC,SHA,E(4,20),SG(3,3),SK(3,3),X(3,20),LO(120)
COMMON/TITLES/ XTTL(1),UTTL(6)
COMMON /TAPES/ 1TP5,1TP6
COMMON/VTAPES/ 1TP13,1TP14,1TPRO,1TPWR
DATA SHAPE/8000.0/,START,CEASE/6HFEAP73,6HSTOP /
DATA WORD/5HELM01,5HELM02,5HELM03,5HELM04,5HELM05,5HELM06,5HELM07,
X ,5HELM08,5HELM09,5HELM10,5HELM11,5HELM12,5HELM13,5HELM14,5HELM15,
X ,5HELM16,5HELM17,5HELM18,5HELM19,5HELM20,5HELM21,5HELM22,5HELM23,
X ,5HELM24,5HELM25,5HELM26,5HELM27,5HELM28,5HELM29,5HELM30/
DATA SGAUSS/50.0,-.57735027, .57735027,3*0.0,-.77459667,0.0,.77459667
C ,2*0.0,-.86113631,-.33998104,.33998104,.86113631,0.0,-.90617985,
C ,-.53846911,0.0,.53846911,.90617985/
DATA WGAUSS/502.5911,.55555556,.88888889,.55555556,2*0.0,.34785485
C ,2*0.65214515,.34785485,0.0,.23692689,.47862867,.56888889,.47862867
C ,.23692689/
DATA LABL(11/8H 1112, /
DATA XTTL/6H 1.6H 2.6H 3/, XH/6H ORD. /
DATA UTTL/6H 1.6H 2.6H 3,6H 4.6H 5.6H 6/
DATA FH,RH,UH/6H FORCE,6H FORCE,6H DISPL/
DATA AWORD1,AWORD2/8H F13.4,8H 6E13.4//,RWORD3/8H F11.2,/
DATA 1TP5,1TP6 /5,6/ , NSIG/7*0/, TIME/0.0/,NUMPLY,NPR,NPL/0,0,1/
DATA 1TP13,1TP14/13,14/
END

```

```

2032 FORMAT (2TH0BANOW(OTH EXCEEDED, MRAND=15)
2033 FORMAT (5SHORLL INFORMATION FOR THIS PROBLEM HAS NOT BEEN PROVIDED/
X 15HMONTERIAL CARDS , L2/
X 15HMONDRAL CARDS , L2/
X 15HOLEMENT CARDS , L2/ )
2334 FORMAT (5X,A6,16H TYPE CARD ERROR/)
2035 FORMAT (20HREQUIRED STORAGE = 17/20HAVAILABLE STORAGE = 17/
X 25HSTORAGE EXCEEDED DURING ,A6/)
2036 FORMAT (20HINPUT SIZE ERROR, ,8H NDM = ,15,8H, NDF = ,15,
C ,8H, NEL = ,15)
2037 FORMAT (18HTRYTEMPT TO INPUT ,A6,20H BEFORE NODAL POINTS )
2038 FORMAT (5X, 98H**NON-FATAL ERROR** INITIAL DYNAMIC VECTORS HAVE NOT
X BEEN INPUT **INITIAL CONDITION ASSUMED ZERO )
2039 FORMAT (43HREQUEST MADE FOR LIMITED AMOUNT OF OUTPUT,
X ,25H ADDITIONAL DATA REQUIRED/1X)
END

```

```

SUBROUTINE TICOCITYME, 11
C
C SUBROUTINE TO TIME PROGRAM SEGMENTS AS MEASURE OF EFFICIENCY
C
DIMENSION TYME(7)
IF (1,LE, 0) GO TO 100
CALL SECOND(11)
TYME (1) = T1 - TO
TYME(1) = TYME(7) + TYME(1)
TO = T1
RETURN
100 CALL SECOND(10)
RETURN
END

```



```

SUBROUTINE INIEGLIM,NC1,NOIM,LINT,STUM1
REAL LABL
DIMENSION STR1(7,3),TTR1(7,3),UTR1(7,3),WTR1(7,3),STUM1(4,1)
DIMENSION SIN(7),TIR(7),UR(7),W(7),SC(2)
COMMON/GAUS/ L77,SGAUSS1(5,5),WGAUSS1(5,5)
COMMON/LABELS/ LABL(6),XHED(3),XH,FHED(6),FH,UHED(6),UH,RHED(6),RH
X ,AWORD1,AWORD2,AWORD3,HEAD(12),START,CEASE,IPG,NSTR,WOR01301
DATA STR1(7,3),3333333,6*0.0,0.5,0.0,0.5,4*0.0,0.3333333,0.05971587,
C 2*0.47014206,0.79742699,2*0.10128651/
DATA TTR1(7,3),3333333,6*0.0,2*0.5,0.0,4*0.0,0.3333333,0.47014206,
C 0.05971587,0.47014206,0.10128651,0.79742699,0.10128651/
DATA UTR1(7,3),3333333,6*0.0,0.0,2*0.5,4*0.0,0.3333333,2*0.47014206,
C 0.05971587,2*0.10128651,0.79742699/
DATA WTR1(7,3),7*0.3333333,0.225,3*0.13239415,3*0.12593918/
DATA STR,TIR,UTR,WTR,1,0,2*0.0,4*0.1,0.0,1.0,2*1.0,-1.0,-1.0,0.0,1.0,1.0,
C -1.0,-1.0,1.0/
DATA WA,SB,MC,SC,1,3333333,0.886426593,1.0,0.795822426,0.0,
C 0.33518055,0.0,0.750786911/
*** INTEGRATION TABLE CONSTRUCTION
IF(INCL,LT,0) NC1 = 0
IF(INCL,GT,2) NC1 = 2
NC = NC1 + 1
GO TO 1241,244,249,NC
*** NC1 = 0, GAUSS INTEGRATION
11 = 0
IF(LIM,LT,2) LIM = 2
IF(LIM,GT,5) LIM = 5
LIM3 = LIM
IF(NDIM,ED,2) LIM3 = 1
D3 243 1 = 1,LIM3
UU = SGAUSS(1,LIM)
WU = WGAUSS(1,LIM)
IF(NDIM,NE,2) GO TO 242
UU = -1.0
WU = 1.0
CONTINUE
D3 243 J = 1,LIM
TT = SGAUSS(J,LIM)
WT = WGAUSS(J,LIM)*WU
D3 243 K = 1,LIM
11 = 11 + 1
STUM1(1,1) = SGAUSS(K,LIM)
STUM1(2,1) = TT
STUM1(3,1) = UU
STUM1(4,1) = WGAUSS(K,LIM)*WT
43 CONTINUE
LINT = 11
GO TO 248
*** NC1 = 1, IRONS INTEGRATION
44 IF(NDIM,NE,3,OR,LIM,EQ,1) GO TO 241

```

```

SUBROUTINE MESH(MC,NUMNP,NUMEL,NUMMAT,NOIM,NOF,NEL,NELL,
X DT,TYPE,D,ICOD,XYZ,F,17)
*** INPUT OF MESH AND MATERIAL PROPERTIES
COMMON /TAPES/ 1TP5,1TP6
REAL LABL
DIMENSION TYPE(1),D(3,21,1),ICOD(1),XYZ(NDIM,1),F(NOF,1),
X 1X(NEL,1),1XD(2D),DX(3),1XP(2D),XWORD(11)
COMMON/GAUS/ LIM,SGAUSS(5,5),WGAUSS1(5,5)
COMMON/LABELS/ LABL(6),XHED(3),XH,FHED(6),FH,UHED(6),UH,RHED(6),RH
X ,AWORD1,AWORD2,AWORD3,HEAD(12),START,CEASE,IPG,NSTR,WOR01301
COMMON/SHAP/ XJAC,SHAPE(4,2D),SG(3,3),SK(3,3),X1(3,2D),LOI(2D)
COMMON/VALUES/ NC1,CON1,CON2,CON3(3)
DATA BLANK/6HBLANK /
GO TO 11,2,3,21,MC
1 CONTINUE
MCT = D
D3 300 1 = 1,NUMMAT
MCT = MCT - 1
IF(MCT,GT,0) GO TO 10
WRITE(1TP6,20D1) HEAD,IPG,NUMMAT
IPG = IPG + 1
MCT = 4
10 CONTINUE
READ(1TP5,10D2) M,DM,XWORD
IF(M,GT,NUMMAT,OR,M,LE,0) GO TO 301
TYPE(M) = DM
WRITE(1TP6,20D2) DM,M,XWORD
D3 280 J = 1,3
D3 290 K = 1,21
DIJ,K,M1=D,0
280 C
K = 0
D3 290 J = 1,3D
IF(OM,FD,WOR01J) GO TO 400
290 CONTINUE
C.... ERROR IF EXIT ON LOOP 290
301 WRITE(1TP6,2D32)M,DM
IPG = 0
RETURN
400 CALL ELMLIBIN,M,NOIM,NDF,NEL,NEL1,NSTR,NS,ZV,NVEC,MCT,DM,D,XYZ,
X 1X,F,FORCE,ESTIF,U,VECT,1)
301 CONTINUE
RETURN
2 CONTINUE
C.... SET XYZ(1,N) TO BLANKS
C
D3 2D N = 1,NUMNP
XYZ(1,N) = BLANK
D3 2D 1 = 1,NDF

```

```

LINT = 6
IF(LIM,GT,2) LINT = 14
NS = SB(L,M)
RW = WB(L,M)
D3 246 J = 1,7
17 = 2*J
11 = 12 = 1
IF(L,NE,4) GO TO 245
NS = SC(L,M)
RW = WC(L,M)
245 CONTINUE
STUM1(1,1) = STR1(1,1)*NS
STUM1(1,2) = -STUM1(1,1)
STUM1(2,1) = TIR(1)*NS
STUM1(2,2) = -STUM1(2,1)
STUM1(3,1) = UR(1)*NS
STUM1(3,2) = -STUM1(3,1)
STUM1(4,1) = W
STUM1(4,2) = RW
GO TO 248
C.... NC1 = 2, TRIANGULAR COORDINATE INTEGRATION
249 LINT = 1
IF(LIM,GT,3) LIM = 3
IF(LIM,EQ,2) LINT = 3
IF(LIM,GE,3) LINT = 7
D3 247 1 = 1,LINT
STUM1(1,1) = STR1(1,LIM)
STUM1(2,1) = TTR1(1,LIM)
STUM1(3,1) = UTR1(1,LIM)
STUM1(4,1) = WTR1(1,LIM)
247 CONTINUE
248 RETURN
END

```

```

20 FILL,N) = 0.0
C
C.... START FILLING DATA
C
N = 0
NXP = 0
NP = N
IF(MC,EQ,2,AND,N,GE,NUMNP) GO TO 30
NX = NXP
READ(1TP5,10D6) N,NXP,1,OX
IF(N,LE,0,OR,N,GT,NUMNP) GO TO 3D
IF(MC,EQ,2) NXP = 1
ICOD(N) = 1
D3 26 1 = 1,NOIM
XYZ(1,N) = OX(1)
IF(NX,ED,0) GO TO 21
IF((N-NP)*NX,GE,0) GO TO 25
NX = -NX
WRITE(1TP6,2D33) NP,N
25 CONTINUE
C.... GENERATE THE NODES BETWEEN NP AND N IN INTERVALS OF NX
C
LX = 1/(ABS(N-NP) + 1/ABS(NX)) - 1/(ABS(NX))
D3 22 1 = 1,NOIM
OX(1) = 1*XYZ(1,N) - XYZ(1,NP)/LX
22 NP = NP + NX
IF(NX,GT,0,AND,NP,GE,N) GO TO 21
IF(NX,LT,0,AND,NP,LE,N) GO TO 21
D3 24 1 = 1,NOIM
XYZ(1,NP) = XYZ(1,NP-NX) + OX(1)
ICOD(NP) = 0
IF(1COD(NP-NX),ED,1COD(NP)) 1COD(NP) = 1COD(NP)
GO TO 23
C
C.... CHECK IF ALL DATA HAS BEEN INPUT OR GENERATED AND PRINT OUTPUT
C
70 CALL PRMTH(1,NUMNP,NOIM,ICOD,XYZ)
RETURN
C.... INPUT ELEMENT CONNECTION ARRAY
3 NSIDE = (NEL+1)/NOIM**2
N=0
MAP = 0
C.... SET UP INCREMENT ARRAY IF NOT INPUT OFF CARDS
GO TO 137
D3 130 L = 1,NEL
131 1X(0) = 1X(1)
IF(1X(0),NE,0) GO TO 157
D3 150 L = 1,NEL

```

```

100 IXXILL = NSIOE
101 N1 = 4*NSIOE + 1
102 N2 = 8*NSIOE - 4
103 IF(N2.GT.NEL) GO TO 154
104 DO 152 L = N1,N2
105 IXXILL = 1
106 N1 = 2*NSIOE
107 N3 = N1 + 2 - NSIOE
108 N4 = N1 + N2
109 DO 156 L = N3,N1
110 IXXILL = 1
111 IXXILL + N11 = 1
112 IF(N2.GT.NEL) GO TO 156
113 IXXILL + N2 = 1
114 IXXILL + N4 = 1
115 CONTINUE
116 CONTINUE
117 READ(ITP,1003) N,NA,IR,IP,IXR
118 IF(M.LE.0) RETURN
119 READ(ITP,1004) (IXI,MI,1=1,NEL)
120 IF(N.EQ.0) 1 = 1
121 (X(NEL,MI) = NA * 10*IP + 100*IR
122 K1 = 1
123 DO 133 11 = 1,NEL
124 IF(IXI(11,MI).EQ.0) GO TO 134
125 K1 = K1 + 1
133 CONTINUE
134 IF(K1.GT.NEL) GO TO 140
135 DO 138 11 = K1,NEL
136 IXXILL = 0
137 N=N+1
138 MCT = 1
139 IF(MCT.GT.0) GO TO 142
140 WRITE(ITP,2011) HEAD, IPG,NUMEL,(1=1,NEL)
141 IPG = IPG + 1
142 MCT = 50
143 CONTINUE
144 IF(M.LE.NI) GO TO 170
145 DO 158 L = 1,NEL
146 IXXILL = (IXI,N-11 + IXXILL)
147 (X(NEL,MI) = MAP
148 ITO CONTINUE
149 K = 0
150 DO 340 11=1,NEL
151 IF(IXI(11,N).EQ.0) GO TO 141
152 DO 325 J1=1,NEL
153 IF(IXI(J1,N).EQ.0) GO TO 340
154 KK=ABS(IXI)11,N1-IXI(J1,N11 + 1
155 IF(K.LE.KK) K=KK
325 CONTINUE

```

```

340 CONTINUE
141 MAP = MOD(IX(NEL,NI,101
142 IR = IX(NEL,NI,100
143 IP = MOD(IX(NEL,NI,100)/10
144 WRITE(ITP,2005) N,NA,IR,IP,(IXI,MI,1=1,NEL,K
145 IF(M-N) 145,180,140
185 WRITE(ITP,2011) N
186 IPG = 0
187 RETURN
188 MAP = NA
189 IF(NUMEL.GT.NI) GO TO 130
190 RETURN
C**** FORMATS
1002 FORMAT(15,1X,A5,11A6)
1003 FORMAT(415,2013)
1004 FORMAT(2014)
1006 FORMAT(215,110,6F10.0)
2001 FORMAT(1H1,1246,30X,4MPAGE,14//15,10H MATERIALS//
X 20H MATERIAL PROPERTIES //1X)
2002 FORMAT(5X,A5,1X, 8H MATERIAL,15,5X,11A6/1X)
2005 FORMAT(2515)
2011 FORMAT(1H1,1246,30X,4MPAGE,14//15,9H ELEMENTS//
X 20H ELMT MATL RE PRNT ,3X,24HNODES CONNECTED TO ELEMENT/
X 20H NO. NO. USES ,1X,20(2H *,12,1H*))
C**** ERROR MESSAGES *
C****
2011 FORMAT (24H0 ELEMENT CARD ERROR, N=15)
2012 FORMAT(26H0 MATERIAL CARD ERROR, N = ,13,2X,8H,TYPE = ,A5/)
2033 FORMAT(
X5X,50H**NON-FATAL ERROR** INCREMENT FOR GENERATION BETWEEN NODES,
X 15,4H AND,15,37H IS OF INCORRECT SIGN ** SIGN CHANGED/1X)
END

```

```

SUBROUTINE BRICKGEN(UMNP,NUMEL,NDIM,NOF,NEL,NEL1,ICOD,XYZ,F,IXI)
REAL LARL
DIMENSION (ICOD),XYZ(NDIM,1),IXI(NEL,1),FINOF,11
COMMON /TAPES/ ITP5,ITP6
COMMON /LABELS/ LABL(6),XHEO(3),XHEO(3),FM,XHEO(6),UM,RHEO(6),RM
X,AWORD1,AWORD2,AWORD3,HEAD(12),START,CEASE,IPG,NSTR,WORD(130)
COMMON /SHAP/ XJAC,SHAPE(4,20),SG(3,3),SK(3,3),X(3,20),LO(120)
.... GENERATION OF NODAL COORDINATES AND BOUNDARY CODES FOR BRICK SHAPE
.... REGIONS USING ELEMENT SHAPE FUNCTIONS * * *
.... INPUT THE REGION PROPERTIES
HEAD(ITP5,10001) NN,NR,NS,NT,N1,NC,NA,NBC,IREUSE,IPRINT,IMSH,IELN
HEAD(ITP5,1001) 11,12,13,14,15,16
READ(ITP5,1002) (IXI,J1,1=1,31,J=1,NN)
IF(NS.LE.0) NS=1
IF(NR.LE.0) NR=1
IF(NT.LE.0) NT=1
IF(N1.LE.0) N1=1
IF(NC.LE.0) NC=1
IF(NA.LE.0) NA=1
WRITE(ITP6,20001) HEAD,IPG,NR,NS,NT,N,NE,NA
WRITE(ITP6,20001) 11,12,13,14,15,16,(XHEO(11,XM,1=1,NOIN)
DO (D=N),NN
WRITE(ITP6,2001) (X(1,N),1=1,NOIN)
.... SET THE CONTROL CONSTANTS
NSIDE = (NN+1)/NDIM**2
OR = 2./FLOAT(NR)
OS = 2./FLOAT(NS)
OT = 2./FLOAT(NT)
NR = NR + 1
NS = NS + 1
NT = NT + 1
IF(NDIM.EQ.2) NT = 1
NRS = NR*NS
NE = NRS*NT + N1 - 1
IF(NF.GT.NUMNP) GO TO 400
IF(NBC.NE.0) GO TO 30
.... SET THE BOUNDARY CONDITION CODES TO ZERO
DO 20 1 = N1,NE
DO 15 J = 1,NOF
F(J,1) = 0.0
20 ICOD(1) = 0
10 CONTINUE
N = N1

```

```

ME = NE - 1
T = -1.0
DO 300 K = 1,NT
S = -1.0
DO 200 J = 1,NS
R = -1.0
DO 100 I = 1,NR
CALL BRICK2(R,S,T,NOIN,MN,NSIOE)
C
C.... COMPUTE THE NODAL COORDINATES OF THE N-TH NODE
C
DO 50 L = 1,NOIN
CC = 0.
DO 40 M = 1,NN
CC = CC + SHAPE(4,M)*X(L,M)
50 XYZ(L,NI) = CC
C
C.... SET THE SURFACE BOUNDARY CONDITIONS TO PRESCRIBED CONDITIONS
C
IF(1.EQ.1) ICOD(NI) = ICOD(N) + 11
IF(1.EQ.NR) ICOD(NI) = ICOD(N) + 12
IF(1.EQ.1) ICOD(NI) = ICOD(N) + 13
IF(J.EQ.NS) ICOD(NI) = ICOD(N) + 14
IF(K.EQ.1) ICOD(NI) = ICOD(N) + 15
IF(K.EQ.NT) ICOD(NI) = ICOD(N) + 16
N = N + 1
IF(K.EQ.NT .AND. K.NE.1) GO TO 100
IF(1.FD.NR .OR. J.EQ. NS) GO TO 100
ME = ME + 1
IXI(NEL,ME) = NA
IXI(1,ME) = N - 1
IXI(2,ME) = N
IXI(3,ME) = N + NR
IXI(4,ME) = N + NR - 1
IF(NDIM.EQ.2) GO TO 100
IXI(5,ME) = N + NRS - 1
IXI(6,ME) = N + NRS
IXI(7,ME) = N + NRS + NR
IXI(8,ME) = N + NRS + NR - 1
100 R = R + OR
200 S = S + OS
300 T = T + OT
IF(IREUSE.EQ.0) GO TO 360
J = (IREUSE - 1)/100 + NA
DO 320 1 = NE,ME,IREUSE
320 (X(NEL,11) = J
360 IF(IPRINT.NE.0) (X(NEL,1,NE) = 1,X(NEL,1,NE) = 10
IF(IMSH.EQ.0) CALL PR1MSH(NI,NF,NOIN,ICOD,XYZ)
IF(IELN.EQ.0) CALL PR1ELMINE(ME,NEL,NEL),(IXI)
IF(ME.GT.NUMEL) NUMEL = ME

```

```

      RETURN
      WRITE(1TP6,2033)
      IPG = 0
      RETURN
000  FORMAT(1615)
001  FORMAT(16110)
002  FORMAT(10X,3F10.0)
000  FORMAT(1H1,12A6,30X,4HPAGE,14//17H NODE GENERATIONS//
      10X,25HNUMBER OF R-INCREMENTS      ,15/
      10X,25HNUMBER OF S-INCREMENTS      ,15/
      10X,25HNUMBER OF T-INCREMENTS      ,15/
      10X,25HFIRST NODES NUMMR          ,15/
      10X,25HFIRST ELEMENT NUMBER        ,15/
      10X,25HELEMENT MATERIAL NUMBER     ,15/ 1X)
100  FORMAT(
      10X,25H1-FACE BOUNDARY CODE        ,110/
      10X,25H2-FACE BOUNDARY CODE        ,110/
      10X,25H3-FACE BOUNDARY CODE        ,110/
      10X,25H4-FACE BOUNDARY CODE        ,110/
      10X,25H5-FACE BOUNDARY CODE        ,110/
      10X,25H6-FACE BOUNDARY CODE        ,110//5X,312A61)
001  FORMAT(1X,1P3E12.3)
010  FORMAT(1X,47H **FATAL ERROR** INSUFFICIENT STORAGE FOR NODOS)
      END

```

```

SUBROUTINE PRTELMINE,ME,NEL,NEL1,IX)
REAL LABL
DIMENSION IXINEL1,11
COMMON /TAPES/ 1TP5,1TP6
COMMON/LABELS/ LABL(4),XHEO(3),XH,FHED(6),FH,UHED(6),UH,RHEO(6),RH
X ,AWOR01,AWOR02,AWOR03,HEAD(12),START,CEASE,IPG,NSTR,WORD(30)
MCT = 0
DO 300 N = ME,ME
MCT = MCT + 1
IF(MCT.GT.0) GO TO 100
WRITE(1TP6,2011) HEAD,IPG,ME,11,1=NEL)
IRG = IPG + 1
MCT = 50
100  CONTINUE
      K = 0
      MA = MOD(IXINEL1,N),10)
      IR = IXINEL1,N/100
      IP = MOD(IXINEL1,N,100)/10
      DO 140 J1 = 1,NEL
      IF(IX(11,N),EQ.0) GO TO 150
      DO 135 J1 = 1,NEL
      IF(IX(J1,N),EQ.0) GO TO 140
      KK = ABS(IX(11,N)-IX(J1,N)) + 1
      IF(K.LT,KK) K = KK
135  CONTINUE
140  CONTINUE
150  WRITE(1TP6,2005) N,MA,IR,IP,IX(11,N),(=1,NEL),K
300  CONTINUE
      RETURN
2005  FORMAT(2515)
2011  FORMAT(1H1,12A6,30X,4HPAGE,14//15,9H ELEMENTS//
      X 20H ELMT MATL RE PRMT      ,3X,26HNODES CONNECTED TO ELEMENT/
      X 20H NO. NO. USES          ,1X,2012H *,12,1H*)
      END

```

```

SUBROUTINE PRINSHINT,NUMNP,ND(M,ICOD,KYZ)
REAL LABL
DIMENSION ICOD(1),XYZ(ND(M),1)
COMMON /TAPES/ 1TP5,1TP6
COMMON/LABELS/ LABL(6),XHEO(3),XH,FHED(6),FH,UHED(6),UH,RHEO(6),RH
X ,AWOR01,AWOR02,AWOR03,HEAD(12),START,CEASE,IPG,NSTR,WORD(30)
DATA BLANK/6HBLANK /
MCT = 0
DO 33 N = N1,NUMNP
MCT = MCT + 1
IF(MCT.GT.0) GO TO 31
WRITE(1TP6,2010) HEAD,IPG,NUMNP,IXHEO(1),XH,1=N,ND(M)
IPG = IPG + 1
MCT = 50
IF(XYZ(1,N),EQ.BLANK) GO TO 32
WRITE(1TP6,2006) N,ICOD(N),(XYZ(1,N),I=1,ND(M))
GO TO 33
32  WRITE(1TP6,2007) N
CONTINUE
RETURN
006  FORMAT(12112,7F13.4)
007  FORMAT(112,5X,31HHAS NOT BEEN INPUT OR GENERATED )
010  FORMAT(1H1,12A6,30X,4HPAGE,14//15,13H NODAL POINTS//
      X 12H NODAL POINT,6X,6H*B,C,*, 711X,2A61)
      END

```

```

SUBROUTINE PRYMAT(HEAD,IPG,NELM,NSTF,ESTIF,FORCE,LD,NT)
COMMON /TAPES/ 1TP5,1TP6
DIMENSION EST(FINT,NT),FORCE(NT),LO(NT),HEAD(12)
MBLK = (NSTF+23)/24
NBLK = (NSTF + 8)/9
N1 = 1
DO 200 NM = 1,NBLK
N2 = N1 + 8
IF(N2.GT.NSTF) N2 = NSTF
M1 = 1
DO 100 MM = 1,NBLK
M2 = M1 + 23
IF(M2.GT.NSTF) M2 = NSTF
WRITE(1TP6,2000) HEAD,IPG,NELM,(J,J=N1,N2)
IPG = IPG + 1
DO 50 L = M1,M2
50  WRITE(1TP6,2002) L,LD(1),(ESTIF(I,J),J=N1,N2)
M1 = M2 + 1
WRITE(1TP6,2001) (FORCE(J),J=N1,N2)
N1 = N2 + 1
RETURN
2000  FORMAT(1H1,12A6,30X,4HPAGE,14//5X,7HELEMENT,15,7H MATR(X//
      X 2X,7HROW/COL,3X,9T12)
2001  FORMAT(/3X,5HFORCE,4X,1P9E12.3)
2002  FORMAT(/14,3H LO,15,1P9E12.3)
      END

```

```

SUBROUTINE AFSET(N,M,NMP,NDF,FI
COMMON /TAPF5/ ITP5,ITP6
REAL LARL
DIMENSION FIDF(1)
COMMON/LABELS/ LARL(6),XHEO(3),XH,FHED(6),FH,UHED(6),UH,RHED(6),RH
X ,AWORD1,AWORD2,AWORD3,M)AD1(2),START,CEASE,IPG,NSTR,WORD(30)
MCT = 0
IF(M,GT,0) GO TO 200
DO 100 I = 1,M,NMP
DO 100 J = 1,NDF
F(I,J)=0.0
IFIN(EQ,0) RETURN
N = - N
CONTINUE
READ(ITP5,1000) J,P(I,J),I,NDF
MCT = MCT - 1
IF(MCT,GT,0) GO TO 250
WRITE(ITP6,2000) MEAD,IPG,M,NMP,(FHEO(I),FH,I= 1,NDF)
IPG = IPG + 1
MCT = 0
250 WRITE(ITP6,2001) J,(F(I,J),I=1,NDF)
IF(J,GE,M,NMP) RETURN
IF(J,GE,N) RETURN
GO TO 200
00 FORMAT(15,5X,TFID,0)
00 FORMAT(1M1,12A6,30X,4HPAGE,(4//15,13M NOODAL FORCES//
X 12M NOODAL POINT,T)1X,2A6))
01 FORMAT(112,4E13,4)
END

```

```

FUNCTION PROPLOIY,NI
DIMENSION TABLE(9,5),TL,B(3)
COMMON /TAPF5/ ITP5,ITP6
DATA TLAR/(DHPOLYNOMIAL,10MUSER INPUT/
IF(N,FD,0) GO TO 200
C.... INPUT TABLE
NTERMS = N
READ(ITP5,1000) (TABLE(I,J),I=1,9,I=1,N)
WRITE(ITP6,2001)
DO 100 J = 1,N
N = TABLE(I,J)
IF(LT,1),OR,A,GT,3) GO TO 700
L = TABLE(2,J)
WRITE(ITP6,2000) TLAR(I,L),TABLE(I,J),I=3,9)
RETURN
200 PROPLO = 0.
C.... INTERPOLATE THE TABLE
DO 300 J = 1,NTERMS
TMIN = TABLE(3,J)
TMAX = TABLE(4,J)
IF(T,LT,TMIN,OR,T,GT,TMAX) GO TO 300
K = TABLE(1,J)
UJ TO (201,202,203),A
TT = 1.0
DO 211 I = 5,9
PROPLO = PROPLO + TABLE(I,J)*TT
211 TT = TT*Y
GO TO 300
202 A = TABLE(2,J)
IF(K,EQ,0) K = 1
PROPLO = PROPLO + TABLE(9,J) + TABLE(5,J)*SIN(TABLE(6,J)*T)*K
X = TABLE(7,J)*COS(TABLE(8,J)*T)*K
GO TO 300
203 CALL EXPRLO(PPROP,T,TABLE(2,A))
PROPLO = PROPO
CONTINUE
RETURN
700 WRITE(ITP6,2030) K
IPG = 0
RETURN
1000 FORMAT(2F5,0,TFID,0)
2000 FORMAT(2X,A10,15,7E14,5)
2001 FORMAT(//5X,23M PROPORTIONAL LOAD TABLE//
X 3X,9M TYPE LOAD,5M EXP,5X,9M MIN. TIME,5X,9M MAX. TIME,5X,
X 2M AD,12X,2M A1,12X,2M A2,12X,2M A3,12X,2M A4/1X)
2030 FORMAT(50M PROPORTIONAL LOAD INPUT TABLE ERROR. INPUT TVRE =,15/1
END

```

```

SUBROUTINE ELMTLIB(N,MA,NDIM,NDF,NEL,NEL1,NSTF,NSIZV,NVEC,MCT,DM,D,
X XVZ,IX,F,FORCE,ESTIF,U,VECT,ISM)
REAL LARL
COMMON/LABELS/ LARL(6),XHEO(3),XH,FHED(6),FH,UHED(6),UH,RHED(6),RH
X ,AWORD1,AWORD2,AWORD3,MEAD(12),START,CEASE,IPG,NSTR,WORD(30)

```

.... ELEMENT LIBRARY FOR FEAPT2

```

.... ISM = 1 FOR MATERIAL CHARACTERIZATION
.... ISM = 2 FOR CHECK ON MESH
.... ISM = 3 FOR ELEMENT STIFFNESS FORMULATION
.... ISM = 4 FOR ELEMENT OUTPUTS
.... ISM = 5 FOR ELEMENT LOAD/VECTOR COMPUTATIONS
.... ISM = 6 FOR NON-LINEAR LOAD VECTOR COMPUTATIONS

DO 50 J = 1,30
IF(DM,EQ,WORD(1)) GO TO 57
CONTINUE
GO TO (1,2,3,4,5,6,7,8,9,10,11,12,13,14,15,16,17,18,19,20,21,22,
X 23,24,25,26,27,28,29,30) , J
CALL ELMT01(N,MA,NDIM,NDF,NEL,NEL1,NSTF,NSIZV,NVEC,MCT,DM,D,XVZ,
X IX,F,FORCE,ESTIF,U,VECT,ISM)
GO TO 99
CALL ELMT02(N,MA,NDIM,NDF,NEL,NEL1,NSTF,NSIZV,NVEC,MCT,DM,D,XVZ,
X IX,F,FORCE,ESTIF,U,VECT,ISM)
GO TO 99
CALL ELMT03(N,MA,NDIM,NDF,NEL,NEL1,NSTF,NSIZV,NVEC,MCT,DM,D,XVZ,
X IX,F,FORCE,ESTIF,U,VECT,ISM)
GO TO 99
CALL ELMT04(N,MA,NDIM,NDF,NEL,NEL1,NSTF,NSIZV,NVEC,MCT,DM,D,XVZ,
X IX,F,FORCE,ESTIF,U,VECT,ISM)
GO TO 99
CALL ELMT05(N,MA,NDIM,NDF,NEL,NEL1,NSTF,NSIZV,NVEC,MCT,DM,D,XVZ,
X IX,F,FORCE,ESTIF,U,VECT,ISM)
GO TO 99
CALL ELMT06(N,MA,NDIM,NDF,NEL,NEL1,NSTF,NSIZV,NVEC,MCT,DM,D,XVZ,
X IX,F,FORCE,ESTIF,U,VECT,ISM)
GO TO 99
CALL ELMT07(N,MA,NDIM,NDF,NEL,NEL1,NSTF,NSIZV,NVEC,MCT,DM,D,XVZ,
X IX,F,FORCE,ESTIF,U,VECT,ISM)
GO TO 99
CALL ELMT08(N,MA,NDIM,NDF,NEL,NEL1,NSTF,NSIZV,NVEC,MCT,DM,D,XVZ,
X IX,F,FORCE,ESTIF,U,VECT,ISM)
GO TO 99
CALL ELMT09(N,MA,NDIM,NDF,NEL,NEL1,NSTF,NSIZV,NVEC,MCT,DM,D,XVZ,
X IX,F,FORCE,ESTIF,U,VECT,ISM)
GO TO 99
CALL ELMT10(N,MA,NDIM,NDF,NEL,NEL1,NSTF,NSIZV,NVEC,MCT,DM,D,XVZ,
X IX,F,FORCE,ESTIF,U,VECT,ISM)
GO TO 99

```

```

11 CALL ELMT11(N,MA,NDIM,NDF,NEL,NEL1,NSTF,NSIZV,NVEC,MCT,DM,D,XVZ,
X IX,F,FORCE,ESTIF,U,VECT,ISM)
GO TO 99
12 CALL ELMT12(N,MA,NDIM,NDF,NEL,NEL1,NSTF,NSIZV,NVEC,MCT,DM,D,XVZ,
X IX,F,FORCE,ESTIF,U,VECT,ISM)
GO TO 99
13 CALL ELMT13(N,MA,NDIM,NDF,NEL,NEL1,NSTF,NSIZV,NVEC,MCT,DM,D,XVZ,
X IX,F,FORCE,ESTIF,U,VECT,ISM)
GO TO 99
14 CALL ELMT14(N,MA,NDIM,NDF,NEL,NEL1,NSTF,NSIZV,NVEC,MCT,DM,D,XVZ,
X IX,F,FORCE,ESTIF,U,VECT,ISM)
GO TO 99
15 CALL ELMT15(N,MA,NDIM,NDF,NEL,NEL1,NSTF,NSIZV,NVEC,MCT,DM,D,XVZ,
X IX,F,FORCE,ESTIF,U,VECT,ISM)
GO TO 99
16 CALL ELMT16(N,MA,NDIM,NDF,NEL,NEL1,NSTF,NSIZV,NVEC,MCT,DM,D,XVZ,
X IX,F,FORCE,ESTIF,U,VECT,ISM)
GO TO 99
17 CALL ELMT17(N,MA,NDIM,NDF,NEL,NEL1,NSTF,NSIZV,NVEC,MCT,DM,D,XVZ,
X IX,F,FORCE,ESTIF,U,VECT,ISM)
GO TO 99
18 CALL ELMT18(N,MA,NDIM,NDF,NEL,NEL1,NSTF,NSIZV,NVEC,MCT,DM,D,XVZ,
X IX,F,FORCE,ESTIF,U,VECT,ISM)
GO TO 99
19 CALL ELMT19(N,MA,NDIM,NDF,NEL,NEL1,NSTF,NSIZV,NVEC,MCT,DM,D,XVZ,
X IX,F,FORCE,ESTIF,U,VECT,ISM)
GO TO 99
20 CALL ELMT20(N,MA,NDIM,NDF,NEL,NEL1,NSTF,NSIZV,NVEC,MCT,DM,D,XVZ,
X IX,F,FORCE,ESTIF,U,VECT,ISM)
GO TO 99
21 CALL ELMT21(N,MA,NDIM,NDF,NEL,NEL1,NSTF,NSIZV,NVEC,MCT,DM,D,XVZ,
X IX,F,FORCE,ESTIF,U,VECT,ISM)
GO TO 99
22 CALL ELMT22(N,MA,NDIM,NDF,NEL,NEL1,NSTF,NSIZV,NVEC,MCT,DM,D,XVZ,
X IX,F,FORCE,ESTIF,U,VECT,ISM)
GO TO 99
23 CALL ELMT23(N,MA,NDIM,NDF,NEL,NEL1,NSTF,NSIZV,NVEC,MCT,DM,D,XVZ,
X IX,F,FORCE,ESTIF,U,VECT,ISM)
GO TO 99
24 CALL ELMT24(N,MA,NDIM,NDF,NEL,NEL1,NSTF,NSIZV,NVEC,MCT,DM,D,XVZ,
X IX,F,FORCE,ESTIF,U,VECT,ISM)
GO TO 99
25 CALL ELMT25(N,MA,NDIM,NDF,NEL,NEL1,NSTF,NSIZV,NVEC,MCT,DM,D,XVZ,
X IX,F,FORCE,ESTIF,U,VECT,ISM)
GO TO 99
26 CALL ELMT26(N,MA,NDIM,NDF,NEL,NEL1,NSTF,NSIZV,NVEC,MCT,DM,D,XVZ,
X IX,F,FORCE,ESTIF,U,VECT,ISM)
GO TO 99
27 CALL ELMT27(N,MA,NDIM,NDF,NEL,NEL1,NSTF,NSIZV,NVEC,MCT,DM,D,XVZ,
X IX,F,FORCE,ESTIF,U,VECT,ISM)

```

```

GO TO 99
CALL ELMT29IN,MA,NOIM,NDF,NEL,NEL1,NSTF,NSIZV,NVEC,MCT,OM,0,XVZ,
X IX,F,FORCE,ESTIF,U,VECT,ISW1
GO TO 99
CALL ELMT29IN,MA,NOIM,NDF,NEL,NEL1,NSTF,NSIZV,NVEC,MCT,OM,0,XVZ,
X IX,F,FORCE,ESTIF,U,VECT,ISW1
GO TO 99
CALL ELMT30IN,MA,NOIM,NDF,NEL,NEL1,NSTF,NSIZV,NVEC,MCT,OM,0,XVZ,
X IX,F,FORCE,ESTIF,U,VECT,ISW1
RETURN
END

```

```

SUBROUTINE MESHCK(MUMNP,MUMEL,MUMMA1,NOIM,NDF,NEL,NEL1,TOT,IOI,
A MT,MB,DT,TYPE,0,ICOD,XVZ,IR,IOEST,ISZA,NEQA,IRL4,NOEG)
PEAL LARL
DIMENSION TYPF(11),O163,11,XVZ1NOIM,11,IXINEL1,11,IOEST(NDF,1)
X ,ICOD(1)
COMMON/LARELS/ LARL161,XHED131,MM,FMED161,FM,UHED161,UM,RHED161,MM
X ,AWOR01,AWOR02,AWOR03,HEAD1121,START,CEASE,IPG,NSTH,WOR01301
COMMON/SHAP/ XJAC,SHAPE16,201,SG13,31,SK13,31,AL13,201,LOT1201
COMMON /TAPES/ 1TP5,1TP6
DATA BLANK/6HBLANK /
IOI = TOT + 1
C.... SET UP THE DESTINATION VECTOR
NDEG = 0
DO 140 N = 1,MUMNP
IC = ICOD(N)
IL = 100000
DO 120 I = 1,NOF
IOEST(I,N) = 0
IF(1C.LT.1L) GO TO 150
100 IC = IC - IL
IF(1C.GT.1L) GO TO 100
GO TO 120
150 NDEG = NDEG + 1
IOEST(I,N) = NDEG
120 IL = IL/10
140 CONTINUE
MCT = 0
DO 160 N = 1,MUMNP
MCT = MCT - 1
IF(MCT.GT.0) GO TO 160
MCT = 50
WRITE(1TP6,20331) HEAD,IPG,(UHED11,1=1,NOF)
IPG = IPG + 1
160 WRITE(1TP6,20001) N,11IOEST(1,N),1=1,NOF)
C.... COMPUTE THE BANDWIDTH OF THE MESH
MB = 0
DO 190 N = 1,MUMEL
MM = 0
NN = 0
DO 170 I = 1,NEL
K = IX(I,N)
IF(K.EQ.0) GO TO 180
DO 170 J = 1,NOF
IC = IOEST(I,K)
IF(1C.GT.MM) MM = IC
IF(1C.EQ.0) GO TO 170
IF(1C.LT.NN.OR.NN.EQ.0) NN = IC
170 CONTINUE
180 IF(MM>NN.GT.MB) MB = MM-NN
190 CONTINUE

```

```

MB = MB + 1
MB1 = MB + 2
NEOB = TOT/MB1
IF( NEOB.GT.NDEG) NEOB = NDEG
IBLK = (NDEG*NEOB - 1)/NEOB
WRITE(1TP6,2031) HEAD,IPG,NDEG,MB,NEOB,IBLK
IPG = IPG + 1
ISZA = NEOB*(MB+1)
C.... CHECK MESH FOR CONSISTENCY OF DATA
DO 50 N = 1,MUMEL
MA = MOD(IXINEL1,N),10)
IF(MA.GT.MUMMAT.OR.MA.LE.0) GO TO 40
OM = TYPE(MA)
FLAG = 1.0
DO 205 I=1,NEL
K = (X(I,N)
IF(K.GT.MUMNP.OR.K.LT.0) GO TO 40
IF(K.EQ.0) GO TO 205
NEN = 1
IF( XVZ(I,K) .NE. BLANK) GO TO 195
FLAG = -1.
WRITE(1TP6,20341)K,N
IPG = 0
GO TO 205
CONTINUE
195 DO 200 J = 1,NOIM
XIJ,II = XYZ(IJ,K)
200 XIJ,II = XYZ(IJ,K)
205 CONTINUE
IF(FLAG.GT.0.0)
X CALL ELML18IN,MA,NOIM,NDF,NEN,NEL1,NSTF,NSIZV,NVEC,MCT,OM,0,XVZ,
X IX,F,FORCE,ESTIF,U,VECT,2)
60 IF(OM.GT.0.0) GO TO 50
40 WRITE(1TP6,20301) N,MA,OM,(IXIJ,N),J=1,NEL)
IPG = 0
CONTINUE
IF(IPG.GT.0) WRITE(1TP6,20321)
RETURN
2000 FORMAT(110,5X,6I6)
2030 FORMAT(10HELEMENT,15,10H, MATERIAL,15,10H, JACOBIAN,E12.4/
X 9H 1X ARRAY,20I5)
2031 FORMAT(1H1,1246,30X,4HPAGE,14//17H EQUATION SUMMARY//
X 5X,21HNUMBER OF EQUATIONS =,16//5X,21HMAXIMUM HALF BAND =,16//
X 5X,21HEQUATIONS PER BLOCK =,16//
X 5X,21HNUMBER OF BLOCKS =,16//4X,20I1H1////1X)
2032 FORMAT(5X,46HNO ERRORS DETECTED DURING A CHECK OF THE MESH )
2033 FORMAT(1H1,1246,30X,4HPAGE,14//19H DESTINATION VECTOR//
X 6X,4HNOOF,2X,3HNOF,6A6)
2034 FORMAT(21H **FATAL ERROR**NOOE, 16, 34H NOT INPUT BUT IS USED IN E
XLEMENT, 16 )
END

```

```

SUBROUTINE CKRRIK(NOIM,NEN,FLAG)
COMMON/SHAP/ XJAC,SHAPE16,201,SG13,31,SK13,31,X13,201,LOT1201
FLAG = 1.
NSIOE = (NEN+1)/NOIM**2
L = 1
IF(NOIM.EQ.2) L = 2
SS = 1.0
DO 30 I = 1,2
SS = -SS
TT = 1.0
ON 30 J = 1,2
TT = -TT
UU = 1.0
DO 30 K = 1,2
UU = -UU
CALL BRICK2IUU,TT,SS,NOIM,NEN,NSIOE1
IF(XJAC.LE.0.0) GO TO 40
30 CONTINUE
RETURN
40 FLAG = XJAC
RETURN
END

```



```

SURROUTINE EXPLCTI,MUMNP,NUMEL,NUMMAT,NOIM,NDF,NEL,NELI,NSTF,NVEG,
X NSIZV,TYPE,0,ICOO,XVZ,F,IX,MASS,FORCE,ESTIF,VECT,U,UO,UO,UV,VV,
X TYME,IOUT,NOEG)
C
C.... EXPLICIT TIME INTEGRATION OF THE UNDAMPED EQUATIONS OF MOTION
C.... MODIFICATION 11 ** MAY 1972
C
REAL MASS
LOGICAL NPR,NPL,IREUSE,ACTFLG
DIMENSION TYPE(1),O(1,2),I(1),ICOD(1),KZIN(1),F(1),XINEL(1),I,
X MASS(1),FORCE(1),NSTF(1),ESTIF(1),TYME(1),J(1),UD(1),UOO(1),
X UUI(1),VV(1)
COMMON/OYNAMO/TIME,NSIG(7),NT,NSTEP,OT,MIMPLT,6,DATA(20,3),NPR,NPL
COMMON /ZAPES/ (TPS,ITPA
COMMON/SHAP/ XJAC,SHAPE(4,20),SG(3,3),SK(3,3),K(3,20),LO(12),
COMMON/LABELS/ LABL(6),XHEAD(13),XHFEDI(6),FH,UHED(6),UH,RHED(6),RH
X ,AWORD1,AWORD2,AWORD3,HEAD(12),START,CEASE,IPG,NSTR,WORD(30)
DATA TWORD1,TWORD2/ 6H**REAL, 6M TIME= /
C
C.... INPUT THE NUMBER OF TIME STEPS, PRINT INTERVAL, TIME INCREMENT,
C.... NEWMARK DAMPING TERM, AND PRINT SUPPRESSOR CODE FOR EXPLICIT
C.... INTEGRATION (BETA = 0)
C
READ(1,TPS,1000) NSTEP,NPRT,OT,DEL,NUNPLT,NPROP,NFOIC,KKK
IF(NPRT.NE.0) NPRT = 1
C
C.... OUTPUT THE INPUT DATA
C
WRITE(1,TP6,1000) HEAD,IPG,NSTEP,NPRT,OT,DEL,NUNPLT,NPROP,NFORC
IF(NFORC.GT.0.AND.NPROP.GT.0) WRITE(1,TP6,4001)
IF(KKK.EQ.0) WRITE(1,TP6,2002)
IF(KKK.NE.0) WRITE(1,TP6,2003)
IPG = IPG + 1
REWIND 7
IF(NUNPLT.LE.0) GO TO 40
REWIND 8
WRITE(1,TP6,2005)
DO 35 N=1,NUNPLT
READ(1,TP5,1006) (NEODATA(N),I=1,3)
WRITE(1,TP6,2006) N,(NEODATA(N),I=1,3)
35 CONTINUE
40 CONTINUE
C
C.... SET THE CONSTANTS AND INITIALIZE
C
DT2 = OT*OT/2.
GPD = 1.5 * DEL*OT
GND = 1.5 * DEL*OT
HEAD(1) = TWORD1
HEAD(12) = TWORD2
NSTEP = NSTEP + 1

```

```

63 IF(NSKIP.GT.0) GO TO 60
NSKIP = (XINEL(1)/100 + 1
MA=MOD(XINEL(1),10)
DM = TYPE(MA)
DO 64 I = 1,NSTF
FORCE(1,I) = 0.0
FORCE(1,2) = 0.0
DO 64 J = 1,NSTF
ESTIF(1,J) = 0.0
CALL ELMIBIN,MA,NOIM,NDF,NEL,NELI,NSTF,NVEG,NSIZV,MCT,DM,O,XVZ,
X (X,F,FORCE,ESTIF,U,VECT,3)
WRITE(1) ESTIF
J=MOD(XINEL(1),100)/10
IF(J.GT.0) CALL PRYMATHEAD,IPG,N,NSTF,ESTIF,FORCE(1,2),LO,NSTF)
C
C.... COMPUTE AN ESTIMATE TO THE LARGEST FREQUENCY IN THE MESH
C
DTMAX = 0.
DO 65 I = 1,M
IF(FORCE(1,2).EQ.0.0) WRITE(1,TP6,4000) N,I
IF(FORCE(1,2).EQ.0.0) GO TO 65
SUM = 0.
DO 66 J = 1,M
SUM = SUM + ABS(ESTIF(1,J))
SUM = SUM/ABS(FORCE(1,2))
IF(SUM.GT.DTMAX) DTMAX = SUM
65 CONTINUE
60 NSKIP = NSKIP + 1
C
DO 70 I = 1,M
J = LO(I)
MASS(I) = MASS(J) + FORCE(1,2)
70 CONTINUE
80 CONTINUE
C
C.... MAXIMUM TIME STEP ESTIMATE
C
DTMAX = 2./SQRT(OTMAX)
WRITE(1,TP6,2001) OTMAX
IF(KKK.EQ.0.AND.OTMAX.LT.OT) RETURN
WRITE(1,TP6,2010) (HEAD(1),I=1,10),IPG
IPG = IPG + 1
MCT = 50
CALL TICTOC(TYME,2)
C
C.... LOOP THROUGH FOR EACH TIME POINT, STARTING WITH TIME = 0.0
C
FACT = 1.0
IF(NPROP.GT.0) FACT = PROPLD(TIME,NPROP)
DO 700 NT = 1,NSTEP
IF(NPROP.GT.0) FACT = PROPLD(TIME+DT,OT)

```

```

TIME = 0.
T3 = 0.0
T4 = 0.0
T5 = 0.0
IREUSE = .FALSE.
DO 50 N = 1,NOEG
MASS(N) = 0.0
DO 51 I = 1,NSTF
LO(I) = 0
IF(NUNPLT.GT.0) CALL PLZEKON,N,N,MASS,MASS,MASS)
IF(XINEL(1)/100.GE.NUMFL-1) IREUSE = .TRUE.
C
C COMBINE BOUNDARY CONDITIONS INTO A SINGLE VECTOR, E.
C FINI .GT. BIG IMPLIES DISPLACEMENT BC.
C EINI .LE. BIG IMPLIES FORCE BC.
C
BIG = F(1)
SIZ = F(1)
DO 54 N=2,NDEG
CC = F(N)
IF(CCC.LT. SIZ) SIZ = CC
IF(CCC.GT. BIG) BIG = CC
54 CONTINUE
SIZ = BIG-SIZ + 1.
J = 0
DO 58 N = 1,NUNMP
IC = ICOD(N)
IL = 100000
DO 57 I=1,NOF
IF(IC.LT. IL) GO TO 57
IC = IC-IL
56 IF(IC.GT. IL) GO TO 56
F(I+J) = F(I+J) + SIZ
57 IL = IL/10
58 J = J + NDF
C
C.... COMPUTE GLOBAL MASS MATRIX
C
NSKIP = 0
DO 80 N = 1,NUMEL
N = 0
DO 59 J = 1,NEL
K = IX(J,N)
IF(K.LE.0) GO TO 63
KK = IX-11*NOF
DO 61 I=1,NDIM
K(I,J) = XVZ(I,K)
61 DO 62 I = 1,NOF
LO(M+1) = KK+1
62 N = M + NDF
59

```

```

IF(NFORC.GT.0) CALL RESETI-NFORC,NUNMP,NDF,F)
C.... COMPUTE AND PRINT NON-ZERO LOADING FOR EACH TIME POINT
C
WRITE(1,TP6,2015) NT
MCT = MCT-6
DO 90 N=1,NOEG
IF(FINI.GT. BIG) GO TO 90
UOO(N) = FINI*FACT
IF(UOO(N).EQ.0.0) GO TO 90
NOOE = (N-1)/NDF + 1
NF = N - NOOE*(NOOE-1)
MCT = MCT - 1
IF(MCT.GT.0) GO TO 88
WRITE(1,TP6,2010) (HEAD(1),I=1,10),IPG
IPG = IPG + 1
MCT = 50
88 WRITE(1,TP6,2020) (NODE,FHED(NF),UOO(N))
90 CONTINUE
C
C.... OUTPUT THE DISPLACEMENTS AND STRESSES AT PRINT INTERVALS
C
NPR = .TRUE.
IF(INT/NPRT) NPRT .EQ. NT) NPR = .FALSE.
NPL = .TRUE.
IF(NUNPLT.GT.0) NPL = .FALSE.
IF(NPR.AND.NPL) GO TO 93
CALL TICTOC(TYME,4)
T4 = T4 + TYME(4)
CALL DISTASINUMNP,NUMEL,NUMMAT,NOIM,NDF,NEL,NELI,NSIF,NVEG,NDEG,
X TYPE,0,ICOO,XVZ,F,IX,U,FORCE,ESTIF,UO,IOUT,0,0)
WRITE(1,TP6,2010) (HEAD(1),I=1,10),IPG
IPG = IPG + 1
MCT = 50
CALL TICTOC(TYME,5)
T5 = T5 + TYME(5)
93 CONTINUE
C
C.... GET THE CURRENT ACCELERATION BY EQUILIBRIUM EQUATION.
C
NSKIP = 0
REWIND 7
DO 400 N = 1,NUMEL
IF(IREUSE) GO TO 96
IF(NSKIP.GT.0) GO TO 95
CALL TICTOC(TYME,4)
T4 = T4 + TYME(4)
NSKIP = (XINEL(1)/100 + 1
READ(1) ESTIF

```



```

CALL TICTOCITYME,3)
I3 = T3 + TYME(3)
C
95 NSKIP = NSKIP - 1
96 M = 0
ACTFLG = .TRUE.
DO 92 J = 1,NEL
K = I(I,J,N)
IFIK,LE,0) GO TO 94
KK = IK-11*NOF
DO 91 I = 1,NOF
CC = U(KK+1)
IF(CC,NE,0.0) ACTFLG = .FALSE.
U(I,M+1) = CC
91 LO(I,M+1) = KK+1
92 M = M + NOF
IF(ACTFLG) GO TO 400
C
C.... ACCUMULATE THE MATRIX PRODUCT OF ESTIF*UU
C.... COMPUTE (MASS*UOD = F - ESTIF*UU)
C
94 DO 250 I = 1,M
CC = 0.
DO 200 J = 1,M
200 CC = CC + ESTIF(I,J)*U(I,J)
K = LO(I,I)
250 UOD(I,K) = UOD(I,K) - CC
400 CONTINUE
C
C.... GET THE ACCELERATIONS AND VELOCITIES AT THE NT TIME STEP
C
OD = 0.0
IFINT,GT,1) OD = GMD
OD 500 N = 1,NOF
CC = FINI
IF(C,LE,0.0) GO TO 550
C
C.... MODIFY FOR PRESCRIBED DISPLACEMENTS
C
UINI = CC - "1
UDN = 0.
UDON = 0.
GO TO 560
550 UDN = U(DINI)
UDON = UOD(INI)
XMASS = MASS(INI)
IF(XMASS,NE,0.0) UODN = UODN/XMASS
UDN = UDN + DD*UODN
C
C.... CURRENT VELOCITY AND ACCELERATION HAVE BEEN DETERMINED, PRINT DR

```

```

X 50X, 10H TOTAL TIME F25.3 )
4DDO FOPMAT(44H**WARNING** THE STABILITY CHECK FOR ELEMENT,15,54H MAY
XNOT BE MEANINGFUL, THE MASS FOR DEGREE OF FREEDOM,15, 0H IS ZERO)
4DDI FOPMAT(85H**WARNING** BOTH THE PROPORTIONAL LOADING AND FORCE ARE
X BEING RESET ON EACH TIME STEP)
END

```

```

C.... PLDT AS REQUIRED.
C
56D CONTINUE
C
C.... UPDATE THE SOLUTION FOR THE NEXT TIME STEP
C
UINI = UINI + OT*UON + OT2*UODN
5DD UOINI = UON + GPD*UODN
TIME = TIME + OT
7DD CONTINUE
C
C
CALL TICTOCITYME,4)
T4 = T4 + TYME(4)
I1 = NSTEP
IFINUMPLT,NE,0) CALL PLOTGO (NUMEL,NOIM,NEL,I1,U,UD,UDO,FORCE)
CALL TICTOCITYME,6)
WRITE(17P6,203D) TYME(1),TYME(2),T3,T4,T5,TYME(6),TYME(1)
RETURN
C
C.... FORMATS
C
100D FOPMAT(1215,2F10.0,415)
1006 FOPMAT(1315)
1010 FOPMAT(F10.0)
200D FOPMAT(1H1,12A6,30X,4HPAGE,14//26H EXPLICIT TIME INTEGRATION //
X 5X,25HNUMBER OF TIME STEPS - ,15/
X 5X,25HPRINT INTERVAL - ,15/
X 5X,25HTIME INCREMENT - ,E12.4/
X 5X,25HNEWMARK DELTA DAMPING - ,E12.4/
X 5X,25HNUMBER OF STRESS PLOTS - ,15 /
X 5X,25HNUMBER PROPORTIONAL LOADS,15/
X 5X,25HLARGEST FORCE NODE - ,15/1K)
2001 FOPMAT(5X,3DHMAXIMUM TIME STEP ESTIMATE IS , 1PE12.5/)
2002 FOPMAT(5X,23HSTABILITY CHECK DESIRED(1X)
2003 FOPMAT(5X,26HSTABILITY CHECK OVERRIDDEN(1X)
2005 FOPMAT(14X, 50H DESCRIPTION OF STRESS EVOLUTION PLOTS TO BE MADE. /
X5X,10H PLOT NO. 5X,8H ELEMENT,7X,9H XYZ-CODE,6X,9H SIG-CODE //
2006 FOPMAT(41TX,15,3X))
2010 FOPMAT(15X,10A6,42X,4HPAGE,14)
2015 FOPMAT(1//44H NON-ZERO LOADING FORCES FOR TIME INTERVAL = 13 //
X 5X,5H NODE,5X,12HDEG. FREEDOM,5X,6HFORCE //)
2020 FOPMAT(5X,15,5X,46,11X,E13.5)
2030 FOPMAT(11H0,61X,12HELAPSED TIME ///
X 50X, 25HINPUT PROPERTIES AND MESH F10.3/
X 50X, 25HFORM LUMPED MASS VECTOR F12.3/
X 50X, 25HELEMENT STIFFNESS TIME F10.3 /
X 50X, 10HEXPLICIT ALGORITHM F17.3 /
X 50X, 25HOUTPUT STRES AND DISPL. F10.3 /
X 50X, 13H PLOTTING TIP: F22.3 /

```

```

SUBROUTINE PACKOIO,I,C11,C12,C33,M)
DIMENSION D13,21,1)
GO TO (291,293,294),I
291 CONTINUE
D(1,1,M) = C11
D(1,2,M) = C12
D(2,2,M) = C11
D(2,1,M) = C12
D(3,3,M) = 4.0*C33
RETURN
293 CONTINUE
D(1,9,M) = C12
D(2,15,M) = C12
D(3,18,M) = C11
294 CONTINUE
D(1,1,M) = C11
D(1,5,M) = C12
D(1,10,M) = C33
D(1,16,M) = C33
D(2,2,M) = C33
D(2,4,M) = C33
D(2,11,M) = C11
D(2,17,M) = C33
D(3,3,M) = C33
D(3,7,M) = C33
D(3,12,M) = C33
D(3,14,M) = C33
RETURN
END

```

PAGE 64

```

SUBROUTINE LDOO3(NDIM,NDF,NOP,NPRES,IPRES,PR,XZ,FS)
DIMENSION IPRES(8),PR(8),FS(6,8)
COMMON/GAUSS/ LIM,SGAUSS(5,5),WGAUSS(5,5)
COMMON/SHAP/ XJAG,SHAPE(4,20),SG(3,3),SK(3,3),X(3,20),LOI(20)
NSIOE = NPRES + 1
LIM = NSIOE + 1
C0000 COMPUTE NORMAL PRESSURE GENERALIZED FORCES
OD 404 JJ = 1,LIM
TT = SGAUSS(JJ,LIM)
WT = WGAUSS(JJ,LIM)
CALL BRICK2(TT,-1.,-1.,NDIM,NPRES,NSIOE)
PN = 0.
RR = 0.0
OD 402 I = 1,NPRES
RR = RR + SHAPE(4,I)*K(1,I)
402 PN = PN + PR(I)*SHAPE(4,I)
PN = PN*WT*RR
OD 406 I = 1,NPRES
RR = SHAPE(4,I)*PN
OD 406 J=1,2
406 FS(J,I) = FS(J,I) + SG(2,J)*RR
404 CONTINUE
RETURN
END

```

4

3

1

1

```

      L1 = L1 + 1
      DD 20 J = 1,NOIM
      CT(J,L1) = DD(J,L1)
20   L1 = L1 + 3 - NOF
22   L1 = L1 + 3*(3 - NOF)
24   FORM STIFFNESS AT EACH INTEGRATION POINT
C**** DD 180 II = 1,LLINT
      SS = STUM(1,II)
      TT = STUM(2,II)
      UU = STUM(3,II)
      VV = STUM(4,II)
      CALL BRICK2(SS,TT,UU,NOIM,NEL,NSTOE)
      OVOL = WU/XJAC
C**** COMPUTE A LUMPED MASS MATRIX
      II = 0
      DD 110 I=1,NEL
      TEMP = RO*SHAPE(4,II)*XJAC*WU
      DD 100 KK = 1,NOIM
100  FORCE(II+KK,2I) = FORCE(II+KK,2I) + TEMP
110  II = II + NOF
      LI = 0
      DD 170 KK = 1,NDF
      DD 170 LL = KK,NOF
      II = KK
      DD 160 I = 1,NEL
      JI = LI
      DD 130 J = 1,NOIM
      JI = JI + 1
      TEMP = 0.
      DD 120 K = 1,NOIM
      TEMP = TEMP + SHAPEIK,II*CT(K,JI)
120  SIG(JI) = TEMP*OVOL
130  L = 1
      IF(KK.EQ.LLI) L = I
      JI = LI + NOF*(L - 1)
      DD 150 J = L,NEL
      TEMP = 0.
      DD 140 K = 1,NOIM
      TEMP = TEMP + SIG(KI)*SHAPEIK,JI
140  ESTIF(II,JI) = ESTIF(II,JI) + TEMP
150  JI = JI + NOF
160  II = II + NOF
      LI = LI + NOIM
170  CONTINUE
180  CONTINUE
C**** CONSTRUCT SYMMETRIC PART OF MATRIX
      LL = NSTF - 1
      DD 190 I = 1,LL
      K = I + 1
      DD 190 J = K,NSTF

```

```

EEI21=EPSI41
EEI31=EPSI61
EEI41=2.*EPSI31
EEI51=2.*EPSI51
275 DD 285 I=1,K
    KI=1
    IF(I,EQ,K) KI=6
    CON=D,O
    DD 280 J=1,K
    LI=J
    IF(J,EQ,KI) LI=6
280 CON=CON+COI(KI,LI)*EEI(LI
285 SIG(I)=CON
    CON=SIG(KI)
    SIG(KI)=SIG(I)
    SIG(I)=CON
    IF(NDIM,EQ,2) GO TO 288
    CON=SIG(I)
    SIG(I)=SIG(I)
    SIG(I)=SIG(I)
    SIG(I)=CON
288 CONTINUE
C.... COMPUTE INVARIANTS FOR TWO D PROBLEMS
    IF(NDIM,NE,2) GO TO 290
    CON = 1.O
    FINV = (SIG(1) + SIG(3))/2.O
    SDIF = (SIG(1) - SIG(3))/2.O
    CRAO = SORT(SDIF*SDIF + SIG(2)*SIG(2))
    SIG(4) = IFINV + CRAO)*CON
    SIG(5) = IFINV - CRAO)*CON
    SIG(6) = D.O
    IF(SDIF,NE,D.) SIG(6) = CON1*ATAN2(SIG(2),SDIF)
290 CONTINUE
    MCT = MCT - 1
    IF(MCT,GT,0) GO TO 330
C**** SET UP HEADS FOR PRINTOUTS
    I = 2
    DD 300 J=1,NDIM
    TAB1(I) = FWORD
    TAB2(I) = KWORD
300 I = I + 1
    DD 310 J = 1,6
    TAB1(I) = EWORD
    TAB2(I) = EWORD
310 I = I + 1
    TAB1(I) = SWORD
    TAB2(I) = SWORD
    TAB2(2) = VWORD
    K = 0
    DD 320 I = 1,NDF

```

```

      DD 320 J = 1,NDF
      X = K * I
      THEN(K) = SHED(I,J)
320  IF(NOPRNT) GO TO 340
      WRITE(1TP6,2002) HEAD,TIME,IPG,(XHED(I),XH,I=1,NDIM),
      X (THED(I),SH,I=1,NL)
      WRITE(1TP6,2001) (BLANK,BLANK,I=1,NDIM),(THED(I),EH,I=1,NL)
      IF(NDIM.EQ.2) WRITE(1TP6,3000)
      IPG = IPG + 1
      MCT = 15
330  IF(NOPRNT) GO TO 340
      WRITE(1TP6,TAR1) N,(XX(I),I=1,NDIM), SIG
      WRITE(1TP6,TAR2) OM,MA,(EPS(I),I=1,NL)
340  IF(NPL) GO TO 350
      CALL PLDATA(NUMEL,NDIM,N,II,THED,XX,SIG,FORCE)
350  CONTINUE
      RETURN
400  IPG = 0
      RETURN
C.... FORMAT STATEMENTS
1000  FORMAT(6F10.0/7F10.0)
2000  FORMAT(5X,14HELASTIC MODULI //13X4HC-11,8X4HC-12,8X4HC-13,
1 8X4HC-22,8X4HC-23,8X4HC-33,8X4HG-32,8X4HG-13,8X4HG-12,
2 //5X,1P9E12.4//13X4HR-11,8X4HR-22,8X4HR-33,5X7HDENSITY//5X,1P4E12
3 .4//)
2001  FORMAT(8X,9(2A6))
2002  FORMAT(1H1,12A6,E13.5,2DX,4HPAGE,13//5X,14HELEMENT STRESSES//
1 1X,7HELEMENT,9(2A6))
3000  FORMAT(12X,8H1-STRESS,4X,8H2-STRESS,7X,5HANGLE )
      END

```

```

SUBROUTINE MODULI (N,MA,NVEC,VECT,D,DD,C,NDIM)
DIMENSION D(6,1)
DIMENSION C(6,1),DD(3,1)
      INITIALIZE
      DD 15 I=1,6
      DD 15 JJ=1,6
15  C(1,JJ)=D.
      DD 20 II=1,3
      DD 20 JJ=1,18
20  DD(1,II)=D.
      CC=D(1,MA)
      C(1,1)=CC
      DD(1,1)=CC
      CC=D(2,MA)
      C(1,2)=CC
      DD(1,5)=CC
      CC=D(3,MA)
      C(1,3)=CC
      DD(1,9)=CC
      CC=D(4,MA)
      C(2,2)=CC
      DD(2,11)=CC
      CC=D(5,MA)
      C(2,3)=CC
      DD(2,15)=CC
      CC=D(6,MA)
      C(3,3)=CC
      DD(3,18)=CC
      CC=D(7,MA)
      C(4,4)=CC
      DD(3,3)=CC
      DD(3,7)=CC
      DD(1,16)=CC
      CC=D(8,MA)
      C(5,5)=CC
      DD(3,12)=CC
      DD(3,14)=CC
      DD(2,17)=CC
      CC=D(9,MA)
      CC=D(9,MA)
      CC=D(9,MA)
      C(6,6)=CC
      DD(2,2)=CC
      DD(2,4)=CC
      DD(1,10)=CC
      DD 25 II=1,6
      DD 25 JJ=1,11
25  C(1,II)=C(JJ,II)
      RETURN
      END

```

Appendix C

Experimental Examination of Wave

Processes in Natural Rock

Section IScope and ObjectivesI.1 Scope of the Experimental Investigation.

The purpose of the experimental work described in the sequel was to design and develop piezoelectric crystal transducers for the detection and recording of stress waves in rocks and to apply them to the experimental study of wave propagation processes in a model anisotropic half-space. A large Yule marble block served as this model and it was loaded by the normal impact of a sphere. Both body wave and surface wave measurements were made to study the pulse propagation phenomena in the model which represented a transversely isotropic material with its axis of elastic symmetry located in any plane parallel to the free surface. The experimental results were compared with both an analytical and a numerical solution, obtained from an integral transform procedure and a finite element method respectively, that yielded the arrival times and numerical values of dynamic stresses with the aid of a computer. In comparing the results, it was assumed that (a) the block was homogeneous and elastic and (b) at sufficient distances from the contact area of the input crystal, which was sandwiched between the free surface of the block and a loading bar, the response of the block was essentially the same as the resultant effect due to a concentrated force of arbitrary time variation. However, the finite element method could circumvent the second hypothesis as it allowed the distribution of the input force over the contact area. The dynamic elastic properties of the material of Yule marble were obtained experimentally as they needed to be included in the theoretical techniques to obtain the numerical results.

The integral transform method is the subject of Appendix A. The details of the finite element procedure are given in a technical report⁽¹⁾ and Appendix B. The methods initially employed and the numerical values of the static and dynamic

elastic properties of Yule marble specimens so obtained are given in Appendix D and Ref. (2). Two sets of values of the properties were obtained, one from samples taken from one of the two blocks utilized in the present investigation and the other from a slab of Yule marble secured separately for this purpose. The slab and the two blocks were not secured from the same source and apparently were quite dissimilar as suggested by some significant differences in their dynamic elastic constants (Table 4 of Appendix D). Hence another set of dynamic elastic constants was obtained from the wave arrival time measurements for the actual blocks based on the procedure adopted in Ref. (2). The details are given in Section VII.

I.2 Objectives of the Experimental Work.

The overall objectives of the present investigation were the experimental determination of the wave arrival times and stress histories in the interior and very near the surface of a block of Yule marble due to normal impact of a sphere, and the comparison of such data with corresponding theoretical predictions. This test configuration models a transversely isotropic elastic half-space subjected to a concentrated time-dependent normal force on the free surface. The task involved the achievement of the following subsidiary objectives:

- (i) The design and development of transducers using piezoelectric crystal elements.
- (ii) The development of an embedding technique which was compatible with the transducer design.
- (iii) The calibration of the transducer and the correlation with the in situ calibration in rock bars.
- (iv) The construction of a large number of transducers.
- (v) The generation and measurement of the input pulse using a crystal transducer sandwiched between the free surface of the model half-space and a loading bar.

- (vi) The drilling of long narrow holes in a rock block and the installation of the transducers using a suitable bonding agent.
- (vii) The detection and recording of body waves and the determination of arrival times and stress histories in an isotropic half-space modeled by a 15" x 15" x 11½" Bedford limestone block.
- (viii) The correlation of the data obtained in the model isotropic half-space with corresponding theoretical results, thus testing the satisfactory nature of the embedding technique.
- (ix) The verification of the in situ calibration procedure by the above correlation.
- (x) The detection and recording of body waves in an anisotropic half-space modeled by a Yule marble block and the measurement of their arrival times and stress histories at specific locations in the interior of the block.
- (xi) The detection and recording of surface waves in the anisotropic half-space modeled by a second Yule marble block and the measurement of their arrival times and stress histories at specific locations near the surface of the block.

The present experimental investigation was undertaken essentially as a continuation of the previous surface-wave study of Ref. (2). However, the use of the piezoelectric crystal transducers instead of the semi-conductor strain gages employed in Ref. (2) considerably facilitated the measurement techniques. In particular, the highly sensitive PZT crystals not only allowed the delineation of a normal transient stress component in a specific direction at a predetermined location of the interior of the rock, but also permitted the use of a low stress level input pulse on the free surface of the rock. This in turn enabled the measurement of the input pulse by means of an x-cut quartz crystal sandwiched between the rock surface and a loading bar. The utilization of a low stress level input

pulse prevented the occurrence of local damage at the impact location. The experimentally determined input pulse was used in the two theoretical techniques to obtain numerical results of wave arrival times and stress histories.

The two blocks of Yule marble measuring 20" x 20" x 10" were mined at Yule, Colorado and the Bedford limestone block was from Bedford, Indiana. The blocks were supplied by the U. S. Bureau of Mines, Twin Cities Mining Research Center, Minneapolis, Minnesota. One of the Yule marble blocks, which was previously used for the surface wave studies⁽²⁾, was employed for the present body wave measurements and the other was utilized for the present surface wave experiments.

Section II

Design, Development and Calibration of the Piezoelectric Transducers

The different stages of the development of the transducer and of a compatible embedding technique are described in this section. The calibration procedure of the transducers is also presented.

II.1 Design and Development of the Transducer.

The purpose of the development work was to design a transducer which could be embedded in a rock model and used to detect and record a stress component of a pulse in a given direction at a certain location in the medium and to develop simultaneously an embedding technique compatible with the transducer design. Initially, a number of experiments were conducted to establish satisfactory techniques of measurement of one-dimensional pulse propagation with piezoelectric x-cut quartz crystals used in a compression mode. Later on, the more sensitive PZT crystals were employed for similar measurements before establishing a final transducer design using the PZT crystals as the transducer elements. The crystal axes for the compression mode x-cut quartz and PZT crystals are shown in Fig. 1 and the corresponding piezoelectric constants are listed in Table 1. The equivalent

electric circuit of a piezoelectric crystal used in the compression mode is described in Ref. (3). Such a crystal may be represented as a charge generator and the potential difference between its faces is given by

$$V = \frac{q}{C_t} \quad (C-1)$$

where q is the charge generated and C_t is the capacitance of the crystal. If the external capacitance of the circuit is C_s which includes the capacitances of the connecting wires, connectors and the input capacitance of the connecting device, then

$$V = \frac{q}{C_t + C_s} \quad (C-2)$$

In the case of the x-cut quartz crystal or a ceramic crystal used in the longitudinal compression mode, the piezoelectric relations reduce to

$$q = \sigma \cdot A \cdot d \quad (C-3)$$

where σ is the uniformly distributed longitudinal stress, A is the area of the crystal, and d is the appropriate piezoelectric constant. Eqs. (2) and (3) may be combined to give

$$\sigma = \frac{V(C_t + C_s)}{A \cdot d} = \frac{VC}{Ad} \quad (C-4)$$

where $d = d_{11}$ for an x-cut quartz crystal and

$d = d_{33}$ for a piezoelectric ceramic crystal, used in the compression mode.

The crystals were utilized to record longitudinal pulse propagation in bars using the established technique of a split Hopkinson bar arrangement⁽⁴⁾. Two procedures of recording the output from an x-cut quartz crystal, which was sandwiched between two aluminum bars of the same diameter as the crystal and subjected to longitudinal impact, were employed, namely a voltage amplification method and a charge amplification method. Comparison of the data obtained from the two methods with the corresponding strain gage pulse shape indicated that the

low frequency response with charge amplification was superior. In the case of PZT ceramic crystals, the voltage amplification method reproduced the longitudinal pulse propagation with good fidelity, indicating a much better low frequency response of the PZT crystals than that of x-cut quartz crystals without any additional shunt capacitance.

Preliminary experiments with circular x-cut quartz crystals, $1/8$ " dia. x $1/32$ " thick, embedded in rock bars indicated that such crystals may be used effectively for the detection of longitudinal pulse propagation⁽⁴⁾. Initial experiments were performed in rock bars of about $3/4$ " in diameter subjected to central longitudinal impact with a crystal completely embedded at one section of the bar. This involved the attachment of lead wires to the crystals using Electrobond #2016 adhesive manufactured by Adhesive Engineering Company. A bar about 18" long was cut into two and a hole $3/16$ " in diameter and $3/16$ " deep was drilled on one end of one of the segments in the center. A diametral groove was sliced across the hole to accommodate the lead wires; the hole was then filled with a mixture of epoxy and rock powder and the crystal was embedded in this composite. The other segment was then bonded to the first to produce a single test specimen with an internal transducer.

Strain gages were mounted on the opposite ends of a bar diameter at a position about 3" from the crystal position. These gages were incorporated in a potentiometric circuit and were coupled in series to eliminate any antisymmetric components of the transients from the records. A $1/2$ " diameter steel ball was dropped from a height of $4\frac{1}{2}$ feet onto the end face of the vertically held bar and the resulting pulse was detected by both the strain gage and the crystal and recorded on an oscilloscope. A comparison of the crystal response with the corresponding signal from the surface strain gages showed a distortion in the former. A second experiment with an x-cut quartz crystal totally embedded in another bar indicated that even though such crystals effectively detect the stress pulse propagation, the crystal

signal consistently showed similar distortion. This was successfully eliminated by the removal of the lateral constraint on the crystal by surrounding the crystal with a rubber ring.⁽⁴⁾ In consequence, it was concluded that the coupling between the polarization in the x-direction, which coincided with the longitudinal direction of the bar, and the stress on the lateral side of the crystal influenced the response of a totally embedded crystal.

This effect was confirmed when two identical x-cut quartz crystals were embedded in the same rock bar. One crystal was totally embedded and the other was laterally unconstrained by surrounding the crystal with an annular rubber ring. The response of the former again exhibited a distortion in the recorded pulse shape as compared to the corresponding response of the latter and the signal from the strain gages. The totally embedded crystal also recorded a lower amplitude. Therefore, to measure a truly one-dimensional stress, a transducer which could be embedded in a rock bar and yet would retain the freedom of the crystal element from lateral constraint had to be devised.

In order to achieve such a design, it was deemed necessary to mount the crystal in a housing which would prevent any bonding material used in the embedment process from surrounding the crystal itself. In principle, the housing consisted of two metal end pieces separated by a glass washer, of the same thickness as the crystal, with the crystal encased in the arrangement. The freedom of the crystal from lateral constraint was achieved by maintaining a small air gap, about 0.002" wide, between the outside diameter of the circular crystal and the inside diameter of the glass washer. Lead wires attached to the metal end pieces completed the transducer assembly. The calibration of such a transducer using a circular x-cut quartz crystal, 1/8" dia. x 1/32" thick, as the transducer element was successfully accomplished by the split Hopkinson bar technique⁽⁴⁾. However, an alternative embedding procedure to the one originally envisaged prevailed, requiring a simple redesign of the transducer as explained below.

In the development of a suitable embedding technique, the preliminary experiments were conducted with rock bars cored from a slab of Yule marble. The following alternatives were considered: (a) The lead wire arrangement of the transducer assembly described above was modified⁽⁴⁾ to permit ready insertion in a relatively deep cored hole of the same diameter as the transducer in a rock bar. A 3" deep hole was core-drilled coaxially in a 9" long bar and the transducer was inserted and anchored at the base of the hole using a mixture of rock powder and epoxy as the bonding agent. The hole was then filled with the same mixture of rock powder and epoxy after extracting the wire leads out of the hole. (b) The same procedure as described in (a) was followed except that the filler material used was a mixture of aluminum oxide and epoxy. Based on the fact that Yule marble has an acoustic impedance higher than that of epoxy and lower than that of aluminum oxide (Table 2), it was thought that such a mixture in appropriate proportions would provide a better impedance match with the Yule marble than the mixture of rock powder and epoxy. (c) A metal bar, whose acoustic impedance matched that of Yule marble with the crystal assembly mounted on one end was considered since such a bar could be inserted easily into a deep hole. Since magnesium has an acoustic impedance closely matching the average acoustic impedance of the Yule marble material (Table 2), a transducer assembly was constructed using a 3/16" diameter bar of magnesium as shown in Fig. 2. Experiments with rock bars and a sandstone block indicated that the embedding of the transducers would be considerably facilitated with such a design. Hence a final transducer design in the form of a magnesium bar with the crystal element attached at one end was adopted. The crystal was again encased in a glass washer and a metal end piece arrangement. A lead wire was attached to the metal end piece and extracted out through a groove machined along the length of the bar and a second lead wire was attached directly to the bar (Fig. 2).

II.2 Choice of the Piezoelectric Crystal Element.

An examination of the piezoelectric constants of quartz and ceramic crystals, shown in Table 1 indicates that when these crystals are used in a compression mode a truly one-dimensional stress measurement is obtained. Now if such a crystal were to be embedded within a rock medium, it would be subjected to a complex stress field in any general three-dimensional stress wave propagation situation. It is then not possible to delineate the stresses at a location of the medium completely with one compression mode crystal. However, if the crystal properly measured the stress in one direction it would give useful information concerning such a component at this position. In some cases, such as for an axisymmetric state of stress, several crystals may be suitably located to take advantage of this symmetry so that more information may be obtained regarding the state of stress for a given pulse at a point in the medium without repeating the test.

To obtain the stress along the axis of an embedded compression mode crystal, the following conditions must be met: (i) The crystal must be free from any lateral stress; (ii) The charge generated across the crystal must be dependent only on the normal stress on the crystal, i.e., there cannot be any coupling between the face shear stress which is the shear component of the stress vector acting on the crystal face and the polarization in the compression mode; and (iii) The crystal must be embedded in a manner so that it responds to both compression and tension.

The first condition was met by the design of the transducer. In the case of x-cut quartz crystals, the cross coupling between the face shear and the polarization in the x-direction is revealed by the non-zero piezoelectric stress constant d_{14} , which is one of the two independent constants relating the electric charge to the stress tensor in this type of crystal material⁽⁵⁾. In general, the electric charge density or polarization and the stress are related by⁽⁵⁾,

$$Q_1 = d_{1j}\sigma_j$$

where the subscript i takes the values 1,2,3 and the subscript j takes the values of 1,2,...,6. With reference to Fig. 1, the x,y,z axes correspond to the subscripts 1,2,3 and the yz, xz and xy planes correspond to the subscripts 4,5,6 respectively. Thus the polarization in the x-direction or 1-direction for an x-cut quartz crystal is given by

$$Q_1 = d_{11}\sigma_1 + d_{12}\sigma_2 + d_{14}\sigma_4$$

where $d_{12} = -d_{11}$ and the other constants vanish (Table 1). The effect of the second term was eliminated by the design of the transducer based on the assumption that there were no end effects due to the encasement of the crystal between the metal end piece and the bar. However, the non-zero constant d_{14} , precludes the use of x-cut quartz crystals for a truly uniaxial stress measurement in a complex stress field. Now, for ceramic crystals, the compression mode direction is the z-direction. Again referring to Fig. 1, the polarization in the z-direction or 3-direction for a ceramic crystal in the compression mode is given by

$$Q_3 = d_{31}\sigma_1 + d_{32}\sigma_2 + d_{33}\sigma_3$$

where $d_{31} = d_{32}$, and the other constants vanish (Table 2). The effect of the first two terms is eliminated by the design of the transducer and hence the second condition cited above was met by the choice of PZT ceramic crystals as the transducer elements. The construction of the transducer and embedment with a strong bonding agent ensured that the crystal would respond to both compression and tension.

Three types of ceramic crystals were used as the transducer elements, namely PZT-4, PZT-5a and PZT-5H. Table 1 lists the various crystals used in the course of the present investigation including their properties, dimensions, the name and address of the supplier and where they were utilized.

II.3 Construction and Assembly of the Transducers.

The initial development work was performed with PZT-5a crystals, $1/8$ " dia. x $1/32$ " thick. A number of $3/16$ " dia. transducers were constructed to the design shown in Fig. 1. Similar transducers utilizing circular PZT-5H crystals, $1/8$ " dia. x $1/32$ " thick, were also fabricated. In the eventual measurements on the Yule marble blocks, PZT-4 crystals, $1/16$ " dia. x 0.020 " thick, were used and the transducer diameter was $1/8$ " (Fig. 3) but the design was essentially the same as for the $3/16$ " dia. transducer.

A special procedure was devised to mount a large number of transducers conveniently, which enabled precision assembly. However, uniformity in assembly could not be achieved due to a number of factors such as the thickness of the epoxy adhesives, small variations in the thickness of the crystals and variations in the thickness of the glass washers. Hence the transducers had to be calibrated individually.

II.4 Development of a Split Hopkinson Bar Arrangement for Calibration.

In order to utilize the crystal transducers for internal dynamic stress measurements, a suitable calibration procedure had to be devised. Initial calibration attempts with an earlier design of the transducer, using an x-cut quartz crystal as the transducer element were quite successful⁽⁴⁾. The split Hopkinson bar technique used in these experiments indicated that a piezoelectric constant could be established for the transducer assembly as opposed to the corresponding constant of the crystal itself (Fig. 4). A comparison of the signals from the surface strain gages, located both before and after the transducer, with the crystal response showed that (i) It was possible to detect and record longitudinal pulse propagation using the crystal transducer with good fidelity based on signals from the strain gages; (ii) Neither the transducer nor the epoxy joints between the transducer and the aluminum split Hopkinson bars caused any significant

reflections of the pulse at the transducer station, as is indicated by the identical signals obtained from both the strain gage stations, and (iii) The small air gap of about 0.002" between the crystal and the surrounding glass washer did not cause reflections of the pulse. In view of the small thickness of the crystal, namely $1/32$ ", compared to the length of the pulse employed in these experiments (about 8 in.), these results confirmed the hypothesis that the introduction of such a discontinuity would not interrupt the wave propagation process⁽⁶⁾. This conclusion was also significant in relation to the subsequent use of the transducers for internal measurements.

The technique of calibrating the transducer by comparing its response with a corresponding strain gage signal was also used for the final transducer design. The transducer in the form of a magnesium bar with the crystal assembly at one end made up one-half of the split Hopkinson bar arrangement (Fig. 5). The second half consisted of another magnesium bar of the same diameter. The two bars were attached together with an epoxy adhesive. Initial experiments were again successful in the sense that the correspondence between the crystal response and signal from the strain gages was very good and a piezoelectric constant could be established for the transducer assembly. However, since the crystal housing was in the middle of the split Hopkinson bar arrangement, the transducer could not be disengaged from the second half of the composite bar without breaking the rather fragile glass washer and end-piece assembly. Hence the bars were repositioned as shown in Fig. 6 to allow a simple removal of the transducer after calibration. By breaking the epoxy joint between the free end of the transducer bar and the second half of the split Hopkinson bar, the transducer could be disengaged easily.

Two more magnesium bars were utilized, one in front of the transducer and the other at the far end of the arrangement and were held firmly against their respective contact faces with a thin layer of wax. The purpose of the former was

to avoid striking the crystal assembly directly and the latter served as a momentum trap to prevent the tension pulse reflected from the far end from damaging the crystal assembly unit. The same physical arrangement was used for calibrating both the 3/16" dia. and 1/8" dia. transducers.

II.5 External Calibration of the Transducers.

The external calibration procedure for the transducers described in this section holds for both the 3/16" dia. and the 1/8" dia. transducers. For illustrating the procedure, a 3/16" dia. transducer using a PZT-5H crystal is chosen.

The experimental arrangement for the calibration of the transducers is shown in Fig. 6. The four bars are designated as the loading bar, the transducer bar, the strain gage bar and the momentum trap. The construction of the transducer ensured that the ends were smooth and square. The end faces of the other bars were previously machined for good contact at the joints. The transducer bar was placed in position and its free end was attached to the strain gage bar with Scotch-Weld 1838 B/A structural epoxy adhesive manufactured by 3M Company, St. Paul, Minn.. The epoxy adhesive was allowed to cure. To accelerate the curing process, heat was applied with a blow lamp; a temperature of about 150°F was attained and the epoxy hardened in about 1 hour. The other bars were assembled as shown in Fig. 6.

Since previous experiments indicated that there would be no reflection of a relatively long pulse at the epoxy joint, only one strain gage station was employed for comparison with the crystal response. This strain gage station, about 4" from the epoxy joint, consisted of a pair of SR-4 strain gages type FAE-12-12S9L manufactured by BLH Electronics, Inc., Mass. bonded with EPY-150 cement. The strain gages, each exhibiting a gage factor of $2.03 \pm 1\%$ and a resistance of $120 \text{ ohms} \pm 0.2\%$, were incorporated in a potentiometer circuit

and were coupled in series to eliminate the antisymmetric components of a pulse. The total capacitance of the crystal circuit was measured by means of an Impedance Bridge type 1650-A manufactured by General Radio Company.

The crystal response was measured by the voltage amplification method. The PZT crystals employed in the transducers were highly sensitive, capable of producing voltages in excess of the maximum that could be recorded on the oscilloscope, thus requiring the use of a 100X attenuator before the output from the crystal could be so recorded. For example, the d_{33} constant of PZT-5H crystals from Table 1 is 2638 pc/Lb while the d_{11} constant for x-cut quartz crystals is 10.2 pc/Lb. Hence, in comparison with the voltages of about 2.0 V obtained with x-cut quartz crystals in the experiments with the earlier design of the transducer, voltages of the order of 400 V may be expected with the PZT crystal transducers. However, even lower impact velocities of about 20-30 ft./sec. were actually sufficient to obtain the necessary comparison with the corresponding pulse from the strain gage station. A Tektronix type 565 dual beam oscilloscope was employed to record both the strain gage signal and the crystal output on the same oscillogram. The channel measuring the crystal response with a band width of dc to 300 kc. was carefully calibrated using the amplitude calibrator.

The pulse was initiated by shooting a 3/16" diameter steel ball from an air gun longitudinally and centrally against the impact end of the loading bar. The oscilloscope was triggered using the amplified output from another crystal attached firmly to the side of the loading bar with some adhesive tape and the various pulse shapes were then recorded photographically. The strain gages were calibrated by the dynamic shunting of external resistances into the potentiometer circuit and recording the corresponding deflections of the trace⁽³⁾. With the aid of a simple experiment involving longitudinal pulse propagation in a 3/16" diameter magnesium bar, the dynamic modulus of magnesium was determined. A value of

6.32×10^6 psi was obtained which compared well with the static modulus of 6.5×10^6 psi⁽⁷⁾.

With the aid of Eq. (C-4), the measured total capacitance of the transducer circuit including the input capacitance of the attenuator, the area of the transducer face (not the area of the crystal face), the peak voltage output from the crystal and the peak stress, the piezoelectric constant for the transducer was evaluated. This gave an equivalent constant for the transducer as explained in Fig. 4. This constant obtained by such an external calibration was designated by the symbol K.

II.6 In Situ Calibration.

Body wave measurements in a limestone block⁽⁸⁾, indicated that the external calibration procedure alone was insufficient to obtain stresses from internal measurements. Such a conclusion was reached after embedded measurements in the limestone block using wax as the bonding agent did not correlate with the corresponding results obtained by the finite element method. The measurements apparently failed to give satisfactory results because:

- (i) The transducers were not calibrated individually. It was originally assumed on the basis of calibrating two transducers externally that the external calibration constant would be nearly the same for all transducers using the same type of crystal element. However, it was later found that the external calibration constants depended on the tolerance of the individual elements making up the crystal units and varied considerably from one transducer to another;
- (ii) The wax used as the bonding agent proved ineffective for transmitting tensile stresses, and;
- (iii) A calibration procedure was not established to correlate the external calibration constant with an in situ calibration.

Hence additional experiments were performed to devise a suitable method for in situ calibration in rock bars. Tests on limestone rock bars with embedded transducers using wax as the bonding agent again indicated an inconsistency between the transducer response and the surface strain gage signal. The transducer output varied depending upon the contact inside the hole between the transducer face and the material of the rock. Since an epoxy type of joint had proven to be effective in a number of earlier applications, such as the external calibration of the transducer, a mixture of aluminum oxide and epoxy was considered a more suitable bonding agent between the transducer and the rock material. Similar experiments with limestone rock bars with embedded transducers and surface strain gages showed that the correspondence between the embedded crystal response and the signal from the strain gages was more consistent when a mixture of aluminum oxide and epoxy was used as the bonding agent.

II.7 Correlation of the External Calibration with In Situ Calibration In Rock Bars.

A limestone bar with a diameter of about $3/4$ " and a length of 15" was chosen for the in situ calibration because the dynamic mismatch between limestone and magnesium was found to be less than 5% as shown in Table 1. An experiment was executed to measure the longitudinal stress pulse propagation in the bar using a transducer in the embedded state. A comparison of the transducer response with surface strain gages was expected to give an in situ calibration constant for the transducer, say K_1 . The objective was to correlate this constant with that obtained by external calibration.

A $3/16$ " diameter transducer 10" long (Fig. 2) was constructed using a $1/8$ " dia. x $1/32$ " thick PZT-5a crystal. A $3/16$ " diameter hole about 8" deep from one end was core-drilled coaxially in the limestone bar. The drilling was performed with a diamond drill supplied by Keen Kut Products, Burlingame, California. The transducer was calibrated externally and the constant K was established. The transducer

was then inserted in the hole, using a mixture of epoxy adhesive and aluminum oxide as the bonding agent, thus securely anchoring the crystal assembly end of the transducer at the bottom of the hole. A pair of SR-4 semiconductor strain gages were mounted at the same section of the rock bar as the crystal station. The strain gages were of the type SPB 3-12-12 manufactured by BLH Electronics Inc., Mass. and EPY-150 epoxy cement was used for bonding the gages to the rock bar. The gages were mounted on the opposite ends of a diameter of the bar and coupled in series to eliminate antisymmetric effects and incorporated in a potentiometer circuit. The experimental arrangement is shown in Fig. 7. A thin layer of Electrobond #2016 conducting epoxy adhesive manufactured by Adhesive Engineering Company was applied to the impact end and a lead wire was taken off the epoxy. The epoxy layer was polished to a smooth surface. The surface was then smeared with some conducting epoxy without the hardener.

The rock bar was subjected to central longitudinal impact through an 1/8" diameter aluminum loading bar with 1/8" dia. x 1/32" thick x-cut quartz crystal sandwiched between the loading bar and the rock bar. Again, a thin layer of conducting epoxy without the hardener was applied to the contact faces of the crystal and the loading bar. A second lead wire was attached to the loading bar close to the crystal. This crystal station was utilized to measure the input pulse with the aid of a charge amplifier. The pulse was generated by shooting the impact end of the loading bar with a 3/16" dia. steel ball from an air gun at a velocity of about 20 ft/sec. The input pulse and the signal from the calibrated strain gages were recorded on a dual-beam oscilloscope and the embedded crystal response was recorded on another oscilloscope.

The input pulse measurement obtained by charge amplification was effectively a force-time record. A comparison of the input pulse and the strain-time record, using the area of the cross section of the limestone bar and a value of 5.0×10^6 psi for the dynamic elastic modulus of limestone, showed good correspondence. This

indicated that the input measurement by means of an x-cut quartz crystal loaded through a loading bar was correct.

The experiment was repeated using voltage amplification for the measurement of the input pulse and similar agreement as above between the strain pulse and the force-time record proved that either method of input measurement was reliable. The capacitance of the transducer circuit was measured and the input capacitance of the oscilloscope was added to give the total capacitance of the circuit. With the aid of Eq. (C-4) the stress-time record was established from the transducer response for both experiments. A comparison of the peak stress from the stress-time record and the peak strain from the surface strain gage data using the same value of the dynamic elastic modulus of limestone enabled the establishment of an in situ calibration constant for the transducer. It was found that this constant K_1 was related to the external calibration constant K by

$$\frac{K_1}{K} = \frac{a}{A} \quad (C-5)$$

where a is the area of the crystal face and A is the area of the transducer face. Similar experiments involving a second limestone bar with an embedded transducer which was previously calibrated externally and surface strain gages yielded the same correlation.

Since it was obviously not practical to establish a correlation between the external calibration constant and the in situ calibration constant for each transducer, the above correlation was accepted to hold for all transducers. Thus, each transducer was calibrated externally and individual constants, K , were established and subsequent internal measurements were expected to yield values for stresses using this constant K and the above correlation.

Section III
Body Wave Propagation In An
Isotropic Rock Model

III.1. Introduction.

The method of the measurement of body wave propagation in a model isotropic half-space, represented by a Bedford limestone block, 15" x 15" x 11 $\frac{1}{2}$ ", generated by sphere impact perpendicular to the free surface is described in this section. These experiments were preceded by body wave measurements with the same block as described in Ref. (8). The earlier experiments failed to give satisfactory results for the reasons given in II.6 and the lack of agreement between the experimental results and the theoretical predictions prompted a reappraisal of the calibration procedure and the bonding technique (cf. II.6 and II.7). The main purpose of the experiments described in this section was to test the validity of the correlation between the external calibration and the in situ calibration in rock bars established in Section II and to confirm the satisfactory nature of the bonding technique. In order to meet these objectives it was necessary:

- (i) To establish the necessary technique for drilling long holes of small diameter, with diamond core drills, in a block of rock material.
- (ii) To install externally calibrated transducers in the holes using a suitable bonding agent.
- (iii) To devise a method of generation and measurement of the input pulse using a spherical steel ball as the striker.
- (iv) To detect and record body wave propagation and obtain arrival times.
- (v) To obtain stress histories in particular directions at certain locations in the rock medium by using the correlation between the in situ calibration and the external calibration established in Section II.

- (vi) To compare the experimentally obtained stress-time records with the corresponding theoretical results obtained by the integral transform analysis and the finite element method and hence to verify the calibration procedure.
- (vii) To confirm the satisfactory nature of the embedding technique, and finally;
- (viii) To establish the experimental techniques that would be used later for the study of the wave propagation processes in the model anisotropic half-space.

III.2 Installation of the Transducers.

The limestone block was drilled using a 3/16" dia. x 10" long core drill on a press especially adapted to provide a continuous supply of water. The transducers previously embedded with wax⁽⁸⁾ were removed. In the process of removal, the crystal assembly ends of two of the transducers broke off inside their respective holes. These ends were removed by drilling them out with an extended 3/16" dia. flat bottomed fluted drill driven by a hand-operated power drill. The deep holes were cleaned by pouring acetone down the holes and inserting the long fluted drill inside the holes and rotating by hand until there was no trace of metal filings or wet rock powder in the flutes when the drill was removed.

A total of four transducers with 3/16" dia. magnesium bars utilizing circular PZT-5 crystals were constructed (Fig. 2); two of the transducers utilized PZT-5a crystals and two featured PZT-5H crystals as the transducer elements. Each transducer was about 10" long and was externally calibrated with constants given in Table 3. The transducers were cleaned with acetone to remove any traces of grease from previous machining operations. The hole depths in the rock were carefully measured and the corresponding lengths were marked on the transducers.

A mixture of aluminum oxide and epoxy was prepared heated with a blow lamp to make it flow more easily, and smeared on the transducers. A liberal coating was applied so that the crystal assembly end of the transducer had a 1/16" thick layer of the bonding agent around it. The transducers were then installed in their respective positions. The secure anchoring of the crystal assembly ends at the bottom of the holes was insured by observing that the previously provided markers on the transducer bars maintained a certain predetermined distance from the rock surface. The transducers were lightly pushed into position. Heat was applied to the rock by means of a blow lamp. A temperature of about 150°F was attained on the rock surface. The bonding agent was allowed to cure for about one day. Low noise cables, each about 3'-0" long with BNC connectors at their ends were attached to the transducer leads. The transducer locations are indicated in Fig. 8. During the calibration of the transducers, the polarity of each transducer was also determined.

III.3 Generation and Measurement of Input Pulse.

A stress pulse of low magnitude such as one generated by tapping the free surface of the block was sufficient to detect pulse propagation with the embedded transducers. Such a pulse was recorded by connecting one of the transducers to a type 549, Tektronix storage oscilloscope and triggering the scope internally. All the embedded transducers were tested this way to make sure they were functioning properly. It was clear that a sufficiently strong impact could be achieved by shooting a 3/16" dia. steel ball with an air gun at a low velocity but it was restricted to such a stress level that the impact through a 1/8" diameter loading bar, as described in II.7, on a 1/8" dia. x-cut sandwiched quartz crystal, Fig. 9, did not break the sensor. The input was measured by means of charge amplification using a Kistler S/N 477 unit. A charge sensitivity of 10.2×10^{-12} coulombs/lb was used; this was the value obtained in the course of the present investigation

as described in Ref. (4). The oscilloscopes were triggered by means of the amplified output of another crystal attached to the loading bar about 4" ahead of the input crystal.

III.4 Measurement of Body Wave Propagation.

The experimental arrangement employed is shown in Fig. 9. The limestone block was set up on a table which could be adjusted in three mutually perpendicular directions by means of cross slides, each provided with a screwed spindle and a handle. The block was aligned with the aid of a precision level and a triangle so that the loading bar was perpendicular to the free surface. The capacitances of the transducers and the respective cables and connectors were measured by means of the impedance bridge cited in II.5. The total capacitance of each transducer circuit was obtained by adding the input capacitance of the oscilloscope plug-in unit to the measured capacitance. The voltage amplification method was employed to record the response of each of the embedded crystals.

The limestone block was adjusted by means of the three perpendicular motions of the table for aligning the chosen impact position on the rock face with the loading bar. The motion of the table parallel to the gun was used to keep the input crystal sandwiched firmly between the free surface of the rock and this bar. At each impact location the rock surface was prepared in the manner described in II.7 so as to attach a lead wire for measuring the input pulse but still allowing the crystal to have a good flat contact with the free surface of the rock. The second lead wire was again attached to the aluminum loading bar close to the crystal station.

The input pulse, generated by shooting a 3/16" dia. steel ball with an air gun, and the internal measurements, called the outputs, were recorded on Tektronix type 565 dual beam oscilloscopes. A number of measurements were taken for

different impact locations. For each such position the experiment was repeated to check reproducibility. The magnitude of the input pulse was varied by changing the velocity of the ball by means of different air reservoir pressures. In Table 3 a summary of the impact locations, measured stresses and appropriate scale factors for the various records are given. Each station sensed the normal stress along the crystal axis, i.e. in the direction of the transducer bar. For example, referring to Fig. 8, stations 1 and 4 measured σ_{zz} and stations 2 and 3 measured σ_{xx} .

No attempt was made to determine the impact velocities. Since the input pulse was observed directly and such a method of measurement was found to be reliable as described in II.7, it was not deemed necessary to ascertain the velocities of impact and rebound and to verify the input impulse by determining the change of momentum. At higher impact velocities, this procedure could not be employed since breakage of the crystal would occur; in this event, the sensor could be replaced by a set of strain gages mounted on the loading bar that would delineate the input as the difference between the records of the initial and the first reflected pulse passage.

A detailed discussion of the results is given in Section VIII. It is only mentioned here that the data agreed well with the theoretical values for arrival times and stress histories as depicted in Fig. 1 of the main report and Figs. 10 to 12 (see Table 3), indicating that the calibration procedure was valid and the embedding technique was satisfactory. The bonding agent also proved effective and the experimental techniques developed provided a reliable means of detecting and recording body waves.

Section IV

Body Wave Propagation In An

Anisotropic Rock Model

IV.1 Direction of the Axis of Elastic Symmetry.

The main objective of the present experimental investigation was the study of body wave propagation in an anisotropic half-space modeled by a 20" x 20" x 10" block of Yule marble that represented a transversely isotropic half-space with the axis of elastic symmetry in a plane parallel to the 20" x 20" free surface. In a previous surface wave investigation⁽²⁾⁽⁹⁾ involving the same block the axis of elastic symmetry was located by crystallographic analysis of a thin sample prepared from a trapezoidal piece of material cut from one corner of the block. However, in Ref. (9) the authors expressed some uncertainty about the actual direction of the axis of elastic symmetry (AES). In the course of the present work, another attempt was made to determine the direction of the AES. Another crystallographic analysis did not locate this direction with any more accuracy, but the discolorations in the block due to impurities indicated that the AES might be located about 15° from the one previously determined, as sketched in Figs. 13 and 14. However, the body wave measurements were expected to give additional evidence through wave arrival times to substantiate the direction of the AES.

IV.2 Determination of Transducer Locations.

With the AES located as shown in Fig. 13, the transducer locations had to be determined so that (i) The transducers may be utilized to detect and record body wave propagation due to the impact of a sphere on the free surface of the block without interference by reflections from the boundaries; (ii) The distances of the transducers from the impact position were such that the signal to noise ratio would

allow the detection of the transients initiated on the free surface by shooting $3/16$ " diameter or $1/4$ " diameter steel balls from an air gun at velocities which would not break the input crystal; (iii) The various observation points in the interior of the block would yield wave arrival times along a number of rays oriented at different directions to the AES; (iv) The transducers would yield representative stress histories, each transducer measuring the stress in a specific direction at the observation point relative to the impact location, and (v) Advantage was taken of the symmetry of the block in locating the transducers so as to obtain stresses in different directions but effectively at the same location relative to the impact position.

The signal to noise ratios from the previous experiments on the limestone block and a comparison of the sensitivities of the $3/16$ " diameter transducers employing $1/8$ " diameter PZT-5 crystals used in these experiments with the sensitivities of the $1/8$ " diameter transducers employing $1/16$ " diameter PZT-4 crystals for measurements in the Yule marble block indicated that the transducers could be located up to about 5" from the impact position. The transducers were required to detect the body waves produced by the impact of a sphere on the free surface achieved by shooting a $3/16$ " diameter ball at velocities comparable to those employed in the limestone block experiments without either significant noise or without breaking the $1/8$ " diameter crystal that monitored the input. A drop test of a $1/4$ " diameter steel sphere from a height of about 4 feet on the top of a sandstone block with a transducer held against the side of the target indicated the capability of transducers to detect pulses of the level described above. Eventually $1/4$ " diameter x 0.1" thick x-cut quartz crystals were also used for the measurement of the input pulse that were capable of withstanding higher input stress levels and hence offered better conditions of measurement. In fact, the transition from the $3/16$ " diameter to $1/8$ " diameter transducers was made after taking into account the above considerations. There was no further need to determine

an acceptable signal level for the present experiments.

The center of the surface, designated P_0 in Fig. 15, was chosen as the principal impact location. The pulse length obtained in the limestone block experiments ranged from 30 to 40 μsec and was expected to be about the same for the marble. This block was 10" deep and previous experiments on the specimen indicated that the fastest wave speed corresponded to about 5 $\mu\text{sec/in}$ in the direction of the depth. It was thus estimated that the first passage of the pulse could be recorded up to a distance of 5" from the impact location without interference due to reflections from the boundaries. Thus the size of the block, the transducer sensitivity, the length of the pulse, the velocity of impact, the requirements of the input measurements and the fact that the response was required at a sufficiently large distance away from the impact position (so that it could be considered essentially as the response due to a concentrated load of arbitrary time variation as was assumed in the integral transform method (Appendix A)) all had to be considered in determining the positions of the transducers.

The locations of the transducers should be such as to display all the distinctive features of the wave propagation phenomena as suggested by theoretical predictions. Originally, significant differences in the slowness surface from the corresponding isotropic case were expected on the basis of the dynamic elastic constants cited in Ref. (9) that resulted in a tripartition of wave surface; the initial selection for the transducer positions reflected these characteristics. However, the present body wave measurements resulted both in a relocation of the axis of elastic symmetry, as shown in Fig. 14, as well as in new dynamic elastic constants, as described in Section VIII, that did not predict a wave surface partition. Hence, the exact locations of the transducers no longer needed to correspond to any particular behavior of the wave propagation phenomena except that they were conveniently located to yield the wave arrival times and stress histories which could be compared with corresponding theoretical predictions.

The transducer locations are shown in Figs. 16 to 21. Impact positions other than the center of the free surface were also employed, primarily to obtain information on body waves detected by transducers located nearer to the impact position. Such data were called the near field response of the block while the data obtained by central impact were termed the far field response. The near field data were obtained primarily for comparison with corresponding results obtained by the finite element method which was not particularly suitable for far field comparison due to excessive computing time required to secure numerical results.

IV.3 Transducers Employed.

Transducers in the form of 1/8" dia. magnesium bars with the crystal assembly on one end, as shown in Fig. 3, employing PZT-4 crystals as the transducer element were used for the body wave measurements. Care was taken in the assembly of the transducers to preserve the outside dimension of 0.126 ± 0.001 ", which was the diameter of the bar, especially near the crystal end. The transducers were identified and externally calibrated using the procedure described in Section II. Linearity of response, repeatability and reproducibility were established. The polarity of individual transducers was also determined. A total of 18 transducers were selected for the body wave measurements. The correlation with the in situ calibration in rock bars and subsequent verification of this by the measurements in the limestone block provided a means of obtaining individual stress factors for the transducers (see Table 3).

IV.4 Preparation of the Yule Marble Block.

The general technique of drilling the Yule marble block was the same as that employed for drilling the limestone block, described in Section III. Previous experience with slabs and rock bars showed that long holes of small diameter could be drilled straight and smooth in Yule marble fabric with diamond core drills.

The drills employed were 1/8" in diameter ($0.128" \pm 0.001"$) purchased from Keen-Kut Products, Burlingame, California.

The block was marked for drilling with depths of the holes carefully noted. Pilot holes were made with an electric hand drill to facilitate the starting of the core drill. During these operations, care was taken to keep the center of the drill free from any clogged-up or powdered material so that a profuse supply of water was constantly kept flowing down its center. The operations of drilling, finishing of the holes by means of a 0.128" dia. flat bottomed extended fluted drill and subsequent clearing of the holes to remove excess powdered rock material were performed as described in Section III. Straight holes with smooth sides of the required diameter were obtained. It was noticed that there was no significant drift of the core drill even in the drilling of the deeper holes; the maximum depth was about $8\frac{1}{2}"$, as checked by inserting a 1/8" dia. bar in the holes and verifying that the extended bar was normal to the rock surface. A total of 18 holes of various depths were drilled, 6 from each of three sides of the block. The three directions corresponded with the X,Y,Z axes defined in Fig. 14.

The previously calibrated transducers were installed in the holes following the same procedure as described in III.3. A mixture of aluminum oxide and epoxy was again used as the bonding agent. Similar precautions as described in III.3 were taken to make sure that the crystal assembly ends of the transducers were securely anchored at the bottom of the holes. Heat was applied to the rock by means of two infrared heat lamps and the bonding agent was allowed to cure for a day. As before, Endevco low-noise cables about 5'-0" long were soldered to the transducer leads and the ends of the cables were provided with BNC connectors.

IV.5 Body Wave Propagation Measurements.

The experimental arrangement for the Yule marble tests was similar to that shown in Fig. 9. The block was arranged on the table employed previously for the

limestone block. It was found convenient to fix the loading arrangement which was attached to the gun and move the block so that the loading bar always remained perpendicular to the free surface once it was so adjusted. The same method of input generation and measurement by charge amplification as used on previous occasions was again employed. This time since circular x-cut quartz crystals 1/8" diameter or 1/4" diameter were utilized, a loading bar of the same diameter as the crystal was used to transmit the pulse.

Three Tektronix type 565 dual beam oscilloscopes were employed for recording the outputs from three embedded transducers for each impact. The input was recorded simultaneously on the three oscilloscopes along with the respective outputs so that the wave arrival times could be directly obtained for each transducer location.

Most of the data were obtained by central impact on the free surface designated P_0 in Fig. 15 although other impact locations, P_1, P_2, \dots , Fig. 15, were also used. For detecting and recording the body waves by some of the more distant transducers at asymmetrical stations, an input pulse with a higher stress level was required. However, this would have broken the 1/8" diameter crystal and damaged the rock surface at the impact location; thus, it was found expedient to use a 1/4" diameter x 0.1" thick x-cut quartz crystal for the nonsymmetrical impact locations. The smaller crystal was adequate for measuring the lower stress level input pulse from central impact. Both 3/16" diameter and 1/4" diameter steel balls were used; the latter produced an increase of about 10 μ secs in the pulse length. With the unsymmetrical impact positions, some of the transducers were about 1-3/4" from the impact locations. The responses from these transducers were recorded to obtain the near field response of the block.

In addition to the above body wave measurements, transducers at special locations relative to the AES were chosen to determine arrival times along directions parallel to the AES inside the block and along directions parallel

to the AES as determined previously⁽⁹⁾. These measurements were made primarily to compare the wave speeds along a number of directions parallel to the initially determined and the relocated AES so as to yield additional evidence regarding the exact location of the AES.

The capacitance of each transducer circuit was measured before and after taking the data and the average value of the two measurements plus the input capacitance of the oscilloscope plug-in unit was taken as the approximate true capacitance of the circuit. Usually a difference of $\pm 2\%$ was observed in the two measurements. The external calibration constants of the transducers, the total transducer circuit capacitances for the body wave measurements and the corresponding stress factors are listed in Table 4. The various runs are described in Table 5a and 5b.

Section V

Surface Wave Propagation In

The Anisotropic Rock

V.1 Anisotropic Model for Surface Waves.

A second Yule marble block of the same dimensions as the one employed for body wave measurements and with the axis of elastic symmetry also located in a plane parallel to the 20" x 20" free surface, was used to study surface wave phenomena. The direction of the AES was determined from the discoloration pattern on the various sides of the block. The crystallographic analysis of a specimen prepared from sample material cut off from one corner of the previous block indicated that the discoloration lines, which were approximately parallel on any one face of the block, correspond to the foliation plane, i.e. to a plane perpendicular to the AES. The average directional properties of these lines on all sides of the block indicated that the foliation plane was perpendicular to the free surface. From these observations, it appeared that the determination

of the direction of the AES as a line perpendicular to the average direction of the discolorations on the free surface was valid. In the same manner, the AES of the second block was located as a line perpendicular to the discolorations on the free surface; the overall pattern of these lines again suggested that the foliation plane was perpendicular to the free surface. In Fig. 22, the AES of the second block and the coordinate system chosen are shown.

V.2 Objectives.

The objectives of the surface wave propagation investigation were:

- (i) To embed suitably modified transducers just below the free surface to measure the dynamic radial and circumferential stresses at given locations due to normal sphere impact;
- (ii) To obtain arrival times, and;
- (iii) To compare the experimental data with corresponding theoretical results.

The general experimental techniques and the methods of measurement developed in the course of body wave measurements were still applicable. However, the transducers had to be modified after individual external calibration for embedment just below the free surface.

V.3 Transducer Modification.

In order to measure stresses just below the surface, it was intended to drill small slots on the surface of the block and embed transducers in the slots. The design of these transducers was essentially the same as the earlier one⁽⁴⁾ which was superseded except that magnesium end pieces replaced the aluminum end pieces employed previously. However, instead of constructing transducers in this manner, the following procedure was adopted. The transducer in the form of a 1/8" diameter magnesium bar, with a 1/16" dia. x 0.020" thick PZT-4 crystal

element, was assembled leaving out the lead wires. Two $1/64$ " dia. and $1/16$ " deep holes were drilled, one in the bar and one in the end piece and wire leads were attached in the holes with Electrobond #2016 conducting epoxy adhesive. The transducer was then externally calibrated. The magnesium bar was now cut off in a lathe. Thus, a transducer was obtained as required that had already been calibrated. Such a procedure was adopted because the transducer in the form of a bar could be calibrated and disengaged easily from the split Hopkinson bar arrangement as explained in II.4, while a similar separation after calibration of the final form of the transducer would have presented some difficulties in that respect.

V.4 Location and Installation of Transducers.

The AES of the Yule marble block was marked on the free surface. The transducer locations were chosen to measure the radial and circumferential stresses as shown in Fig. 22. To measure the radial stress, the crystal compression mode direction must coincide with a radial line and to measure the circumferential stress, it must be perpendicular to a radial line as shown in Fig. 23.

From the center of the free surface a circle of 5" radius was drawn. Diametral lines were marked off every 15° from the AES. Locations were chosen on either end of the 10" diameters, one end of the diameter for the radial stress and the other end for the circumferential stress measurement.

To embed the transducers just below the free surface, small holes with dimensions of $1/4$ " x $1/4$ " x $1/8$ " were milled with a $3/32$ " dia. end mill. A total of 14 slots were made including two on the AES and two on a perpendicular axis that represented the direction of the foliation plane. The slots were $1/8$ " deep identical to the diameter of the transducer so that the average stress measured corresponded approximately to the stress at a point $1/16$ " below the surface.

The slots were cleaned with acetone and allowed to dry. The transducers were embedded in the slots using a mixture of aluminum oxide and epoxy as the bonding agent and low noise cables were attached to the exposed lead wires.

V.5 Surface Wave Propagation Measurements.

The experimental arrangement was similar to that shown in Fig. 9. The input measurement and the loading bar arrangement was similar to the system used previously. A 1/4" dia. aluminum loading bar and a circular x-cut quartz crystal 1/4" dia. x 0.1" thick were used. The input pulse was initiated by shooting a 1/4" dia. steel ball with an air gun. A central impact location was chosen with all the transducers located at a 5" radius from the impact position. Two Tektronix type 565 dual beam oscilloscopes were utilized to record simultaneously the outputs from two transducers located on either end of a diametral line. Since the diametral line represented a ray at a certain angle to the AES, both lying in the plane of the free surface, the two transducers effectively measured the propagation of the pulse at the same point relative to the impact location. The input was also simultaneously recorded on the same dual beam oscilloscopes. The other techniques of measurement utilized for the body wave measurements were again employed. The external calibration constants of the transducers employed are listed in Table 6, which includes the total transducer circuit capacitances and the corresponding stress factors for internal measurements. The various runs are described in Table 7.

Section VI

Summary of the Experimental InvestigationVI.1 Stress Factors from External Calibration Constants.

The various stress factors are listed in Tables 3, 4 and 6 corresponding to a 1 volt output from the transducers, i.e., if the gain level for a measurement was 5 mv/div, the stress/div was $(5 \times 10^{-3} \times \text{stress factor})$ psi.

VI.2 Body Wave Measurements in the Isotropic Model.

The details of the input and output measurements for the body wave tests in limestone are given in Table 3. The corresponding figures depicting the input and output data are also listed. The dynamic elastic properties of limestone employed in the two theoretical analyses were⁽¹⁰⁾

Young's modulus, $E = 5.0 \times 10^6$ psi

Poisson's ratio, $\mu = 0.29$

Density, $\rho = 0.0805$ lb/in³

VI.3 Body Wave Measurements in the Yule Marble Block.

The body wave measurements in the Yule marble block are described in Tables 5(a) and 5(b). The dynamic elastic properties of Yule marble are listed in Table 4, Appendix D. The procedure of determining the properties from the body wave and surface wave measurements on the Yule marble blocks is included in Section VII.

VI.4 Surface Wave Measurements in the Yule Marble Block.

The surface wave measurements are described in Table 7 which includes the details of input and output measurements and a list of the corresponding figures.

Section VII

Determination of Dynamic Elastic

Properties From Arrival Times

VII.1 Dynamic Elastic Constants of Yule Marble.

In the course of previous theoretical and experimental investigations of surface waves produced by the normal impact of a sphere on a half-space modeled by one of the Yule marble blocks⁽²⁾ which was again used in the present investigation, the theory was developed for linearly elastic constitutive behavior of the material. The dynamic values of the elastic constants were determined from the measurements of wave speeds along specific directions in the block. In addition, the static and dynamic properties of the material were also determined from samples of the material cut from the block by means of standard procedures. However, in the more extensive experimental investigation described in Appendix D, the dynamic elastic of Yule marble were again obtained from samples of a slab secured from another source. Since the two sets of values appeared to differ in some respects (Table 4, Appendix D) a procedure was devised to determine the constants by utilizing the actual body wave and surface wave measurements from the two blocks of Yule marble. The procedure of determining the constants was based on formulating a programming problem for the minimization of a function of an arbitrary number of variables. A least square approximation method was applied to devise an objective function using the velocity equation for the propagation of elastic waves in a transversely isotropic medium⁽¹¹⁾. Rosenbrock's method⁽¹²⁾ of functional optimization was used for the minimization.

VII.2 Elastic Stiffness Matrix and Velocity Equation.

The coefficients of the generalized Hooke's law are also referred to as elastic stiffnesses. Their matrix, which reduces to a 6 x 6 symmetric matrix due to the

symmetry of the stress and strain tensors, the constitutive law, and a positive definite energy function may be shown to have the following non-zero elastic stiffnesses for a transversely isotropic material⁽¹¹⁾

$$\begin{aligned} c_{11} &= c_{22}, c_{33} \\ c_{12}, c_{13} &= c_{23} \\ c_{44} &= c_{55} \\ c_{66} &= \frac{1}{2}(c_{11} - c_{12}) \end{aligned} \quad (C-6)$$

A set of five independent constants completely specifies the elastic behavior of the solid.

If the source of the disturbance is chosen as the origin of an orthogonal coordinate system (x_1, x_2, x_3) , where the x_3 -axis coincides with the axis of elastic symmetry, the equation for the phase velocity of elastic waves has the form⁽¹¹⁾

$$[H - \frac{1}{2}(1-n^2)c][H^2 - [(1-n^2)a + n^2h]H + n^2(1-n^2)(ah-d^2)] = 0 \quad (C-7)$$

Here

$$\begin{aligned} a &= c_{11} - c_{44} \\ c &= c_{11} - c_{12} - 2c_{44} \\ d &= c_{13} + c_{44} \\ h &= c_{33} - c_{44} \\ H &= \rho v^2 - c_{44} \end{aligned} \quad (C-8)$$

ρ is the density of the material, v is the phase velocity and n is the direction cosine of a radius vector from the origin with respect to the x_3 -axis. The equation gives the phase velocity as a function of orientation of a certain direction with respect to the axis of elastic symmetry and constitutes a sextic in v that has three real roots.

With the aid of Eq. (C-7), the geometrical features of the velocity and slowness surfaces for a particular set of elastic constants can be studied. However, the present discussion is concerned only with the following concepts⁽¹¹⁾

- (i) With the source of the disturbance of the medium chosen as the origin, the velocity surface is formed by all the radius vectors passing through the origin, each having a length proportional to the phase velocity permissible in its direction. Thus, Eq. (C-7) represents three sheets of the velocity surface; the first factor is associated with a true transverse displacement expressed by

$$H - \frac{1}{2}(1-n^2)c = 0 \quad (C-9)$$

and the second factor is a quadratic in H and represents the other two sheets of the velocity surface which cannot be separately factored. The latter may also be written as

$$(H-m^2a)(H-n^2h) - m^2n^2d^2 = 0 \quad (C-10)$$

where $1-n^2 = m^2$

- (ii) In view of the elastic symmetry of the block and the chosen coordinate system, the orientation of a given direction is completely determined by one direction cosine with respect to the axis of elastic symmetry (x_3).
- (iii) The first factor of Eq. (C-7) is associated with a pure shear velocity but the second factor is neither associated with a pure shear velocity nor a pure longitudinal velocity except in specific directions, namely, along the coordinate axes.

VII.3 Velocities from Experimental Measurements.

With the embedded transducers, the detection and recording of wave propagation processes in the two Yule marble blocks furnished the wave arrival times at various locations situated in different directions relative to the impact points. From these arrival times and the distances of the transducers from the various impact positions, wave speeds in different directions were calculated. These do not truly represent p-wave phase velocities even though they were calculated from the first arrival of the wave because the wave propagation undergoes considerable refraction⁽¹¹⁾. However, since the maximum difference in the p-wave velocities along the x_3 -axis and x_1 or x_2 axis was about 20%, it was assumed that the experimental wave speeds may be considered as the approximate p-wave velocities.

The coordinate axes are directions along which exact p-wave velocities would be obtained. Both the body wave and the surface wave measurements furnished information regarding the approximate p-wave velocities in a number of directions relative to the axis of elastic symmetry (x_3 -axis). In addition, an examination of the surface wave records indicated that the Rayleigh wave velocity was approximately 65% of the corresponding p-wave speed in any given direction. Since the Rayleigh wave speed differs but little from the shear wave speed, it was assumed that the latter also bears approximately the same relationship to the p-wave velocity along any particular direction (see VII.8(V)).

VII.4 Determination of c_{11} and c_{33} from p-Wave Tests⁽⁶⁾.

The constants c_{11} and c_{33} are each associated with the p-wave speeds along the AES and in the isotropic plane normal to this axis. The fact that these two extremal p-wave speeds are each associated with a distinct elastic constant may be seen by putting $n = 0$ and $n = 1$ in Eq. (C-10).

$$n = 0 : \rho v^2 = c_{11} \quad (C-11)$$

$$n = 1 : \rho v^2 = c_{33} \quad (C-12)$$

This will not occur in Eq. (C-7) because the first factor is associated with a true transverse displacement. Thus, c_{11} and c_{33} were obtained directly from the measured p-wave speeds. The directions of the AES (x_3) and the normal to the AES (either x_1 or x_2) exhibited purely longitudinal wave velocities of 162,000 in/sec and 210,000 in/sec, respectively. Hence the elastic constants c_{11} and c_{33} were found to be 6.5×10^6 and 12.0×10^6 psi.

The density of Yule marble was determined by measuring the dimensions of conveniently shaped samples of the material (the samples were taken from the slab and not from the two blocks but this inconsistency was ignored) and weighing the samples on a precision balance. It is to be noted that the values of the two constants lie in between the corresponding values cited previously. A total of 40 values of the p-wave speeds were obtained for as many independent directions with respect to the AES.

VII.5 Requirements Imposed by the Positive Definite Form of the Strain Energy.

In Ref. (13), it was shown that the necessary and sufficient condition for the quadratic form of the strain energy to be positive definite for the particular case of a transversely isotropic material implies that

$$\begin{aligned} c_{11} > 0, c_{33} > 0, c_{44} > 0, c_{11} > c_{12} \\ \frac{1}{2}(c_{11} + c_{12}) \cdot c_{33} > c_{13}^2, c_{11} \cdot c_{33} > c_{13}^2 \end{aligned} \quad (C-13)$$

It is to be noted that there is no restriction that c_{12} and c_{13} should be positive.

VII.6 Formulation for Determining the Elastic Constants.

The objective function formed as a sum of the squared deviations

$$R = \sum_{i=1}^m (H_i - \frac{1}{2}(1-n_i^2)c)^2 \{H_i^2 - [(1-n_i^2)a + n_i^2h]H_i + n_i^2(1-n_i^2)(ah-d^2)\}^2$$

where $H_i = \rho v_i^2 - c_{44}$ (C-14)

The elastic constants were chosen as the variables x_k ($k=1, \dots, 5$) with $x_1 = c_{11}$, $x_2 = c_{33}$, $x_3 = c_{44}$, $x_4 = c_{12}$ and $x_5 = c_{13}$; a sixth variable x_6 was chosen to represent the ratio of an approximate p-wave velocity to an approximate shear wave velocity in the same given direction. The minimization of the objective function $R(x_j)$, $j=1, \dots, 6$ subject to the constraints specified by inequalities (C-13) was expected to yield the optimum values of x_j . Since previously measured values of the elastic constants as well as the two values of c_{11} and c_{33} obtained from the present tests were available, the inequality constraints were reduced to a set of equality constraints, the extreme admissible values still satisfying the inequalities (C-13). The set of initial values required were then chosen so as to include the two values of c_{11} and c_{33} already established and other data for c_{12} , c_{13} and c_{44} lying between the corresponding values of the two sets of constants obtained previously.

VII.7 Minimization Technique.

The minimization of the objective function was performed by means of a computer program that was divided into two parts. The first part served to control the program, to compute the velocities and to calculate the objective function using the initial values of the variables as specified above. The second part involved the minimization using a standard library subroutine, CLIMBS. The latter was constructed based on a method devised in Ref.(12). The main program calls the minimization subroutine CLIMBS which in turn repeatedly calls the

subroutine to compute the value of the objective function for any values for the x_j . The search for optimal x_j was terminated by a predetermined convergence criterion. The minimization of the objective function was performed in a number of steps. At each step the initial values and constraints were appropriately altered. The various steps were chosen to put the emphasis of optimization on particular variables representing the elastic constants at each stage by either suppressing some variables or constraining them over a limited range.

Step 1: Since there was no restriction on the sign of c_{12} and c_{13} , these constants were allowed to take on negative values. The variable x_6 was omitted and the function R was minimized over the whole range of observations. The initial values of x_i ($i=1, \dots, 5$) were chosen to satisfy the reduced equality constraints. The upper and lower limits of the variables were chosen to include the previously obtained values for the elastic constants.

Step 2: The same procedure was used as in Step 1 except that c_{12} and c_{13} were also constrained to be positive.

Step 3: The first factor of Eq. (C-7) was removed from the velocity equation since it represents a truly transverse displacement and the approximate p-wave speeds were again employed to minimize the modified objective function

$$R_1 = \sum_{i=1}^m \{H_i^2 - [(1-n_i^2)a + n_i^2 \cdot h]H_i + n_i^2(1-n_i^2)(ah-d^2)\}^2 \quad (C-15)$$

Step 4: The factor x_6 was introduced as a constant by multiplying all the velocities by 0.65 and using these approximate shear wave velocities instead of the approximate p-wave velocities. The objective function was taken as R .

Step 5: The factor x_6 was introduced as a variable with upper and lower limits of 0.7 and 0.6 and the objective was again taken as R .

Step 6: The factor x_6 was introduced as a variable with the same limits as above but this time the objective function was R_1 .

The various initial values, constraints on the variables and the final values are listed in Table 8 where each step of the minimization procedure is identified. The final values of the constants were as follows:

$$\begin{aligned} c_{11} &= 11.22 \times 10^6 \text{ psi} \\ c_{33} &= 7.25 \times 10^6 \text{ psi} \\ c_{44} &= 3.33 \times 10^6 \text{ psi} \\ c_{12} &= 3.82 \times 10^6 \text{ psi} \\ c_{13} &= 2.52 \times 10^6 \text{ psi} \end{aligned} \quad (C-16)$$

VII.8 Remarks.

The method of estimating the dynamic elastic constants, employed to establish values of c_{12} , c_{13} and c_{44} makes certain approximations regarding the p-wave velocities in different directions. However, it has furnished some interesting information in the course of the minimization procedure which appears to substantiate that the values were representative of the material, namely,

- (i) The values of c_{11} and c_{33} remained reasonably constant at each step.
- (ii) The introduction of the variable x_6 established with certainty that c_{12} and c_{13} were positive.
- (iii) The final results were in the range of values obtained previously as listed in Table 4, Appendix D.
- (iv) A reasonable value of c_{12} was obtained by introducing the shear factor x_6 . It was noted in Ref. (9) that the same factor could not be obtained from the p-wave tests using Eq. (C-7).

Section VIIIDiscussionVIII.1 General Outline

In this section the following matters are considered:

- (i) A discussion of the information obtained from the experimental results;
- (ii) The comparison of the experimental results with the corresponding theoretical predictions; and
- (iii) A critical discussion of the method of detecting and recording wave propagation phenomena with embedded transducers in the light of the above comparison.

With the input crystals and an embedded transducer, the detection and recording of wave propagation processes in a rock model furnished the following information:

- (a) The history of the stress component in the direction of the transducer bar which coincided with the crystal axis in compression mode.
- (b) The wave arrival time, determined directly from the time difference of the two records obtained on a dual-beam oscilloscope by simultaneous triggering of the two traces as shown, for example, in Fig. 10.
- (c) The input pulse or the force history of the impulse on the free surface of the model half-space which could be used directly to obtain the corresponding theoretical results with the aid of the computer programs of Appendices A and B.

VIII.2 Body Wave Measurements in the Isotropic Model.(1) Experimental Results.

Records were obtained from three of the four transducers embedded in the limestone block. With reference to Fig. 8, body wave measurements were recorded

with transducers 2, 3 and 4. Transducer 4 detected σ_{zz} and transducers 2 and 3 detected σ_{xx} . Fig. 1 of the main report and Figs. 10 to 12 show the input and output measurements; the corresponding impact locations and the stresses measured are also indicated. The data were not extensive since the main objective of the experiments was primarily to verify the calibration procedure of the transducers. It is recalled, the latter was established by comparing the external calibration constant with the in situ calibration in rock bars, and the stress factors of the transducers listed in Table 3 were based on this correlation. Hence a comparison of the experimental stress-time records with the corresponding theoretical results was mainly expected to substantiate generally the reliability of the experimental techniques as well as the validity of the theoretical solutions.

(ii) Comparison with Theoretical Results.

Both the finite element technique and the integral transform analysis were chosen for comparison with the experimental data from the limestone block; however, the integral transform approach could not be applied directly to the case of an isotropic solid as the solution became degenerate. Consequently, a small degree of transverse isotropy was introduced by the judicious choice of the dynamic elastic constants so that the analytical solution could virtually be considered as the response of an isotropic half-space subjected to normal point force history of arbitrary shape. Accordingly, the dynamic elastic properties were chosen to correspond to those of the Bedford limestone block used in the experiments and are listed in Section VI.4. The experimental input pulse was digitized and a table of values of the impulsive force on the free surface at each time step was obtained. A step of $1/4 \mu\text{sec}$ was chosen for this process that was considered optimal for accuracy of the numerical computations and the computer time required. With this input pulse, the stress histories and arrival times were obtained corresponding to those measured by the embedded transducers. In Fig. 1

of the main report and Fig. 11 results from the integral transform solution are superposed on the experimental stress histories.

The finite element computer program was devised to solve a similar boundary value problem. However, here the isotropic and anisotropic media could be considered independently. Thus, using the dynamic elastic properties of limestone cited above and the experimental input pulse in the form of tabulated values at convenient time intervals, the stress histories and wave arrival times corresponding to the experimental measurements were obtained. These finite element predictions are superposed on the previous results in Fig. 1 of the main report and Figs. 10 to 12. The previously-stated conclusion that the experimental techniques employed provide a reliable means of detecting and recording body waves inside a rock is thus substantiated by the satisfactory agreement of both the stress levels and the arrival times.

Comments on the Wave Propagation Phenomena.

Even though the data obtained on the limestone block were not extensive, the results reveal a number of ideas associated with the theory of body wave propagation in an isotropic half-space.

(a) p-Wave Velocity.

The wave velocity calculated on the basis of the first signal arrival corresponds to the p-wave speed in an isotropic medium since it is the fastest of the two possible wave speeds; yielding an average value of 170,000 in/sec. This compares well to that obtained from the material constants used in the theoretical solutions, namely, 174,000 in/sec and the corresponding rod wave velocity of 141,400 in/sec⁽¹⁴⁾.

(b) Precursor to the Main Pulse.

In the stress history depicted in Fig. 1 of the main text, the precursor to the major effect of the pulse also corresponds to the first arrival of the p-wave.

It clearly shows a shape similar to that predicted by theory. The second peak is mainly the effect of the shear wave. A comparison of the arrival times of the two pulses gives a reasonable estimate of the ratio of the shear wave speed to the p-wave speed namely about 0.65.

(c) Attenuation of the Pulse.

The σ_{xx} stress histories shown in Figs. 11 and 12 indicate the degree of attenuation along a 45° ray at distances of 2.83" and 4.3" from the impact location. Both the theoretical and the experimental results showed that the attenuation in the tensile stress was significantly less than the corresponding attenuation in the compressive stresses which appears to be due to the dispersion of the pulse. The peak compressive stress in the x-direction (σ_{xx} in Fig. 9) decreased as $r^{-1.5}$ where r was the distance of the observation point from the impact location. The peak tensile stress in the same direction did not attenuate according to the same law.

(d) First Passage of the Pulse and Reflections from the Boundaries.

The first passage of the pulse was recorded for a sufficient length of time before the reflections from the boundaries distorted the data. In Fig. 1 of the main text it is estimated that the reflections arrived at about 65 μ sec after the initiation of the pulse on the free surface which means that the theoretical solution was not compared with the experimental stress history for the complete passage of the first pulse. This was necessarily so in the case of the finite element method because of the finite size of the block chosen to represent the isotropic half-space as well as the computation time required for obtaining the transient. However, the integral transform solution predicted a more rapid decay of the transient. This indicates that there might have been some reflections at the rock/transducer bar interfaces.

The less rapid decay of the measured transient indicates a possible source of errors in the measurements, namely the scattering of the wave and the additional dispersion of the pulse due to the presence of the transducers. Since the pulse length employed for the input, about 40 μ sec, was long compared to the discontinuities introduced by the embedment of transducers, it was expected that these errors would be small; of the same order as encountered in the one-dimensional experiments of II.7. Both in Fig. 1 of the main text and Fig. 10, the large oscillations immediately after the first cycle were not caused by reflections from the boundaries of the block, the first arrival of which is indicated in the respective figures. The theoretical solution by the finite element method does predict such oscillations of the stress even though the integral transform method predicts a more rapid decay. The reason for this discrepancy is not immediately obvious. It may be due to the fact that the integral transform analysis assumed a concentrated load while the actual load was distributed on the area of the input crystal; the latter type of loading would create a more complicated dispersion of the pulse. It is noted that the finite element method invariably assumes some smearing of the input impulse. In any case, the reflections from the boundaries of the block arrived before the measured transient decayed completely.

VIII.3 Body Wave Measurements in the Anisotropic Model.

(1) Experimental Results.

The information obtained from the experimental results was similar to that described in VIII.2. The size of the block and the length of the input pulse insured the observation of the first passage of the pulse for sufficient lengths of time at various locations. The experimental data with P_0 as the impact location, Fig. 15, corresponding to observation points about 5 to $5\frac{1}{2}$ inches from the impact position were termed far field response. The data obtained with

P_1, P_2, P_3, P_4 as the impact locations, Fig. 15, from the transducers which were about 1.8 inches and 3.4 inches from these locations were chosen to represent the near field response. These data were compared with corresponding theoretical predictions of arrival times and stress histories.

In order to discern the information obtained experimentally, the stress histories depicted in Figs. 29, 30 and 31 are described in some detail. These three transient normal stress components were obtained for the same impact. The input pulse was also recorded simultaneously as shown in the respective figures. With reference to Fig. 19, transducer Y_4 detected σ_{yy} and with reference to Fig. 21, transducer Z_4 detected σ_{zz} . These two stress histories are shown in Fig. 30 and Fig. 31 respectively. In view of the symmetry of the block these two records give the stress histories at the same location, namely $(5", \frac{\pi}{12}, 1\frac{1}{2}")$ corresponding to the cylindrical coordinate system shown in Fig. 14. Along with these two stress histories a σ_{xx} record was obtained at a second location, $(5", \frac{3\pi}{4}, 1\frac{1}{2}")$ as shown in Fig. 29. The corresponding stress transient was of the shape and of the same order of magnitude as the σ_{yy} stress of Fig. 30. This is another indication of the previously mentioned finding that the new set of dynamic elastic constants obtained in Section VII did not predict significant differences in the slowness surface from the corresponding isotropic case. The other stress transients described in Table 6 show the same pattern in the similarity between the σ_{yy} stress at (R, θ_1, Z) and σ_{xx} stress at (R, θ_2, Z) .

Other experimental results yielded arrival times and stress histories which were not all compared with corresponding theoretical results. However, all arrival times obtained were utilized to determine approximate p-wave speeds in various directions and, in conjunction with similar results obtained from surface wave investigation, were used in devising a procedure for estimating the dynamic elastic stiffness matrix of the material as described in Section VII. In particular, the

p-wave speed along the AES was obtained as 162,000 in/sec and the p-wave speed along the AES determined in Ref. (2) was obtained as 171,000 in/sec. This additional evidence, namely the lower p-wave speed along the relocated AES, Fig. 14, reasonably confirmed its actual direction.

The mathematical theory of propagation of elastic waves in a transversely isotropic medium, with the particular dynamic elastic constants of Yule marble, predicts that the p-wave speed along the AES is the lowest while that normal to the AES is the highest. An average value obtained for the latter was 210,000 in/sec which was computed from both the body wave and the surface wave measurements. In the former, a ray normal to the free surface with a transducer located in line with the impact position was utilized whereas in the latter case, a radial stress measurement along the axis of foliation plane was utilized. The fact that such data as well as those along the AES yield the exact p-wave speeds has also been used in Ref. (9). However, since the present experimental investigation utilized a more reliable method of determining wave arrival times, it is believed that the previously obtained values of 203,000 in/sec and 237,000 in/sec⁽⁹⁾ are too high; compared with the speeds of 162,000 in/sec and 210,000 in/sec obtained in the present work. This is attributed to the possible specific experimental error in Ref. (9) caused by the late triggering of the oscilloscope by the output from an accelerometer placed near the impact point and the estimation of the wave arrival time as that corresponding to the length of trace before the first arrival of the wave at the observation point as recorded on the oscillogram.

(11) Comparison with Theoretical Results.

(a) Near Field Response.

A typical comparison of the near field response with the corresponding theoretical results is depicted in Fig. 2 of the main report, which shows that the stresses obtained by the integral transform analysis were much higher than the corresponding measured stresses and those obtained by the finite element method.

In general, the finite element method predicted stress histories that were in closer agreement with the experimental transients than the integral transform analysis for observation points which were in such close proximity to the impact location. In the finite element method, since the near field experimental data were obtained by using a 1/4" dia. input crystal, the input force was approximated as a uniformly distributed impulse over a circular area of 1/4 in. diameter. Hence, it appears that poorer agreement obtained with the integral transform method was due to the approximation involved in assuming that the response of the block was effectively due to a concentrated time-dependent load; indicating that such an assumption is valid only for observation points which are located at relatively larger distances from the impact position.

Therefore, it was considered inappropriate to compare the experimental data more in detail with the corresponding integral transform results for the near field response of the block and such a comparison was made only for the far field. On the other hand, a meaningful comparison with the finite element method results could be achieved only with the near field data in view of the constraints imposed regarding the size of the block, the size of the mesh, the time interval chosen and the computation time required. Thus, the rest of the comparison of the near field results with the finite element method is depicted in Figs. 24 to 28. In Figs. 24 to 26, the transducers were located about 1.8" from the impact position as well as in Fig. 2 of the main text discussed above. In figs. 27 and 28 the transducers were situated in a ray normal to the free surface in line with, and at a distance of 3-3/8" from the impact location. For such locations, i.e. for observation points vertically below the normal load on the horizontal free surface, the finite element method solution was closer in agreement with the experiment in the case of a stress component normal to the z-direction, Fig. 28, than in the case of a stress component in the z-direction, Fig. 27. This discrepancy is consistent

with similar disagreement between the integral transform analysis and experiment discussed below in relation to the far field response of the block.

(b) Far Field Response.

The comparison of the experimental data was effected only with the corresponding integral transform results as depicted in Figs. 29 to 35, reasonable agreement prevails for the stress levels. However, the exact shape of the predicted transient appears to be susceptible to numerical errors especially in the digitization of the experimentally-determined input pulse and subsequent numerical differentiation. In most cases, the input pulse was somewhat asymmetric and the disagreement between experiment and theory appeared to be more marked where such asymmetry was more pronounced. The actual input frequently closely resembled the shape of a single sine-squared pulse with a duration twice that of the rise time; consequently, such a boundary condition with an amplitude equal to the measured peak force was also used in the stress computation. Another alternative used for the numerical input consisted of a symmetrical loading with the rising portion mirrored about the peak force. A comparison of a number of stress histories with the corresponding theoretical results using the three possible input shapes showed that except for some improvement in isolated cases with the last input pulse shape, there was little difference in the agreement with the experimental results. Hence, the actual pulse has been used for comparison in the sequel.

As in the case of the limestone block, the analysis predicted a more rapid decay of the pulse than was observed. Since the first passage of the pulse could be recorded for sufficient lengths of time without distortion due to reflections from the boundaries of the block, the oscillations observed in the transient were again in disagreement with the integral transform predictions as shown in Fig. 30. In Fig. 3 of the main text, a comparison of the far field response with corresponding predictions of both the theoretical techniques was shown to

illustrate the comparison with the integral transform analysis as described above as well as the inability to obtain satisfactory results with the finite element method at such a distant observation point for the reasons stated in VIII.3 (ii)(a).

The comparison of the experimental results with the integral transform analysis was not entirely conclusive regarding the accuracy of the measurements, especially those involving the σ_{zz} stress history as shown in Fig. 34. Here, the second peak in the measured transient appears to be due to the reflection of the pulse as it propagated through the embedded transducer by virtue of an impedance mismatch. Similar anomaly was observed in the comparison of the σ_{zz} transient with the analysis at other locations such as shown in Fig. 35.

VIII.4 Surface Wave Propagation Measurements in the Anisotropic Model.

(i) Experimental Results.

Since the transducers were approximately 5" away from the impact location, the measured transients could again be compared only with the corresponding integral transform results. A total of 6 complete sets of data were obtained, each set consisting of the radial and circumferential stress histories, effectively at the same location relative to the impact location. Out of the 7 pairs of transducers, stress histories were recorded with 6 pairs; only the circumferential stress history was recorded at location θ_6 .

At any location such as (R_3, θ_3) , Fig. 22, the radial stress transient distinctly exhibits the p-wave and Rayleigh wave effects as shown in Fig. 4 of the main report. The shear wave effect was not clearly distinguishable. The tangential stress histories as depicted for example in Fig. 37 did not record the effect of the p-wave. The tangential stress was of the same order of magnitude at (R_1, θ_1) and (R_3, θ_3) but was negligibly small at (R_7, θ_7) (foliation plane). This latter effect appears to be due to the absence of quasi-Rayleigh effects at a location such as (R_7, θ_7) , the quasi-Rayleigh wave being one which exhibits a

transverse component of motion in the plane of the free surface. Such a component seems to exist up to 15° from the direction of the foliation plane. These stress histories were obtained at about $1/16$ " below the free surface and even if the attenuation of the Rayleigh wave were large, these stress components may be considered as representative of the surface wave effects.

(ii) Comparison with Theoretical Results.

The experimental results were compared with corresponding theoretical predictions of the integral transform method as shown in Fig. 4 of the main report and Figs. 36 and 37. The first two diagrams show the comparison of two typical radial stress histories while the third shows the comparison of a tangential stress history. The good agreement indicates that the theoretical model agrees remarkably well with experiment. However, the integral transform method did not predict the diminution of the transverse effect due to the Rayleigh wave as the direction approaches the direction of the foliation plane. It is not clear whether the failure of the analysis to predict such a phenomenon was due to numerical errors and also whether the observed absence of the quasi-Rayleigh waves may have been due to experimental vagaries. This discrepancy was left unresolved and is not shown in the figures.

VIII.5 Determination of Dynamic Elastic Constants from Body Wave and Surface Wave Measurements.

The values determined in Section VII lie between those obtained previously (Table 4, Appendix D). Thus, it appears that such a method may be applied in general to other rock materials. The actual values may be improved by adding other refinements to the technique such as weighing the various data obtained experimentally and a more general program may be written. Some other features could be built into the program such as automatically reverting from one function to

another, and approximation procedures other than least square methods may be used for part or all of the functions which may be also changed as required as the minimization progresses.

It is noted that it is possible to obtain the dynamic elastic stiffness constants c_{11} , c_{33} , c_{44} and c_{13} from the phase velocity equation cited in Section VII directly using the approximate p-wave speeds obtained for a number of directions. Such a procedure was adopted in Ref. (9). However, the fifth constant c_{12} cannot be obtained by using p-wave tests⁽⁹⁾. The same procedure failed to give satisfactory results in the course of the present investigation and hence the method of Section VII was devised.

VIII.6 Stress Wave Measurements with Embedded Transducers.

The results show that the PZT ceramic crystal transducers are suitable for detecting and recording body wave pulse propagation in rocks. The choice of magnesium as the material for the transducer bar was originally made on the basis of average value of the acoustic impedance of Yule marble. However, it appears that the anisotropy of the Yule marble block employed was such that the use of another material such as aluminum would have been more appropriate in some directions such as the z-axis in Fig. 14. The embedding technique was quite effective even if there is some uncertainty about entrapped air bubbles between the transducer bar and the rock. To achieve intimate contact between the crystal unit and the rock and in order that the calibration should apply and that the same calibration may be used for all transducers to obtain internal stress uniformity of embedment is required, with crystal assembly unit completely embedded in the rock with an epoxy and aluminum oxide mixture surrounding the unit.

The voltage amplification was employed for recording the embedded transducer response since the initial testing of the PZT crystals by this method in a split Hopkinson bar gave good correspondence of the pulse shapes between the crystal

and the strain gage records. The general techniques of the experimental measurements provided a reliable means of detecting and recording waves in the interior and near the surface of the rock.

References

- (1) Katona, M., "Wave Propagation with FEAP-72", Berkeley, University of California, 1972.
- (2) Ricketts, T. E., "Sphere Impact on an Anisotropic Half-Space", Ph.D. Dissertation, University of California, Berkeley, 1970.
- (3) Dove, R. C. and Adams, Paul H., Experimental Stress Analysis and Motion Measurement, Columbus Ohio, Charles E. Merrill Books, Inc., 1964.
- (4) Goldsmith, W. and Sackman, J. L., "Wave Propagation in Anisotropic Rocks", Annual Technical Report No. 1, Contract No. H0210021, ARPA Order No. 1579, Amend. 2, Program Code 1F10, University of California, Berkeley, 1972.
- (5) Mason, Warren P., Physical Acoustics, Principles and Methods, Volume 1-Part A, New York, Academic Press, 1964.
- (6) Kenner, V. H. and Goldsmith, W., "One-Dimensional Wave Propagation Through a Short Discontinuity", J. Acoust. Soc. Amer., Vol. 45, No. 1, 1969, p. 115.
- (7) Timoshenko, S. and Young, D. H., "Elements of Strength of Materials", Fourth Edition, Princeton, New Jersey, D. Van Nostrand Company, Inc., 1962.
- (8) Goldsmith, W. and Sackman, J. L., "Wave Propagation in Anisotropic Rocks", Semiannual Technical Report No. 1, Contract No. H0210021, ARPA Order No. 1579, Amend. 3, Program Code 62701D, University of California, Berkeley, 1972.
- (9) Ricketts, T. E. and Goldsmith, W., "Wave Propagation in an Anisotropic Half-Space", Int. J. Rock Mech. Min. Sci., v. 9, 1972, p. 493.
- (10) Krech, W., Henderson, F. A. and Hjelmstead, K., "A Standard Rock Suite for Rapid Excavation Research", U.S. Bureau of Mines, Twin Cities Mining Research Center, Minneapolis, Minnesota, 1972.
- (11) Musgrave, M. J. P., Crystal Acoustics, San Francisco, Holden Day, 1970.
- (12) Rosenbrock, H. H., "An Automatic Method of Finding the Greatest or Least Value of a Function". Computer Journal, Vol. 3, 1960, pp. 175-184.
- (13) Das Gupta, Sushil Chandra, "Propagation of Rayleigh Waves in Transversely Isotropic Medium in Three Dimensions", Transactions, American Geophysical Union, Vol. 36, No. 4, 1955.
- (14) Ricketts, T. E. and Goldsmith, W., "Dynamic Properties of Rocks and Composite Structural Materials", Int. J. Rock Mech. Min. Sci., Vol. 7, pp. 315-335, 1970.
- (15) Espe, W., Materials of High Vacuum Technology. Pergamon Press, 1966.

- (16) Lion, K. S., Instrumentation in Scientific Research; Electrical Input Transducers, New York, McGraw-Hill, 1959.

PIEZO-ELECTRIC MATERIAL	NONZERO PIEZOELECTRIC CONSTANTS AND RELATIONS	PIEZO-ELECTRIC CONSTANT FOR COMPRESSION MODE			DIMENSIONS OF CRYSTALS USED	SUPPLIER OF CRYSTALS	WHERE USED IN THE PROJECT
		DESIGNATION	PUBLISHED VALUE pc/lb.	EXPERIMENTAL VALUE pc/lb.			
QUARTZ	$d_{11}, d_{12}, d_{14}, d_{25}, d_{26}, d_{12} = -d_{11}, d_{25} = -d_{14}, d_{26} = 2d_{11}$	d_{11}	10.01 [16]	10.2 [4]	1/8" dia. x 0.031" thick	X-Tron Electronics Hayward, California	Rock Bars
CERAMIC PZT-5H	$d_{33}, d_{31}, d_{32}, d_{15}, d_{24}$	d_{33}	2638 [5]	†	1/8" dia. x 0.031" thick	Valpey-Fischer Corp. Holliston, Mass.	Limestone Block
CERAMIC PZT-5a	$d_{31} = d_{32}, d_{15} = d_{24}$	d_{33}	1650 [5]	†	1/8" dia. x 0.031" thick	Valpey-Fischer Corp. Holliston, Mass.	Limestone Block
CERAMIC PZT-4		d_{33}	1232 [5]	†	1/16" dia. x 0.020" thick	Int'l. Transducer Corp. Goleta, California	Yule Marble Blocks

† Not needed, in view of the calibration procedure adopted.

TABLE 1: COMPARISON OF PIEZOELECTRIC CONSTANTS OF QUARTZ AND PZT CERAMIC CRYSTALS

Material	Density ρ Lbf./in. ³	Rod Wave Velocity Co in./sec.	Specific Acoustic Impedance ρC_0 Lb.Sec/Ft. ³	Modulus of Elasticity E psi	Reference
Magnesium	0.0628	193,400	54,800	6.32×10^6 Dynamic (Compressive)	Experimental - by determined
Glass	0.108	190,000	91,800	9.0×10^6	[15]
Epoxy	0.05	76,100	16,200	0.7×10^6 Dynamic Compressive	[14]
Aluminum Oxide	~0.133	~400,000	~240,000	$\sim 50 \times 10^6$	[15]
Limestone	0.0805	141,400	51,100	4.3×10^6 to 6.1×10^6	[14]
Yule Marble	0.096	~110,000 (average)	~50,000 (average)	~3.2 (average)	[2]

TABLE 2: COMPARISON OF THE VALUES OF ACOUSTIC
IMPEDANCE OF THE MATERIALS USED IN
THE EXPERIMENTAL INVESTIGATION.

RUN NO.	IMPACT LOCATION FIG. 8	INPUT SCALE FACTOR lb/div.	OUTPUT									
			STATION NO. FIG. 8	CRYSTAL USED 1/8" DIA.	EXTERNAL CALIBRA- TION FACTOR K	TOTAL CRY- STAL CIR- CUIT CAP- ACITANCE	STRESS FACTOR psi/volt C/K-256/n	STRESS MEASURED	FIG. NO.	GAIN mv/div	STRESS/DIV psi	
3	P ₁	50	4	PZT-5H	689	330	39.1	σ_{zz}	10	200	7.81	
11	P ₂	50	2	PZT-5a	305	353	94.4	σ_{xx}	11	50	4.72	
			3	PZT-5H	971	365	30.6	σ_{xx}	12	50	1.53	
			4	PZT-5H	689	330	39.1	σ_{zz}	FIG 1 MAIN REPORT	100	3.90	

TABLE 3: LINSTONE BLOCK MEASUREMENTS: TRANSDUCERS
EMBEDDED WITH EPOXY/ALUMINUM OXIDE MIXTURE.

TRANSDUCER LOCATION	COORDINATES (R, θ , Z) (Fig. 14)	EXTERNAL CALIBRATION FACTOR K	TOTAL TRANSDUCER CIRCUIT C CAPACITANCE C-pF	STRESS FACTOR $\frac{C \cdot 256}{K \cdot \pi} \cdot 4$
X_1	(5", $\pi/2$, $1\frac{1}{2}$ ")	110	966	2850
Y_1	(5", $\pi/3$, $1\frac{1}{2}$ ")	81	1097	4421
$^\dagger Z_1$	(5", $4\pi/3$, $1\frac{1}{2}$ ")	981	652	54.17
X_2	(4", $\pi/2$, $3\frac{3}{8}$ ")	82.45	1165	4605
Y_2	(4", $\pi/3$, $3\frac{3}{8}$ ")	149	777	1794
Z_2	(4", $4\pi/3$, $3\frac{3}{8}$ ")	158	718	962
X_3	(1 $\frac{3}{4}$ ", $\pi/4$, 5")	94.7	977	3364
Y_3	(1 $\frac{3}{4}$ ", $\pi/3$, 5")	314.8	847	845
Z_3	(1 $\frac{3}{4}$ ", $4\pi/3$, 5")	243.2	557	747
X_4	(5", $3\pi/4$, $1\frac{1}{2}$ ")	251.7	446	578
Y_4	(5", $\pi/12$, $1\frac{1}{2}$ ")	376.9	677	586
Z_4	(5", $13\pi/12$, $1\frac{1}{2}$ ")	170.6	907	1734
Y_5	(4", $\pi/2$, $3\frac{3}{8}$ ")	169.46	1287	2475
Z_5	(4", $13\pi/12$, $3\frac{3}{8}$ ")	134.3	963	2337
X_6	(1 $\frac{3}{4}$ ", $3\pi/4$, 5")	149.4	959	2092
Y_6	(1 $\frac{3}{4}$ ", $\pi/12$, 5")	177	1107	2038
Z_6	(1 $\frac{3}{4}$ ", $13\pi/12$, 5")	118.1	1107	3055

† 3/16" Dia. \therefore S.F.: $C/K \times 256/\pi$

TABLE 4. EXTERNAL CALIBRATION FACTORS
AND STRESS FACTORS FOR TRANSDUCERS USED
IN YULE MARBLE BODY WAVE MEASUREMENTS.

Run No.	Impact Location Fig. 15	Input Scale Factor Lb/div.	Output				
			Observation Point	Fig. No.	Stress Measured	Gain mv/div	Stress/div. psi.
34	P ₁	100	Z ₁	24	σ_{ZZ}	0.2 V	10.84
			Z ₂	27	σ_{ZZ}	20	19.25
			Z ₃	†	σ_{ZZ}	-	-
41	P ₂	200	Y ₄	FIG 2 MAIN REPORT	σ_{YY}	0.1	58.60
45	P ₃	200	Y ₁	25	σ_{YY}	10	-44.21
			Y ₂	28	σ_{YY}	10	16.13
55	P ₄	200	Z ₄	26	σ_{ZZ}	50	86.7

† FIG. 3 MAIN REPORT - FAR FIELD.

TABLE 5(a) BODY WAVE MEASUREMENTS
YULE MARBLE BLOCK 1 -
NEAR FIELD.

RUN NO.	IMPACT LOCATION FIG. 15	INPUT SCALE FACTOR Lb/div.	OUTPUT				
			OBSERVATION POINT	FIG. NO.	STRESS MEASURED	GAIN MV/div	STRESS/div. psi
3	P _o	50	X ₁	--	σ_{XX}	1	2.85
			Y ₁	--	σ_{YY}	0.5	2.21
			Z ₁	--	σ_{ZZ}	20	1.084
7	P _o	50	X ₂	--	σ_{XX}	0.2	0.921
			Y ₂	--	σ_{YY}	0.5	0.897
			Z ₂	--	σ_{ZZ}	1	0.962
10	P _o	50	X ₃	32	σ_{XX}	0.5	1.682
			Y ₃	33	σ_{YY}	5	4.225
			Z ₃	34	σ_{ZZ}	2	1.493
51	P _o	200	X ₄	29	σ_{XX}	10	5.78
			Y ₄	30	σ_{YY}	10	5.86
			Z ₄	31	σ_{ZZ}	5	8.67
16	P _o	50	Y ₅	--	σ_{YY}	0.5	1.238
			Z ₅	--	σ_{ZZ}	1	2.337
18	P _o	50	X ₆	--	σ_{XX}	0.5	1.046
			Y ₆	--	σ_{YY}	2	4.076
			Z ₆	35	σ_{ZZ}	2	6.11

TABLE 5(b) BODY WAVE MEASUREMENTS
YULE MARBLE BLOCK 1 - FAR FIELD.

Transducer Location (Fig. 22)	Coordinates (R, θ , Z) (Fig. 22)	External Calibration Factor K nc/Lb	Total Transducer Circuit Capacitance C-pF	Stress Factor $\frac{C}{K} \cdot \frac{256}{\pi} \cdot .4$
R_1	(5", $\pi/2$, 1/16")	29.05	315	3534
θ_1	(5", $3\pi/2$, 1/16")	39.97	192	1566
R_2	(5", $5\pi/12$, 1/16")	169.5	314	603.8
θ_2	(5", $17\pi/12$, 1/16")	22.14	172	2532
R_3	(5", $\pi/3$, 1/16")	19.44	333	5583
θ_3	(5", $4\pi/3$, 1/16")	58.24	224	1254
R_4	(5", $\pi/4$, 1/16")	53.18	333	2041
θ_4	(5", $3\pi/4$, 1/16")	38.64	199	1679
R_5	(5", $\pi/6$, 1/16")	44.05	320	3590
θ_5	(5", $7\pi/6$, 1/16")	25.84	207	2611
R_6	(5", $\pi/12$, 1/16")	52.95	Did not function	--
θ_6	(5", $13\pi/12$, 1/16")	27.93	155	1809
R_7	(5", 0, 1/16")	84.41	330	1274
θ_7	(5", π , 1/16")	45.69	171	1220

TABLE 6. EXTERNAL CALIBRATION FACTORS AND STRESS FACTORS FOR TRANSDUCERS USED IN SURFACE WAVE MEASUREMENTS.

Run No.	Impact Location Fig. 22	Input Scale Factor Lb/div	Output				
			Observation Point	Fig. No.	Stress Measured	Gain mv/div	Stress/div. psi
3	Center	100	R_1	--	σ_{RR}	2	7.068
			θ_1	--	$\sigma_{\theta\theta}$	1	1.566
6	Center	100	R_2	--	σ_{RR}	20	12.076
			θ_2	--	$\sigma_{\theta\theta}$	1	2.532
7	Center	100	R_3	FIG 4 MAIN REPORT	σ_{RR}	1	5.583
			θ_3	37	$\sigma_{\theta\theta}$	1	1.254
11	Center	100	θ_4	--	$\sigma_{\theta\theta}$	2	3.358
12	Center	100	R_4	--	σ_{RR}	5	10.21
13	Center	100	R_5	--	σ_{RR}	5	17.95
14	Center	100	θ_5	--	$\sigma_{\theta\theta}$	1	2.611
16	Center	100	R_7	--	σ_{RR}	10	12.74
18	Center	100	θ_6	--	$\sigma_{\theta\theta}$	2	3.618
20	Center	50	R_7	36	σ_{RR}	5	6.37
			θ_7	--	$\sigma_{\theta\theta}$	1	1.220

TABLE 7. DETAILS OF INPUT AND OUTPUT FOR
SURFACE WAVE MEASUREMENTS ON YULE MARBLE BLOCK

LIST OF FIGURES

Figure	Page No.
1. Crystal Axes for X-cut Quartz and PZT-Compression Mode	C-69
2. Transducer Employing 3/16" Diameter Magnesium Bar and 1/8" Diameter Crystal	C-70
3. Transducer Employing 1/8" Diameter Magnesium Bar and 1/16" Diameter Crystal	C-71
4. Definition of External Calibration Constant of Transducer	C-72
5. Transducer Calibration Arrangement-Strain Gage Station Before Crystal Unit	C-73
6. Transducer Calibration Arrangement-Strain Gage Station After Crystal Unit and with Loading Bar and Momentum Trap	C-73
7. Experimental Arrangement for In Situ Calibration in Rock Bars	C-74
8. Sketch Showing the Embedded Transducers in Limestone Block	C-75
9. Experimental Arrangement of Impact Test of Limestone Block for Body Wave Measurements	C-76
10-12 Comparison of the Body Wave Measurements on the Limestone Block with Theory (See also Fig. 1 of Main Report)	C-77 C-78 C-79
13. Yule Marble Block for Body Wave Measurements with the Axis of Elastic Symmetry of Ref. (2)	C-80
14. Block of Fig. 13 with Relocated AES	C-80
15. Impact Positions on the Free Surface for Body Wave Measurements	C-81
16-21 Transducer Locations in the Interior of Yule Marble Block	C-82-C-86
22. Transducer Locations for Surface Wave Study	C-87
23. Transducer Configurations for Radial and Circumferential Stress Measurement	C-88

LIST OF FIGURES (Continued)

Figure	Page No.
24-28 Comparison of Near Field Results with Theory (See also Fig. 2 of Main Report)	C-89-C-93
29-35 Comparison of Far Field Results with Theory (See also Fig. 3 of Main Report)	C-94-C-100
36,37 Comparison of Surface Stress Histories with Integral Transform Results (See also Fig. 4 of Main Report)	C-101 C-102

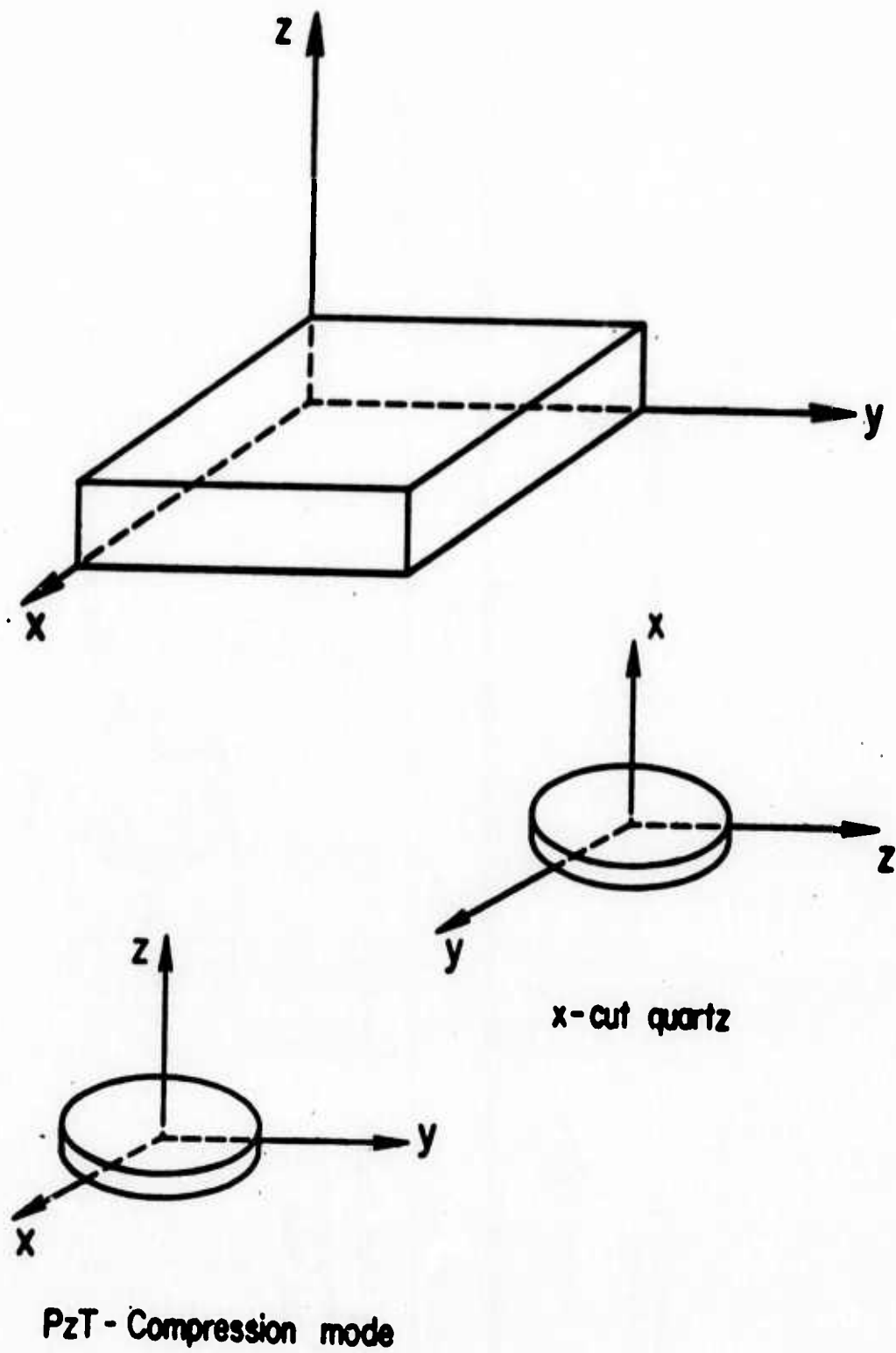


FIG. 1

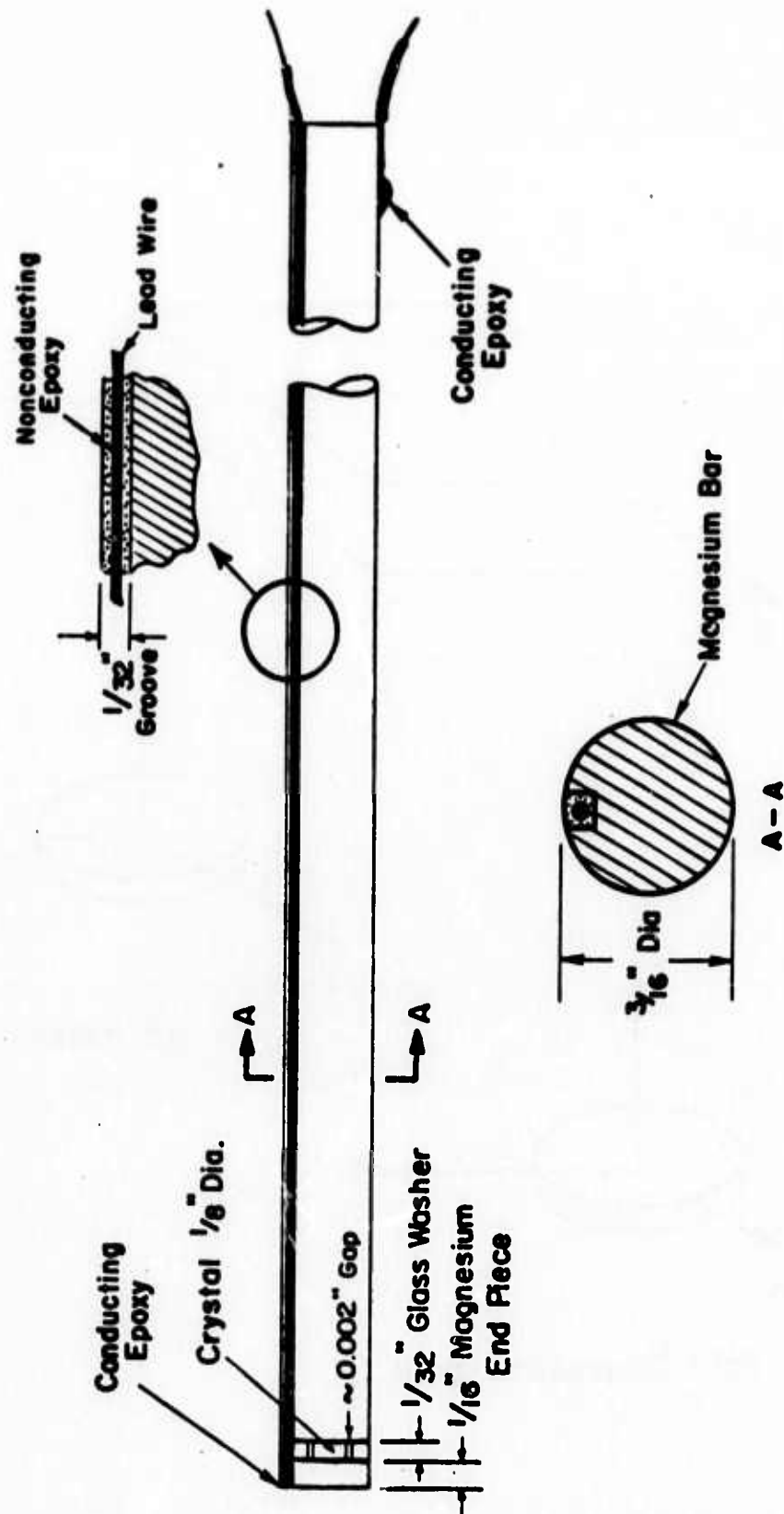


Fig. 2

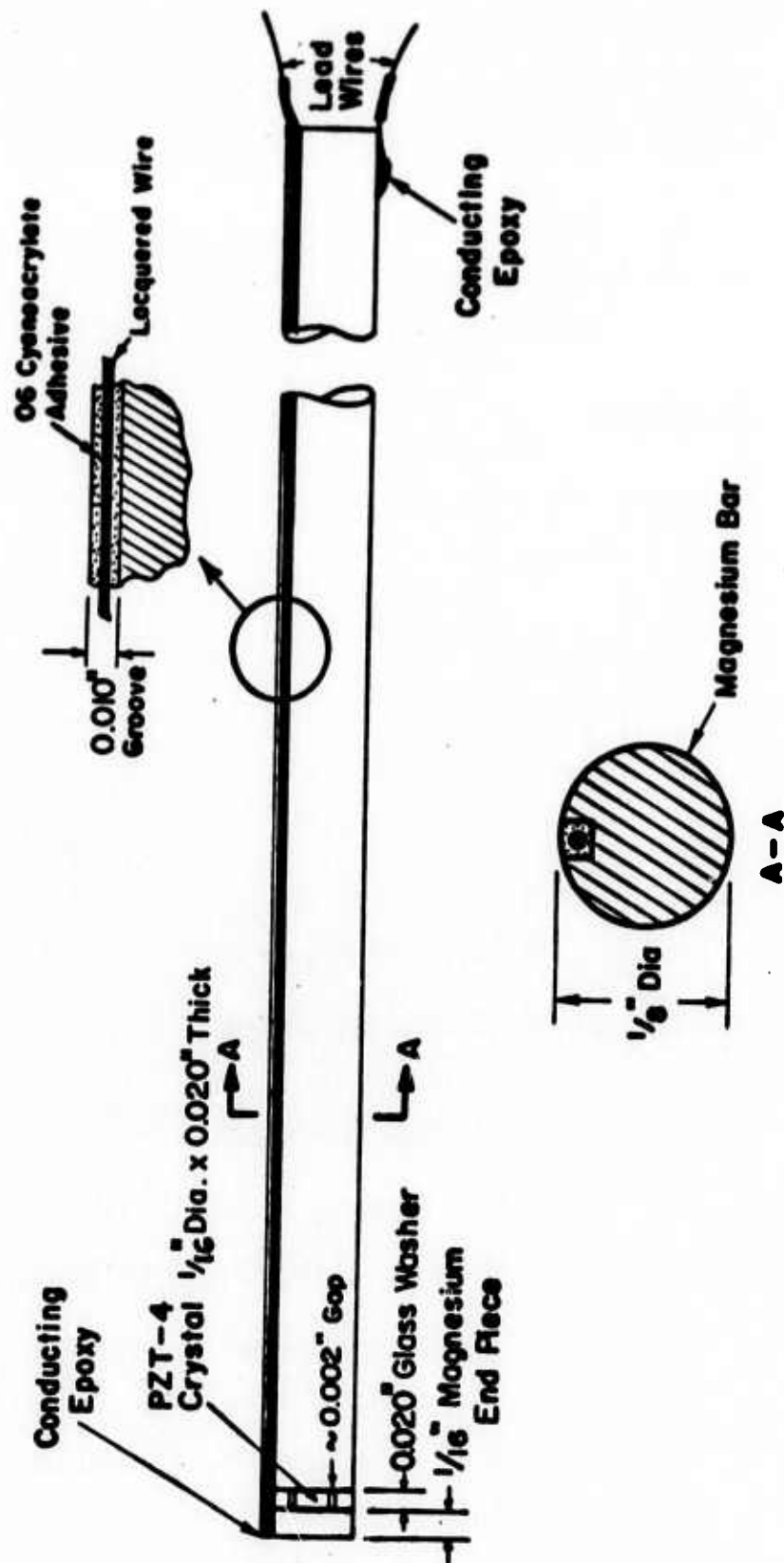
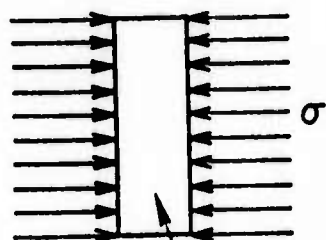


Fig. 3

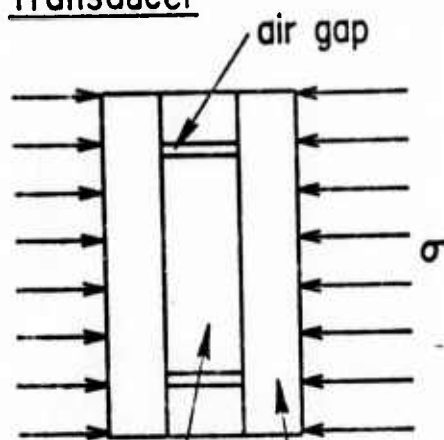
Crystal

area of cross-section of circular crystal a

Compression Mode:

$$Q = \sigma \cdot a \cdot d = F \cdot d = C \cdot V$$

$$\text{Piezoelectric constant } d = \frac{C \cdot V}{F}$$

Transducer

area of cross-section of transducer A

area of cross-section of crystal a

Compression Mode:

$$\text{Force} = \sigma \cdot A = F$$

$$Q = F \cdot K = C \cdot V$$

$$\left. \begin{array}{l} \text{Equivalent} \\ \text{piezoelectric} \\ \text{constant} \end{array} \right\} K = \frac{C \cdot V}{F}$$

- Notes:
- (i) Air gap is neglected
 - (ii) For same C , σ , $K = \frac{a}{A} \cdot d$
if force is distributed uniformly
 - (iii) Since transducer construction is not ideal
 K varies with individual transducer
 - (iv) K is determined by external calibration in
split Hopkinson bar

FIG. 4

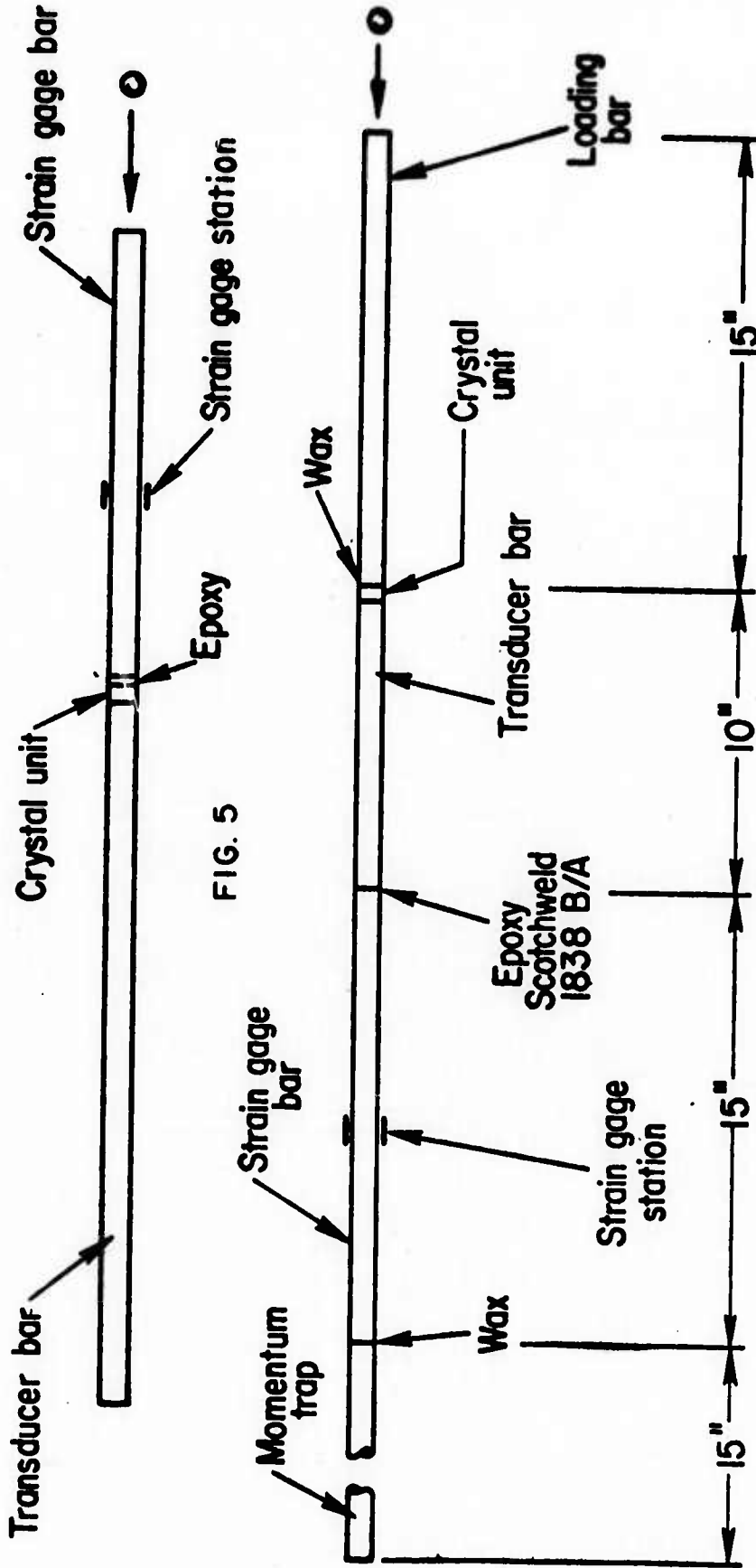


FIG. 5

FIG. 6

Note: All bars were of the same diameter as the transducer bar ($3/16''$ or $1/8''$)

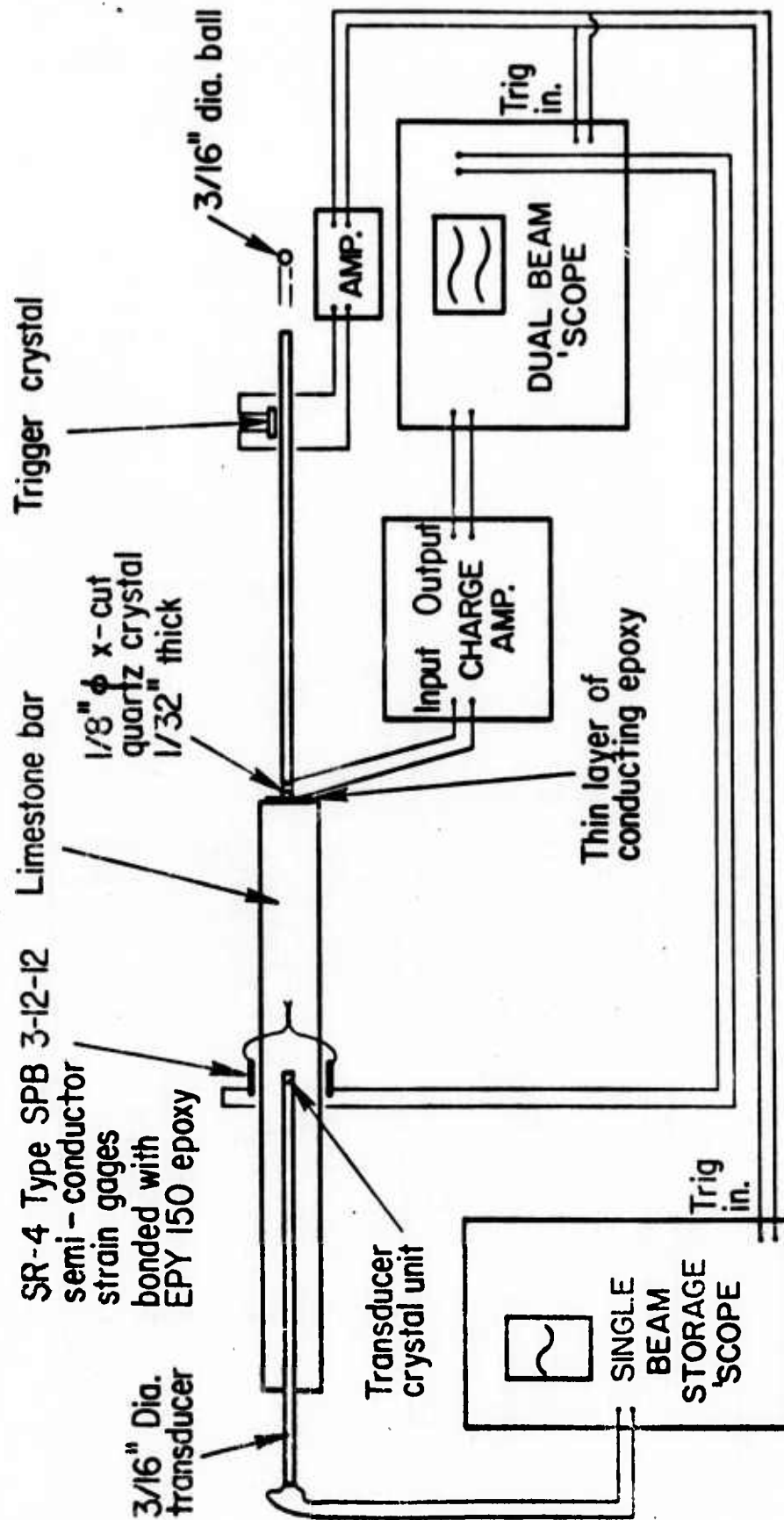


FIG. 7

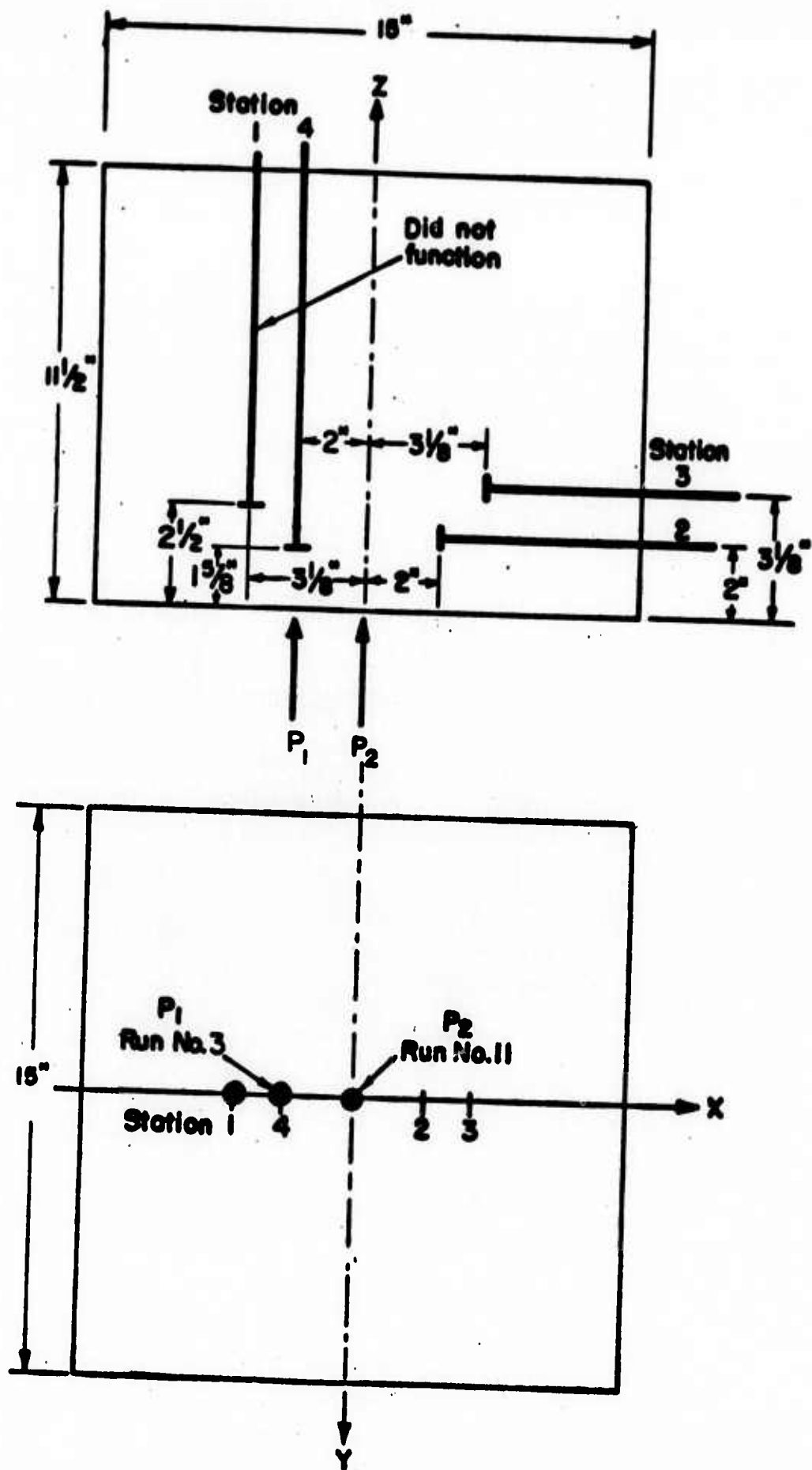


Fig. 8

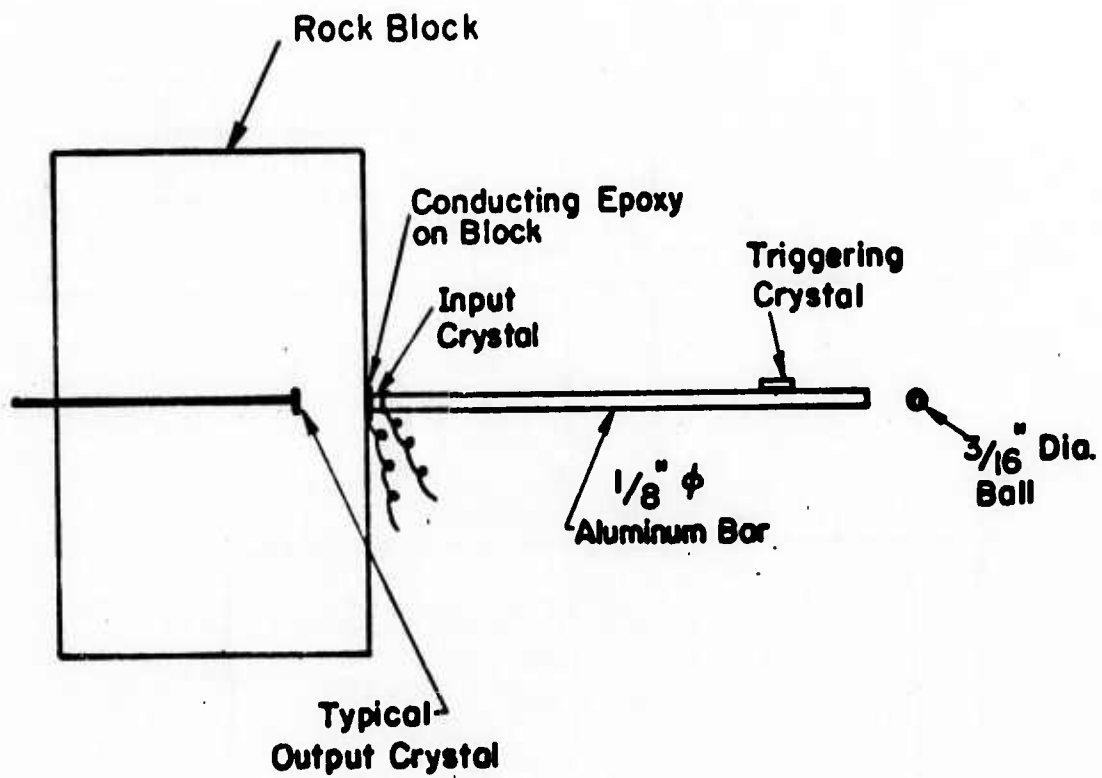


Fig. 9

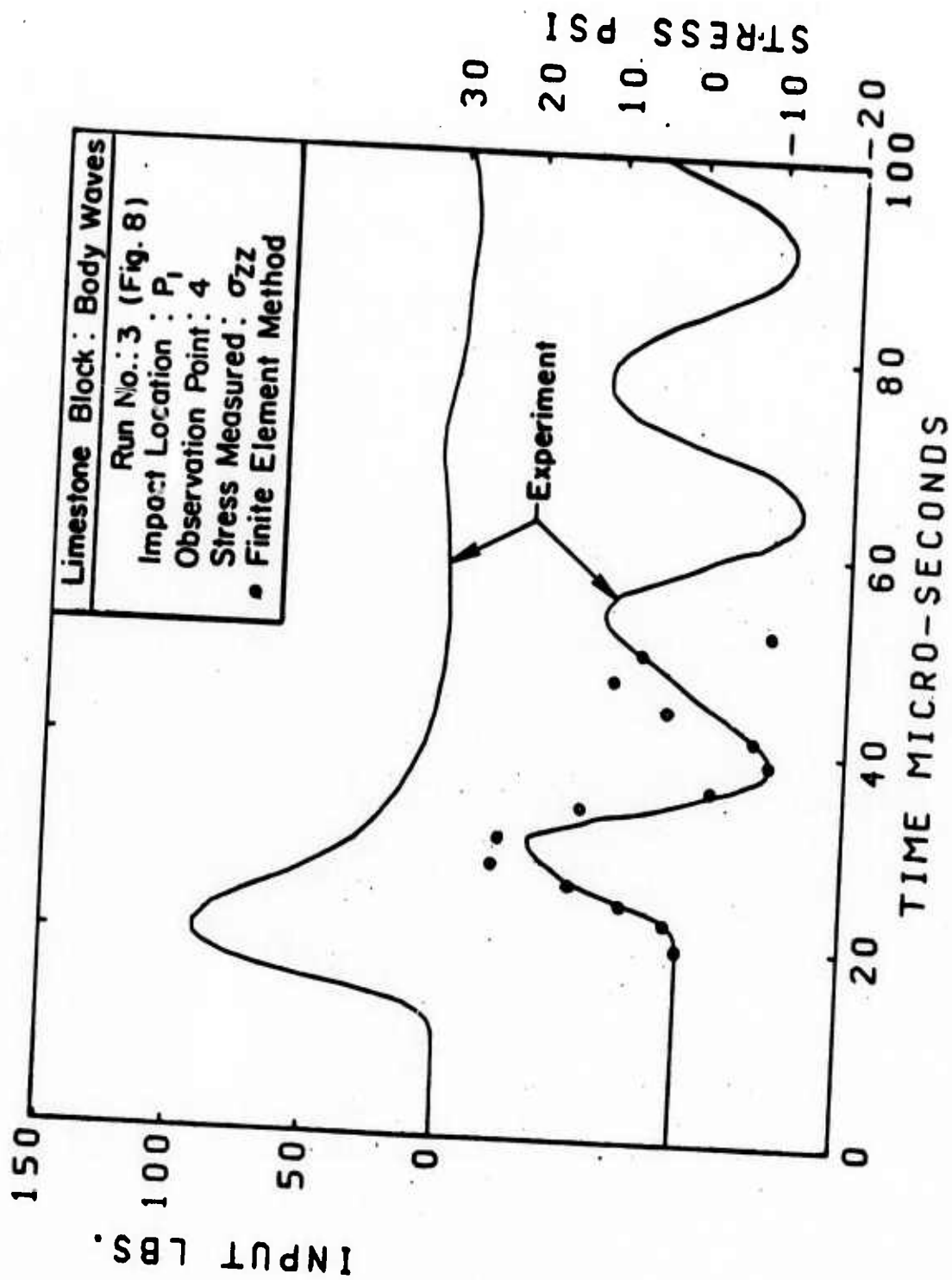


FIG. 10

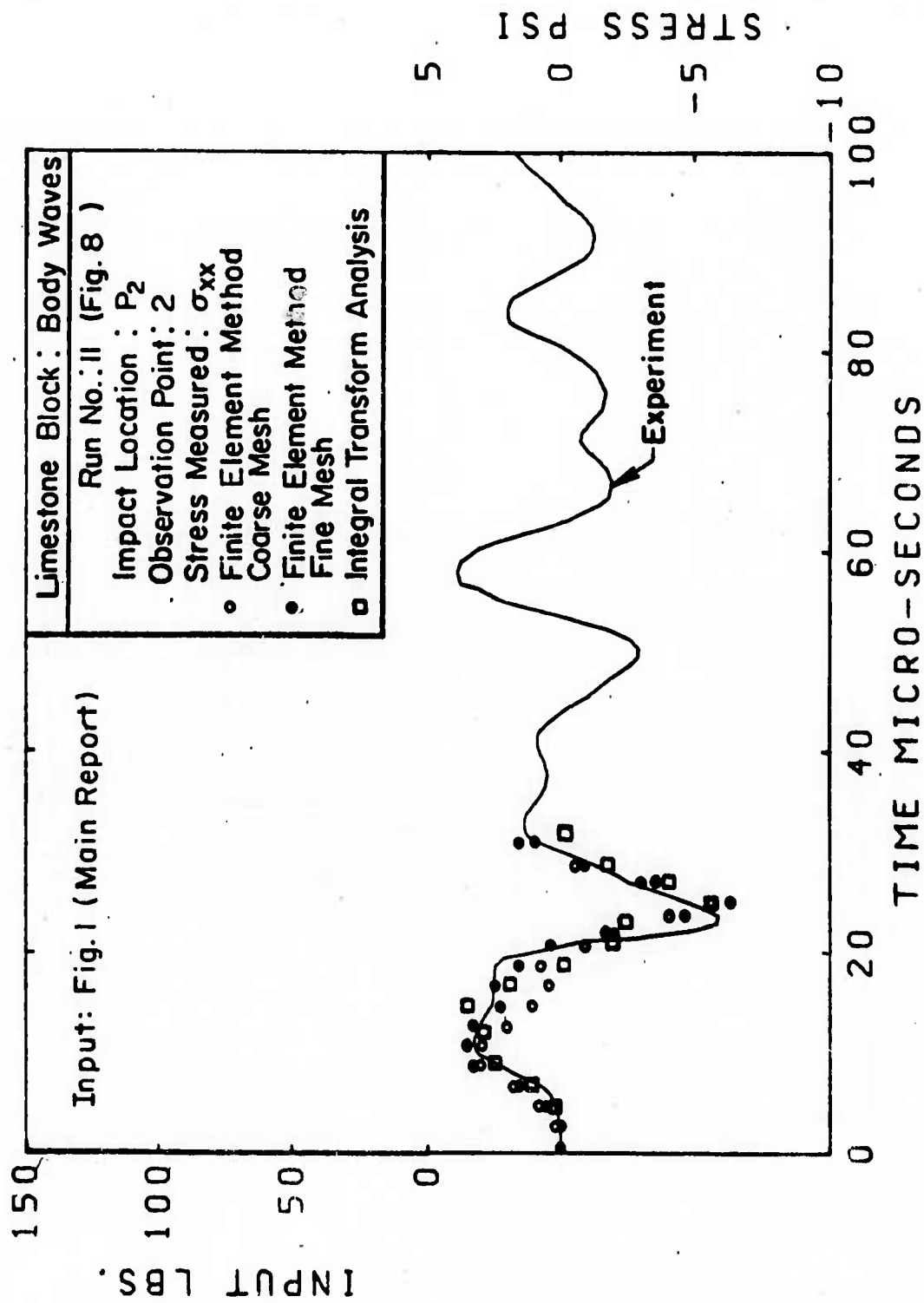


FIG.11

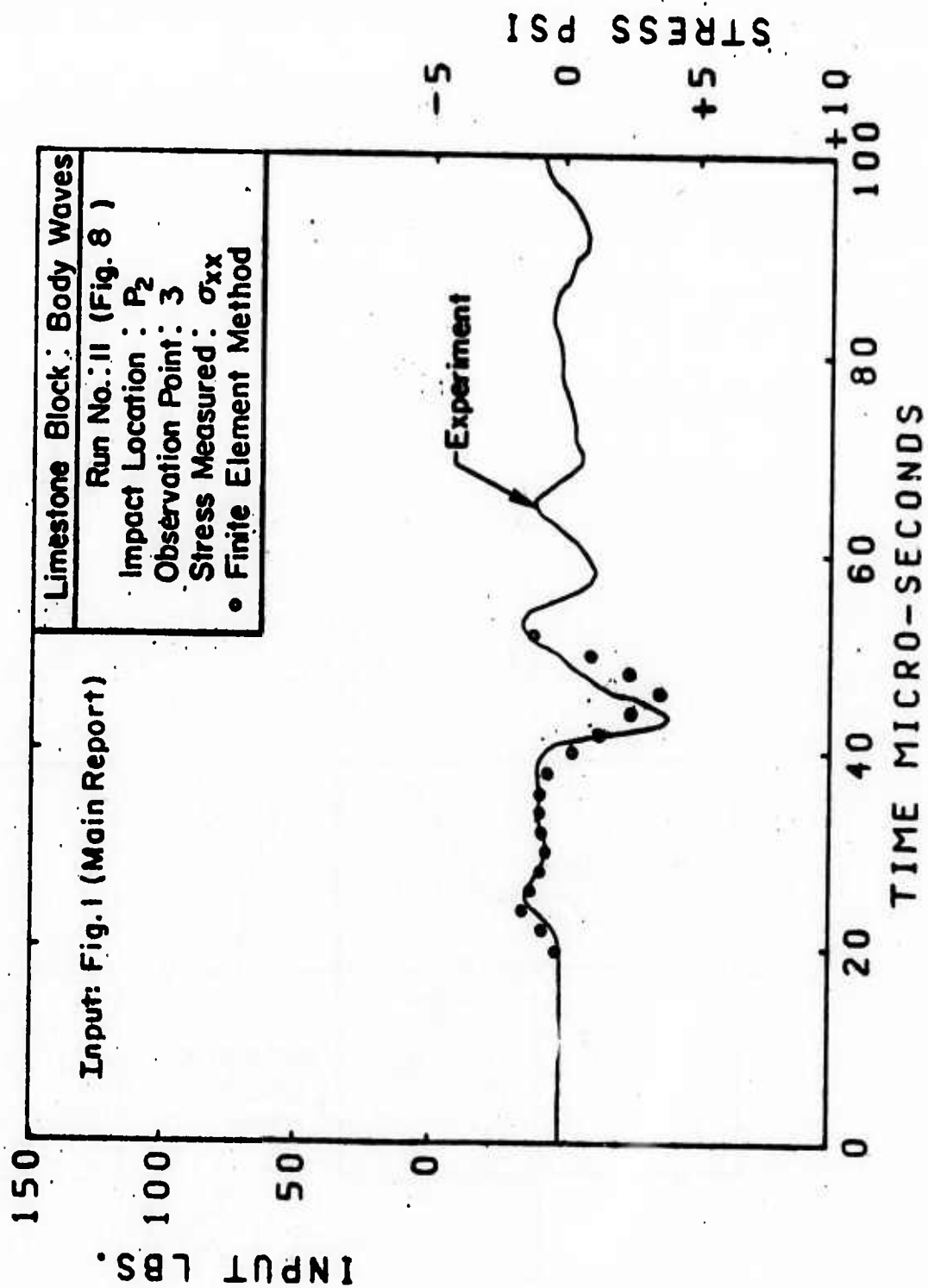


FIG. 12

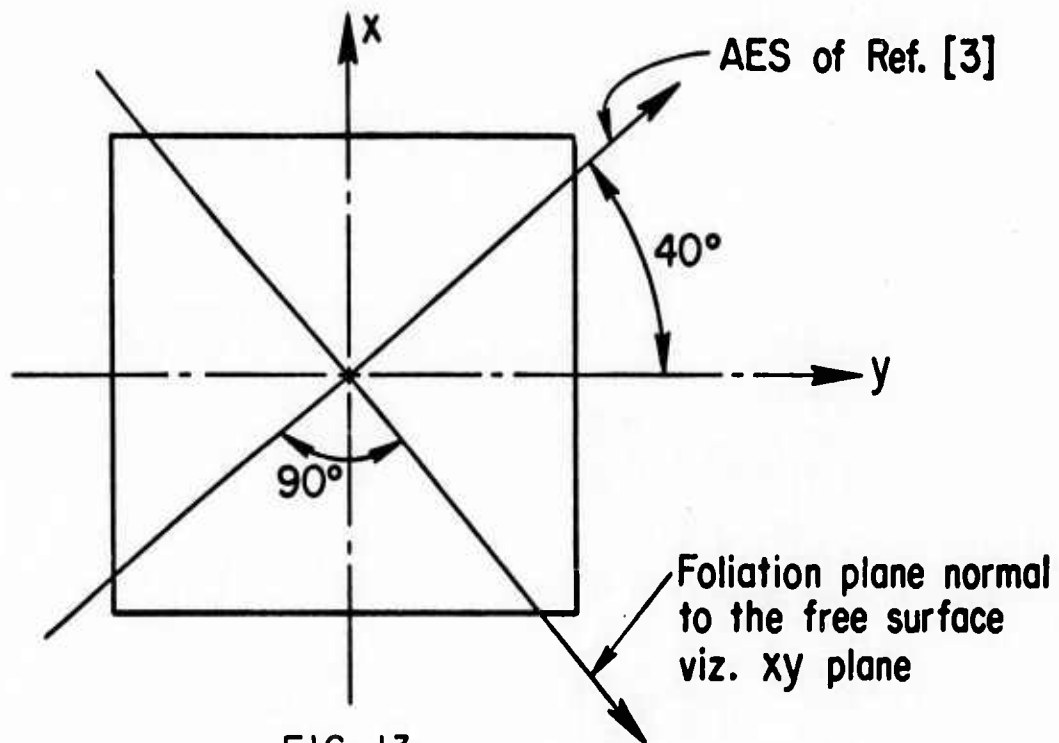
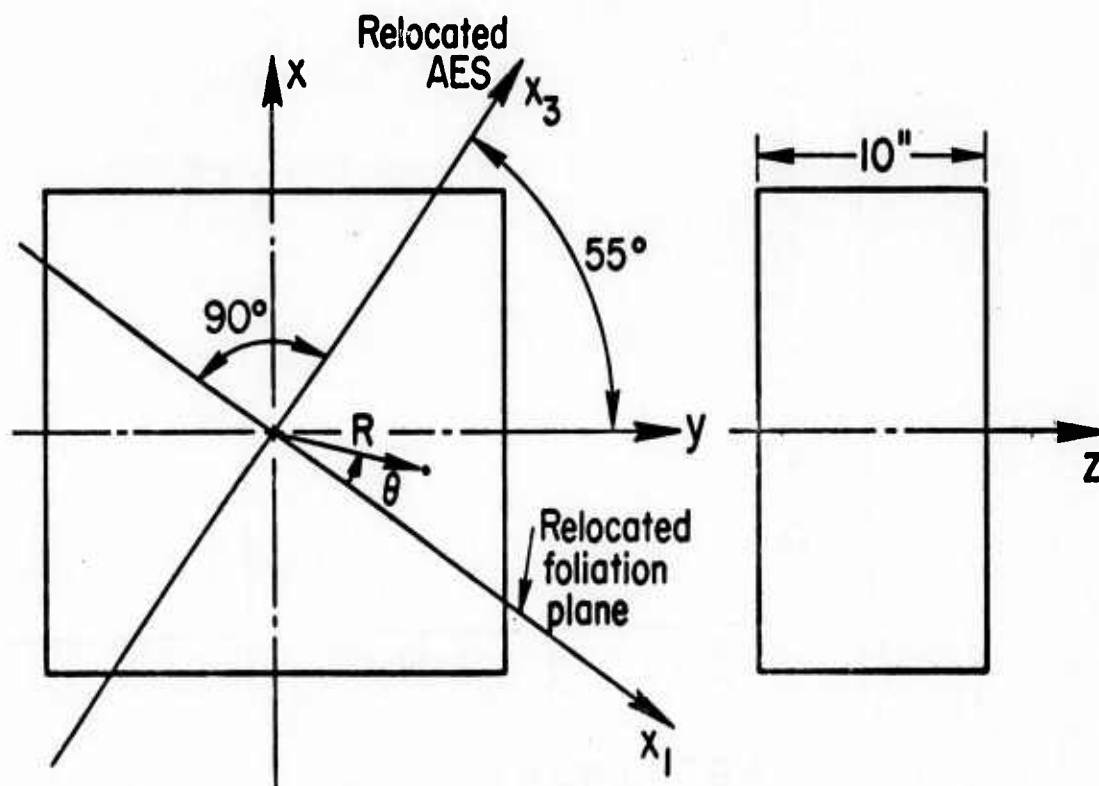


FIG. 13



YULE MARBLE BLOCK I, FOR BODY WAVES

FIG. 14

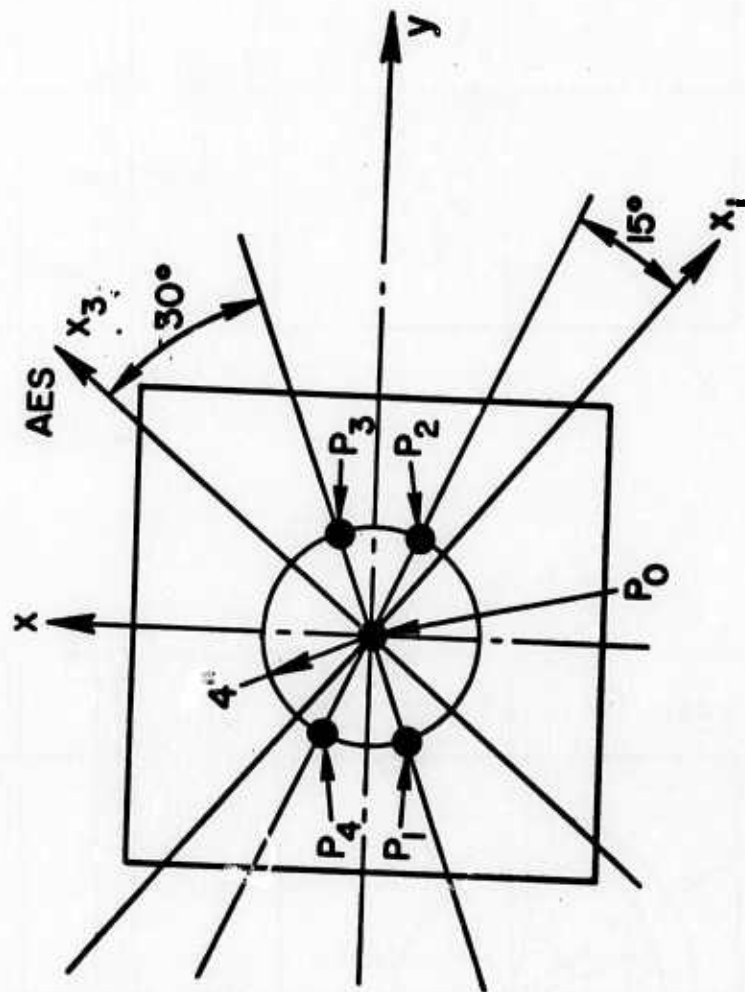
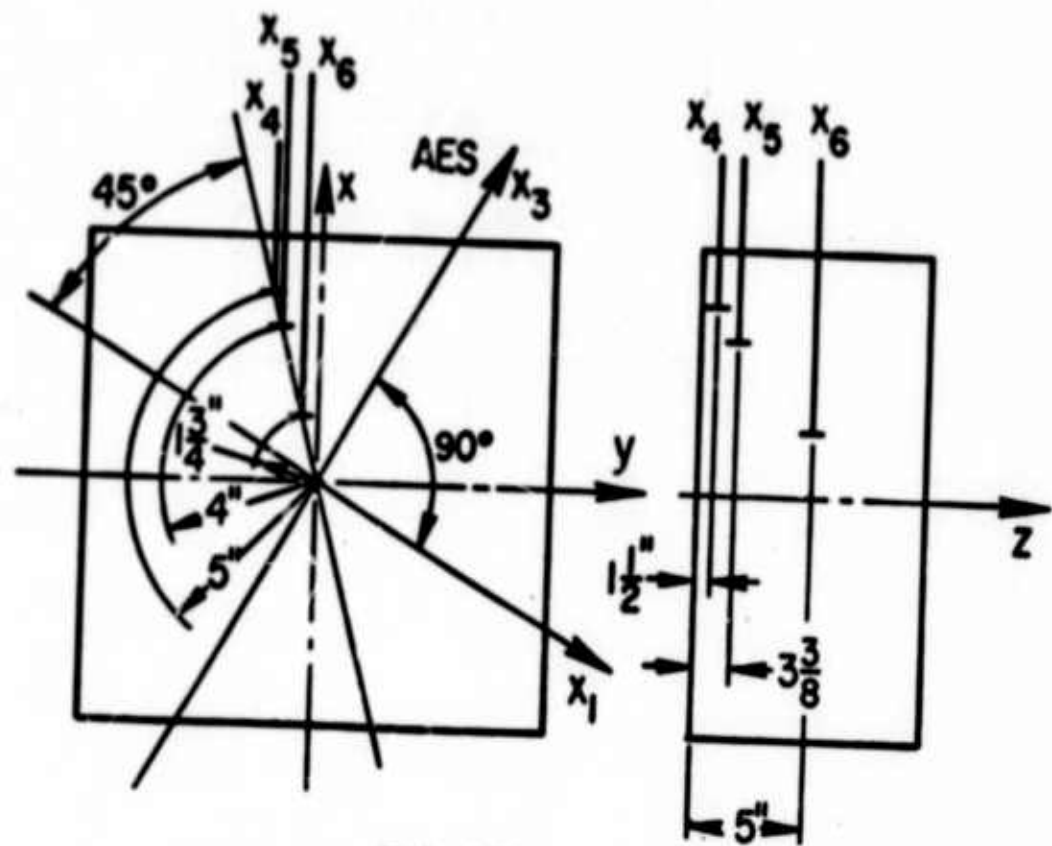
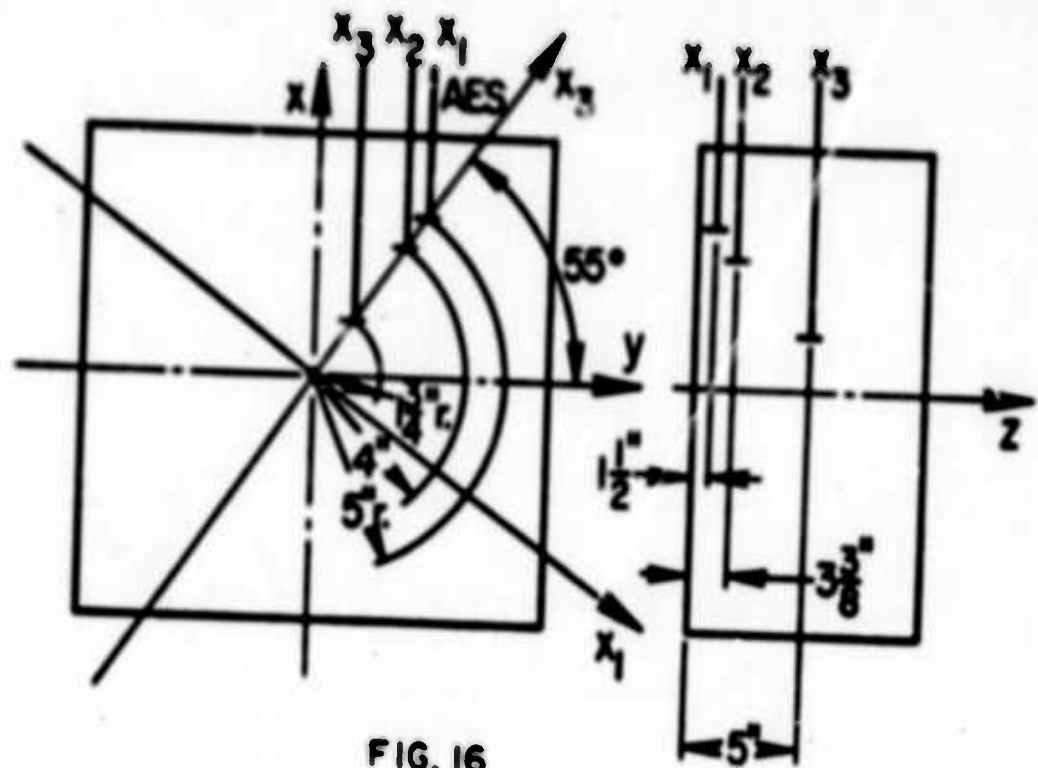


FIG. 15



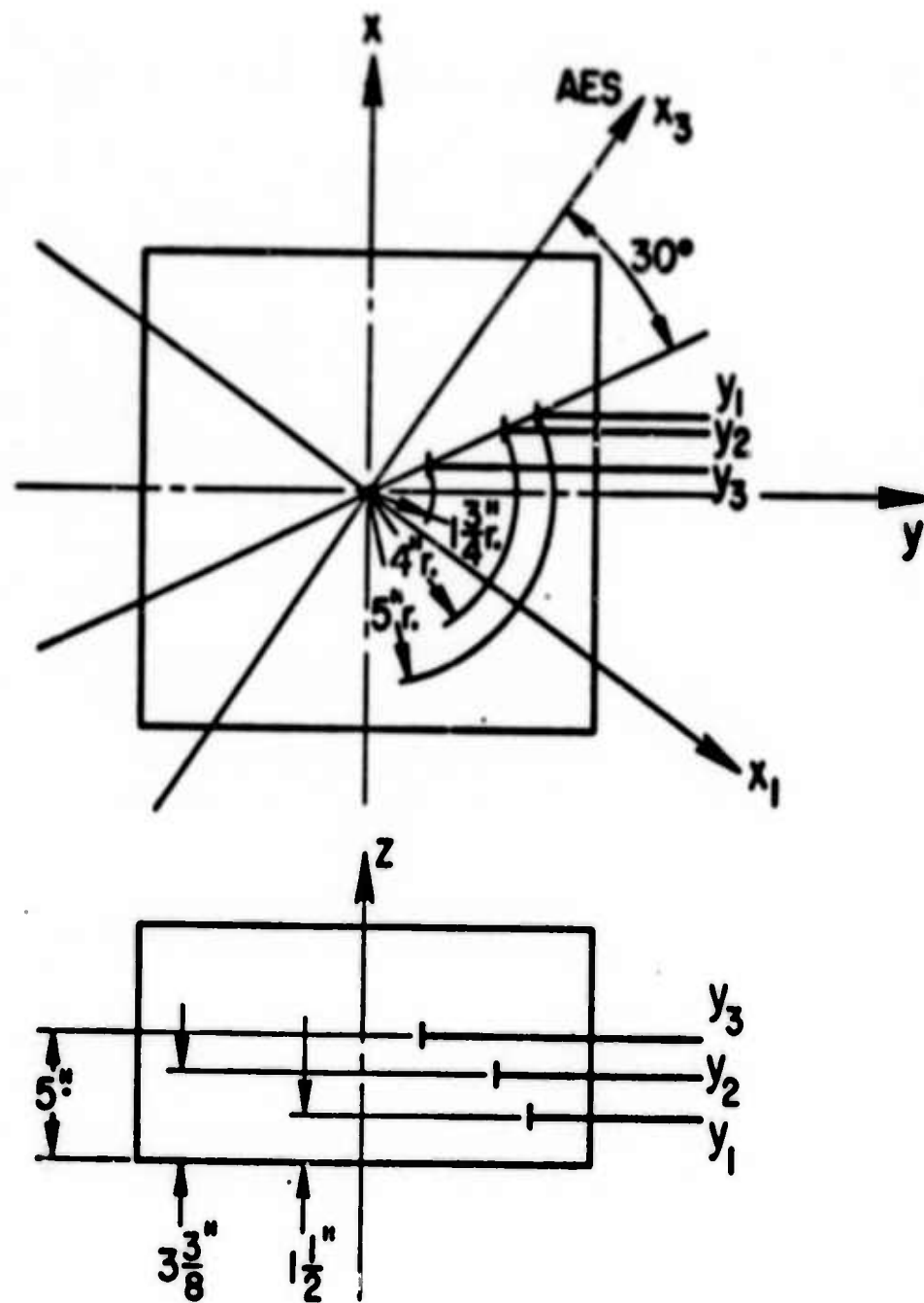


FIG. 18

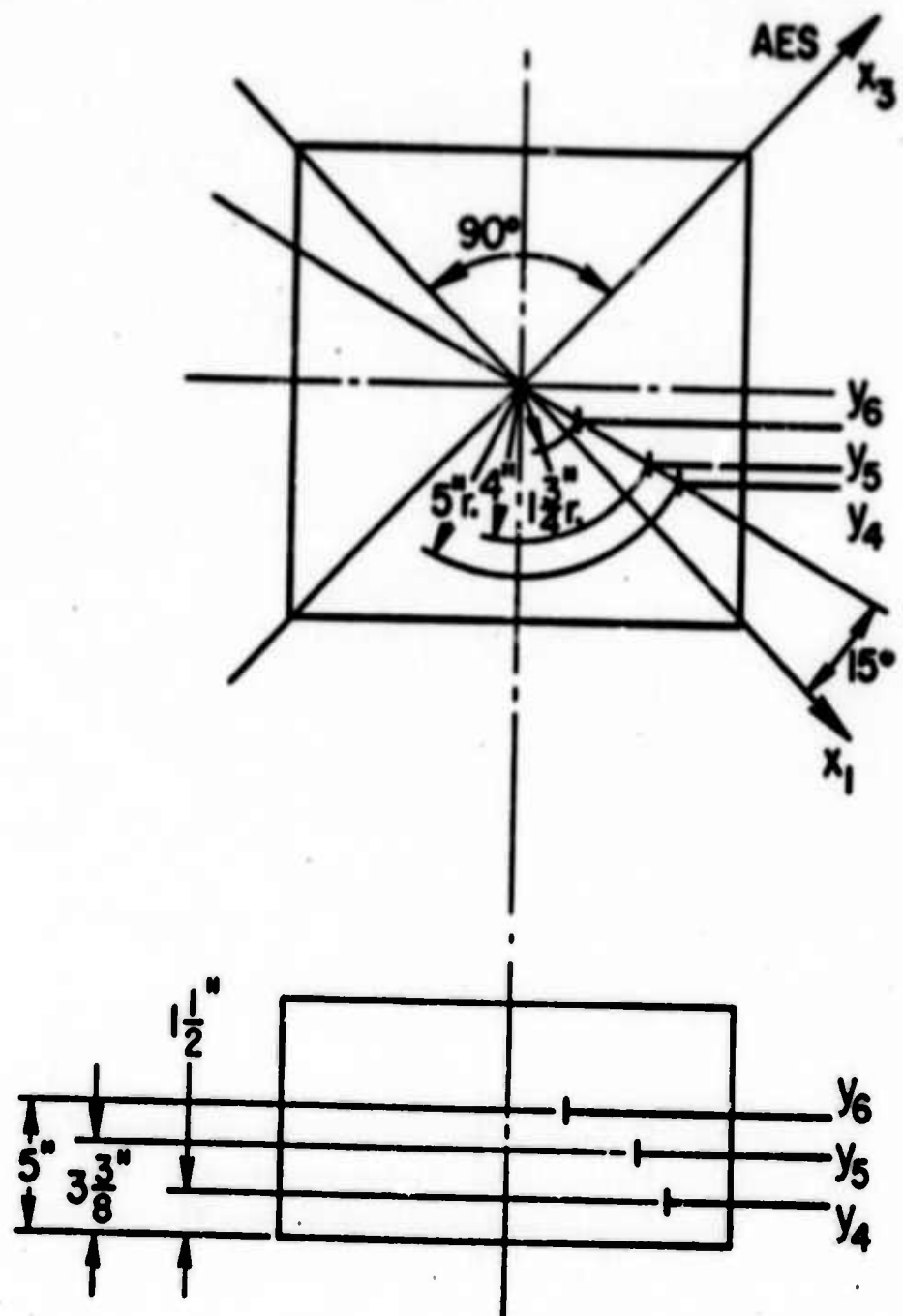


FIG. 19

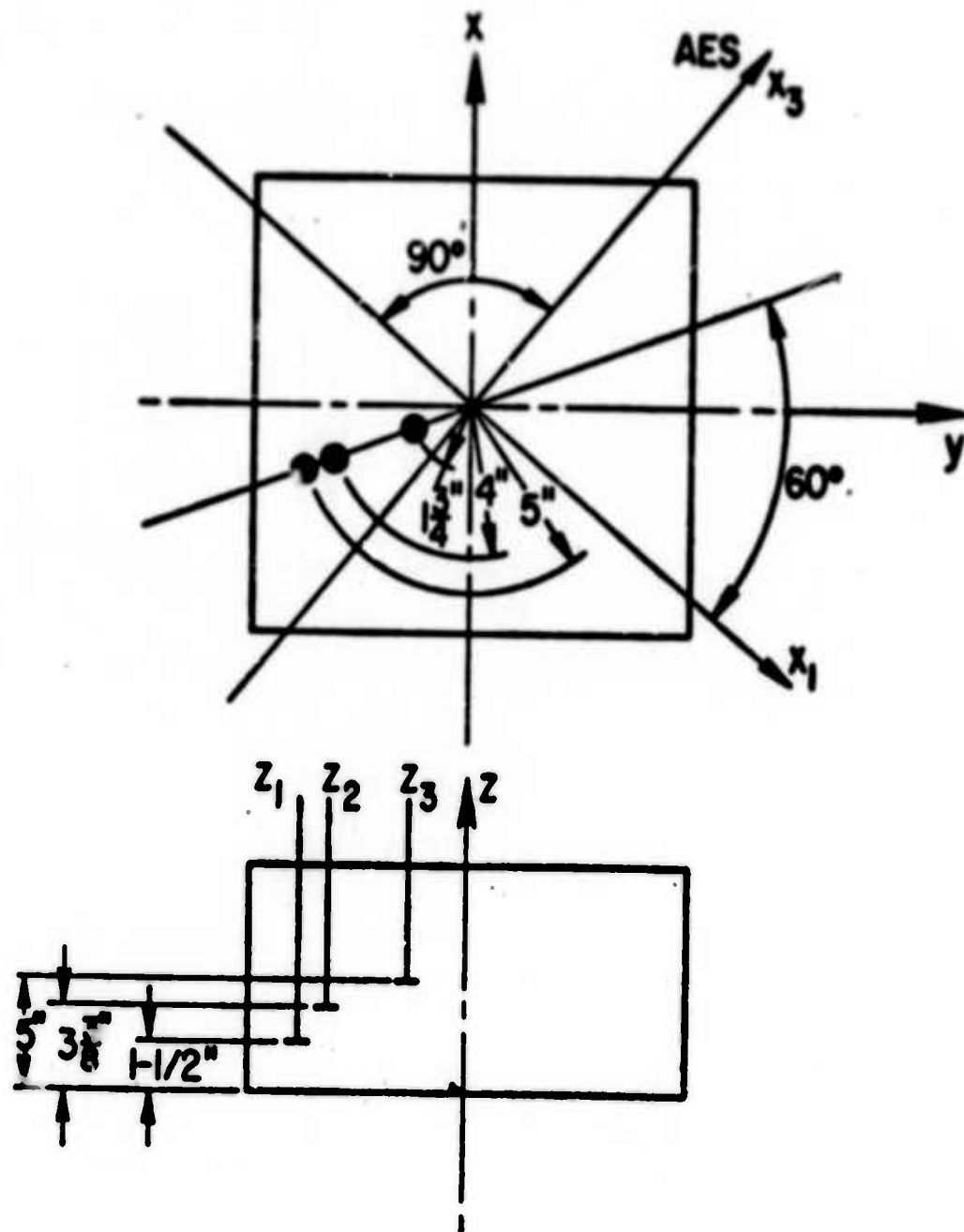


FIG. 20

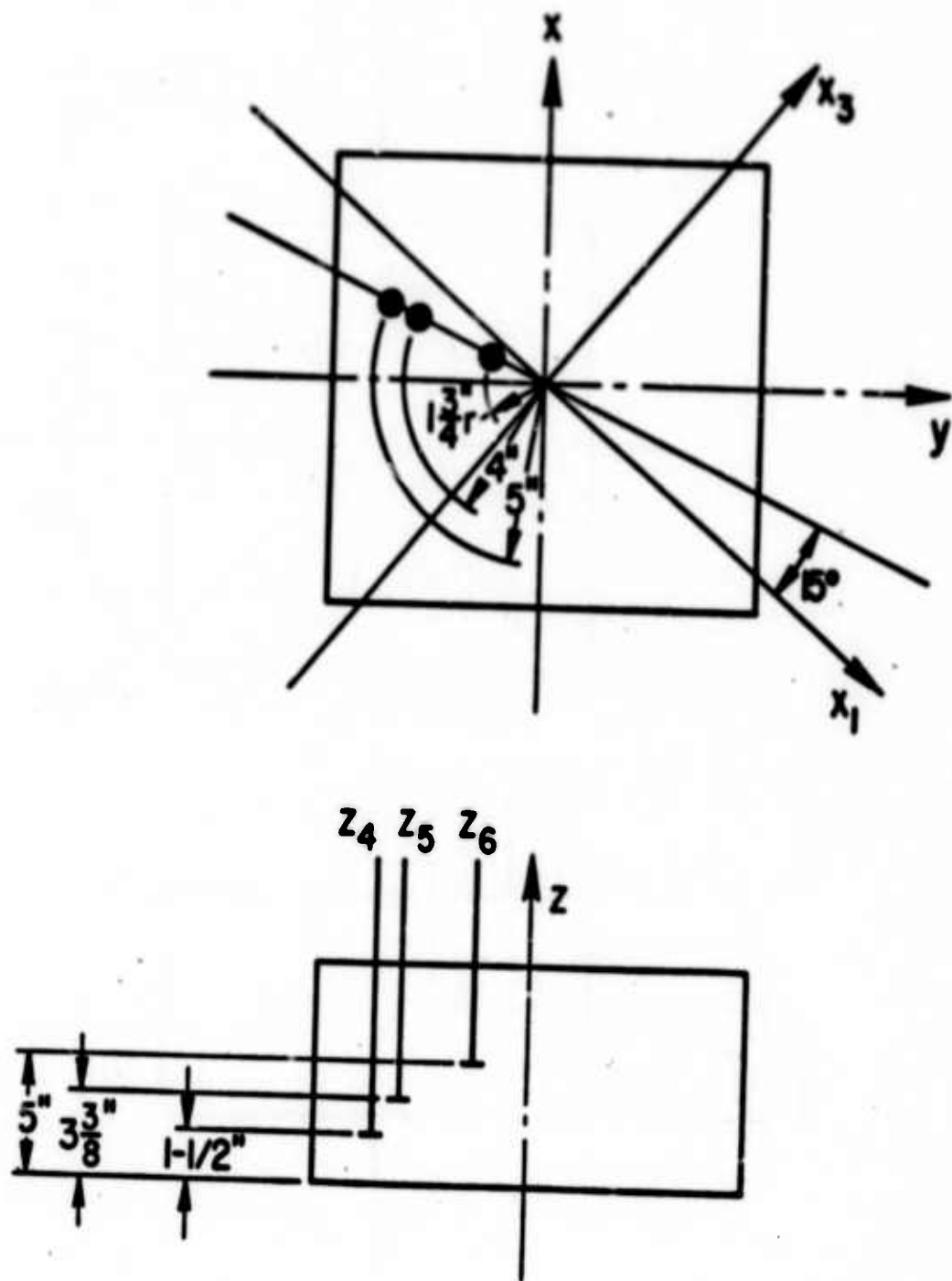


FIG. 21

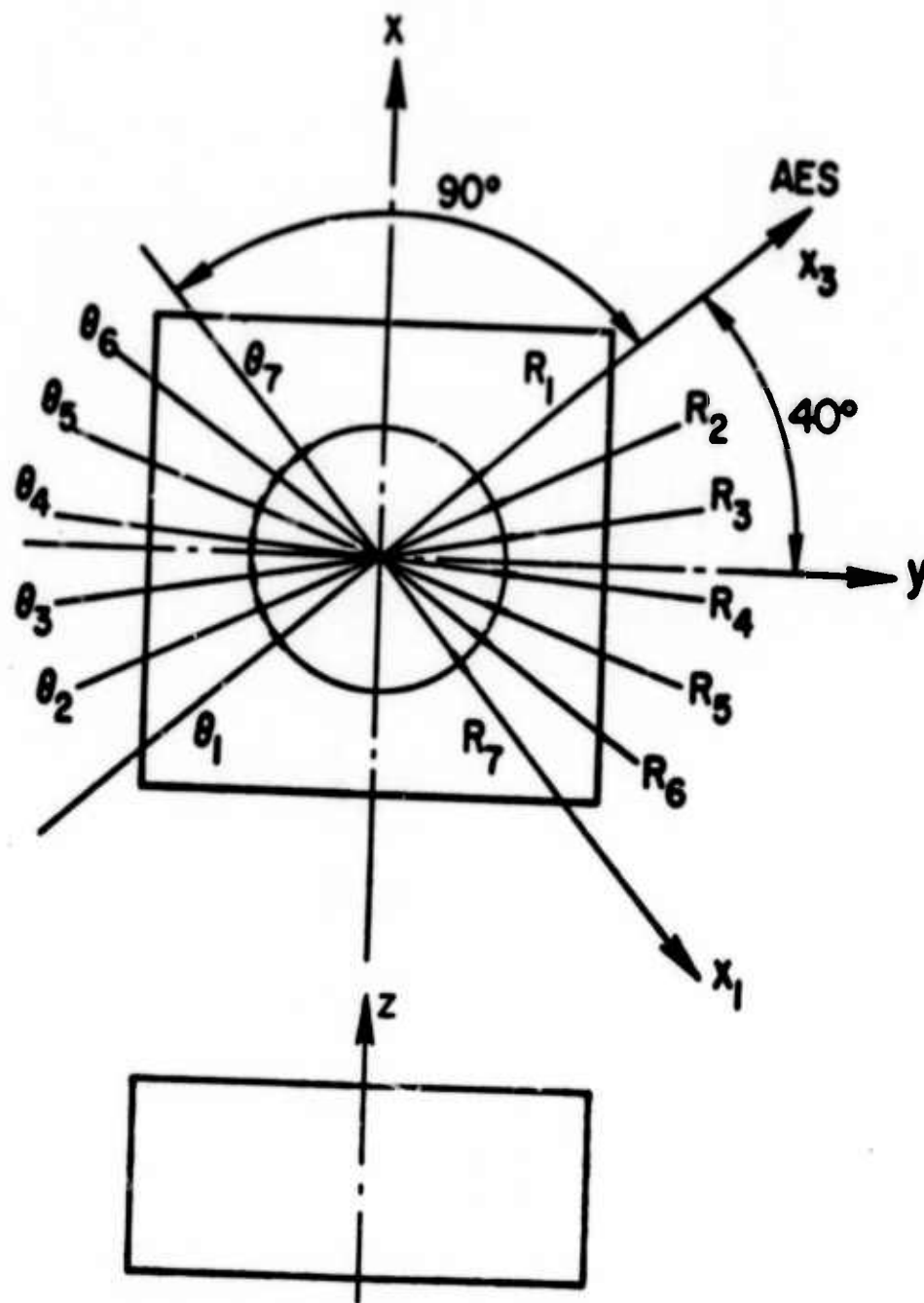


FIG. 22

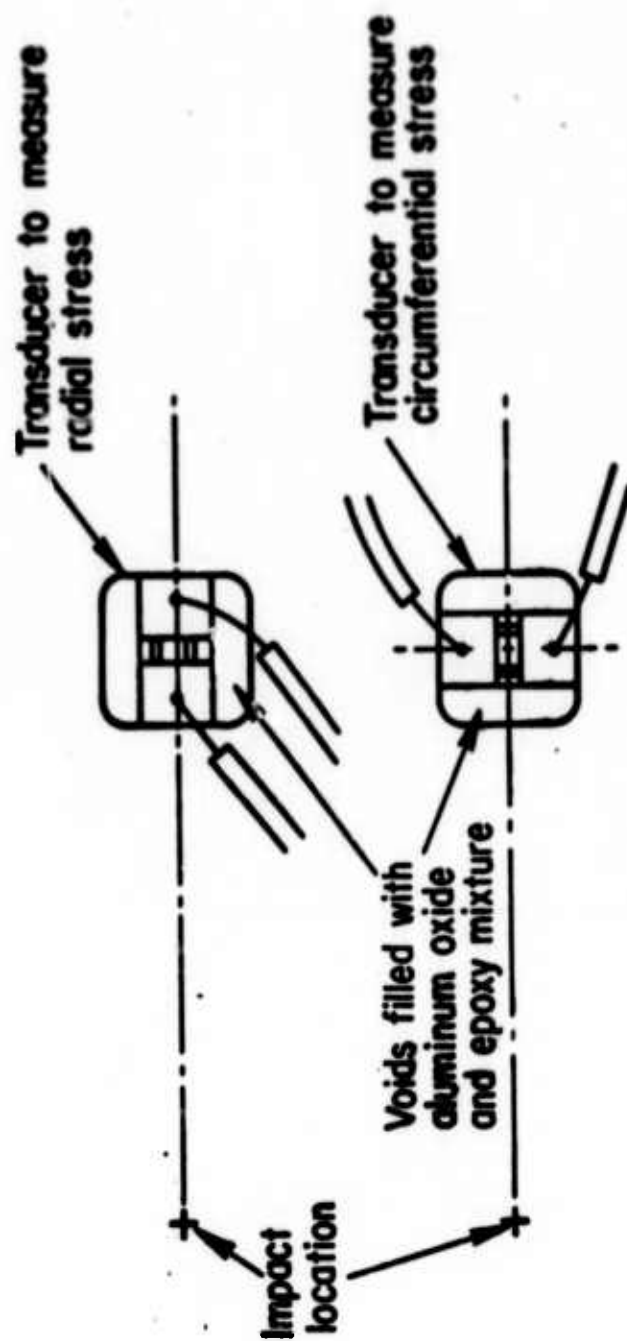


FIG. 23

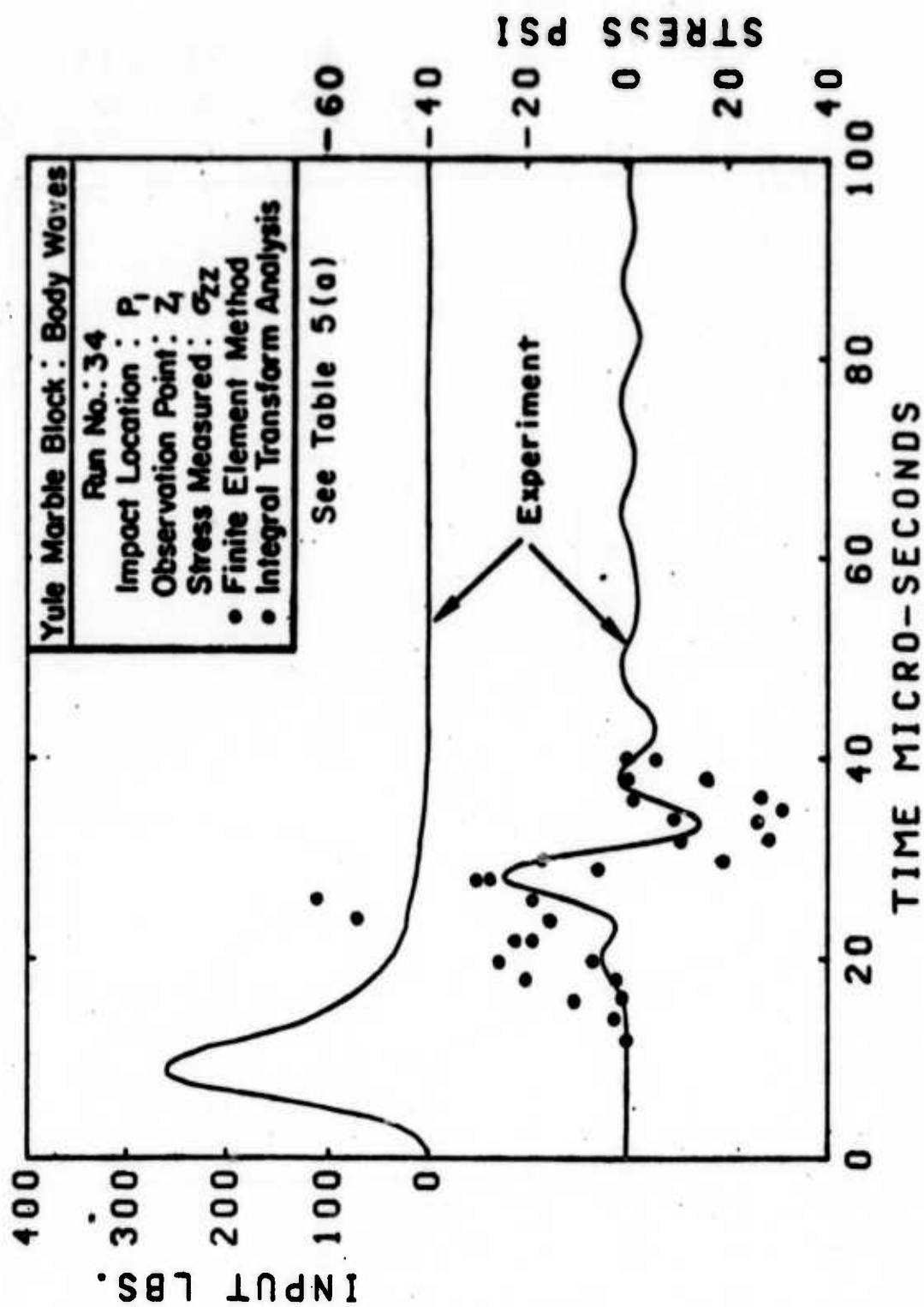


FIG. 24

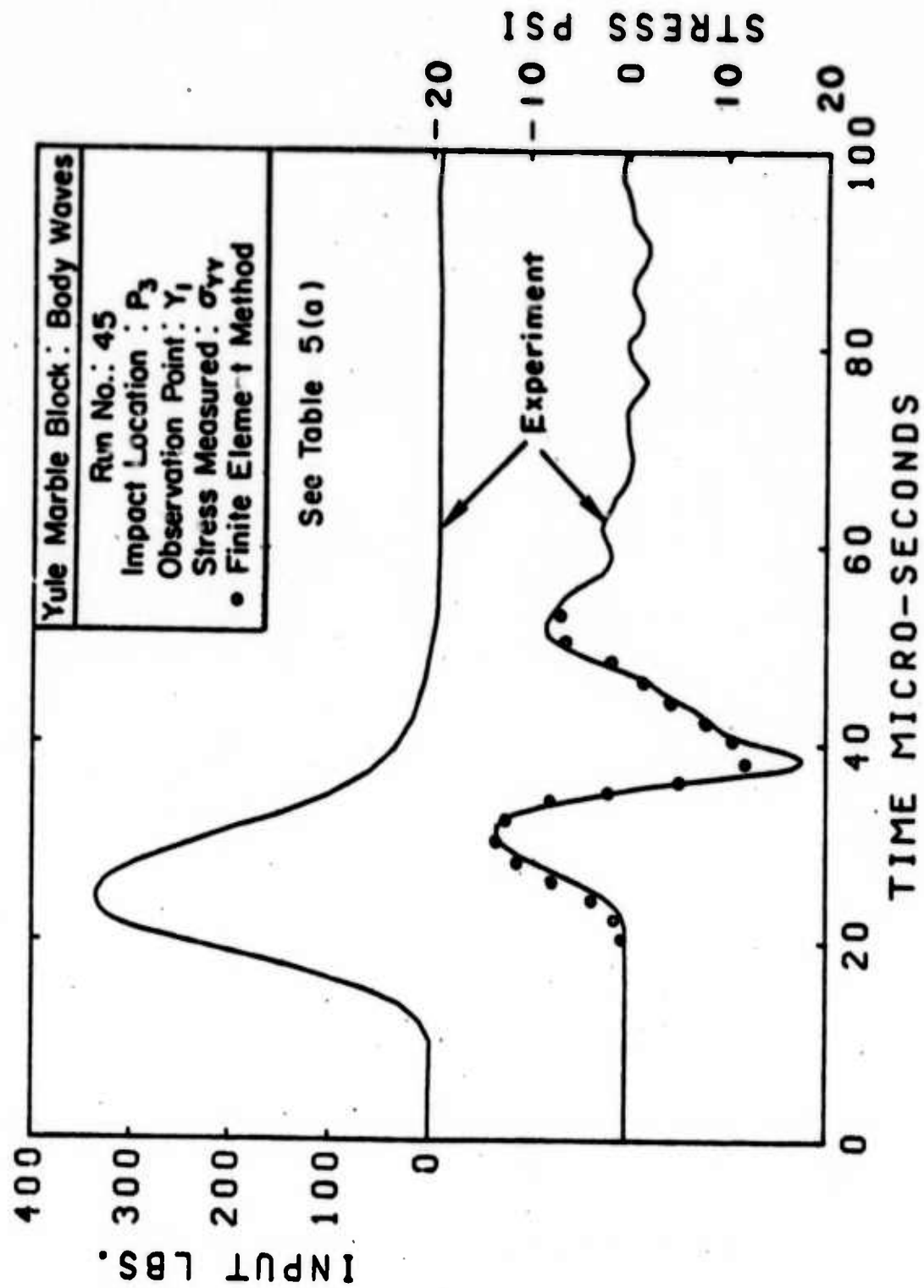


FIG. 25

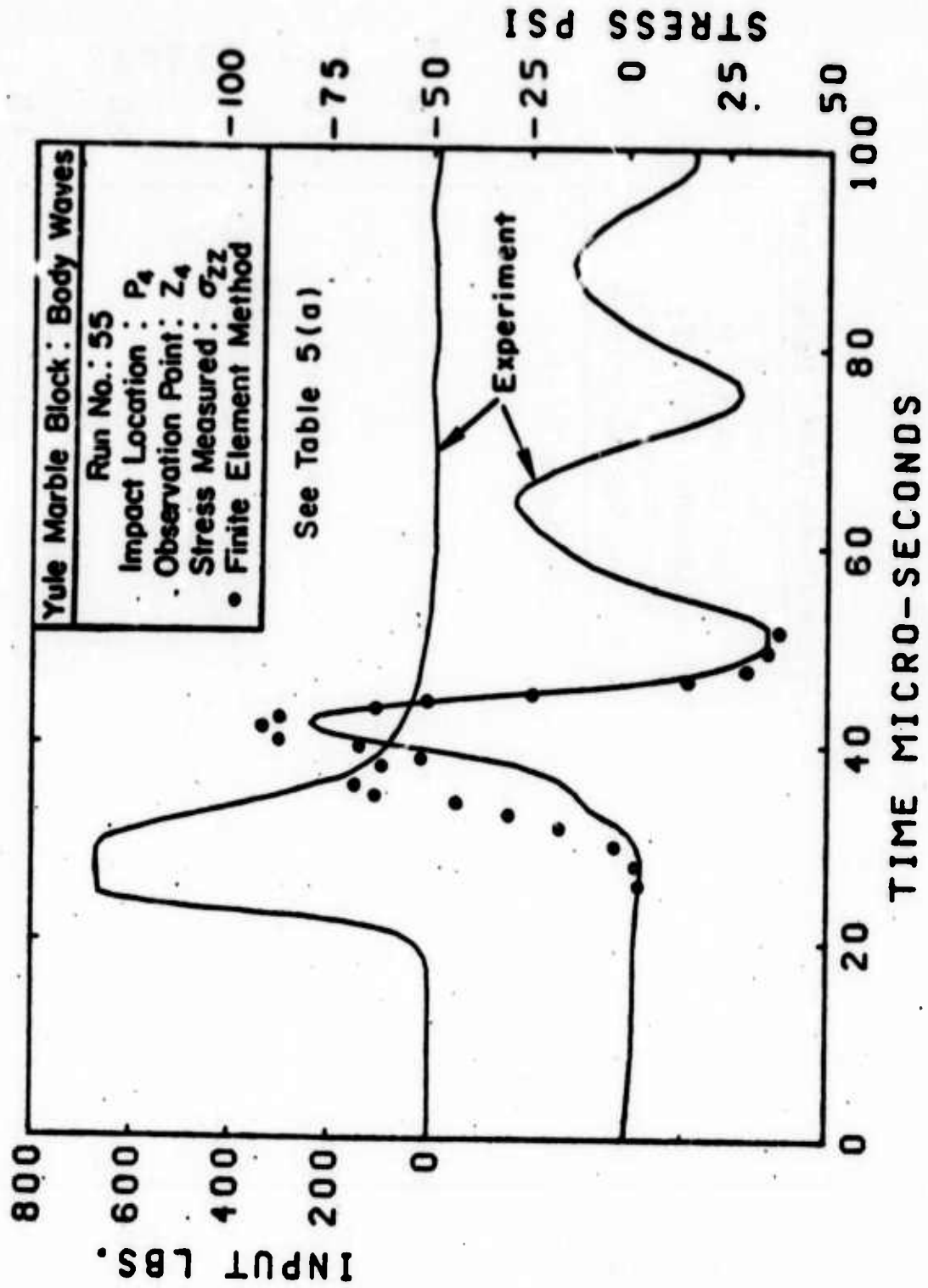


FIG. 26

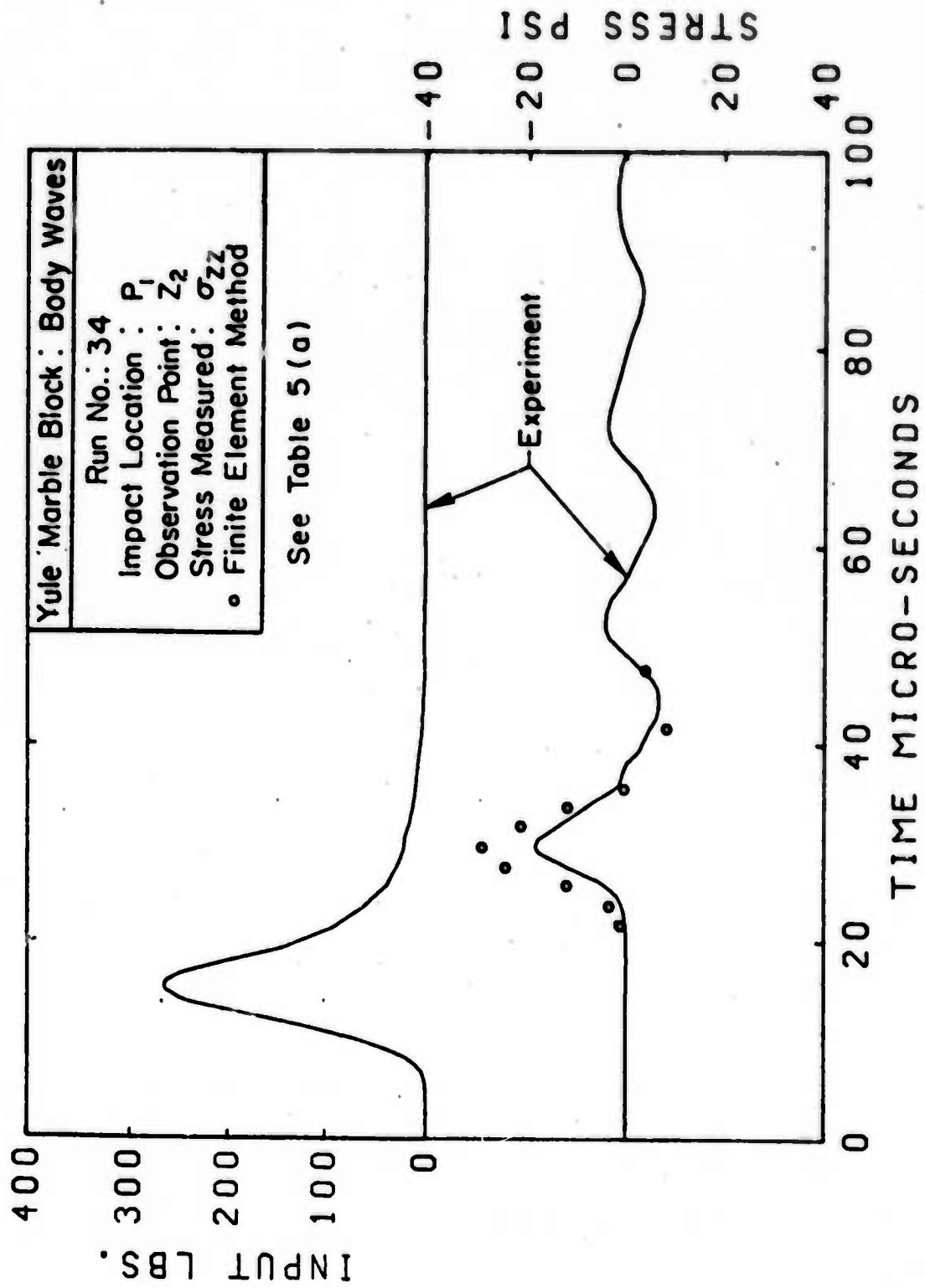


FIG. 27

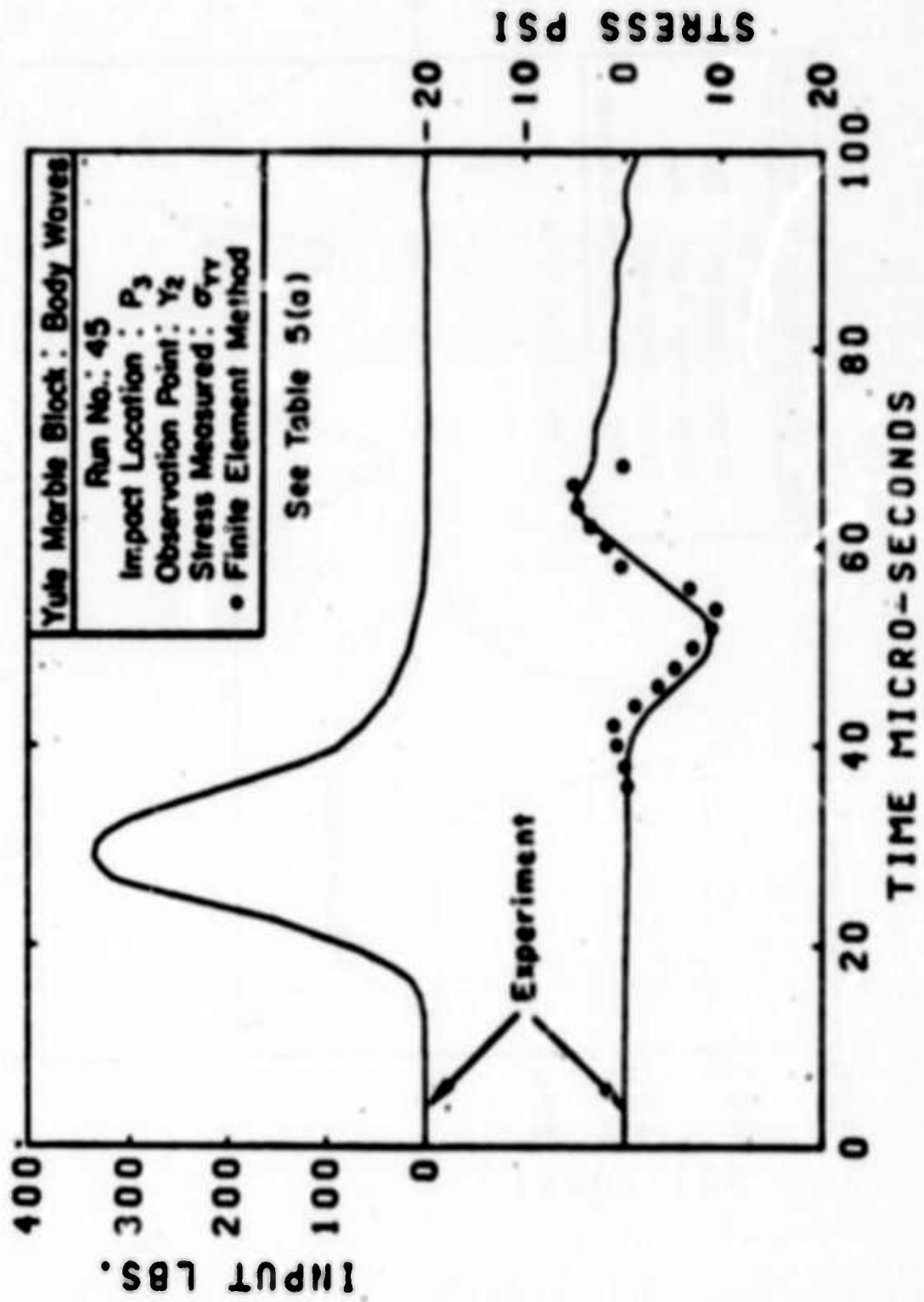


FIG. 28

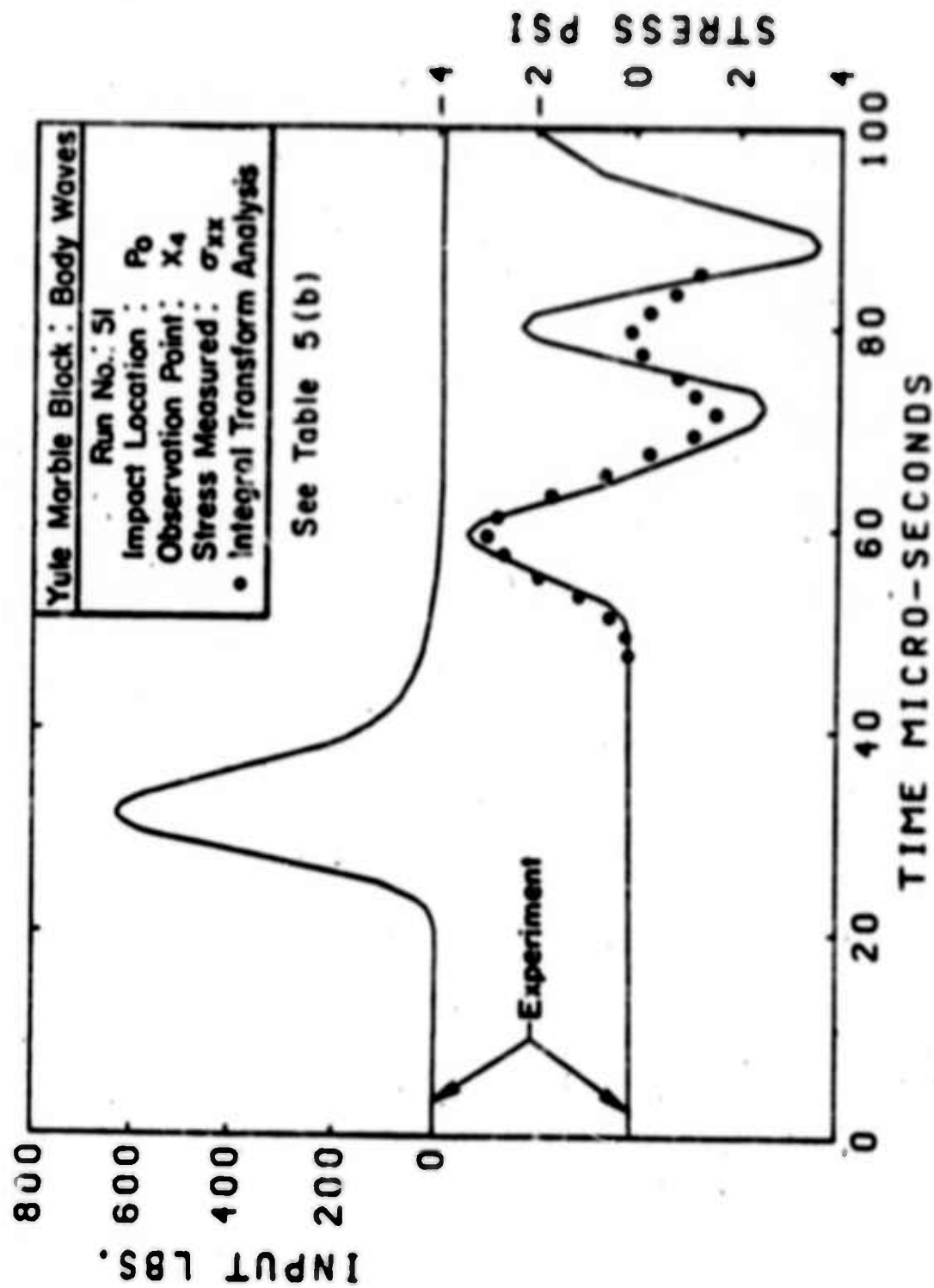


FIG. 29

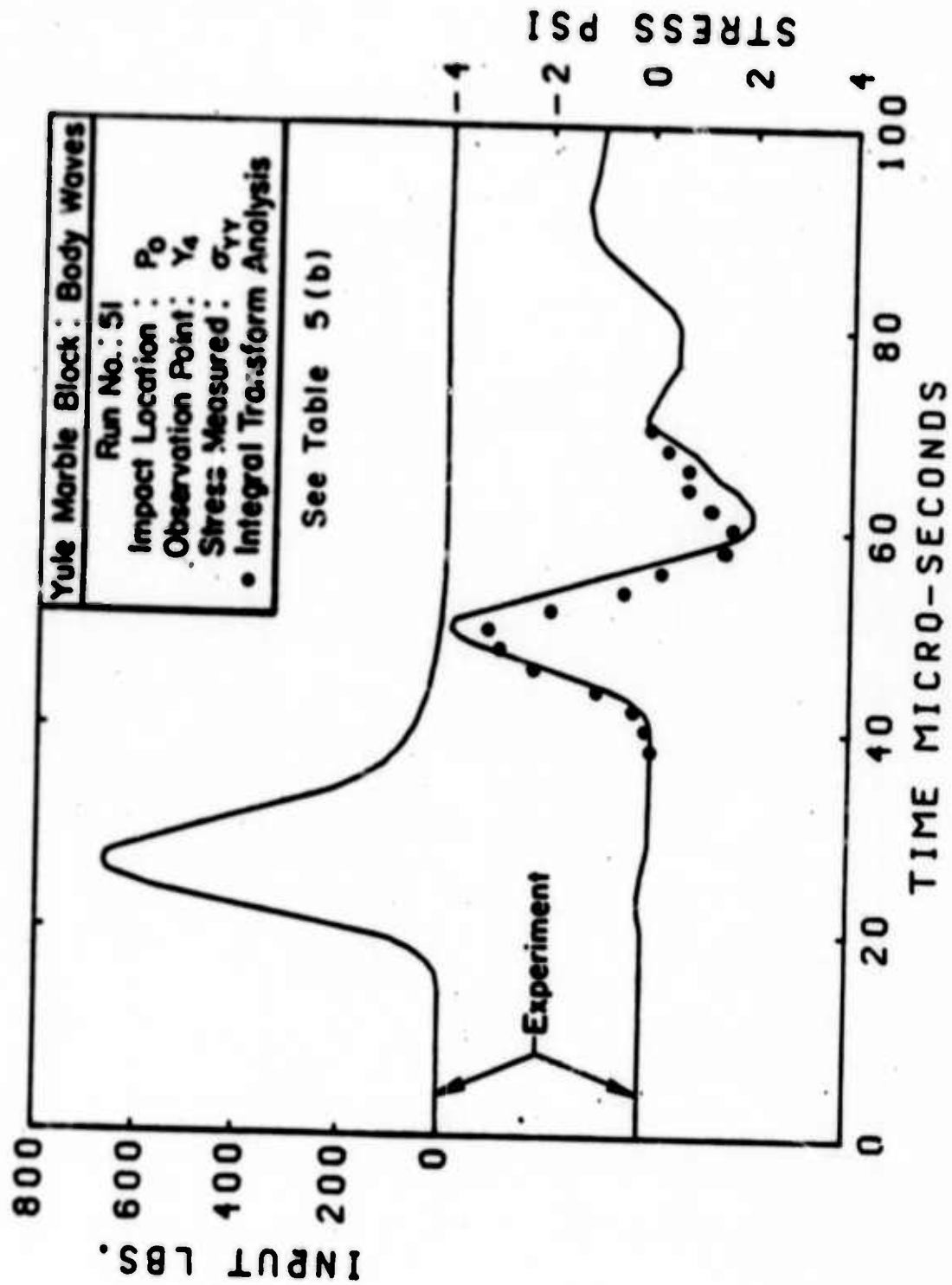


FIG. 30

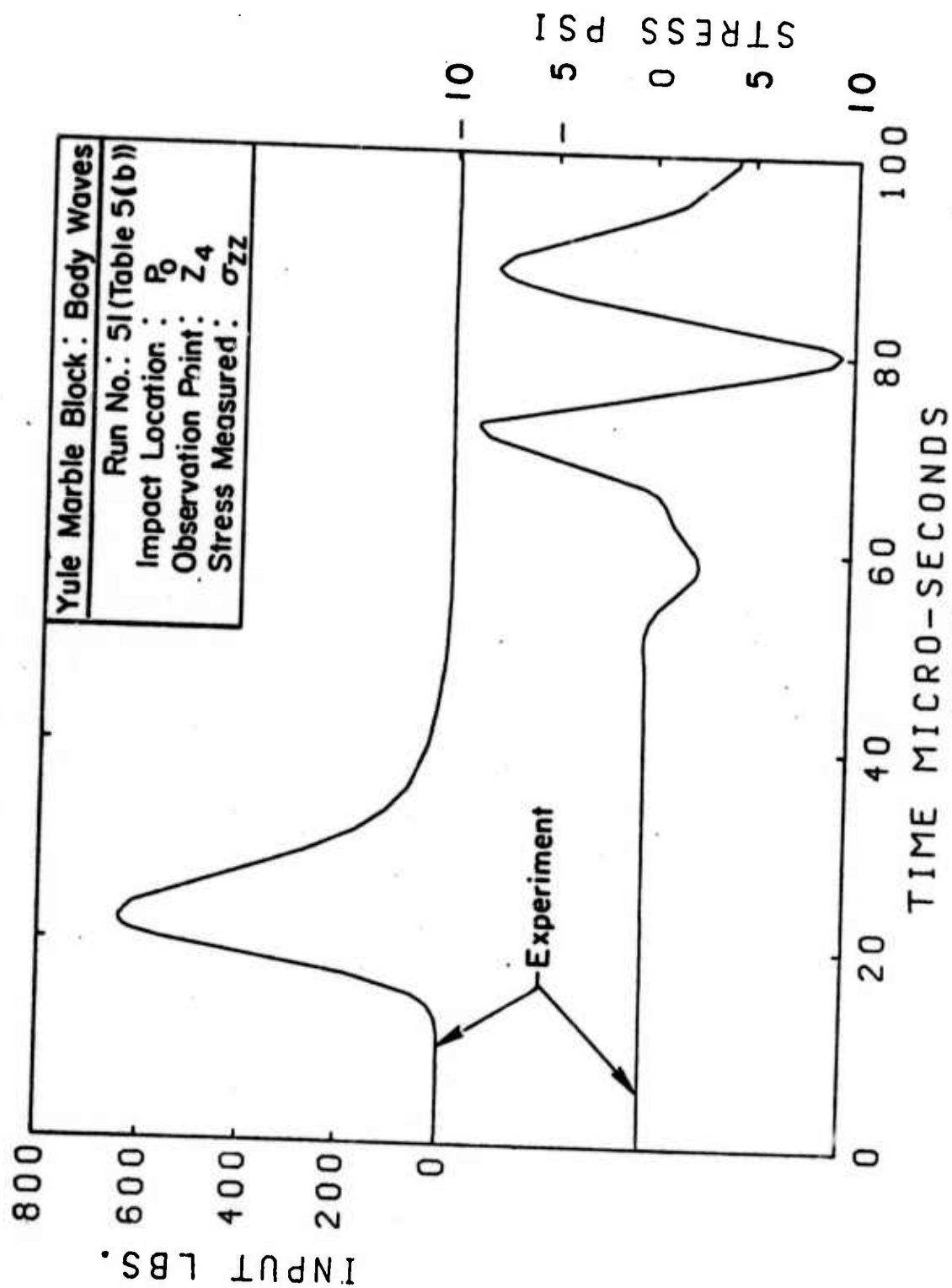


FIG. 31

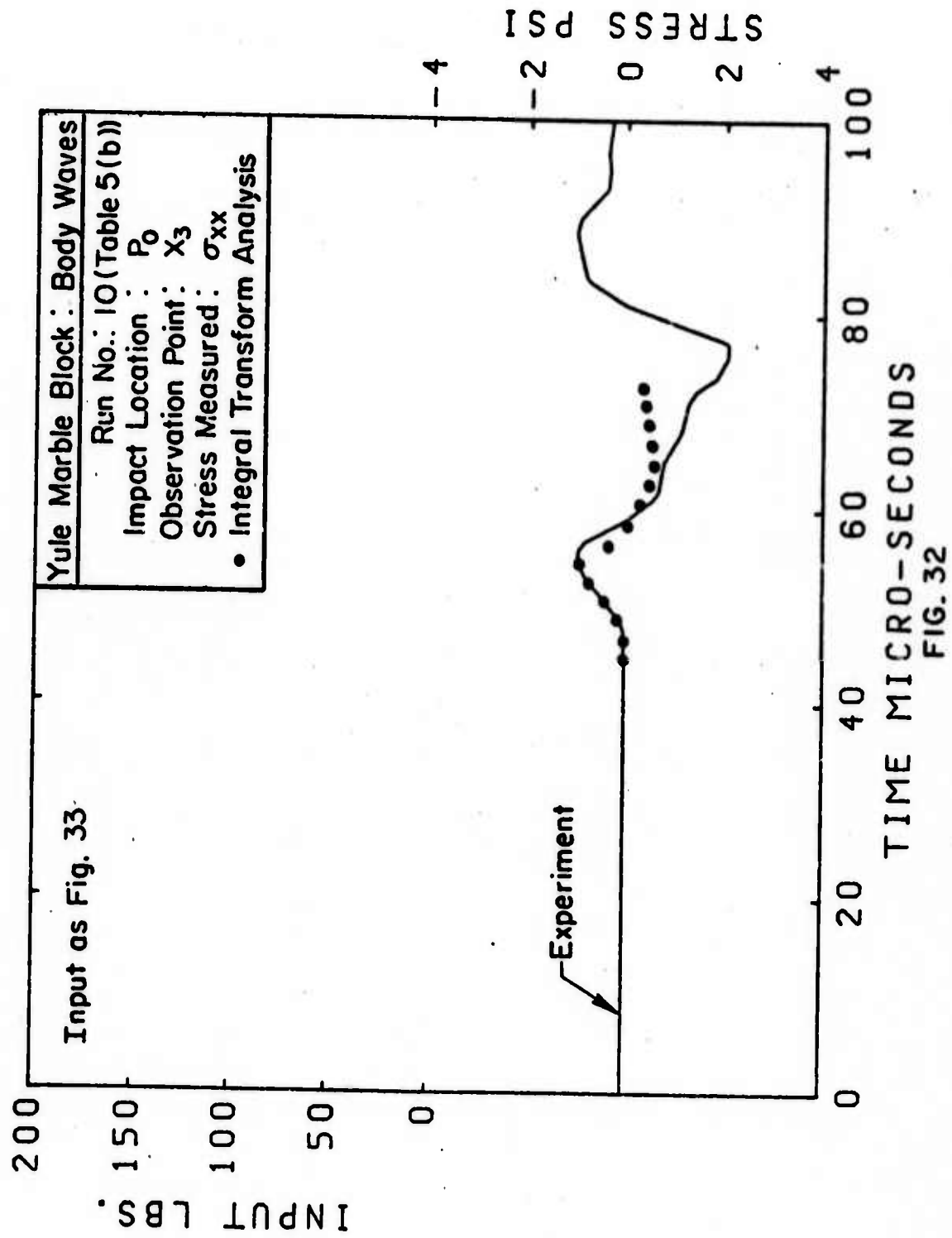


FIG. 32

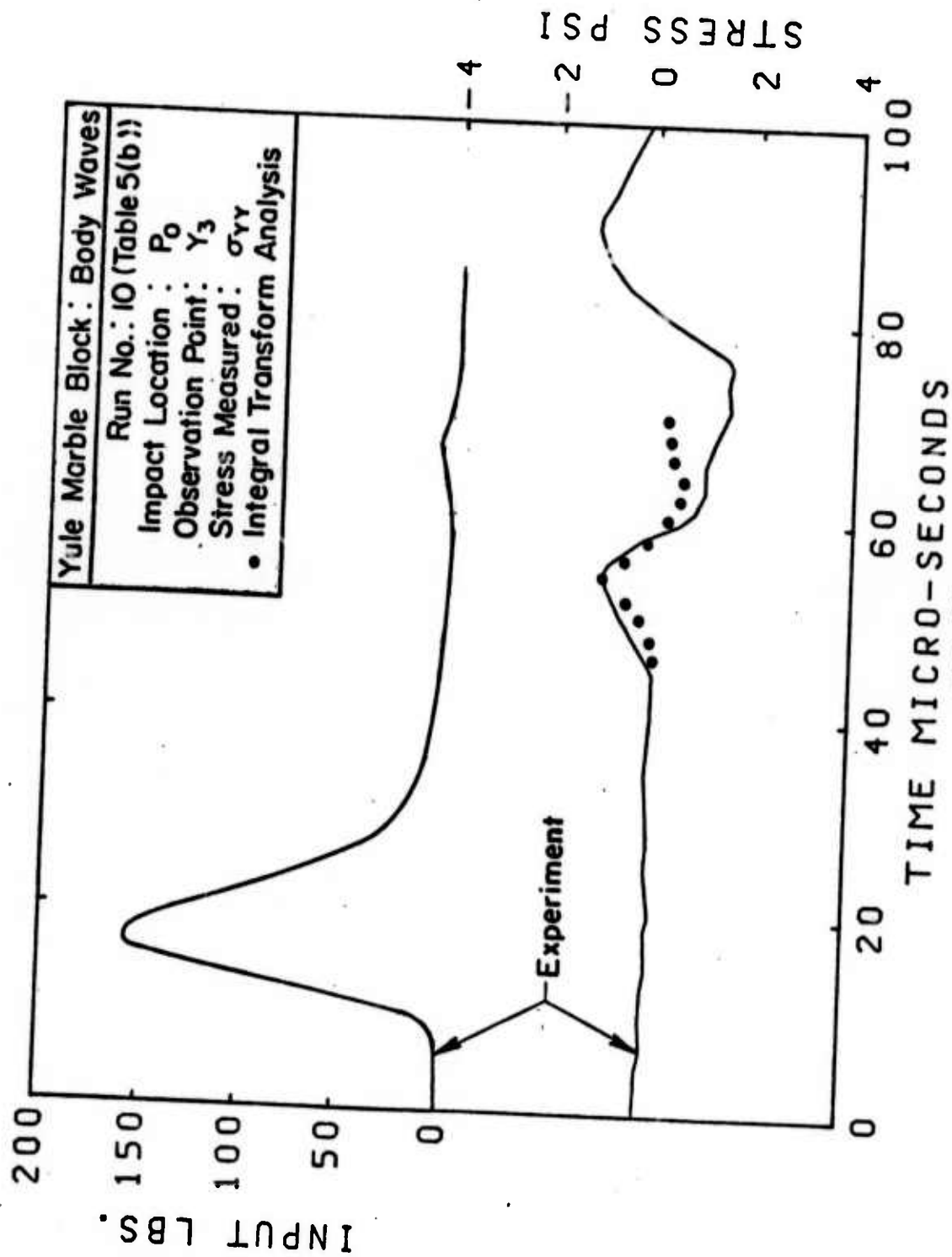


FIG. 33

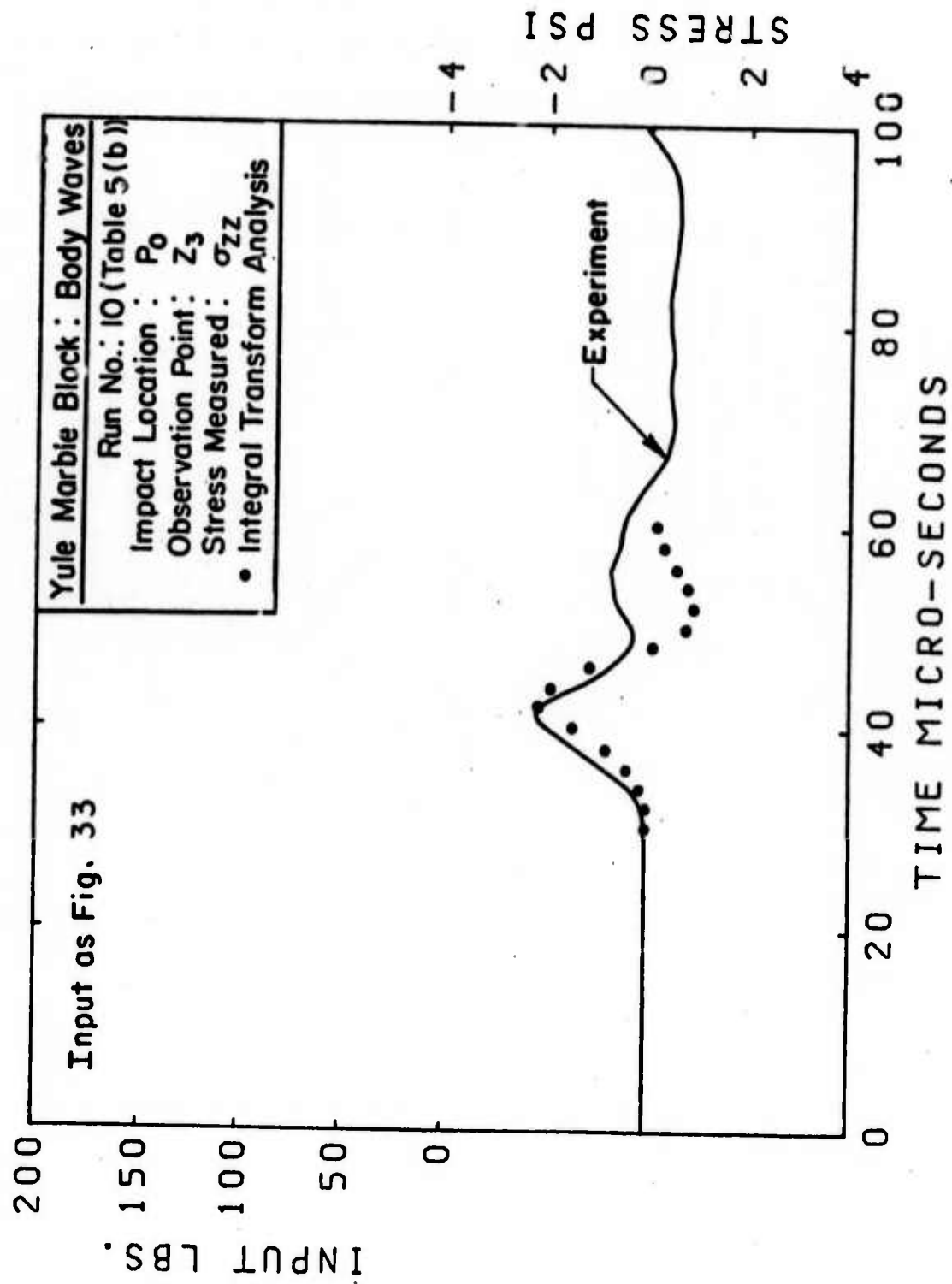


FIG. 34

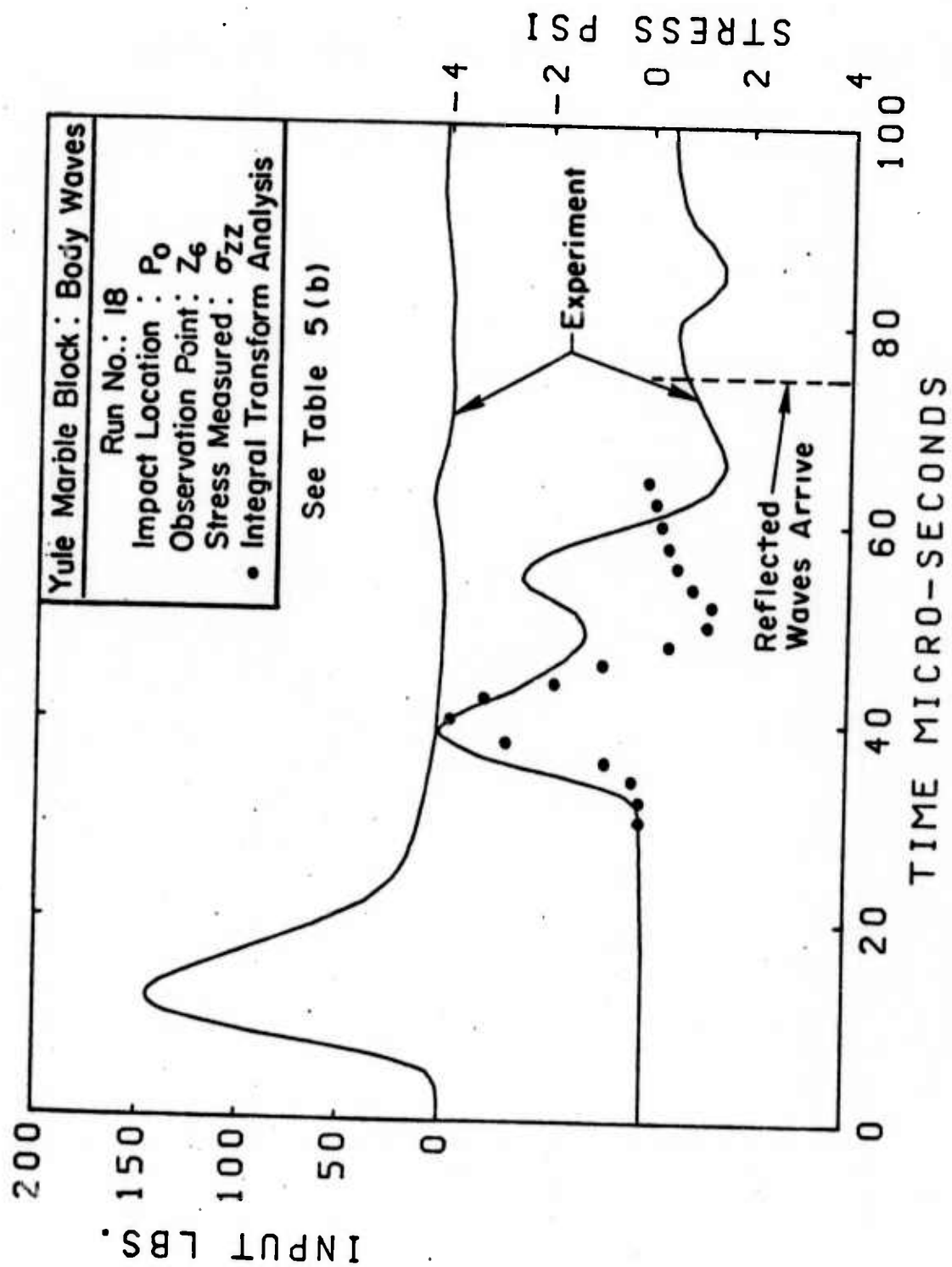


FIG. 35

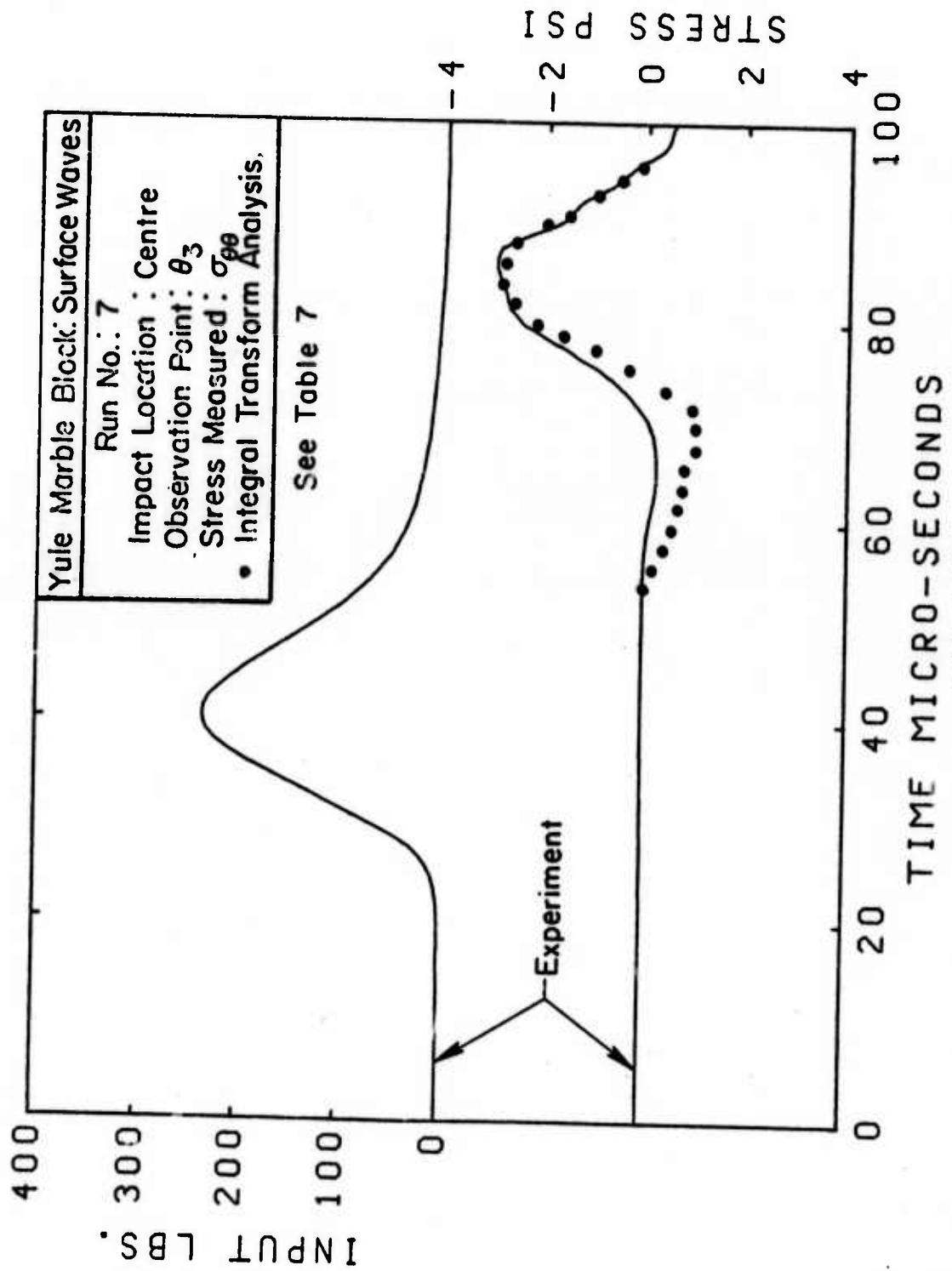
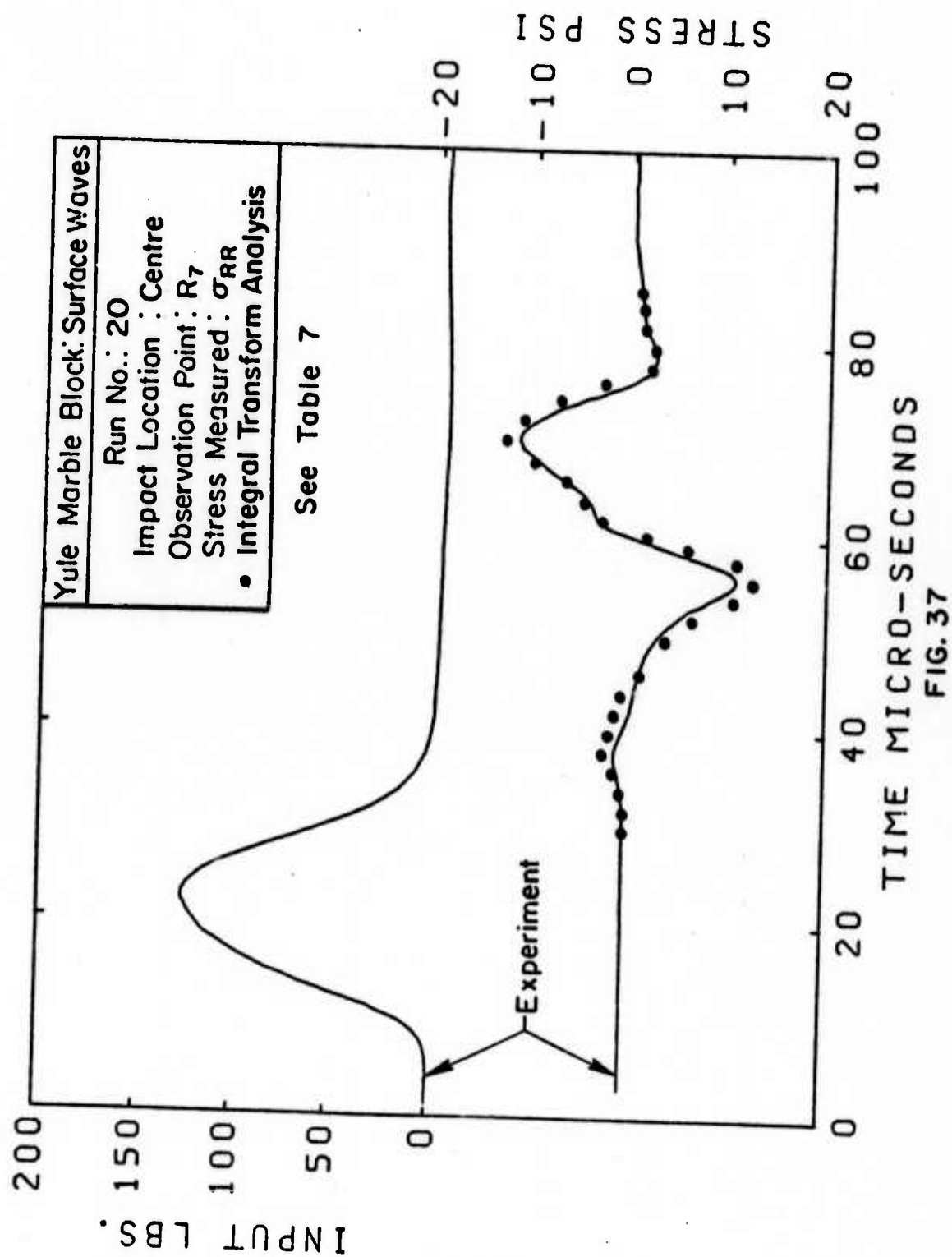


FIG. 36



D-19

APPENDIX D: DETERMINATION OF STATIC AND DYNAMIC MECHANICAL PROPERTIES
OF YULE MARBLE

DETERMINATION OF STATIC AND DYNAMIC MECHANICAL
PROPERTIES OF YULE MARBLE

I. Introduction

The application of any scientific or technological procedure to a material requires a precise knowledge of its response to both static and dynamic loading, whether for the purpose of understanding the phenomenological processes produced as the result of the application of forces, whether for the purpose of predicting events, or whether for the purpose of design and construction. In the case of rock, such information is vital in the areas of drilling and excavation, the analysis of foundations for the support of surface structures, and geophysical prospecting, to mention but a few. Large quantities of mechanical data have been collected about a variety of rocks in the past, but, to the author's knowledge, there has not been a concentration of tests on a single material by one investigator for the purpose of ascertaining the strength characteristics of this substance by a variety of techniques. This portion of the report details such efforts as applied to Colorado Yule marble, the material employed in the parallel theoretical and experimental investigations concerning wave propagation produced by surface impact on large blocks of this material that simulate a half-space.

Yule marble was chosen as the test material for a variety of reasons: (a) The rock has been the subject of extensive previous geological and petrographic examinations^{(1)(2)(3)*}, including the effects of strain rate at high temperatures and confining pressures⁽⁴⁾ and the nature of fabric changes under large hydrostatic pressures⁽⁵⁾⁻⁽⁸⁾; (b) The fabric is macroscopically homogeneous (with respect to wave lengths of interest) and nearly transversely isotropic with a well-defined crystal structure⁽⁶⁾⁽⁸⁾, and it can be secured in large sample sizes without faults

* Numbers in superiors indicate References listed at the end of the text.

or cracks. Thus, it is an ideal substance to be experimentally employed for the verification of wave propagation analyses utilizing transverse isotropy; and (c) Previous (9)(10) and concurrent surface and body wave studies were executed with the aid of two 24" x 24" x 10" blocks of this material furnished by the U. S. Bureau of Mines, Minneapolis. The investigations of Refs. (9) and (10) required the determination of some of the properties of the marble; however, some anomalies were observed that the present more detailed examination resolved. It should be mentioned that all the previous dynamic tests with the exception of the measurement of transit times of one of the two blocks (which were eventually utilized for the calculation of the elastic constants of the material) were performed on randomly obtained specimens. The samples utilized in the present investigation were all derived from a 5' x 2' x 1½" slab obtained from the Clervi Marble Company of San Francisco, California. Differences in the data cited here and that obtained from other previous and concurrent tests may thus, at least in part, be attributable to natural differences in composition and/or structure of the raw material (since no quality control could be exercised).

The general objectives of the present investigation consisted of the determination of the axis of symmetry and the mechanical properties of the marble, including fracture properties, as a function of strain rate; the effects of temperature, confining pressure, porosity, water content and similar parameters were not considered. Specifically, the location of the axis of transverse isotropy of the slab was obtained by crystallographic techniques; the five constants characterizing a transversely isotropic elastic material were obtained in tension and compression and under static and dynamic loading; the influence of strain rate and specimen orientation on the modulus and unconfined strength of tensile and compressive specimens was examined; and the nonlinear and/or anelastic behavior of the rock was characterized. Standard testing equipment was employed to secure the quasi-static

mechanical properties, while Hopkinson and split Hopkinson-bar procedures (cf. 11, 12) were utilized to derive the corresponding dynamic information. A considerable amount of developmental work was required to select specimen shapes that permitted fabrication without brittle failure occurring during the manufacturing process. In many cases, the test technique was verified by the use of aluminum specimens whose known properties could be checked against experimental results.

II. Physical and Geometrical Characteristics.

Yule marble has been described by Thill⁽³⁾ as a pure calcite marble with specific gravity of about 2.70 and grain sizes ranging from 0.3 mm to 0.5 mm with an average of 0.4 mm for the spherical specimen examined ultrasonically. Knopf⁽⁶⁾ observed a porosity of about 0.15 percent and called the crystalline calcite grains to be medium-sized ellipsoidal grains whose short axes are oriented predominantly normal to the marble "grain". It has been shown⁽⁶⁾⁽⁸⁾ that Yule marble displays a distinct pattern of preferred orientation of calcite optic axes. A 1000-point-count modal analysis indicated that the marble comprised about 99 percent calcite and 1 percent accessory minerals, notably biotite, epidote, magnetite and muscovite by volume.

The present 5' x 2' x 1½" test slab exhibited bedding planes as evidenced by the presence of grey bands of opaque mineral throughout the specimen. Although not totally uniform, the average normal to these planes is relatively constant and is located in the largest plane of the slab; this will be termed the Z-direction. The specific gravity of the material was found to be 2.81 with crystal sizes ranging from 0.2 mm to 0.7 mm and a mean of 0.5 mm. All test samples were cut from this slab and are identified by two letters followed by a single or two-digit number. The first letter shows the general coring location as indicated in Fig. 1, the second denotes the direction of coring for the sample, while the numbers identify a more initial position of the specimen in the slab.

The initial assumption of coincidence of the axis of transverse isotropy with the Z-axis, the average normal to the bedding planes, was verified by preparing a thin section cut from the slab (Fig. 1) perpendicular to the Z-direction and examining the orientation of each of 100 calcite crystals of the specimen. This was accomplished by recording the inclination of the universal stage incorporated in the crystallographic microscope that was required to produce the interference pattern of a crystal whose optical axis is perpendicular to a fixed direction⁽¹³⁾. Only those crystals with optical axis angles less than 50° with the bedding normal could be detected due to instrument limitations; however, 91 percent of the crystals were located within the observation region. Consideration of the visible domain, represented by that portion of the surface of a hemisphere enclosed by a 50° cone with the apex at the origin, indicates that the ratio of this area to that of the hemisphere is about 0.30. Consequently, a purely random crystal orientation such as found in the case of an isotropic material would indicate that 70 percent of the observed crystals (rather than 9 percent as found here) should be outside the zone of possible crystallographic examination. The highly anisotropic nature of this material is thus established.

The location of the crystal axes was found to be quite cylindrically symmetric with respect to the Z-axis, the initial assumption concerning the coincidence of the bedding plane normal with the axis of transverse isotropy appeared to be substantiated. This conclusion is based on the hypothesis that the distribution of optical properties is directly correlative with the orientation of macroscopic mechanical properties and that other rock characteristics, such as, for example, the orientation of cracks either also confirms this result or else is an effect of second order. This trend is strongly supported by evidence that velocity anisotropies obtained by ultrasonic measurement techniques on Yule marble coincide with crystallographic anisotropies corresponding to a transversely isotropic material⁽³⁾.

III. Quasi-Static Tests.

a) Compression.

Ten uniaxial compressive test specimens with a diameter of 1.05 in. were cored in each of the three principal directions using an oil-cooled diamond bit mounted on a specially converted milling machine. Nominal lengths of the samples were 2 in. for the Y- and Z-directions, while the slab thickness limited that in the X-direction to $1\frac{1}{2}$ in. The specimens were ground flat with an abrasive diamond wheel with a maximum difference of 0.0015 in. in the dimensions of the axis and two generators 90° apart. In spite of extreme care in the fabrication process, there is a possibility of the disturbance of the fabric relative to its virgin state, although it is expected that any such damage will have only secondary effects on the mechanical response of the samples.

BLH FAE-12-12S9L epoxy-backed strain gages with a length of $1/8$ ", a resistance of 120 ohms and a gage factor of 2.01 were mounted longitudinally with EPY-150 epoxy at the two ends of the midsection diameter of each specimen; for the G-series of samples (cored normal to the X-direction), a pair of transverse gages were additionally mounted in a similar manner near the specimen center. All gages were wired in series to eliminate any flexural components and were incorporated in an AC-excited bridge circuit; they were calibrated with the aid of shunting a known resistance across each gage pair. The compressive force applied through bearing plates by means of a 0-20,000 lb. capacity Instron testing machine was determined by a calibrated load cell. Both a variable time base strip chart recorder and a dual-trace oscilloscope were employed to record the strain and load histories. The arrangement was checked out by the determination of the known elastic constants for a 7075 aluminum test specimen.

Two specimens from each direction were tested to fracture at each of five strain rates ranging from $\dot{\epsilon} = 10^{-6}$ to 10^{-2} per second, yielding the results shown

in Figs. 2, 3, and 4 for the highest and lowest rate in each instance; apparently, rate effects are small or negligible in this domain. The curves characteristically exhibit three regions: an initial concave upward shape with an original tangent modulus E_1 up to about one-third of the failure stress, followed by a linear region with slope E_2 in the middle third of the stress range, followed by a concave-downward portion up to maximum stress σ_m which is always larger than failure stress σ_f . The average values for each of the three directions X, Y, and Z were $5.6, 6.6$ and 2.6×10^6 psi for E_1 and $8.9, 8.1$ and 5.8×10^6 psi for E_2 over the entire quasi-static range; there was far less variation between specimens for the linear modulus E_2 than for E_1 , where errors in its determination were estimated at 20 percent, the extremal values for the latter occurring in the X-direction at a rate of 0.9×10^{-2} per second and amounting to 6.9 and 4.4×10^6 psi, respectively, for the two specimens. The strain rates quoted were assumed to be uniform up to the value of $(2/3)\sigma_m$, but their values at fracture sometimes were considerably greater than this average.

In the region near fracture, strain recorded by the gages no longer is an accurate measurement of average cross-sectional specimen strain ϵ . Almost without exception, fracture paths initiate at the corners of the specimen and travel diagonally through along one failure plane. In the X and Y directions, these planes were invariably oriented such that their normal lay in the plane defined by the axis of the cylinder and a point lying in the Z-direction. Gages mounted such that this plane of failure traveled through them produced larger strain readings than those located away from the fracture path. This conclusion was reached after mounting four gages at 90° intervals at the midsection of both Y- and Z-direction specimens and comparing the stress-strain curves derived from the two orthogonal gage pairs as shown in Fig. 5. Gages on specimens in the X-direction were unintentionally located so that they were as far as possible from the fracture

path while those on specimens in the Y-direction were positioned such that the fracture path always passed through the gages. Thus, the apparent difference in material properties near failure -- X-direction specimens appearing brittle, while Y-direction samples exhibiting a region of large strains and low modulus -- is explained by the difference in gage location with respect to failure planes. Fig. 5 clearly indicates how the structure of the material is such that the assumption of one-dimensionality breaks down in the prefailure region.

Specimens in the Z-direction show no preference in fracture plane orientation, although they also split diagonally, sometimes accompanied by secondary cracks initiating at the bearing plates and running parallel to the cylinder axis. In the four-gage test, there was very little difference in strain between the two sets of gages even though the fracture passed directly through one set of transducers.

The maximum stress in the X-direction varied from about 8340 to 9400 psi over the strain-rate range of about 10^{-6} to 8×10^{-3} with maximum strains ranging from 982 to 1300×10^{-6} ; the corresponding values for the Y-direction were 7600 to 9300 psi for strains of about 3300 to 2100×10^{-6} and values for the Z-direction of $\sigma_m = 10,350$ to 16,500 psi at strains of 3070 to 4750×10^{-6} , respectively. The failure stress increased weakly with strain rate for directions in the plane of isotropy, and more sharply with this parameter along the axis of transverse isotropy. In most cases the fracture stress was somewhat lower than the failure stress, but it was difficult to determine this parameter precisely, particularly at high strain rates.

The constitutive equations for a transversely isotropic elastic material, given by

$$\begin{aligned}
 \epsilon_{xx} &= \frac{1}{E} (\sigma_{xx} - \mu \sigma_{yy}) - \frac{\mu'}{E'} \sigma_{zz} & \epsilon_{yz} &= \sigma_{yz} / 2G' \\
 \epsilon_{yy} &= \frac{1}{E} (\sigma_{yy} - \mu \sigma_{xx}) - \frac{\mu'}{E'} \sigma_{zz} & \epsilon_{xz} &= \sigma_{xz} / 2G' \\
 \epsilon_{zz} &= -\frac{\mu}{E} (\sigma_{xx} + \sigma_{yy}) + \frac{1}{E'} \sigma_{zz} & \epsilon_{xy} &= \frac{\sigma_{xy}}{2G} = \frac{(1+\mu)}{E} \sigma_{xy}
 \end{aligned} \tag{D-1}$$

contain five elastic constants: E , μ and E' , μ' denote Young's modulus and Poisson's ratio in the plane of isotropy X-Y and parallel to the axis of transverse isotropy, Z, respectively. The fifth constant G' is the shear modulus in any plane perpendicular to the plane of isotropy. Four elastic constants can be obtained with the aid of Eqs. (D-1) by measuring axial load and longitudinal and transverse strain in uniaxial specimens oriented parallel to the Y and Z-axes, while G' can be determined from values of these quantities in a specimen cut parallel to a line 45° counterclockwise from the Z-axis in the X-Y plane. Transformation of both stress and strain tensors yield the relation

$$G' = \frac{\sigma_{45^\circ}}{2(\epsilon_{45^\circ L} - \epsilon_{45^\circ T})} \quad (D-2)$$

where subscripts L and T refer to longitudinal and transverse strain, respectively, and 45° refers to the specimen orientation.

These constants were evaluated from specimens 1.05" x 2" long cut along the Y, Z and 45° directions as indicated by the G-series in Fig. 1. The samples were first loaded from 0 to 1200 psi and then unloaded at about 100 psi/sec for seven cycles in the Instron machine and then loaded and unloaded to 6000 psi at a rate of about 300 psi/sec for three additional cycles. Typical results are shown in Fig. 6, 7, and 8. The material exhibits a "first cycle" effect as shown in Fig. 8: a permanent deformation accompanies each virgin stress level, but upon subsequent loading to this level, there is hysteresis, but no appreciable permanent set. The ratio of transverse to longitudinal strain was found to be non-linear (or perhaps bilinear) for both Y- and Z-direction specimen. In order to avoid the problems of non-linearity and first cycle variations, the elastic constants were determined from the seventh 0-1200 psi loading cycle as

$$E_1 = 4.7 \times 10^6 \text{ psi}; \mu_1 = 0.13; E'_1 = 2.3 \times 10^6 \text{ psi}; \mu'_1 = 0.05; G'_1 = 1.4 \times 10^6 \text{ psi}$$

b) Tensile Tests

After two initially-selected specimen geometries proved to be unsatisfactory, 0.768-in. diameter rods were cored from the Y, Z and 45° directions with the aid of a converted water-cooled gravity drill press and cut to lengths of approximately 5-3/4 in. by a diamond saw. Two 3/4-in. diameter x $1\frac{1}{2}$ in. threaded aluminum endcaps were glued flat to the specimens with Scotchweld Structural Adhesive and wrapped with transparent tape so that their diameter approached that of the rock cores.

In order to estimate the magnitude of the bending stresses that are invariably extant to some extent in any tensile specimen during testing, three gages were mounted at 120° intervals around the midsection of a sample yielding readings of ϵ_1 , ϵ_2 and ϵ_3 . A simple analysis⁽¹⁴⁾ shows that the pure tensile strain ϵ_t , the angle between the neutral axis and the gage reading ϵ_1 , namely θ_0 , and the peak bending stress σ_b are given by

$$\epsilon_t = \sigma_t/E = \frac{1}{3} [\epsilon_1 + \epsilon_2 + \epsilon_3] ; \tan \theta_0 = \frac{\sqrt{3}[\epsilon_1 - \epsilon_t]}{2\epsilon_2 + \epsilon_1 - 3\epsilon_t}$$

$$\sigma_b = \frac{(\epsilon_1 - \epsilon_t)}{\sin \theta_0} E \quad (D-3)$$

With a value of $E = 7 \times 10^6$ psi, the ratio of the outer fiber bending stress to average tensile stress was about 15 percent for a specimen loaded about two-thirds to fracture.

Four specimens each from the Y- and Z-directions, supplied with two diametrically opposed strain gages at the rock midsection were loaded to fracture at various strain rates with results as shown in Figs. 9 and 10; all of the Y-direction samples broke at the glue joint, whereas two of the four Z-direction specimens broke near the gages. The data presented are most likely in error since (a) the measured strain is probably smaller than that at the interface where failure generally occurred, (b) the fracture stress is underestimated since a stress concentration

apparently exists at the interface, and (c) the apparent increase in fracture stress with strain rate may be partly due to the property of the glue rather than that of the rock.

In order to overcome these deficiencies, an initial attempt was made to produce a special contour previously employed for fracture investigations of bone⁽¹⁵⁾ that had been photoelastically and analytically shown to yield a nearly uniform stress distribution across the section⁽¹⁶⁾, but the production of the geometry proved to be very time-consuming and, further, most often resulted in specimen failure during fabrication. A contoured specimen geometry was then machined from a 3/4-in. diameter cylinder with a length of 2-7/16", consisting of a central 15/16" long reduced section exhibiting a uniform 3/8" long region with a diameter of 1/2 in. where a pair of gages was attached, and end fillets of 1/4-in. radius that did not break in the manufacturing process. Contouring by means of sandpaper applied to a rotating workpiece yielded an ellipsoidal section exhibiting a distinct "grain" and requiring the use of a powertool to fabricate a cylindrical test specimen. It was subsequently determined analytically that a 3/4-in. radius fillet would have been more satisfactory by significantly reducing stress concentrations in the region of the section change.

Table 1 presents the results of the quasi-static tensile tests both for the 3/4-in. diameter by 6" long and special contour specimens, including two special samples represented by the last two entries that were examined at comparable strain rates to provide a direct comparison of the effect of a change in the test section geometry on mechanical properties. Here a much lower total fracture strain was noted for the contoured specimens, although the maximum stress σ_m for the two cases agreed closely. The gages were found to be located at the maximum possible distance from the fracture path and thus yield different results as explained in conjunction with Fig. 5. Fig. 11 shows the stress-strain curves for three contoured Z-direction samples. While there appears to be an increase with strain rate of

initial modulus E_1 for the Y-direction, this does not appear to be the case along the axis of transverse isotropy.

IV. Creep Tests.

Creep tests were performed on both tensile and compressive specimens in order to determine the approximate stress levels where viscoelastic effects begin to dominate the material behavior. Instrumented compression specimens fabricated as described previously were loaded in approximately 700 psi increments at a rate of 700 psi/sec by an MTS testing machine in the constant load mode. Each level was maintained for 100 sec, after which the next load increment was applied; the strain gage output was continuously monitored. The results are shown in Figs. 12 and 13 for the Y- and Z-directions, respectively. An additional creep test on a Z-direction sample involving a load of 3600 psi applied for 15 minutes yielded less than 20 μ in/in of creep strain. It is evident from these data that there is no significant creep except in the vicinity of failure which appears to be brought about by this flow.

Rock specimens equipped with aluminum endcaps as employed in the quasi-static tensile tests were rapidly loaded to a constant stress level of up to 230 psi by the attachment of weights to the lower loading chain of the Instron machine. The constant strain response for loads applied up to 10 minutes indicated the absence of noticeable viscoelastic effects in this range. Employment of higher stress levels required the use of the Instron machine in a constant load capacity; however, this mode of operation limited loading rates to about 30 psi/sec so that only the last part of the creep curves were obtained. Here, too, with stress levels up to 650 psi, no significant viscoelastic behavior was observed either in the Y- or Z-direction.

V. Dynamic Tests.

a) Hopkinson-Bar Experiments.

One Y- and one Z-direction Hopkinson bar, samples JZ and IY, respectively, were fabricated by gluing together three appropriately oriented 3/4-in. diameter rods 6" long, similar to those employed in the tension tests, and were supplied with two sets of diametrically opposed longitudinal gages mounted on the central section about 4-13/16" apart as well as with one transverse pair immediately adjacent to the farthest longitudinal transducer set. Another specimen, M45, but 5-3/4" long was cored at 45° in the Y-Z plane with identical bedding to IY and instrumented with a single pair of longitudinal and transverse gages, the former being located 2-5/16" from the rock impact end. All specimens were pre-faced by 3/4-in. diameter x 1/2" aluminum end caps attached with wax to prevent local fracturing. They were held vertically in an arrangement permitting loading by the impact of a 1/2-in. diameter steel ball dropped from a height of 22 1/2 in. through an aligning tube onto the aluminum cap. The strain pulses detected by the gages were recorded simultaneously by a 565 dual-beam Tektronix oscilloscope whose amplifier had a bandpass flat to 3 megahertz using a potentiometric circuit that permitted gage calibration by observation of the effect of inclusion of known shunt resistors in the loop. Triggering of the device was achieved from the signal generated by a piezoelectric crystal taped to the side of the specimen. Peak arrival times were used to calculate both rod wave velocities c_0 and the ratio of transverse to longitudinal strains for both compressive and tensile pulses, the latter being generated by reflection at the distal bar end. Wave speed determination for specimen M45 required the use of both incident and reflected pulses.

A uniaxial elastic analysis without correction factors was employed to evaluate the dynamic elastic constants. Since minimum pulse lengths of 6 inches prevailed throughout the tests, yielding a bar radius to wavelength of about 0.06, geometric

dispersion will be minimal⁽¹⁷⁾ and this theory should accurately describe the phenomenon. This was substantiated by the virtual congruence of the strain pulses at the two gage stations. Again assuming transverse isotropy, the constants were determined from the relations

$$\begin{aligned}
 E_d &= \rho c_o^2 & \mu_d &= \frac{\epsilon_T}{\epsilon_L} & \text{for the rod in the Y-direction} \\
 E'_d &= \rho c_o^2 & \mu'_d &= \frac{\epsilon'_T}{\epsilon'_L} & \text{for the rod in the Z-direction (D-4)} \\
 & \quad \epsilon_{45^0 L} (c_{o45} / \rho)^{\frac{1}{2}} \\
 G' &= \frac{\epsilon_{45^0 L} (c_{o45} / \rho)^{\frac{1}{2}}}{2[\epsilon_{45^0 L} - \epsilon_{45^0 T}]} & & & \text{for the rod at } 45^\circ \text{ to Y-Z (M45)}
 \end{aligned}$$

where ρ is the mass density and the subscript 45° refers to data from bar M45. It should be noted that the results are not affected at all or negligibly by the presence of glue joints due to the manner of construction of the specimens. The results of these tests are summarized in Table 2.

b) Split Hopkinson-Bar Experiments.

The split Hopkinson-bar tests⁽¹²⁾ were performed not only for the purpose of obtaining the dynamic elastic constants of the material by an alternative technique, but also to examine the strength characteristics of the substance at loading rates higher than those produced in the quasi-static experiments. The sample examined consisted of the contoured specimen employed for the quasi-static tensile tests; its size is large compared to that usually employed in this type of test, but it was believed that this geometry represented the minimum distance necessary to prevent the alteration of macroscopic mechanical properties due to the fabrication process. The shape exhibited the advantages of known boundary conditions on the end faces of the contoured region that is integral with the larger diameter rock cylinder and consequent elimination of any frictional effects, the use of identical geometries for both tensile and compressive tests and comparison with quasi-static results for the same geometry, and the localization of the maximum stress in the vicinity of the strain gage location at the contour center approximating the achievement of

the goal of simultaneous stress and strain measurement at the same position. Concomitant disadvantages include the difficulties of specimen fabrication and the problem of accurate determination of the stress history for short pulses and/or anelastic material properties. However, since the ratio of specimen length to wavelength is less than $1/8$ and the material is nearly elastic/brittle, the second objection is mitigated.

Fig. 14 presents the configuration of the split Hopkinson bar tests;⁽¹⁵⁾ a compressive and essentially one-dimensional pulse of about 200 μ sec duration produced by the impact of $\frac{1}{2}$ -in. diameter 30° cylindro-conical hardened steel projectile fired from a pneumatic propulsion device travels through an elastic aluminum loading bar to the specimen which passes the major portion of the wave onto the succeeding output or record bar where the transmitted stress history is recorded by a pair of coupled longitudinal strain gages. The strain history is monitored by a pair of gages at the center of the contoured section. An important feature of these waveforms is the nearly linear wavefront that yields a relatively constant strain rate. Tensile pulses were produced with the aid of a somewhat shorter projectile by permitting the initial transient to reflect at the distal end of the unit and reversing the role of the loading and recording bars, with the stress histories deduced from strain outputs on the loading bar. The transient recording and triggering arrangement has been previously described.

Each specimen was cemented between the loading and recording bars by means of Scotchweld Structural Adhesive; the entire unit was carefully aligned both in a horizontal position and coaxially with the centerline of the gun to minimize the introduction of bending. Two other steps were taken to reduce flexural effects: a bending suppressor consisting of a 1" O.D. x 6" long section of acrylic tubing $1/8$ " thick, which was successfully employed in previous Hopkinson bar experiments⁽¹⁵⁾, was slip-fit over the loading bar $4\frac{1}{2}$ in. from the specimen, and the length of the loading bar was chosen as 5 feet to reduce any interference by the much more slowly

travelling flexural components with the primary longitudinal pulse in the test section.

The stress history at the center of the gage section was deduced from the strain gage outputs on the aluminum bar with the aid of uniaxial elastic wave propagation theory. The assumptions present in such an analysis include the uniform distribution of stress across the section and the neglect of lateral inertia and shear as well as the hypothesis of plane sections, the elastic behavior of the specimen and small values of the measured strain, the equivalence of a system composed of a uniform cylindrical rod of the same length and constant minimum diameter for the contoured specimen actually utilized, and the absence of an effect of an initial compressive wave on the tensile properties of the sample. The equivalent system hypothesized here actually represents an extremal case since the discontinuity actually present is not as severe. The other assumptions are either reasonable or have been deliberately satisfied by the choice of the experimental conditions.

Based on the above considerations, the stress at the center of the test specimen $\sigma(t)$ can be evaluated from measured data by means of the relation

$$\sigma(t) = \frac{A_a}{A_r} E_a \epsilon_r(t) \left[t - \left(\frac{l_r}{2c_{or}} + \frac{l_a}{c_{oa}} \right) \right] \quad (D-5)$$

where A is the cross-section area, t is time, l_r is the specimen length, l_a is the distance of the record gage from the rock-aluminum interface, and subscripts r and a refer to rock and aluminum, respectively. The most serious error in the proper application of Eq. (D-5) results from even small inaccuracies in the time lag t_d between stress and strain readings and not in the analytical model of the process. Utilizing the relations developed for one-dimensional wave propagation in bars with discontinuities⁽¹⁸⁾, the abrupt change in geometry involved providing the equivalent system for the use of Eq. (D-5) yields a stress-strain curve with only

a 5 percent higher modulus and maximum stress, albeit with noticeable hysteresis relative to the correct results produced for an infinite ratio of wavelength to specimen length^(*).

A total of nine contoured specimen from the Y- and Z-direction were tested in tension or compression by means of the split Hopkinson bar technique. Typical results are shown in Figs. 15, 16, 17 and 18, where d represents the eccentricity of the striking projectile. A summary of the tests is presented in Table 3.

VI. Discussion and Conclusions.

The accuracy of the assignment of the Z-direction as the axis of transverse isotropy as shown in Fig. 1 is supported by optical observation of the preferred orientation of calcite crystals, by visual examination of the slab bedding planes, by the "grain" of the rock experienced when specially-contoured tensile and split Hopkinson bar specimens were fabricated, by the maximum strength anisotropy observed experimentally, and by the anisotropy of initial and secondary moduli associated with the static stress-strain curves obtained. If maximum compressive stress transverse isotropy is to coincide with the Z-axis, the maximum compressive stress in the X- and Y-directions should be identical. Using the formula suggested by Obert et al ⁽¹⁹⁾ to correct for the short column length used in the X-direction specimens,

$$\sigma = \sigma_0 \left(0.8 + \frac{0.2}{L/D} \right) \quad (D-6)$$

where $\sigma = \sigma_0$ at $L/D = 1$, L is the specimen length and D is the specimen diameter, X-direction specimens exhibit compressive strengths approximately 5% higher than Y-direction specimens. However, Z-direction specimens have compressive strengths from 38% to 77% higher, depending on strain rate. From the data of Section IIIa, the initial modulus E_1 and secondary modulus E_2 show the same anisotropy; thus, the orientation of the axis of transverse isotropy for the slab is well established.

The determination of the five elastic constants from quasi-static compression

* cf. Thesis by S. P. Howe

tests was hampered by the fact that the material exhibited a hysteresis loop even at low stress levels. Another serious problem was presented by the existence of an apparent "first cycle" effect such as shown in Fig. 8. At stresses below 300 psi, this effect could be neglected permitting the calculation of "elastic constants"; however, the extremely low strain at this level prevented the determination of accurate value results. It is tempting to ignore the initial non-linear region of the stress-strain curve and consider only elastic constants based on the region $\frac{\sigma_m}{3}$ to $\frac{2\sigma_m}{3}$. This concept suffers from two deficiencies: the region is only one third the stress range of the material and the generalized Poisson's ratio μ and μ' are not constant in this region. In the range $\frac{2\sigma_m}{3}$ to fracture, the instantaneous tangent modulus decreases as stress increases. Since the creep tests performed indicated a strong time dependence at stresses higher than $\frac{2\sigma_m}{3}$, any hope of the existence of a linear elastic constitutive equation in that region vanishes.

The stress-strain curves from quasi-static tension tests, such as Figs. 9 and 10, were linear only at very low stress levels. In contrast to the compression tests, the instantaneous tangent modulus continued here to decrease with increasing stress. The values of E_1 in tension agree closely with those of E_2 in compression while the magnitudes of E_1' in tension lie between those of E_1' and E_2' in compression.

In the range of quasistatic strain rates employed, 10^{-7} to 10^{-2} per second, the general shape of the stress-strain curves did not change. Although maximum stress increases with increased strain rate, there seems to be virtually no rate effect on the initial or tangent modulus in this domain. A comparison between compressive and tensile static and dynamic moduli is presented in Table 1 of the main report. The dynamic data is generally higher than corresponding static values; this effect is greater in compression than tension, and greater in the Y- than in the Z-direction. Values obtained using Hopkinson or split Hopkinson bars are similar in spite of the difference in the strain regions over which the moduli were computed.

Ricketts⁽⁹⁾⁽¹⁰⁾ obtained the static elastic constants for one of the marble blocks employed in the present wave propagation tests by cutting out small wedges from one edge and subjecting the samples to compressive tests in an Instron machine at the rate of 0.01 in/min. The specimens were chosen along directions believed to be principal axes; however, the orientation deviates by about 15° from the axis of elastic symmetry selected in the present tests. He also obtained four corresponding dynamic constants for the same block by p-wave velocity measurements in different directions; the fifth constant could not be obtained without an actual shear wave measurement which was not executed. Consequently, this quantity was scaled upwards from its static value by the average increase of the other constants under dynamic conditions. These constants are compared in Table 4 with the results from the wave velocity measurement utilizing the embedded crystals that also involve the same block as well as the compressive Hopkinson bar data of the present investigation for the initial (or tangent) modulus. It should be emphasized that the latter data were obtained from a different parent block and are based on the values given in Table 1 of the main part. The conversion of the moduli E , E' , G' and Poisson ratios μ and μ' to the stiffness coefficients c_{ij} is accomplished by means of the relations⁽⁹⁾

$$\begin{aligned} c_{11} &= \frac{1}{2} \left[\frac{1}{E'S} + \frac{E}{1-\mu} \right] ; \quad c_{12} = \frac{1}{2} \left[\frac{1}{E'S} - \frac{E}{1-\mu} \right] ; \\ c_{13} &= \frac{\mu'}{E'S} ; \quad c_{33} = \frac{1-\mu}{ES} \quad \text{and} \quad c_{44} = G'; \quad S = \frac{1}{E'} \left(\frac{1-\mu}{E} \right)^2 - 2 \left(\frac{\mu'}{E'} \right)^2 \end{aligned} \quad (D-7)$$

The values of the elastic constants obtained in the Hopkinson bar tests with specimens cored from the marble slab are generally somewhat higher than those derived from the internal velocity measurements of the marble block, but lower than the corresponding data obtained by Ricketts⁽¹⁰⁾. It is believed that there may be a systematic error in the wave speed data due to an inability to account for circuit delay in the triggering of the initial signal in these experiments,

yielding a shorter transit time and, consequently, a higher value of the elastic constant. It is also clear that it might be possible to obtain values of the dynamic constants lower than presumably corresponding static values if the former are based on values of the initial tangent modulus, whereas the latter are calculated from the slope of the middle third of the compressive stress-strain curve. Comparison between any constants should always be executed at approximately the same strain level and strain rate and in the same mode of loading. A comparison of the moduli and Poisson ratios obtained in the present sequence of tests is presented in Table 1 of the main body of the report; dynamic constants uniformly exhibited higher values than the corresponding static magnitudes.

The variation of compressive and tensile strength as a function of strain rate is presented in Figs. 19 and 20, respectively. Increased maximum compressive stress with increased strain rate is more pronounced along the axis of transverse isotropy while this trend is reversed in tension. These results reinforce an intuitive feeling for Yule marble as a material extremely weak in tension, particularly when tensile forces act perpendicular to the bedding planes.

The creep tests performed, although of a preliminary nature, provide additional insight into the mechanical response of the material. The test results imply that Yule marble cannot be treated as a brittle solid even at ambient temperatures and pressures. It appears that time effects become important to material response at stresses near $\frac{2\sigma_m}{3}$ for compressive loading. It must be emphasized that these tests point to the presence of some time dependence and the importance of this effect at stresses above $\frac{2\sigma_m}{3}$ in a small range of quasi-static strain rates rather than an attempt to formulate a complete constitutive equation for the material. Tensile tests also indicate little time dependence at low stress levels but a definite time-dependence near failure.

In conclusion, it may be stated that the characteristics of this particular rock, homogeneous and of low order anisotropy as it is, present major problems relative to an attempt to formulate a three-dimensional constitutive equation. Initial elastic constants are valid only for extremely small strains. Tensile and compressive moduli differ. The material exhibits a "first cycle" effect. The rock is not brittle but rather has some small time-dependent plastic region. Although the general shape of stress-strain curves both along the axis of elastic symmetry and perpendicular to it are of a characteristic shape and show little time dependence at quasi-static strain rates, hysteresis accompanies unloading at any stress level above the small region where the initial elastic constants are valid. Dynamic elastic constants are higher than corresponding static values. In the dynamic range of strain rates, tensile and compressive elastic constants differ significantly. As a result, Yule marble is "characterized" by a set of experimental data rather than an analytical formulation and does not conform to any published constitutive equation cited in the literature to date.

REFERENCES

- (1) Ferreira, M. P. and Turner, F. J., "Microscopic Structure and Fabric of Yule Marble Experimentally Deformed at Different Strain Rates", Jour. Geol., 72, 861, 1964.
- (2) Lepper, H. A., "Compression Tests on Oriented Specimens of Yule Marble", Amer. Jour. Sci., 247, No. 8, 570, 1949.
- (3) Thill, R. E., Willard, R. J., Bur, T. R., "Correlation of Longitudinal Velocity Variation with Rock Fabric", Jour. Geo. Phy. Res., 74, 1969.
- (4) Heard, H. C., "The Effect of Large Changes in Strain Rate in the Experimental Deformation of Yule Marble", Jour. Geol., 71, 162, 1963.
- (5) Griggs, D. and Handin, J., eds., Rock Deformation, Memoir 79, Geol. Soc. Amer., New York, N.Y., 1960.
- (6) Knopf, E. B., "Fabric Changes in Yule Marble After Deformation in Compression, I: Preliminary Petrofabric Analysis of Yule Marble", Amer. Jour. Sci., 247, 433, 1949.
- (7) Turner, F. J., "Nature and Dynamic Interpretation of Deformation Lamellae in Calcite of Three Marbles", Amer. Jour. Sci., 251, 276, 1953.
- (8) Turner, F. J., "Preferred Orientation of Calcite in Yule Marble", Amer. Jour. Sci., 247, 593, 1949.
- (9) Ricketts, T. E., "Sphere Impact on an Anisotropic Half-Space", Ph.D. Dissertation, University of California, Berkeley, 1970.
- (10) Ricketts, T. E. and Goldsmith, W., "Dynamic Properties of Rocks and Composite Structural Materials", Int. Jour. Rock Mech. Min. Sci., 7, 315, 1970.
- (11) Goldsmith, W., Austin, C. F., Wang, C. C., and Finnegan, S., "Stress Waves in Igneous Rocks", Jour. Geophys. Res., 71, 2055, 1966.
- (12) Hauser, F. E., "Techniques for Measuring Stress-Strain Relations at High Strain Rates", Exp. Mech., 6, 395, 1966.
- (13) Bloss, F. D., An Introduction to the Methods of Optical Crystallography, Holt, Rinehart and Winston, New York, 1967.
- (14) Howe, S. P., "Macroscopic Mechanical Properties of Yule Marble", M. S. Thesis, University of California, Berkeley, 1973.
- (15) Lewis, J. L., "Dynamic Mechanical Properties of Compact Bone", Ph.D. Dissertation, University of California, Berkeley, 1972.
- (16) Haywood, Designing by Photoelasticity, Chapman and Hall, London, 336, 1952.

- (17) Davies, R. M., "A Critical Study of the Hopkinson Pressure Bar", Phil. Trans. Roy. Soc., London A, 240, 375, 1948.
- (18) Kenner, H. K. and Goldsmith, W., "One-Dimensional Wave Propagation through a Short Discontinuity", Jour. Acoustical Soc. Amer., 45, 115, Jan. 1969.
- (19) Obert L., and Duvall, W. I., Rock Mechanics and the Design of Structures in Rock, John Wiley and Sons, Inc., New York, 1967.

CAPTIONS FOR FIGURES

- Fig. 1 Directions of Samples Procured from Marble Slab
- 2 Quasistatic Compression Data in the X-Direction
- 3 Quasistatic Compression Data in the Y-Direction
- 4 Quasistatic Compression Data in the Z-Direction
- 5 Quasistatic Compression Data from Four Gages on the Sample
- 6 Quasistatic Compressive Loading and Unloading Stress-Strain Curve for 3 Samples
- 7 Quasistatic Compressive Loading and Unloading Stress-Strain Curve for 3 Cycles of Sample GY-11
- 8 Quasistatic Compressive Loading and Unloading Stress-Strain Curve for 3 Cycles of Sample GZ-13
- 9 Quasistatic Tensile Stress-Strain Curves for Y-Direction Samples
- 10 Quasistatic Tensile Stress-Strain Curves for Z-Direction Samples
- 11 Quasistatic Tensile Stress-Strain Curves Using the Contoured Specimen Shown in Fig. 24b
- 12 Y-Direction Compression Creep Test Results
- 13 Z-Direction Compression Creep Test Results
- 14 Split Hopkinson Bar Geometry
- 15 Stress-Strain Histories from a Split Hopkinson Test on Specimen LY-12-1
- 16 Stress-Strain Histories from a Split Hopkinson Test on Specimen JZ-9-2
- 17 Stress-Strain Histories from a Split Hopkinson Test on Specimen LY-12-2
- 18 Stress-Strain Histories from a Split Hopkinson Test on Specimen JZ-11-2
- 19 Effect of Strain Rate on Maximum Compressive Stress
- 20 Effect of Strain Rate on Maximum Tensile Stress

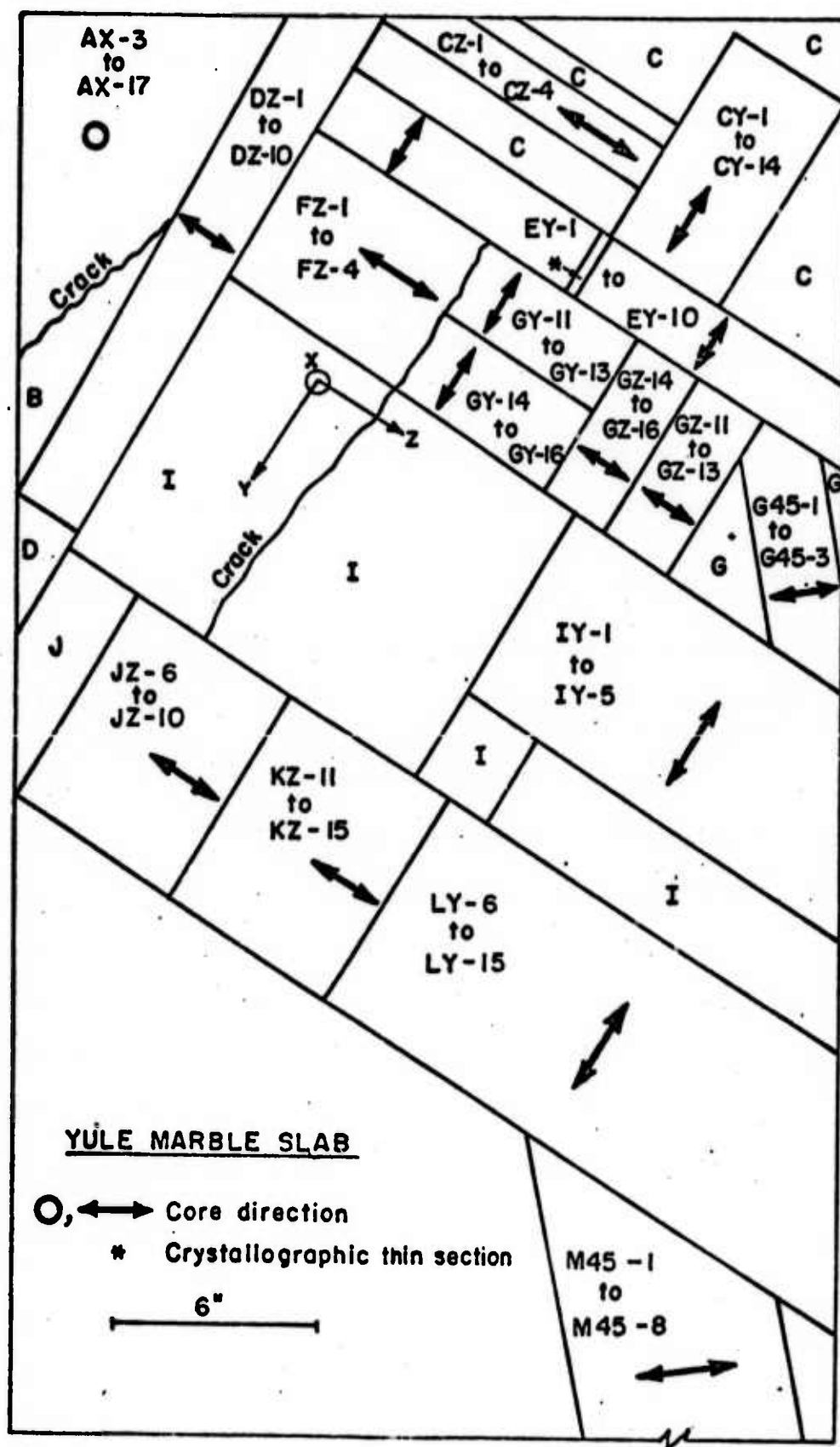


FIG. 1

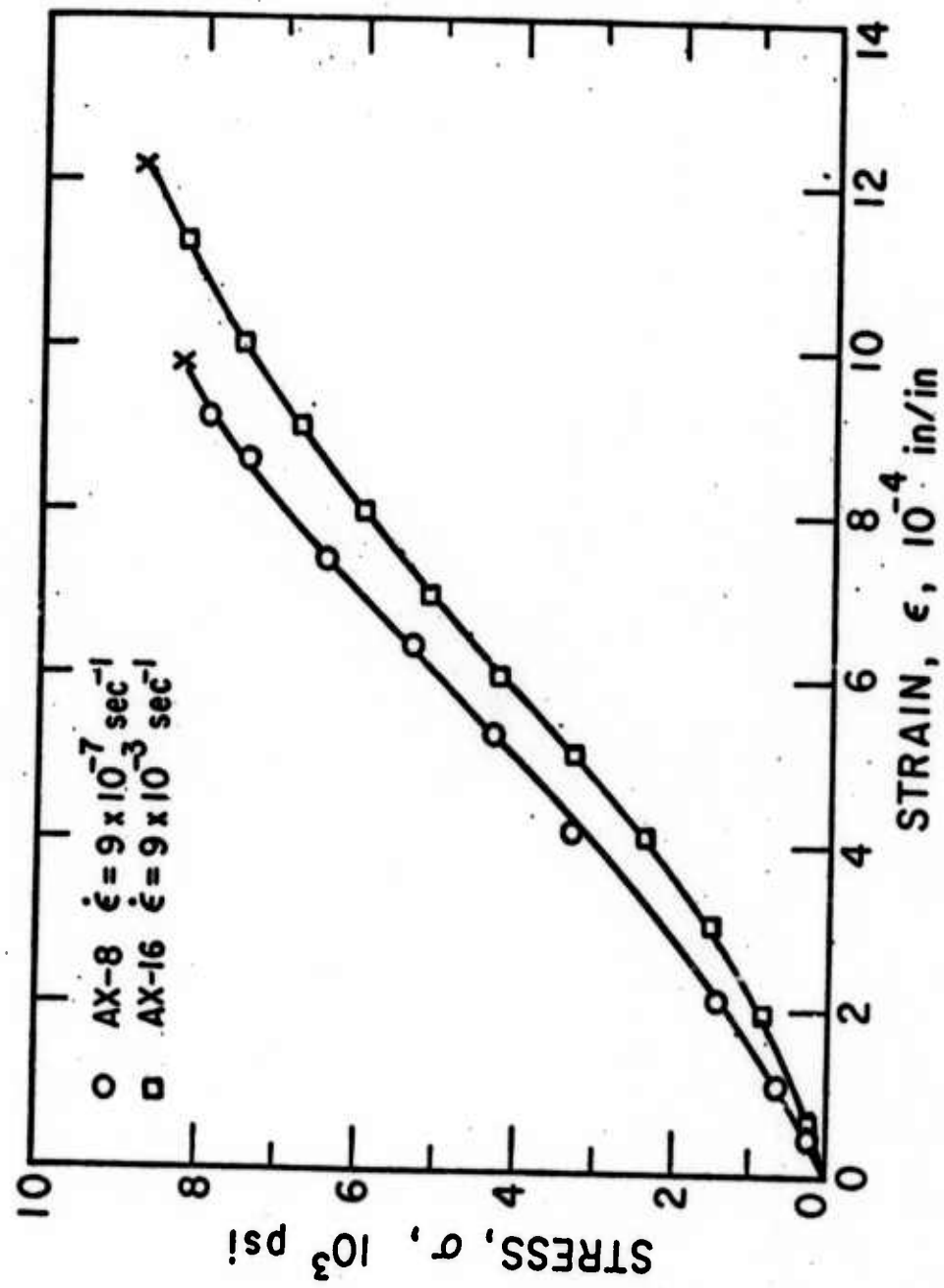


FIG. 2

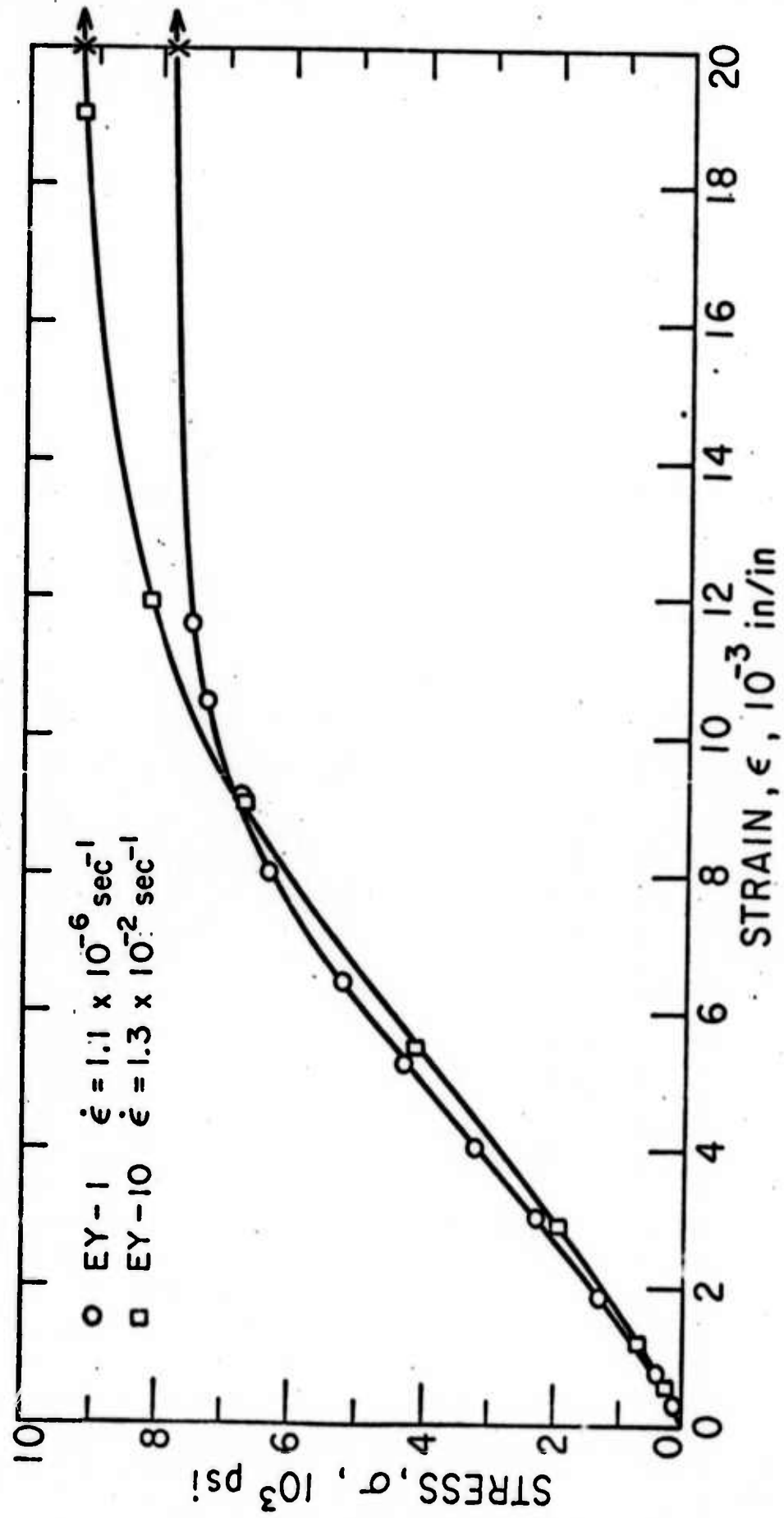


FIG. 3

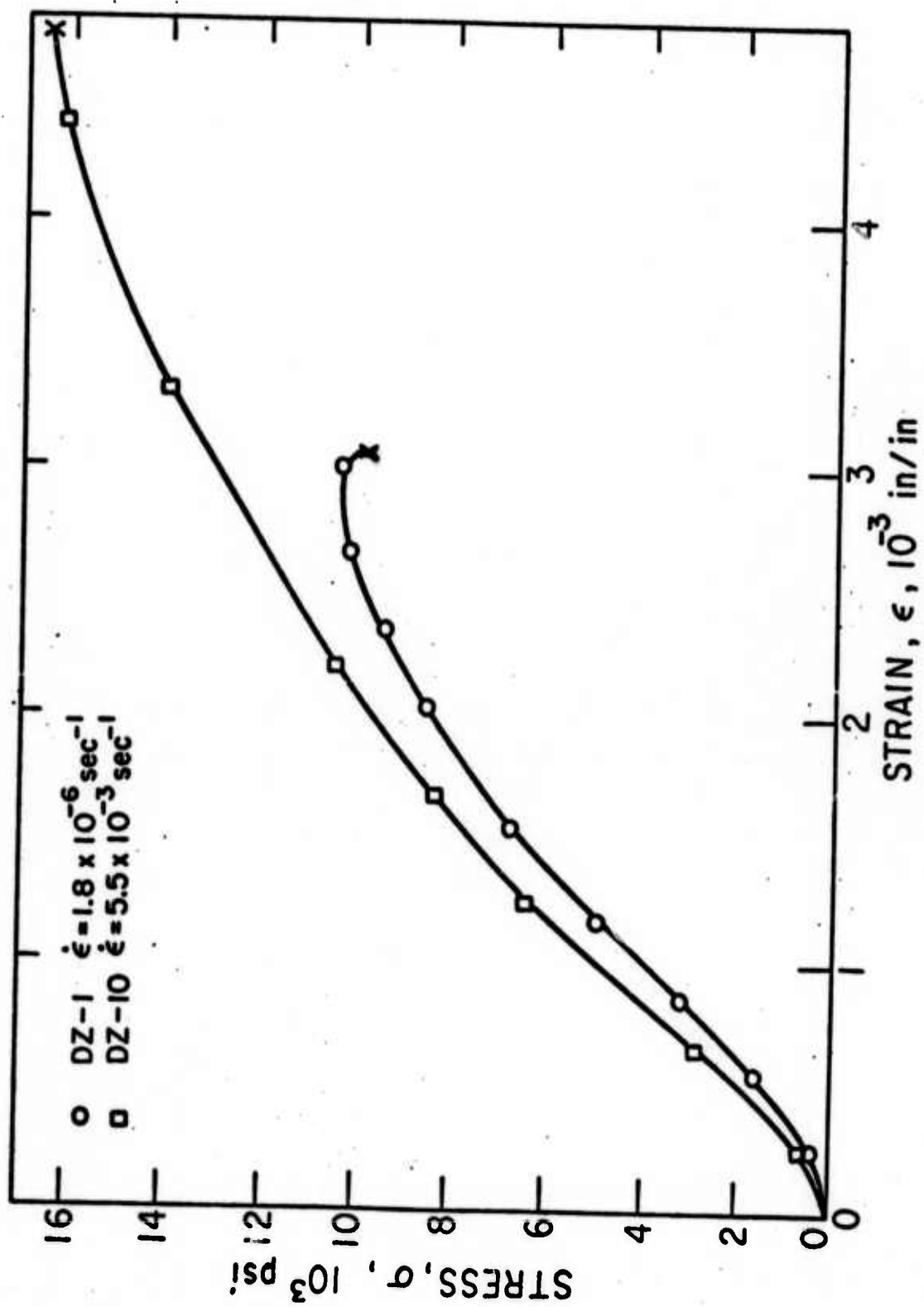


FIG. 4

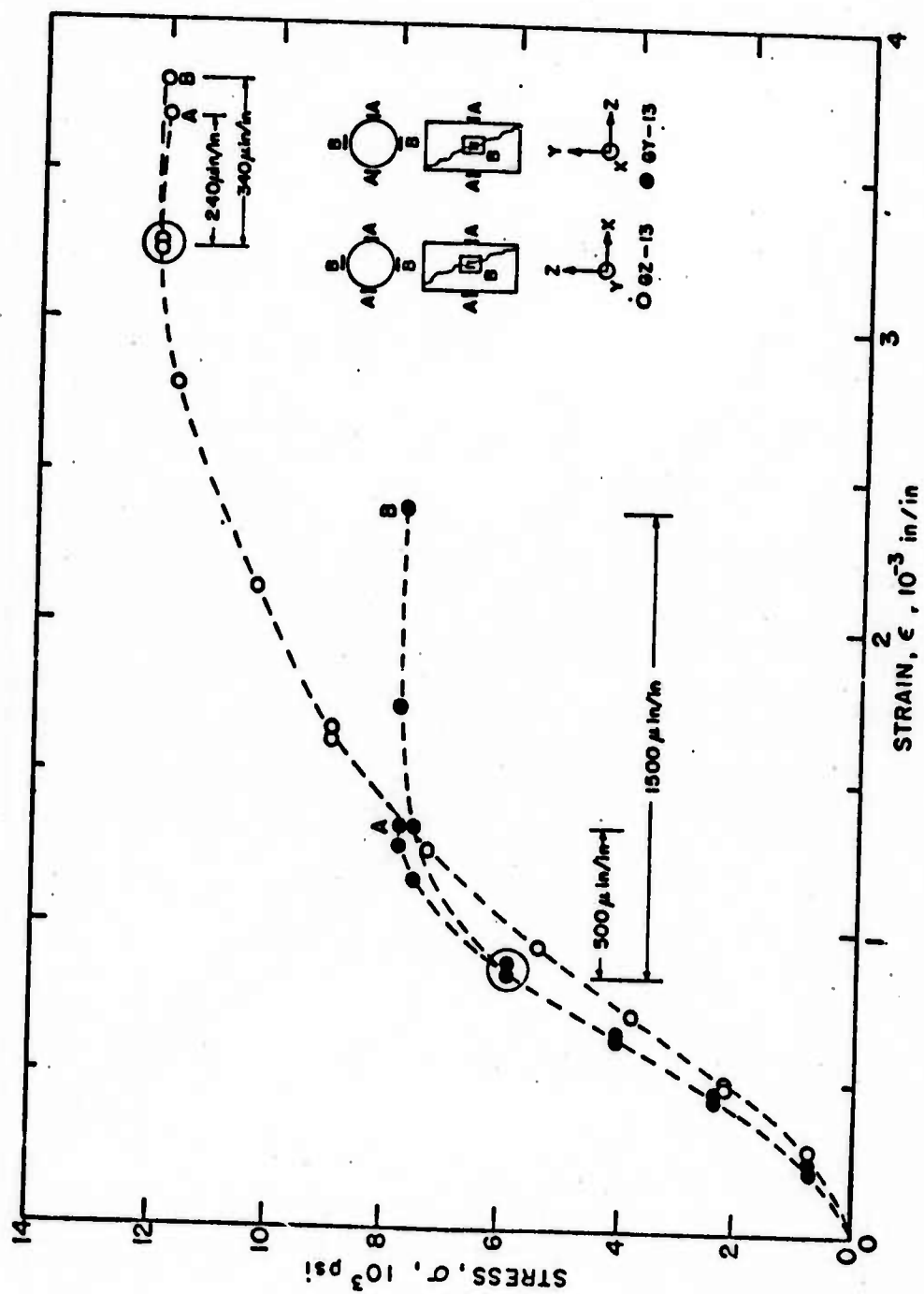


FIG. 5

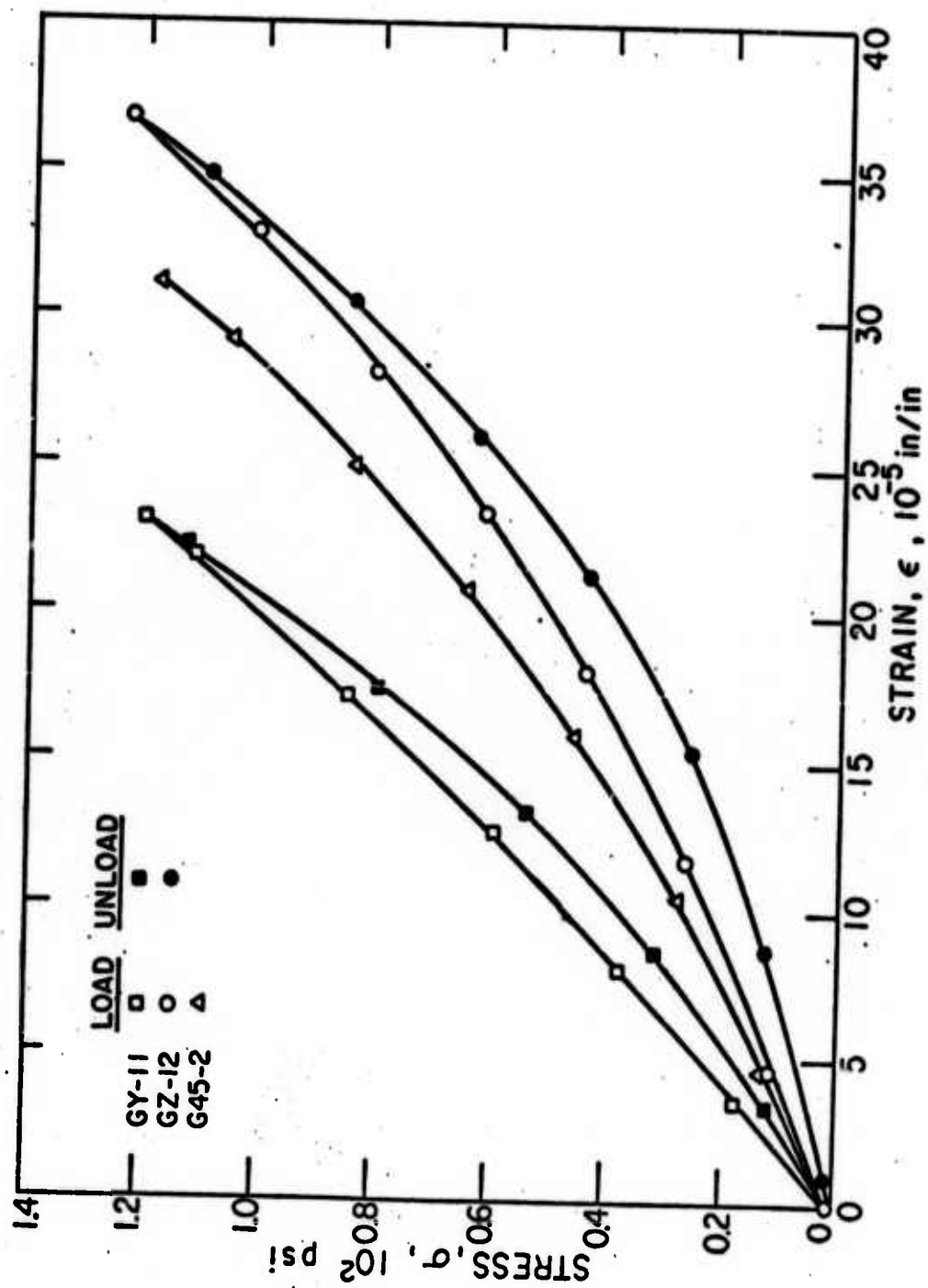
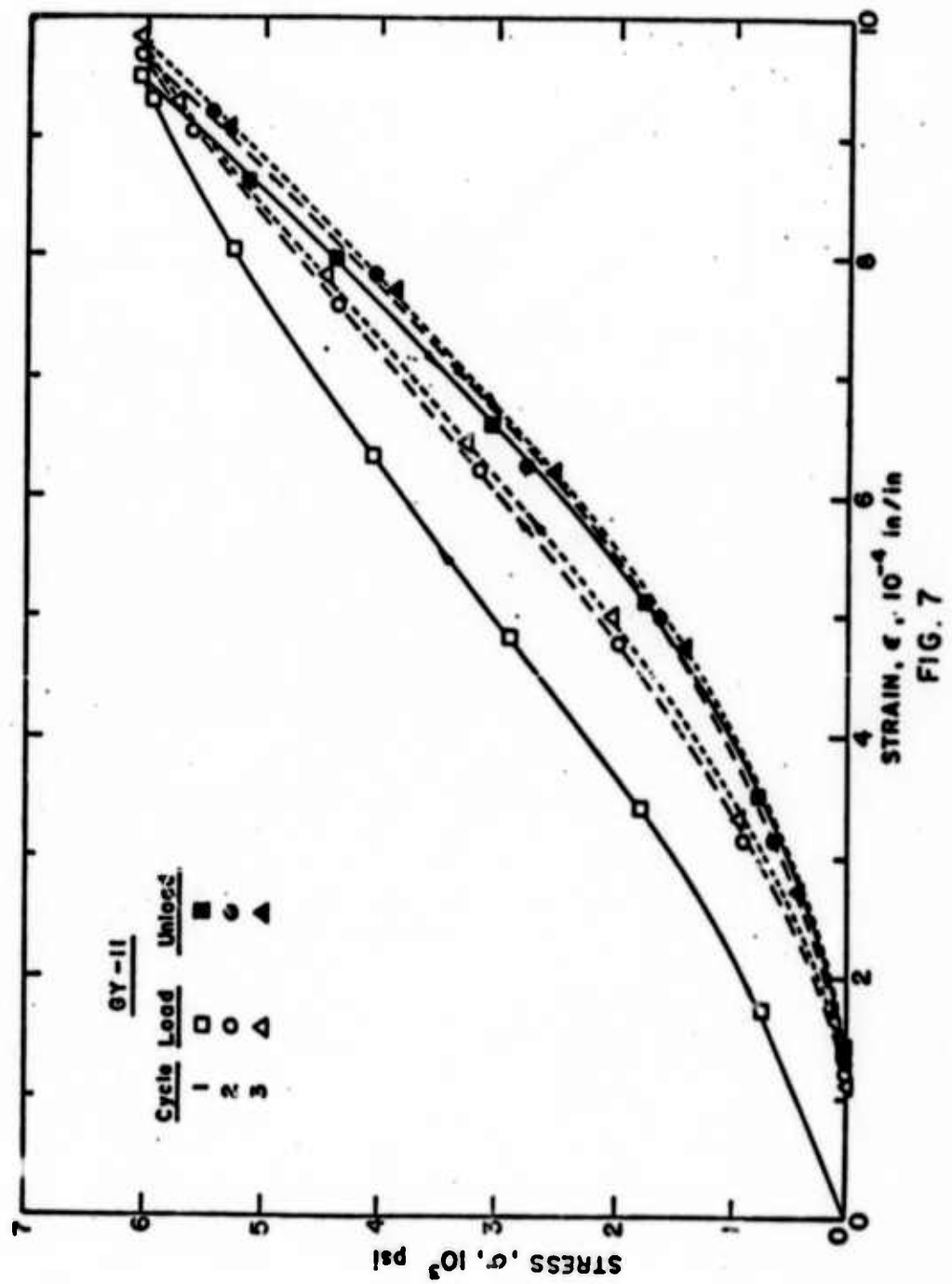


FIG. 6



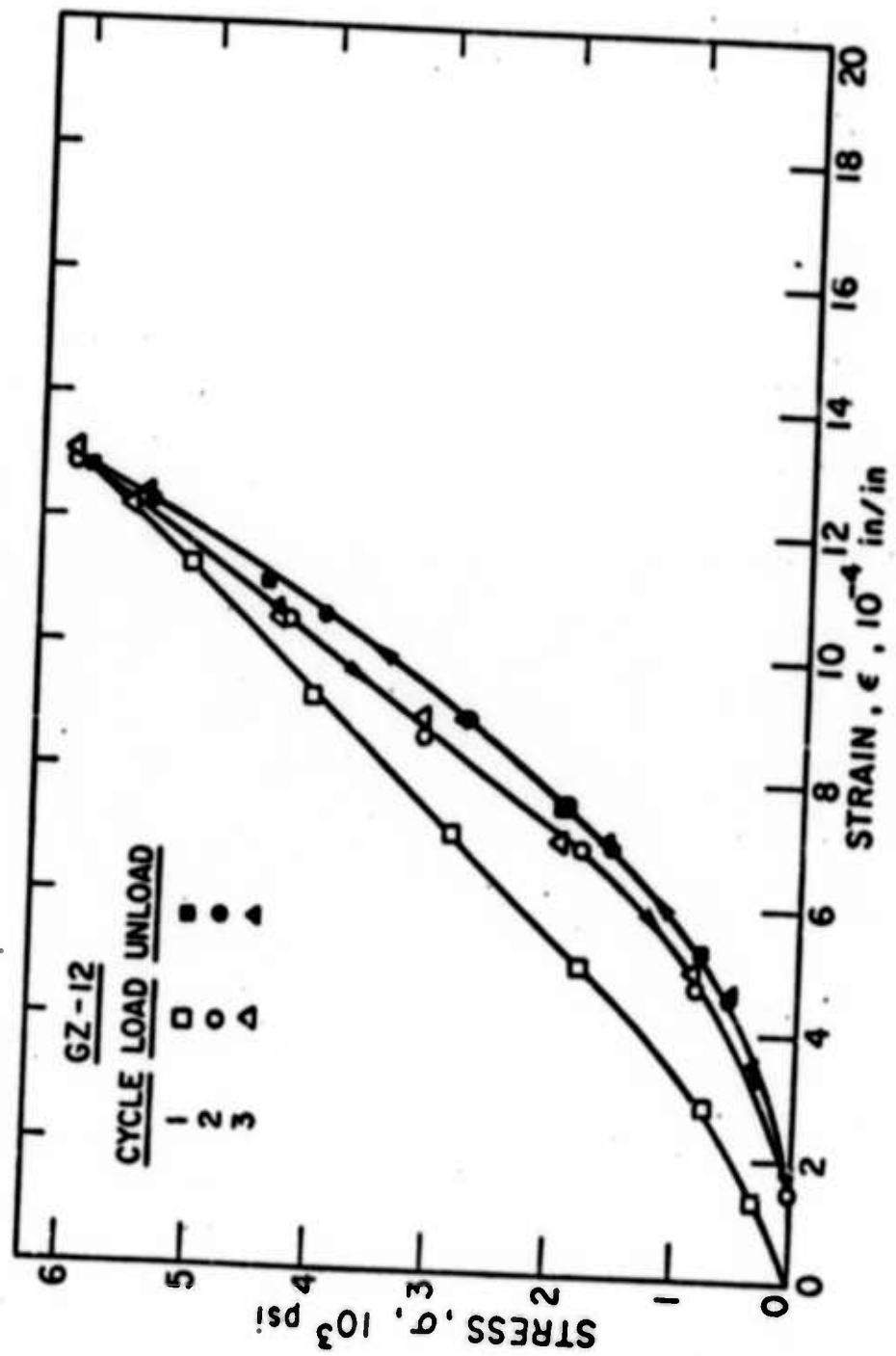


FIG. 8

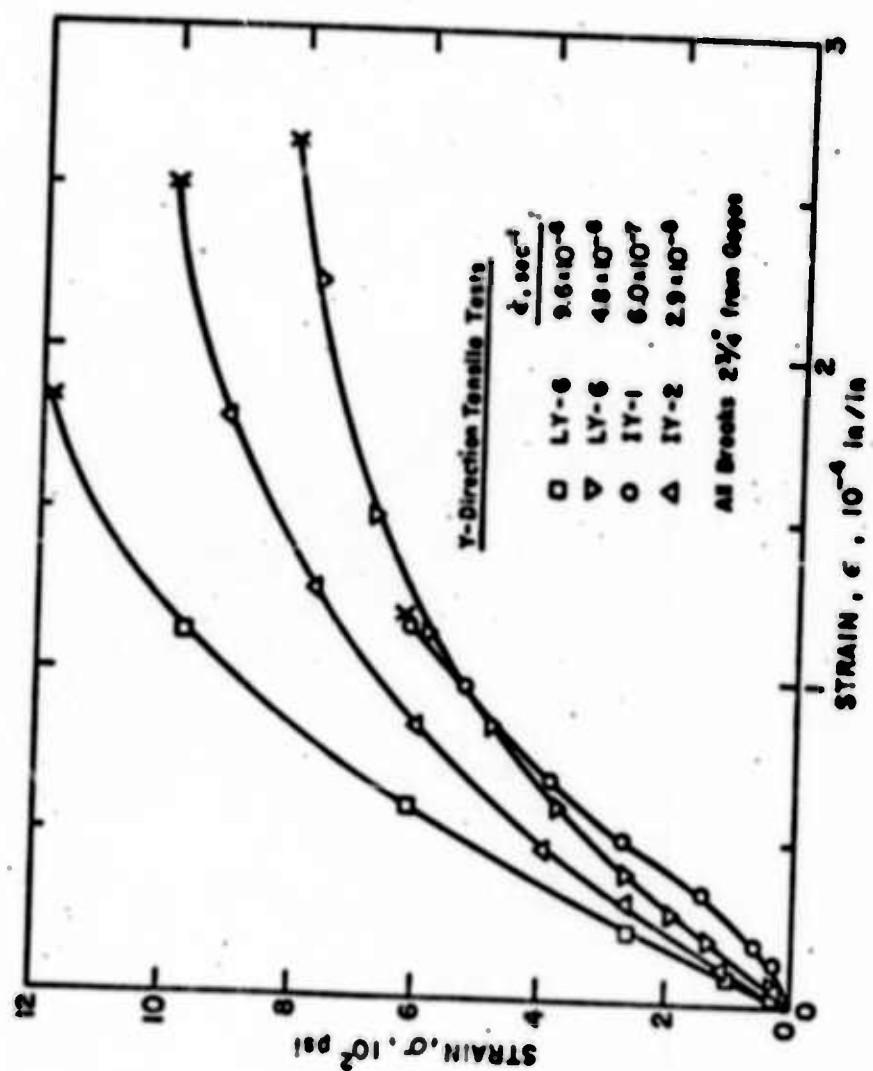


FIG. 9

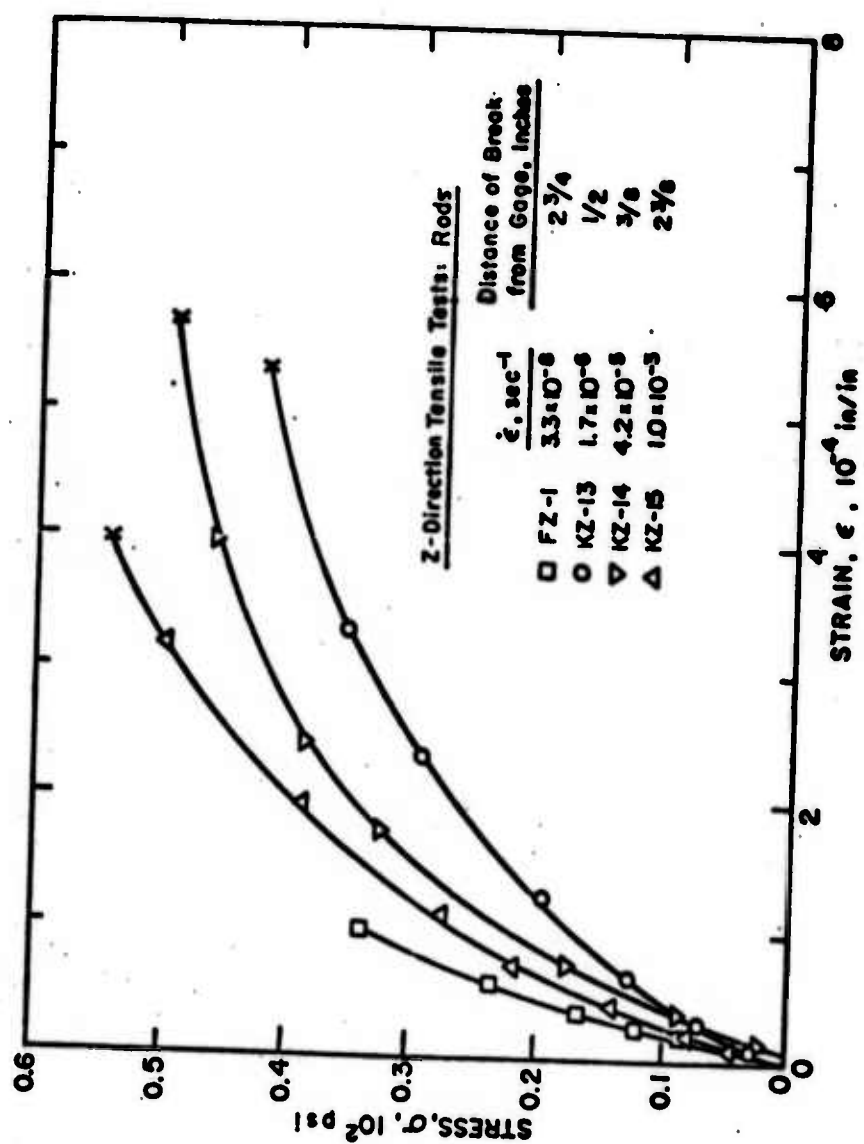


FIG. 10

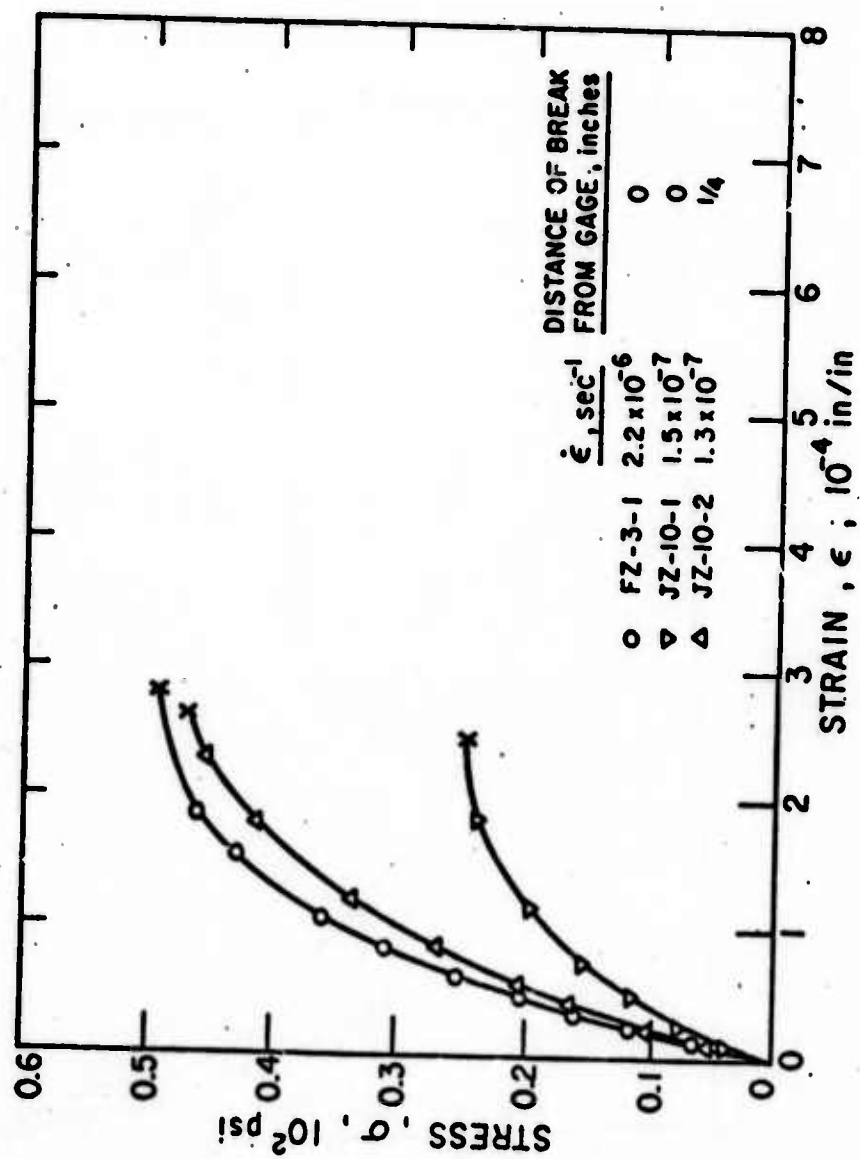


FIG. 11

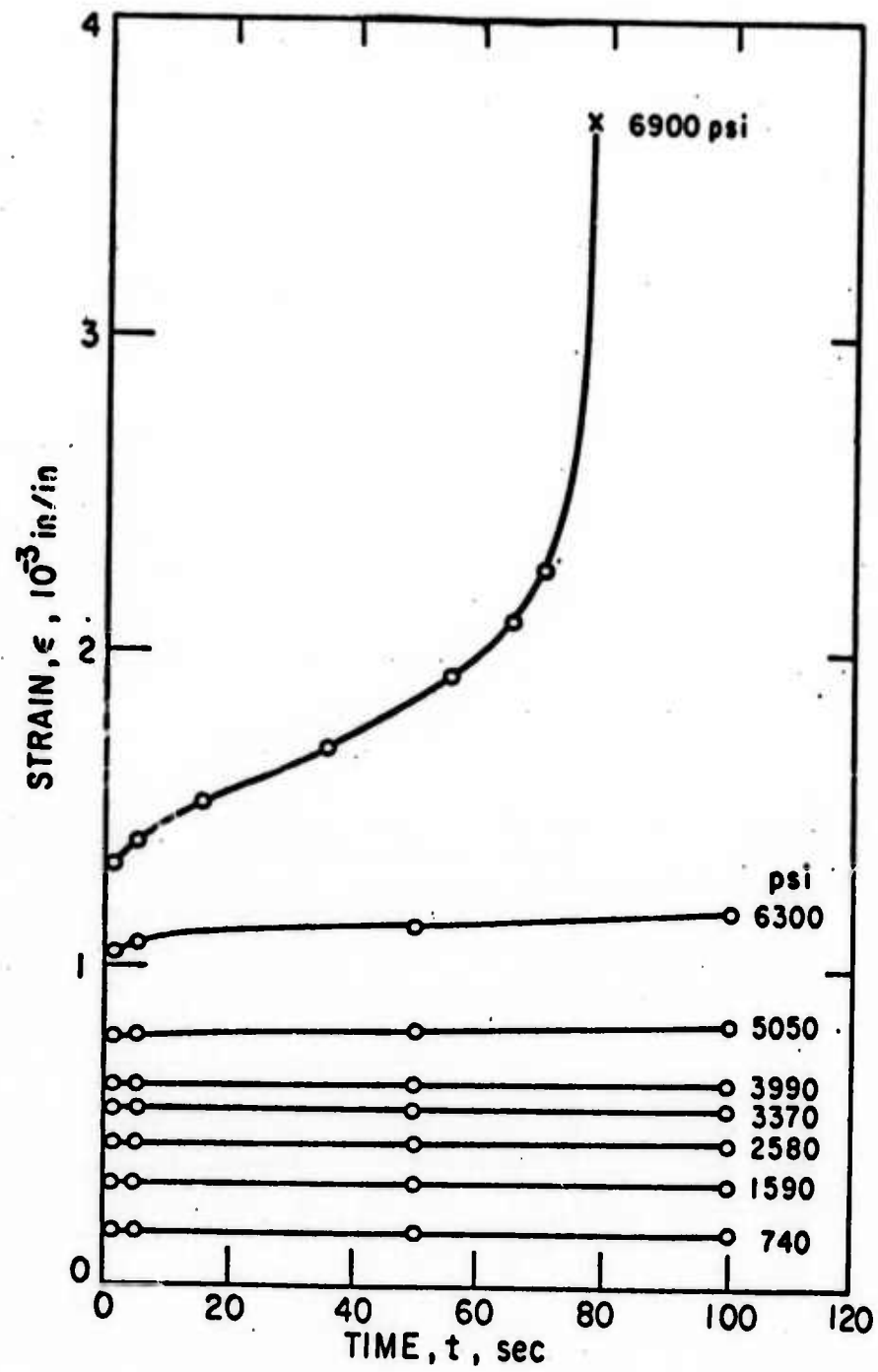


FIG. 12

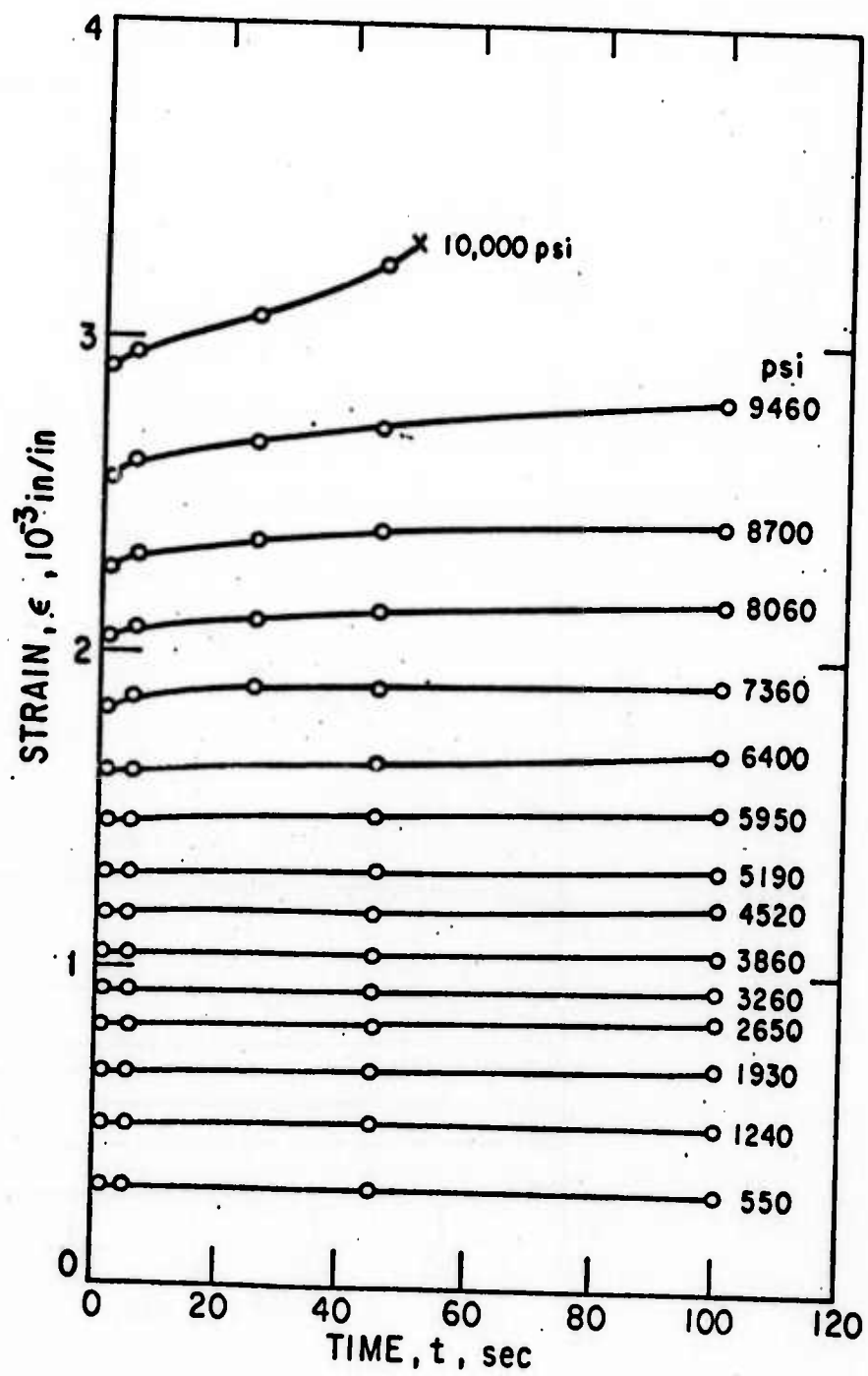


FIG. 13

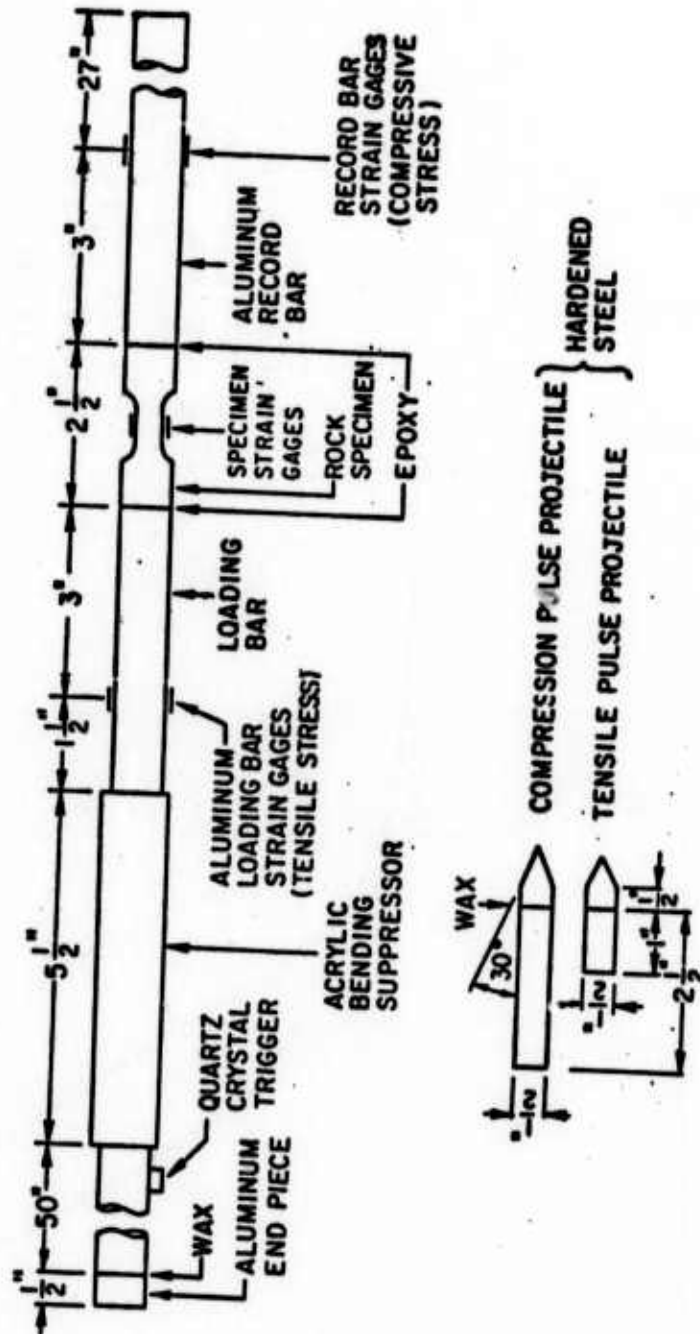


FIG. 14

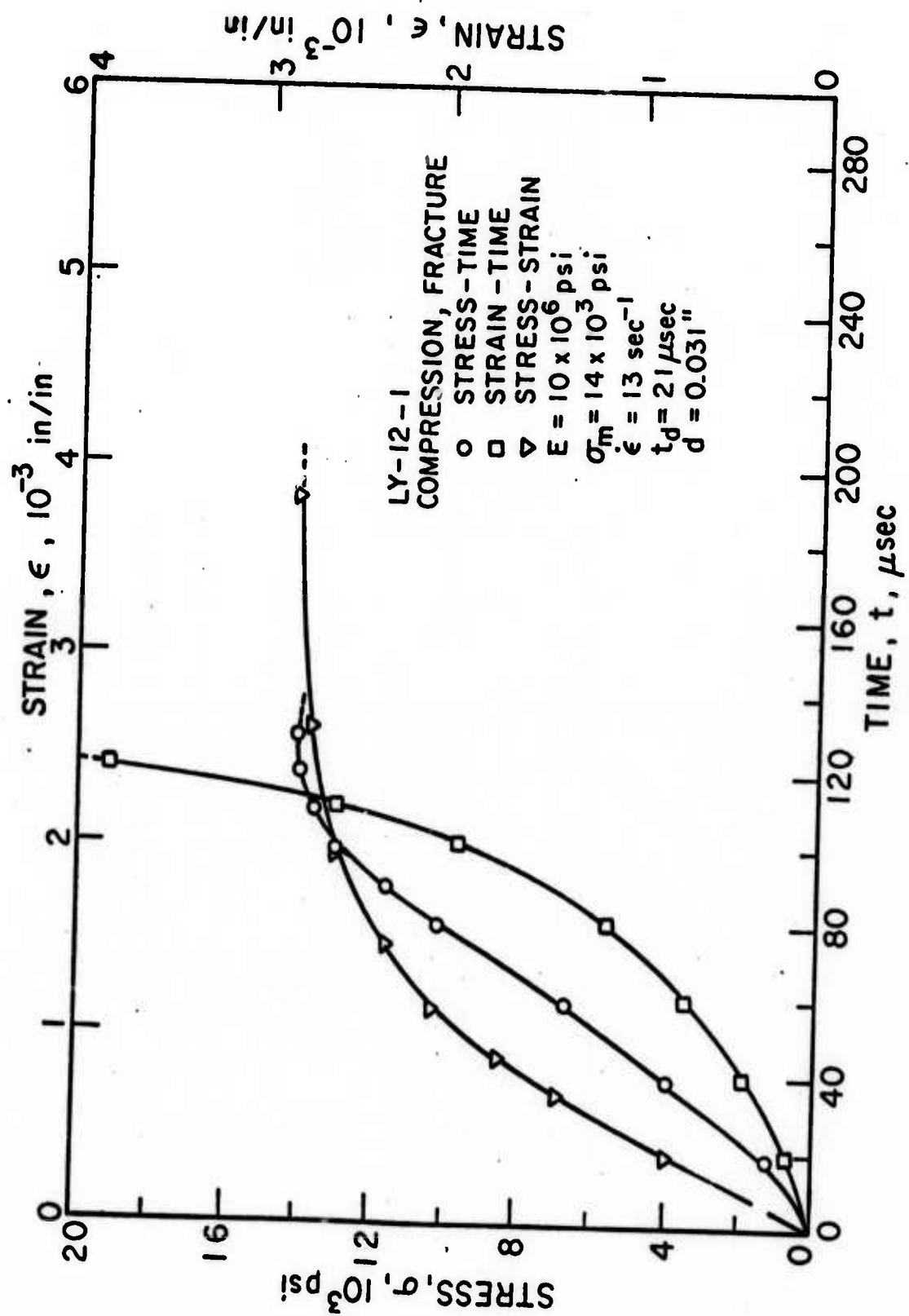


FIG. 15

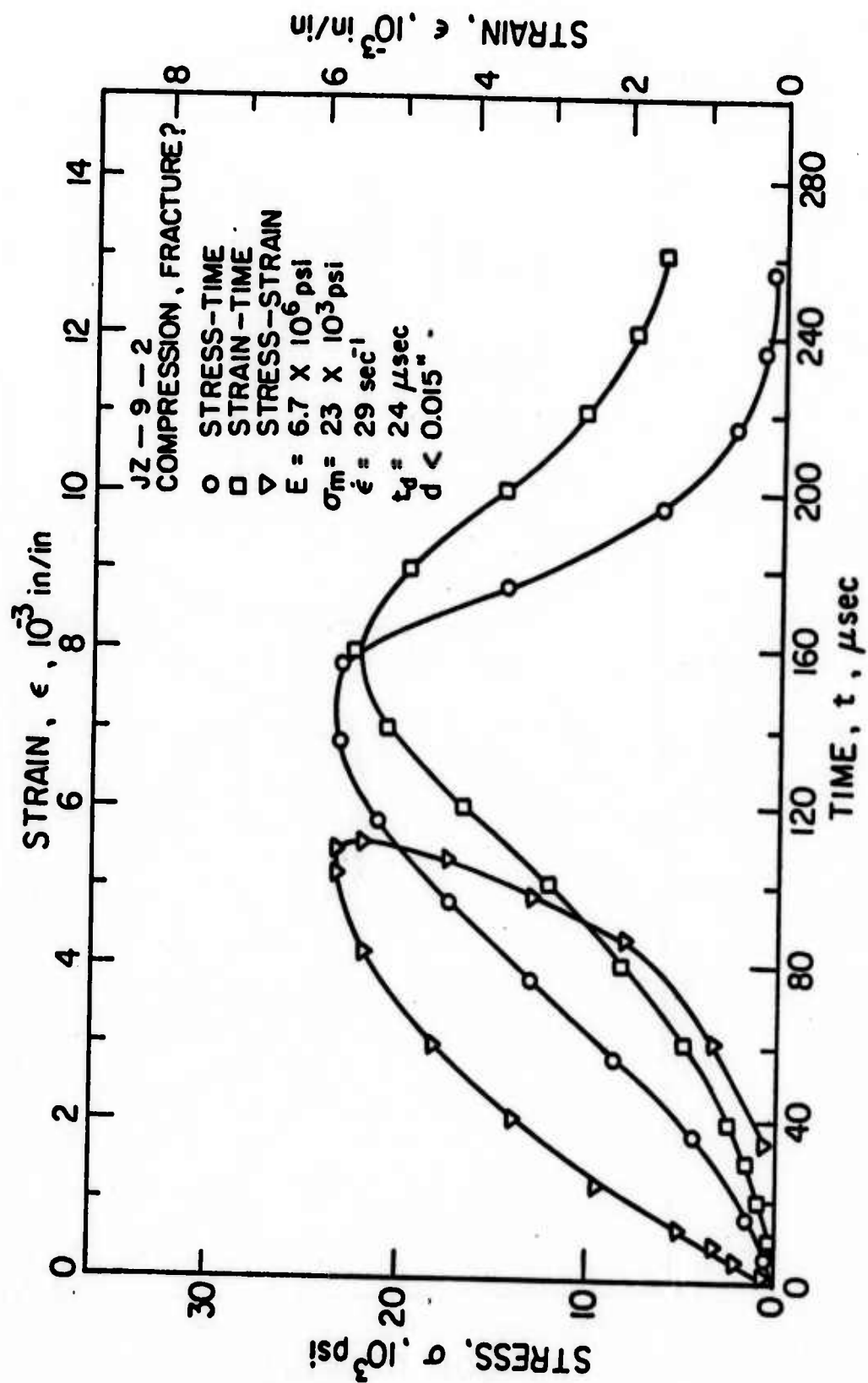


FIG. 16

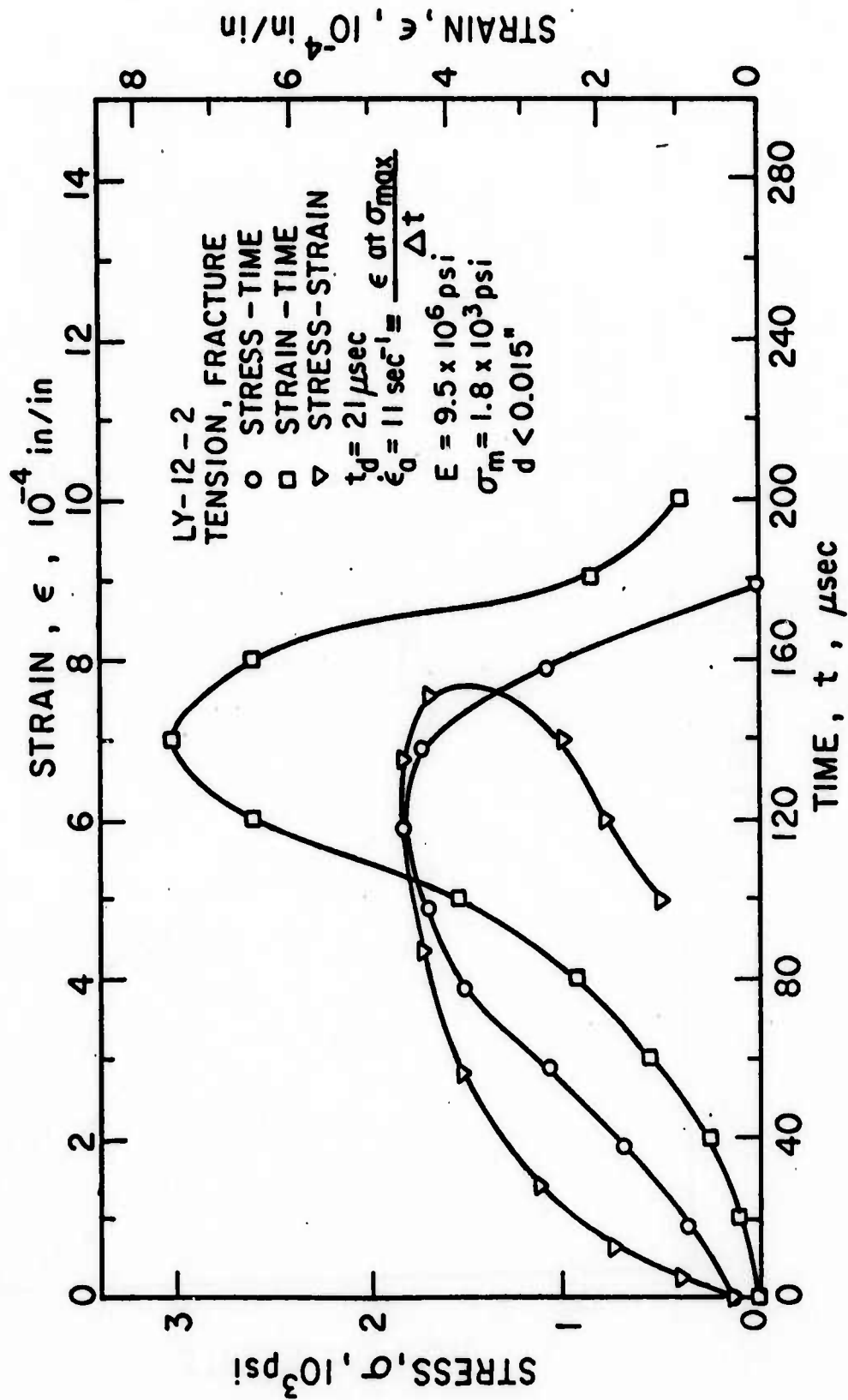


FIG. 17

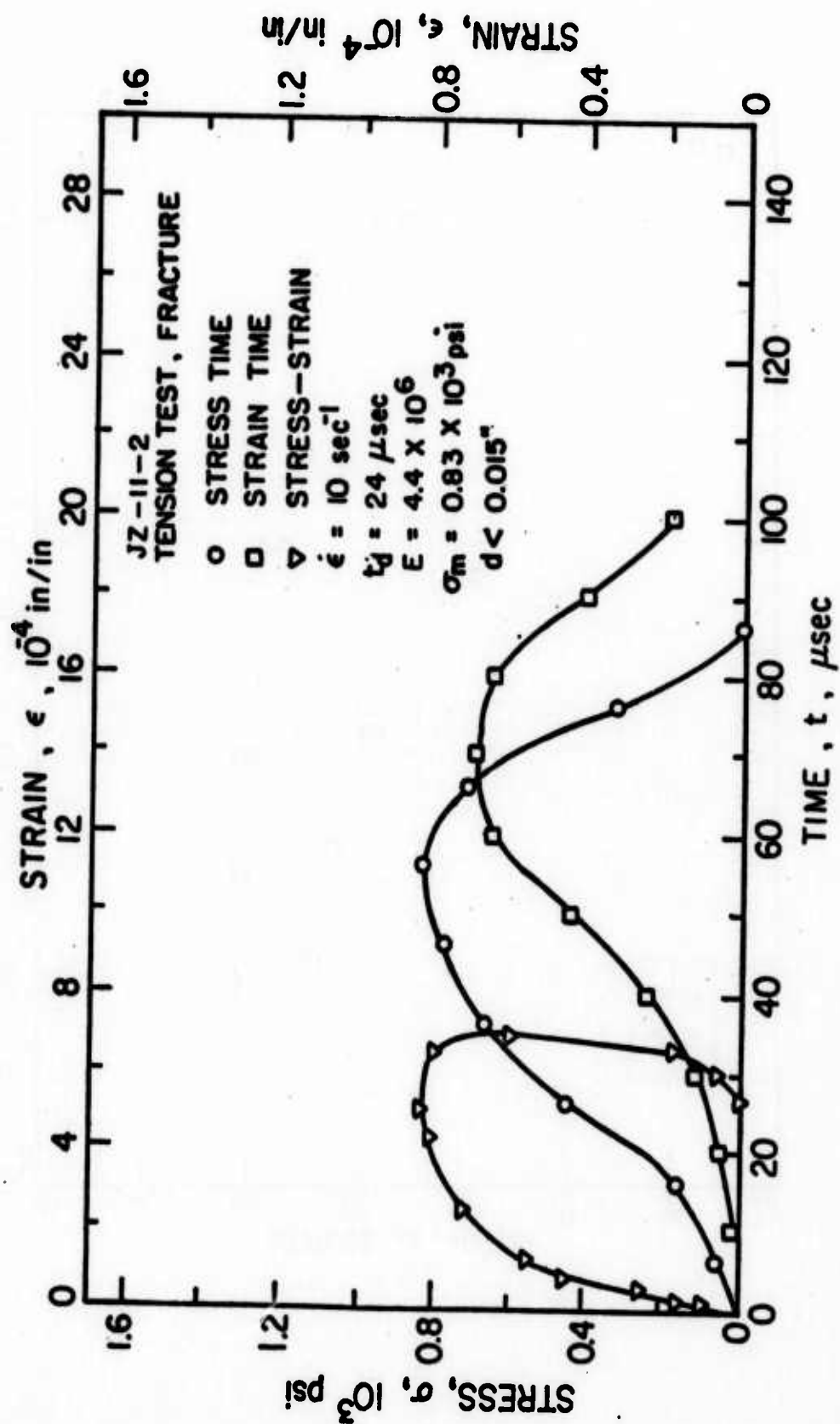


FIG. 18

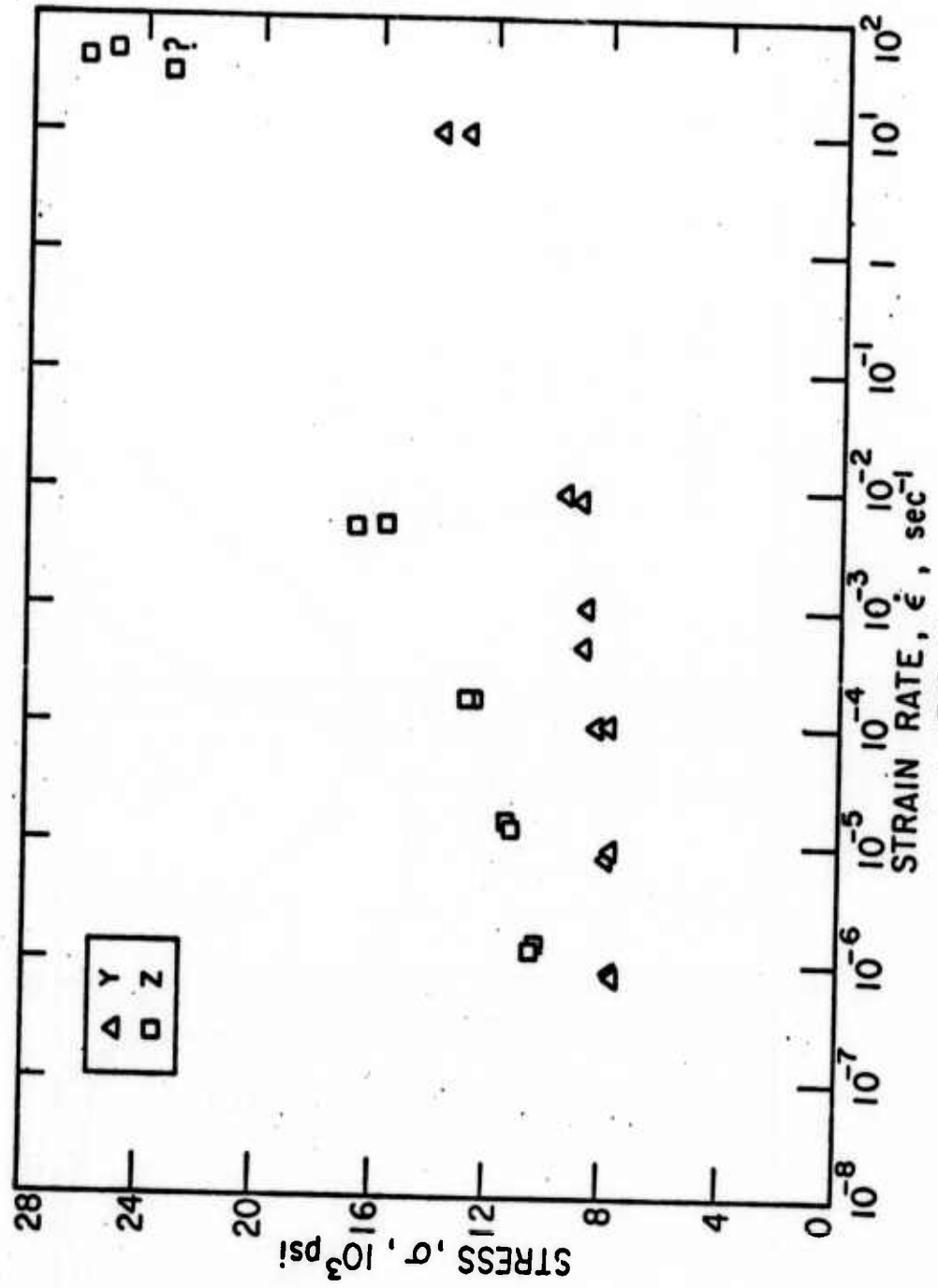


FIG. 19

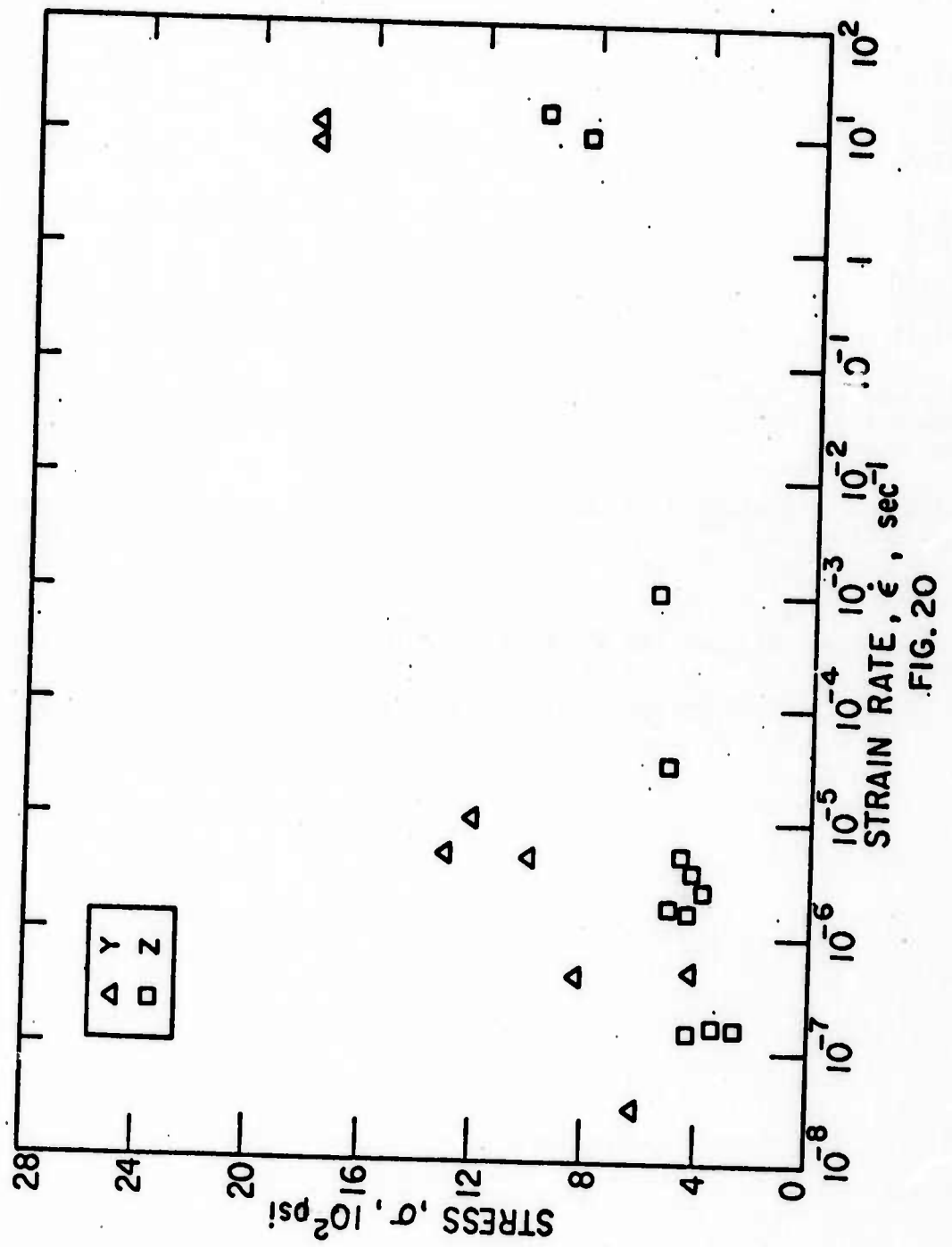


FIG. 20

TABLE 1: QUASI STATIC TENSILE TEST RESULTS

SPECIMEN	GEOMETRY	$\dot{\epsilon}$ sec ⁻¹	$\dot{\epsilon}_m$ sec ⁻¹	E_1 X10 ⁶ psi	E_{26} X10 ⁶ psi	σ_m 10 ³ psi	ϵ_m µin/in	σ_f 10 ³ psi	x_g^* inches
IY-1	6"x3/4"D	2.8X10 ⁻⁸	-	6.7	-	.62	120	-	2-3/4
IY-2	"	5.8X10 ⁻⁶	-	7.8	-	1.0	250	-	2-3/4
LY-5	"	4.9X10 ⁻⁶	-	9.6	-	.83	270	-	2-3/4
LY-6	"	1.0X10 ⁻⁵	-	11.0	-	1.2	180	-	2-3/4
FZ-1	"	1.7X10 ⁻⁷	-	4.2	-	.34	100	-	2-3/4
FZ-3	"	4X10 ⁻⁶	-	-	-	.41	-	-	-
KZ-13	"	1.7X10 ⁻⁶	-	2.3	-	.42	540	-	1/2
KZ-14	"	4.2X10 ⁻⁵	-	3.2	-	.50	570	-	3/8
KZ-15	"	1.0X10 ⁻³	-	3.2	-	.55	400	-	2-3/8
FZ-3-1	S.C. **	2.2X10 ⁻⁶	-	4.8	-	.49	280	-	0
JZ-10-1	"	1.5X10 ⁻⁷	-	3.8	-	.25	250	-	0
JZ-10-2	"	1.3X10 ⁻⁷	-	4.2	-	.46	260	-	1/4
EY-3	2"x1.05"D	8.6X10 ⁻⁶	2.4X10 ⁻⁴	6.3	8.3	7.6	3290+	7.4	-
LY-11-1	S.C. **	1.1X10 ⁻⁵	4.0X10 ⁻⁵	10.5	9.4	8.0	865	6.6	-

* x_g is the distance of fracture path from gage.

** S.C. Special contour specimen

TABLE 2: AVERAGE VALUES OF HOPKINSON BAR TEST RESULTS

MODE Tens. Comp.	Rod Wave Velocity $c_o, 10^3 \text{ in/sec}$	Dynamic Elastic Constant	Approximate Strain Level, $\mu\text{in/in}$
C	210 ± 5	$E_d = 11.6 \pm 0.7 \times 10^6 \text{ psi}$	70
T	205 ± 5	$E_d = 10.8 \pm 0.6 \times 10^6 \text{ psi}$	55
C	140 ± 2	$E'_d = 4.9 \pm 0.2 \times 10^6 \text{ psi}$	145
T	112 ± 4	$E'_d = 3.2 \pm 0.4 \times 10^6 \text{ psi}$	80
C,T	152 ± 2	$G'_d = 4.3 \pm 0.3 \times 10^6 \text{ psi}$	120
C	----	$\mu_d = 0.29 \pm 0.01$	75
T	----	$\mu_d = 0.24 \pm 0.03$	80
C	----	$\mu'_d = 0.13 \pm 0.01$	150
T	----	$\mu'_d = 0.09 \pm 0.01$	95

TABLE 3: SPLIT HOPKINSON BAR RESULTS

SPECIMEN	MODE Tens. Comp.	E_1 10^6 psi	$\dot{\epsilon}$ sec ⁻¹	σ_m 10^3 psi	ϵ_{max} μin/in
LY-13-1	C	10	11	13	3000*
LY-12-1	C	10	13	14	3800*
JZ-9-2	C	6.7	29	23*	5500*
JZ-9-1	C	6.7	40	26	8500
JZ-11-1	C	7.3	45	25	7700
LY-13-2	T	13.0	8	1.8	700
LY-12-2	T	9.5	11	1.8	770
JZ-12-1	T	2.8	16	.97	1200*
JZ-11-2	T	4.4	10	.83*	650*

* Uncertain

TABLE 4: STATIC AND DYNAMIC ELASTIC CONSTANTS FOR THE YULE MARBLE BLOCK AND SLAB

Elastic Constants c_{ij} , 10 ⁶ psi	Marble Block Static Tests (9)	P-Wave Tests (10)	Present Internal Crystal Velocity Measurements	Present Hopkinson Bar Tests Specimens Obtained from SLAB
c_{11}	9.66	14.30	11.22	13.68
c_{12}	3.12	4.37*	3.82	4.7
c_{13}	2.90	5.35	2.52	2.39
c_{33}	8.48	10.48	7.25	5.62
c_{44}	1.90	2.39	3.33	4.30

* Increased by 40 percent over its static value.